ELECTRON TRANSPORT AND NOISE IN MAGNETIC TUNNEL JUNCTIONS WITH MgO BARRIER

David Herranz Aragoncillo

Departamento de Física de la Materia Condensada

Universidad Autónoma de Madrid

Submitted in Partial Fulfillment of the Requirements for the Degree of Doctor of Physics Science

Thesis supervisor: ***Farkhad Aliev Kazanski***

March 2012

List of publications

1. **D. Herranz**, A. Gomez-Ibarlucea, M. Schafers, A. Lara, G. Reiss, and F. G. Aliev, "Low frequency noise due to magnetic inhomogeneities in submicron FeCoB/ MgO/ FeCoB magnetic tunnel junctions", *Appl. Phys. Lett.*, vol. 99, pp. 062511 (2011)

2. **D. Herranz**, F. G. Aliev, C. Tiusan, M.Hehn, V. K. Dugaev and J. Barnas, "Tunneling in Double Barrier Junctions with "Hot Spots"", *Phys. Rev. Lett.*, vol. 105, pp. 047207 (2010)

3. **D. Herranz**, F. Bonell, A. Gomez-Ibarlucea, S. Andrieu, F. Montaigne, R. Villar, C. Tiusan, and F. G. Aliev, "Strongly suppressed 1/f noise and enhanced magnetoresistance in epitaxial Fe-V/ MgO/ Fe magnetic tunnel junctions", *Appl. Phys. Lett.*, vol. 96, pp. 202501 (2010)

4. **D. Herranz**, R. Guerrero, R. Villar, F.G. Aliev, A.C. Swaving, R.A. Duine, C. van Haesendonck, I.Vavra, "Anomalous low-frequency noise in synthetic antiferromagnets: Possible evidence of current-induced domain-wall motion", *Phys.Rev.B*, vol. 79,pp. 134423 (2009)

5. F. G. Aliev, R. Guerrero, **D. Herranz**, and R. Villar, F. Greullet, C. Tiusan, and M. Hehn, "Very low 1/ f noise at room temperature in fully epitaxial Fe/ MgO/ Fe magnetic tunnel junctions", *Appl. Phys. Lett.*, vol. 91, pp.232504 (2007)

6. R. Guerrero, **D.Herranz**, F.G. Aliev, F. Greullet, C. Tiusan, M. Hehn, and F. Montaigne, "High bias voltage effect on spin-dependent conductivity and shot noise in carbon-doped Fe(001)/

MgO(001)/ Fe(001) magnetic tunnel junctions", *Appl. Phys. Lett.*, vol. 91, pp. 132504 (2007)

7. **D. Herranz**, R. Guerrero, Juan P. Cascales, F.G. Aliev, M. Hehn and C. Tiusan, "Strong reduction of 1/f noise by Carbon doping in epitaxial Fe/MgO(100)12ML/Fe magnetic tunnel junctions with barrier defects", Invited paper to be published in proceeding of European Conference Physics of Magnetism PM'11, Acta Phys. Pol., B (accepted, 2012)

Me han dicho que hay vida después de la Tesis.....

Creo que voy a investigarlo

A Guada y Adriana con mucho cariño

Agradecimientos

Me gustaría empezar agradeciendo su apoyo y paciencia a los miembros con los que he trabajado del grupo MAGNETRANS, codo con codo, en estos años. Destacar, en primer lugar, a mi director de tesis, Farkhad Aliev, quien me ha permitido iniciar mi carrera en este mundo científico. Gracias a él he aprendido que con esfuerzo, perseverancia y sacrificio se pueden lograr tus objetivos. Pero, en mi hasta ahora breve carrera científica, he tenido la suerte de cruzarme en el camino con varias personas sin las que no habría podido finalizar este arduo trabajo. Rubén Guerrero, que no sólo me cedió un sistema experimental, sino que me guió en mis primeros pasos. De Raúl Villar y de Arkadi Levanyuk he aprendido mucho, gracias a su paciencia y a esas charlas de grupo que sabías cuando empezaban pero nunca cuando acababan. Raúl gracias por el tiempo que has tenido que invertir en la correción de mi tesis. Qué decir de Ahmad Awad (y su "mucho chau chau, pero poco guao guao"), gracias por tener siempre una crítica constructiva y soportarme tantas veces fuera de nuestra tierra. A Juan F. Sierra decirle que por fín podemos medir ruido de alta frecuencia!!!, que nos ha costado más de un disgusto. Del señor Volodia sólo podría tener buenas palabras y por supuesto una sonrisa. A Juan Pedro Cascales gracias por revisarme siempre el ingles, a Antonio Lara por esas simulaciones tan chulas y a Andrés Gomez por su trabajo.

Agradecer a todo el Dpto. de Física de la Materia Condensada, en especial a bajas temperaturas, y al IMDEA por haberme abierto sus puertas. También me gustaría destacar a todos los técnicos que me han ayudado (Santiago, José Luis, Rosa, Juanma, Andrés). Agradecer

también al SEGAINVEX su apoyo, en especial a Manolo y Jose por su suministro continuo de He. Así como a Elsa que siempre nos ha ayudado con tanto papeleo. Y a Macarena, por hacer que sea agradable estar en el laboratorio.

I would like to thank the Poincare University Nancy for their hospitality and collaboration in these years and C. Tiusan, S. Andrieu, M. Hehn, F. Bonell and F. Greullet for teaching me about the growth of magnetic tunnel junctions. I would also like to thank G. Reiss and M. Schäfer for those submicrom magnetic tunnel junctions. To V. K. Dugaev, J. Barnaś and A. C. Swaving and R. A. Duine, because your theoretical support allowed us to explain our experimental results.

"Correr no solo te libera del sudor". A juzgar por los kms que he hecho con Tomás y Edu no nos deberían quedar muchas cosas encima. Gracias por compartir esos momentos.

A la vieja guardia del pabellón B (Oscar y Juanjo), a la menos vieja (Andrés y Guille) y a toda la nueva, muchas gracias por hacer de la comida la mejor parte del día. Bueno, y por alguna que otra fiestecilla...

Agradecer también a toda la gente que me ha hecho ser quien soy, mis padres, hermanos, abuelos, suegros, tios, primos, etc; a los del Lourdes, a esos alpedreteños y a los que son un poco membrillos.

Por último, quisiera agradecer y dedicar esta tesis a mis chicas. Sin ellas no hubiera tenido las fuerzas necesarias para llegar a la meta. Os querré siempre.

Abstract

Recientemente Albert Fert y Peter Grünberg han sido galardonados con el premio Nobel de Física por el descubrimiento de la magnetorresistencia gigante (GMR) y el fenómeno de acoplamiento antiferromagnético [1, 2]. Este descubrimiento [1, 2] abrió un nuevo campo de la física conocido como "espintrónica"o, a veces también llamado "magnetoelectrónica", que crea e investiga dispositivos donde el espín de los electrones, además de la carga, juega un papel importante en los procesos de transporte. Todo empezó a finales de los años ochenta, cuando Grünberg y coautores demostraron el acoplamiento intrínseco en capas de hierro (Fe) a través de cromo (Cr). Más tarde su grupo, así como el de Albert Fert, comprobaron que, alternando capas nanométricas de estos metales, se podía modificar (a voluntad) la dirección de espín de los electrones sobre las capas de Fe. La espintrónica explora un nuevo grado de libertad suplementario del electrón, el espín (momento magnético interno de electrón), que es una propiedad cuántica. En presencia de un eje determinado, el espín del electrón puede tener dos estados posibles: "up"o "down". En su primera charla sobre historia y descubrimiento de la GMR presentada en la Escuela Nicolás Cabrera "MAGNETIC NANOSTRUCTURES"en el año 2004, Albert Fert subrayó que fue la primera vez que se aprovechó la influencia del espín de los electrones en su movilidad para crear dispositivos nanométricos.

El estudio de las propiedades fundamentales en sistemas espintrónicos ha ido acompañado durante las últimas dos décadas por la creación de nuevos tipos de materiales magnetoelectrónicos como son los basados en el efecto de la GMR. Debido a su rápida incorporación en dispositivos funcionales, los sistemas espintrónicos representan un ejemplo fascinante de transición rápida entre la fase de investigación hasta su posterior aplicación tecnológica. De hecho, el primer instrumento comercializado basado en GMR y utilizado como sensores de campo magnético apareció en 1994 [3], solo seis años después de su descubrimiento, y las cabezas lectoras/escritoras de disco duro fueron incorporadas en ordenadores por IBM en 1997 [4]. Posteriormente, fue sustituido el espaciador no magnético (Cr, Cu, etc) por una barrera aislante de tipo AlO_x o MgO [5, 6, 7, 8]. Este tipo de dispositivos se conoce como unión túnel magnética y ha alcanzado valores de magnetorresistencia superiores a los obtenidos gracias a la GMR. El fenómeno de la magnetorresistencia túnel (TMR) ha sufrido recientemente un gran desarrollo con la incorporación, en su estructura, de barreras de tipo MgO [9, 10], permitiendo así un túnel coherente en la unión. La utilización de este nuevo tipo de cabezas en los discos duros supone un enorme incremento de su capacidad. Gracias al fenómeno de la TMR, así como de TMR inverso (current induced spin torque -CIST), como elementos principales de MRAM (Magnetic Random Access Memory), podemos aumentar aún más este impacto. La electrónica basada en el espín que incorpora procesos pasivos (TMR) así como activos (CIST) revolucionará la electrónica del futuro. Recientemente se están dando pasos para la integración de las tecnologías convencionales (basadas en el silicio) y las nuevas (basadas, por ejemplo, en nanotubos de carbono) en dispositivos magnetoelectrónicos.

Como ya he mencionado anteriormente, las estructuras magnéticas y espintrónicas, entre ellas multicapas (con o sin acoplamiento antiferromagnético) y uniones túnel magnéticas, han revolucionado las tecnologías de la información durante los últimos 20 años. Sin embargo, se conoce poco sobre las propiedades dinámicas de estos materiales, especialmente sobre el ruido a baja y alta frecuencia. El estudio de estas propiedades, sin embargo, tiene una gran importancia cuando estos materiales se utilizan como memorias magnéticas u otros dispositivos magnetoelectrónicos, como por ejemplo sensores de campo. El descubrimiento revolucionario llevado a cabo entre los años 2001-2004, realizado sobre el túnel coherente a través de la barrera de MgO, abrió nuevas expectativas, antes sin explorar. El objetivo general de esta Tesis ha sido realizar un estudio exhaustivo sobre el transporte electrónico y ruido de baja frecuencia en diferentes tipos de uniones túnel magnéticas (simples y dobles con barrera MgO), la mayoría relevantes para aplicaciones espintrónicas, con el fin de entender el origen de las fluctuaciones en la corriente túnel y poder optimizar su comportamiento en futuras aplicaciones.

Las uniones túnel magnéticas estudiadas en esta Tesis han sido crecidas gracias a la colaboración con diferentes universidades europeas(CNRS-Nancy University y la Universität Bielefeld). Los materiales que hemos estudiado incluyen uniones túnel magnéticas plenamente epitaxiales, con dopaje en la barrera y/o en los electrodos, con reestructuración en la intercara y con doble barrera aislante. Las uniones túnel magnéticas con doble barrera tienen como ventaja, sobre las simples, que debido a su electrodo central se poduce túnel resonante por estados cuánticos bien definidos en el electrodo central. También se han investigado nanopilares magnéticos de tamaño submicrométrico, los cuales

tienen una gran importancia en el campo tecnólogico. Así pues, esta Tesis pretende profundizar en el conocimiento del transporte túnel, en los materiales anteriormente mencionados, con particular atención en uniones túnel magnéticas plenamente epitaxiales con barrerera de MgO en función del voltaje aplicado, campo magnético y temperatura.

Para medir el transporte túnel y el ruido de baja frecuencia nos hemos basado en el sistema experimental descrito en la Ref. [11]. En el desarrollo de esta Tesis, se ha mejorado dicho sistema, con lo que nos ha permitido tener mayor eficacia (tanto en el tiempo de medida, como en en la capacidad de medir mayor número de muestras) y mayor precisión en las medidas. Para minimizar la contribución electrónica del sistema experimental se ha aplicado la técnica de cuatro terminales. El sistema experimental consta de dos etapas de amplificación. En la primera etapa, se amplifica la señal tanto AC como DC de la muestra (usando preamplificadores construidos en nuestro laboratorio). En la segunda etapa, se filtra la parte DC y se amplifica únicamente la parte AC hasta cerca de un millón de veces, y posteriormente se medirá en un analizador de espectros hasta 102 kHz. Utilizando la transformada de Fourier de la señal se puede medir en el espacio de frecuencias y con la técnica de correlación cruzada obtendremos mayor precisión en las medidas realizadas.

También se incluyen medidas de ruido de disparo en las que se precisa el uso de bajas temperaturas para reducir así el valor de ruido térmico de la muestra bajo estudio. Con este fin se ha utilizado un sistema criogénico basado en un sistema He-3 que permite aplicar campo magnético vectorial. El ruido de disparo ofrece información acerca del proceso túnel en la barrera. En una unión túnel magnética sin defectos

se espera que el túnel sea directo, es decir que cada electrón que llegue a la barrera la cruce. Para ello, se determinará el factor de Fano (ruido de disparo normalizado respecto al ruido Poissoniano) en función del estado magnético y del voltaje aplicado al dispositivo. Con este tipo de medidas se puede determinar la presencia de defectos dentro de la barrera y estimar su localización (simétrico o antisimétrico respecto al centro de la barrera) [12]. Se espera que las medidas del factor de Fano en función del voltaje aplicado, permitan determinar la posible presencia de estados resonantes dentro de barrera.

El principal foco de atención de esta Tesis será el estudio de ruido 1/f, dado que su origen no es del todo conocido, aunque esté presente en prácticamente cualquier elemento resistivo. El modelo fenomenológico más utilizado para describirlo es el propuesto por Hooge en 1981 [13]. Por ello en esta Tesis hemos querido profundizar en su estudio. Las medidas de ruido 1/f se han realizado en función del estado magnético del dispositivo así como del voltaje aplicado. En el estado paralelo, lejos de la transición, el ruido 1/f es atribuido al tiempo de relajación de los defectos dentro o en la intercara de la barrera. En las medidas de ruido 1/f en el estado paralelo, hemos buscado la posible anticorrelación entre los valores de TMR y ruido 1/f de origen no magnético, debido a la presencia inevitable de defectos en la barrera. En cooperación con la Universidad Poincarè de Nancy, hemos buscado regímenes de crecimiento de uniones túnel magnéticas (dopando los electrodos con carbon o vanadio) que nos han llevado a la reducción de valores de ruido no magnético normalizado. Se ha investigado la dependencia del ruido 1/f y su dispersión en función de la corriente aplicada para ambos estados magnéticos (paralelo y antiparalelo). Como es de esperar, el ruido 1/f en el estado antiparalelo tiene una contribución fuertemente

magnética, con lo que hemos buscado posibles influencias de la corriente de espín polarizada sobre la estabilidad de dominios magnéticos que determinan el valor de ruido .

Por otro lado, en los últimos años, se está reduciendo el tamaño de los dispositivos magnéticos para poder alcanzar así mayores densidades de grabación en memorias magnéticas. Por este motivo, es necesario profundizar el estudio de transporte y ruido de baja frecuencia en uniones túnel magnéticas de tamaño submicrométrico a temperatura ambiente. Hemos realizado un estudio detallado en este tipo de uniones aplicando densidades de corriente elevadas (del orden de 2×10^6 A/cm^2 cerca del regimen de transferencia del momento de espín), observando una gran influencia del momento magnético con el área del electrodo magnéticamente blando.

Contents

1

Introduction

1. Introduction

1.1 Brief historical introduction and motivation:

The progress in the development of new techniques of the growth of thin films and the development of concept of spin-polarized current, permitted to discover in late 80th the giant magnetoresistance (GMR) phenomenon [1, 2], awarded by Nobel price in physics in 2007 to Albert Fert and Peter Grünberg. This discovery lead to the development of a new branch in nanoscience - "spintronic". The GMR is a quantum mechanical *(spin related)* magnetoresistance effect observed in metallic thin film structures with ferromagnetic layers separated by non-magnetic metallic layers (*magnetic multilayers, MMLs*). Another big step forward came from the replacing the non-magnetic metallic spacer layer by a non-magnetic insulating layer, thus creating a magnetic tunnel junctions (MTJ) and observation of the tunneling magnetoresistance (TMR) effect [14]. These devices consist of two or more (as in Double Magnetic tunnel Junctions, DMTJs) ferromagnetic electrodes separated by a thin insulating barrier(s). Depending on the relative direction of the magnetization of the ferromagnetic layers is possible to obtain two (or more) different magnetic states with different related resistance values. In the simplest case of trilayers, one has transition between who states only: parallel (P) and antiparallel (AP) states. The first experimental evidence of the TMR was reported by M. Julliere in 1975 in his PhD Thesis and related publication [14]. Julliere used two electrodes (Fe and Co) separated by an insulating germanium barrier. He observed a tunnel magnetoresistance (TMR = $(R_{AP}$- $R_P)/R_P$) of 14% only at low temperature (T=4.2K). Since then, for almost 20 years, different groups tried to improve the quality of the MTJ devices, making then functional and robust at room temperatures. This objective was reached by two different groups [5, 6] simultaneously in 1995, who demonstrated, the possibility of large values of TMR (of about 15%) at room temperature, in MTJs with amorphous aluminium oxide barrier (Al−O). Since then, room temperature TMR values approached to 70% with Al_2O_3 barriers [4]. Trying to find more accurate devices with high magne-

toresistance (MR) ratios, a new barrier, in order to use coherent spin-dependent tunneling in epitaxial MTJ with crystalline tunnel barrier such as MgO (001), have been introduced [7, 8]. In the actually, exceeded roughly 600% [15], making these MTJs suitable for various industrial applications.

The record high room temperature TMR values in MTJs with MgO barrier lead to "technological revolution" in spintronics. This discovery initiated with theoretical calculations by W.H. Butler *et al.* [9] and J. Mathon *et al.* [10] who predicted coherent spin tunneling phenomena in single-crystal MTJs with bcc ferromagnetic Fe electrodes and MgO insulating barriers. It was shown numerically, that it is possible to reach several thousand percent of TMR, in the conditions of the high quality of the MgO barrier. However, experiments realized to verify this proposal, showed that the TMR is restricted by few hundred % [16]. The discrepancy is being debated and has been attributed to structural asymmetry of the interfaces, possibly due to dislocations and impurities, defects at the interface, interface oxidation and strain [16, 17]. Despite this, MTJs with MgO barriers lead to revolution in the information technology (actually hard disk drives (HDD) already implement read heads based on MTJs with MgO barrier [18, 19]). Also, the high quality of the MgO barrier in comparison of the MTJs with amorphous barrier facilitates the possibility of making much more sensitive field detecting devices with variety of possible applications [20]. Experimental findings were pioneered in 2004 by Yuasa's group from AIST, Japan [7] who reached TMR ratios in Fe/MgO/Fe systems grown by molecular beam epitaxy (MBE) of ∼230%. Simultaneously, Parkin's group at IBM Almaden, by using an ANELVA sputtering plant, reported similar value (∼220%) of TMR in the CoFe/MgO MTJs [8]. One of next steps in the evolution of spintronics devices to being more sensitive, it was related with growth of DMTJs: $F_1/I/F_c/I/F_2$ (here F_1 and F_2 are ferromagnetic layers, I - insulating barrier, and F_c is central layer). The DMTJs are expected to have numerous advantages in comparison with the standard MTJs, mainly due

to their enhanced the TMR [21, 22, 23, 24, 25] and resonant spin-torque effects [26, 27, 28].

As we have already mentioned the discovery of GMR has allowed the development of a new field of physics (spintronics) with numerous demonstrated already application (such as magnetic sensors) and even more to come. Already one year after the discovery of GMR, Stuart Parkin and coworkers from IBM understood great application potential of these devices in the technology [3]. As a consequence, already in 1997, only nine years later, the read heads in the magnetic HDD technology were already based on GMR (spin valve) effect. Since then, the GMR and TMR have been used extensively both in the read heads of the HDD and as other types of magnetic sensors [18, 19, 29]. The advantage of these devices in information the technology is their possibility to read in binary codes, due to different the difference in resistance between parallel and antiparallel states. Both MMLs and MTJ's have potential applications in different types of spin-electronic devices such as magnetic sensors and magnetic random-access memories (MRAMs), spin torque [30], vortex oscillators [31], etc. Although the MMLs are very robust, there is still need to improve reliability of MTJs based on sensitive magnetic devices, because of their high sensitivity of statics discharges. One of the main advantages of MTJ over the GMR based on devices is their possibility of high area densities and perpendicular recording [18]. Due to the improved thermal dissipation of the current-perpendicular-to-plane geometry, TMR devices run cooler and have better lifetime performance. These advantages permit to use MTJ's like a MRAM solid state hard disks and reprogrammable magnetic logic devices. For MTJ's with single-crystal MgO barrier, another advantage over the amorphous MTJ's and MML is that high density MRAM's need to have MR ratios higher than 150% at RT, and the read head, in the next generation, ultrahigh-density HDD need to have both a high MR ratio and an ultra-low tunneling resistance.

As to the qualitatively different (analog) application of the spintronic devices, the number of magnetic sensors applications has increased greatly in recent years,

due to the needs in medicine, military activities and different industrial communities [29, 32]. Actually, detection of the small magnetic fields with values between 1 nT (10^{-5} Oe) and 1 pT (10^{-8} Oe) is dominated by sensors such as fluxgates (is an electromagnetic device that is formed by two or more small coils around a core of highly permeable magnetic material, that sense the direction of the horizontal component of magnetic field), optically pumped magnetometers used to measure the strength and/or direction of the magnetic field in the vicinity of the instrument, Hall probes (is a sensor that varies the output voltage in response to changes in magnetic field) and SQUIDs (Superconducting Quantum Interference Device).

The disadvantage for the industry of these devices is that they have relative large dimensions and are relatively expensive. In addition, their resolution in time and scalability is not good enough. Precisely for these reasons, the industry demands development of new GMR and TMR based device. The MTJs based on MgO barrier with room temperature tunneling magnetoresistance ratios in excess than 300% and the possibility of control the resistances values (through barrier thickness), allows the design and fabricate the ultrasensitive field detectors [33], capable of room temperature operation in the $pT/Hz^{0.5}$, due to the high quality of the barrier. The great perspectives of incorporating the MTJs, as a field detectors, is due to their low cost, low-power consumption and potentially low frequency noise sensors and high resolutions ($pT/Hz^{0.5}$).

Also an important factor which gives advantage to MTJs is there scalability, i.e. that they practically maintain their sensitivity when being scales done to tens of nm size [34]. Finally, MTJs are demonstrating small response times and can work up to GHz regimes. Their disadvantage is that MTJs may have strong dependence of their properties (particularly the noise) on the defects inside the barrier.

Last decade a novel "conjugative" to GMR and TMR effect was discovered in spintronics (MML and MTJ) devices. As long as both electrodes are ferromagnetic, and owing that the electrons can become partially spin polarized leaving one

of the electrodes, they may also influence on the orientations of the magnetization when reaching the second electrode. This new effect is named spin-transfer torque (STT) [35, 36] and has a great promise for applications in the wireless and radar communication, spin-transfer torque RAM (STT-RAM) for data/information storage and other areas. The spin torque oscillators (STO) are a nano-sized spintronic device capable of microwave generation at frequencies in the 1-65 GHz range with high quality factors [37]. Although the STO have a great potential in application for future telecommunication. Another related phenomenon is the possibility of create and manipulate the magnetic vortex state in one of the electrodes [31]. The magnetic vortex is used to generate high frequency response applying DC current. Currently the effect is under very active investigation because of the possibility of its incorporation into MRAMs and read sensors.

As to the potential application of GMR and TMR devices in biomedical imaging, magnetocardiography or magnetoencephalography the source biological field cannot be modulated, and low frequency noise suppression mechanisms must be used [32]. In spintronic biochips, magnetic nanoparticles replace fluorescent markers are detected by magnetic sensors, and is to provide a good alternative to traditionally used. In comparison with fluorescent markers this biochip have fast response and high sensitivity.

1.2 Manuscript overview

The main motivation of this Thesis is to investigate different fundamental aspects of electron transport and low frequency noise in MTJs based on MgO barriers. The manuscript is organized as follows. After a brief introduction in the state of the art of spintronics and main contributions into noise at low frequency, we divide in two parts our experimental results. In the first part (Chapters from 3 to 5) is devoted to study of fully epitaxial MTJs based on Fe/MgO/Fe(100).

- Chapter 3 studies the influence of Carbon doping in Fe(100)/MgO/Fe fully epitaxial magnetic tunnel junctions on electron transport and low frequency noise.

- Chapter 4 describes the strongly suppressed 1/f noise and enhanced magnetoresistance in epitaxial Fe-V/MgO/Fe magnetic tunnel junctions.

- Chapter 5 discusses the electron transport in double magnetic tunnel junctions with soft dielectric breakdown.

In the above Chapters, we have studied the tunneling transport and low frequency noise in single and double fully epitaxial magnetic tunnel junctions based on MgO(100) barrier. We have focused on improving the tunneling transport, doping the barrier or the electrodes with different elements (Carbon, Vanadium and Nitrogen), which is after called the "interface engineering". The main goal is to understand the fundamental mechanisms of electron transport and noise behavior in MTJs with strategic idea of "interface engineering", for ultrasensitive field sensors needed in the industry. The low-frequency noise is dominated by thermal noise, 1/f noise and shot noise. We shall investigate the electron transport in fully epitaxial MTJs as a function of the applied bias and magnetic field, in order to clarify mechanisms leading to variation of electron transport and noise. The obtained information could permit "engineering" of fast, sensitive and robust MTJs for various applications. We also will investigate electron transport in "gently" broken DMTJs which conductance signals determined by nanometer size breakdown region.

The second part is the Chapters 6.

- Chapter 6 describes the low frequency noise in submicron sputtered FeCoB/MgO/FeCoB magnetic tunnel junctions.

In this Chapter, we have studied the tunneling transport and low frequency noise in submicron elliptical nanopillars, now growing by sputtering techniques,

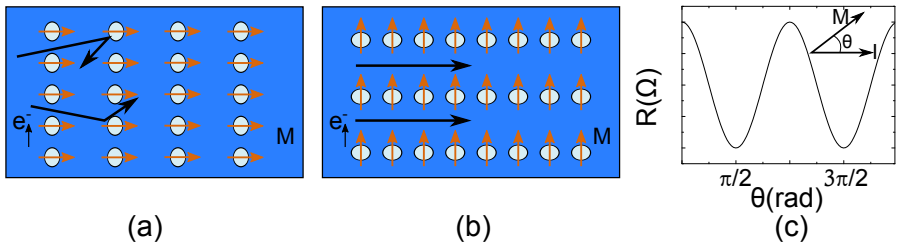

Figure 1.1: (a), (b) Schematic representation of AMR effect showing distortion of electron orbitals and resulting difference in scattering when the magnetization is parallel or perpendicular to the current direction, respectively. (c) Variation of resistance as a function of angle between the current and magnetization, obtained from equation 1.2.

which have a greater application in the industry. With low frequency noise and random telegraph noise measurements, we are able to obtain new information on the domain wall-induced or magnetic inhomogeneities low frequency noise at the high current densities.

1.3 Magnetoresistance

The magnetoresistance is the property of a material that results in a change of resistance when it is exposed to an external magnetic field. The discovery of large magnetoresistive effects has led to the development of solid-state magnetic sensors that can replace more expensive wire-wound sensors in a variety of applications.

1.3.1 Anisotropic magnetoresistance (AMR)

The anisotropic magnetoresistance (AMR) was discovered in 1857 by William Thomson (Lord Kelvin)[38] and occurs in ferromagnetic materials. It is termed anisotropic because, in contrast to the previously known ordinary magnetoresistance, it depends on the angle between the electric current and the magnetization direction. The magnetic anisotropy in magnetic conductors is characterized by the resistivity of the material and has a dependency on the angle between the direction

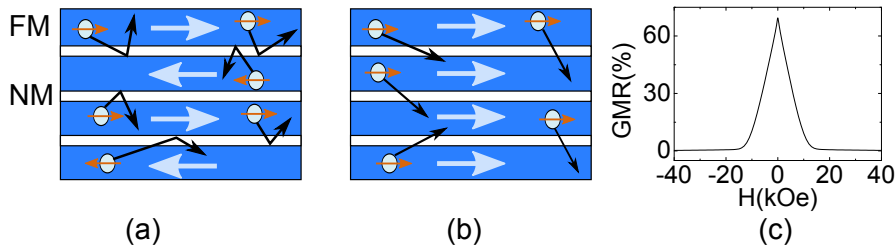

Figure 1.2: GMR effect with (a) multilayers of alternating magnetization (known as synthetic antiferromagnetic system) producing lots of scattering process and (b) reduced scattering when the magnetization of the layers are aligned in the same direction. (c) GMR dependence as a function of applied field, adapted from [39].

of the external applied magnetic field and current which crosses the material. The AMR effect is defined by $\Delta\rho = \rho_{\parallel} - \rho_{\perp}$, where $\rho_{\parallel}$ and $\rho_{\perp}$ define the resistivity parallel and perpendicular to the magnetization, respectively.

$$AMR = \frac{\Delta\rho}{\rho_0} = \frac{\rho_{\parallel} - \rho_{\perp}}{\frac{1}{3}\rho_{\parallel} + \frac{2}{3}\rho_{\perp}} \tag{1.1}$$

The angular dependence of magnetic saturation AMR is described as:

$$\rho(\Theta) = \rho_{\perp} + \Delta\rho\cos^2(\Theta) \tag{1.2}$$

Where Θ is the angle formed by the current (I) and the magnetization (M), as it is shown in *Figure 1.1.*

1.3.2 Giant magnetoresistance (GMR):

In 2007 Albert Fert and Peter Grünberg were awarded with Nobel Price for the discovery of a large variation in resistance as a function of applied magnetic field in ferromagnetic multilayer (FM) metal layers separated by nonmagnetic (NM) spacer. This effect was called giant magnetoresistance (GMR) [1, 2]. The presence of antiferromagnetic coupling was confirmed more directly in Co/Cu multilayers using neutron measurements by Cebollada et. *al.* [40]. The origin of this effect

is the spin dependent scattering of electrons (schematic representation in *Figure 1.2*).

$$GMR = \frac{\rho_{AP} - \rho_P}{\rho_P} \tag{1.3}$$

In the simplest model, the total current flowing-through the device is presented as composed of two parallel currents, one due to spin-up and the other due to spin-down electrons. If the FM layers are in the parallel state (P), electrons with spin along the magnetization direction will have the minimum scattering probability (lower resistance), while the electrons with opposite spin will present the maximum scattering probability (higher resistance) as it is shown in *Figure 1.2*.

Based on GMR effect, the spin valve is a modified version of the multilayer devices, which uses only two magnetic layers separated by a nonmagnetic layer. The layers are made of two materials with different magnetic coercivity and this structure has been termed a spin valve [41]. The bottom layer has its magnetization pinned along one orientation. Usually, the bottom magnetic layer is deposited directly on top of an antiferromagnet and it is known as a "pinning"layer. The antiferromagnetic layer has no net magnetization of its own, but tends to hold the magnetization of the adjacent ferromagnetic layer in fixed direction. The other layer is free to rotate its magnetization in response to the field. The rotation of the free layer magnetization then "open"(in P configuration with low resistance) or "closes"(in AP configuration with high resistance) the flow of electrons, acting as a sort of valve. This property has made these devices have been widely used as HDD read heads between 1997 and 2006.

1.3.3 Tunnel magnetoresistance (TMR):

Another big step forward came from replacing the non-magnetic metallic spacer layer of the spin valve by a thin non-magnetic insulating layer, thus creating a new kind of device known as a magnetic tunnel junction. The electrons tunnel from one

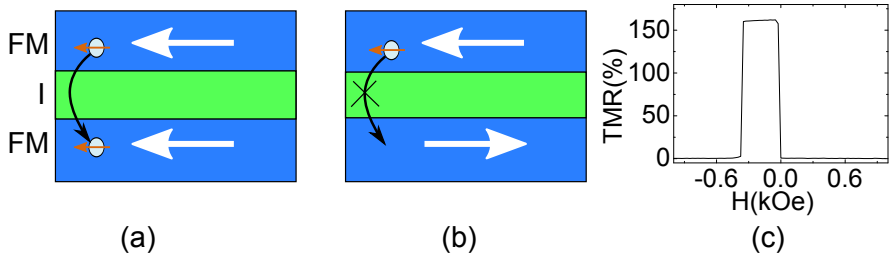

Figure 1.3: Sketch of a MTJ. (a) When the layer magnetizations are aligned in the parallel configuration, the electrons from the top layer can find available states in the bottom layer to tunnel into. (b) When the magnetizations are opposite directions, then the majority electrons in the top layer can not tunnel into the bottom layer. (c) TMR vs external magnetic field.

ferromagnetic layer to the other through the insulator barrier by a quantum mechanical tunneling, which conserves the spin (see *Figure 5.6*). The two electrodes have different coercive field, because one of them is harder since the magnetic point of view, either by their magnetic characteristics or by being coupled with another ferromagnetic harder. This means that depending on the relative orientation of the magnetization of the both layers, we have different states similar to spin valves. Now, when the magnetization of the two layers are aligned in the same directions, many states are available in the bottom layer for spin-polarized electrons from the top layer to tunnel into. In the simplest pictures, when the magnetization directions are opposite, the spin-polarized electrons are prevented from tunneling because they have the wrong orientation to enter the bottom layer. The process is also known as spin-dependent tunneling, making MR values are larger than in the above cases. Below, we will describe in more detail the tunneling transport phenomenon in these kind of devices.

1.4 Magnetic tunneling phenomena

As we have mentioned above, a MTJ is composed by two ferromagnetic electrodes separated by a thin insulator barrier (tunnel barrier). From the physical point of

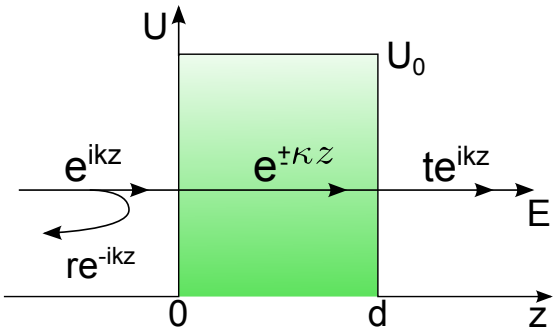

Figure 1.4: A simple barriers model for tunneling in which incident electrons with energy E tunneling a barrier with width d.

view, there are two important aspects that influencing the tunneling transport. Firstly, the quantum process (due to the tunnel barrier itself), and secondly the magnetic process (because depending on the relative orientation of the magnetization of the two ferromagnetic electrodes the tunnel probability of spin-polarized electrons is high or low). Then, if we consider the tunnel barrier only will have the case of quantum tunneling barrier.

1.4.1 Electron tunneling (from 1D to 3D)

Quantum mechanics predicts that an elementary particle such as an electron has a nonzero probability of tunnel from one side of any physical barrier to the other. Let us suggest that electron arrives to the tunnel barrier with height $U_0 > E$ and width d with kinetic energy E (see *Figure 1.4*). We suppose that the temperature is $0K$. Then the electron wavefunction $\Psi(z)$ is

$$\Psi(z) = \begin{cases} e^{ikz} + re^{-ikz} & z < 0 \\ ae^{-\kappa z} + be^{\kappa z} & 0 < z < d \\ te^{ikz} & z > d \end{cases} \tag{1.4}$$

Consider the time-independent Schrödinger equation in one dimension. The tunneling current can be written in the forms:

$$J_k = \frac{i\hbar}{2m}\left(\Psi\frac{\partial\Psi^*}{\partial z} - \Psi^*\frac{\partial\Psi}{\partial z}\right) \tag{1.5}$$

We define the momentum in metal as a $k = \sqrt{2mE/\hbar^2}$ and inside the barrier $\kappa = \sqrt{2m\left(U_0 - E\right)/\hbar^2}$. In the tunneling process will be involved only those electrons whose energy is about the Fermi energy. This allows us to restrict the k_σ and κ moments, to those closest to the Fermi level. Is obtained in this manner the transmission probability an electron spin ($\sigma = \uparrow, \downarrow$) through the Barrier.

$$J_k \propto \left|\mathbf{T}_k\right|^2 \propto e^{-2\kappa d} \tag{1.6}$$

Where $\mathbf{R}$ and $\mathbf{T}$ are the reflection and transmission probabilities respectively. In fact, the conductance (G) of a mesoscopic system can be deduced from reflection and transmission properties. In the case of tunnel conductance, where transmission is still small compared with the reflection.

$$G^\sigma = \frac{e^2}{h}\sum_i \mathbf{T}_i^\sigma \tag{1.7}$$

In three dimensions where the wave function is

$$\Psi\left(x, y, z\right) = \Phi\left(z\right)e^{i(k_x x + k_y y)} \tag{1.8}$$

Now, $\Phi\left(z\right)$ has the same form as before, but here k is replaced by k_z and, κ and k_z depend on $k_\parallel$ $\left(k_\parallel = (k_x, k_y)\right)$.The wave function present in-plane oscillations perpendicular to the propagation direction (z). Then in ferromagnetic electrode and the insulator the wavevector are

$$k_z = \sqrt{2m\frac{E}{\hbar^2} - k_\parallel^2} \quad \text{and} \quad \kappa(k_\parallel) = \sqrt{2m\frac{(U_0 - E)}{\hbar^2} - k_\parallel^2} \tag{1.9}$$

Then we have the Landuer formula for the conductance as

$$G^\sigma = \frac{e^2}{h}\sum_{k_\parallel} \mathbf{T}_{k_\parallel}^\sigma \tag{1.10}$$

In our situations with MTJ with MgO (100) barriers, the transmission probability will be very small ($\mathbf{T}^{\sigma}_{k_{\parallel}} << 1$).

1.4.2 Electron tunneling in magnetic tunnel junctions:

As we have mentioned above, the resistance of the MTJ's depends of the relative magnetic alignment of the both electrodes. The parallel state (P) is when the magnetization of both electrodes are aligned in the same direction (applied field greater than the coercive field of the two electrodes $H > Hc_{1,2}$) which is showed in *Figure 1.5*. On contrary, when the two electrodes have opposite directions of magnetization (applied field smaller than the coercive field of the electrodes $H < Hc_1$, $H > Hc_2$) is called antiparallel state(AP) (see *Figure 1.5*). This sandwiched exhibits tunnel magnetoresistance (TMR) due to spin-dependent electron tunneling.

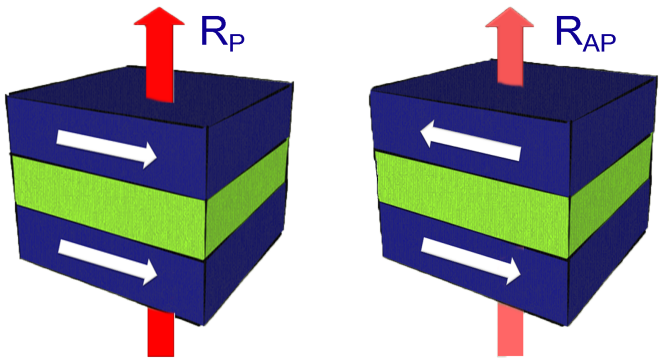

Figure 1.5: Magnetic tunnel junctions are formed by two ferromagnetic electrode separated by one insulator barrier. When the magnetization of the two electrode are aligned in the same direction is parallel state and where it align in the opposite direction is antiparallel.

$$TMR = \frac{R_{AP} - R_P}{R_P} \tag{1.11}$$

A model that has been widely used to describe the tunnel magnetoresistance (based on the free-electron model) is the phenomenological model of Julliere [14]. This model relates the TMR effect to the polarization and consequently, the TMR effect is due to spin-dependent electron tunneling. We define $\mathcal{P}_i$, in ferromagnetic electrodes, like a polarization ($i = 1, 2$) related to the spin dependent density of states $n_{i\sigma}$. When the electrode is nonmagnetic $\mathcal{P} = 0$, and the contrary, when it is fully spin-polarized at E_F is one.

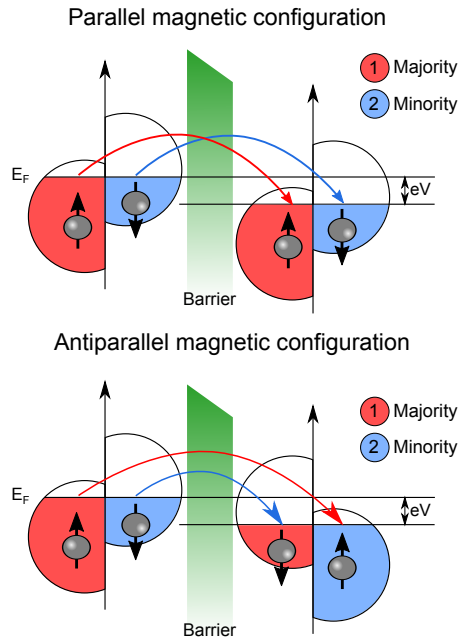

Figure 1.6: Schematic illustration of Jullire model. In the ferromagnetic electrodes, the bands are shifted by the magnetic change. In this model the tunneling process conserves the spin. When electron states on each side of the barrier are spin-polarized, then electrons will more easily find free states to tunnel to when the magnetizations are parallel (top picture) than when they are antiparallel (bottom picture).

$$\mathcal{P} = \frac{n_i^{\uparrow} - n_i^{\downarrow}}{n_i^{\uparrow} + n_i^{\downarrow}} \tag{1.12}$$

Within Julliere approximations [14], the tunneling probability is only a product of the density of states in the electrodes on each side of the barrier, and the transmission probability is neglected. The TMR as a function of the polarization is given by relation:

$$TMR = \frac{G_P - G_{AP}}{G_{AP}} = \frac{\left(n_1^{\uparrow} n_2^{\uparrow} + n_1^{\downarrow} n_2^{\downarrow}\right) - \left(n_1^{\uparrow} n_2^{\downarrow} + n_1^{\downarrow} n_2^{\uparrow}\right)}{n_1^{\uparrow} n_2^{\downarrow} + n_1^{\downarrow} n_2^{\uparrow}} = \frac{2\mathcal{P}_1\mathcal{P}_2}{1 - \mathcal{P}_1\mathcal{P}_2} \quad (1.13)$$

For application of this model, one needs that the tunneling barrier to be thick enough, in order to have a very small wavefunctions overlap. The averaged interfacial transmission polarization must be determined for the considered electrode-barrier coupling. The Julliere model implies that the TMR depends exclusively on the nature of the electrodes (more precisely their densities of states at the Fermi level) and neglects in particular properties of the barrier as its nature or thickness. For this reason, the previous considerations are valid for MTJs with amorphous barriers, where an incoherent tunneling process through the amorphous AlO tunnel barrier occurs. When 3d ferromagnetic electrodes are used, various Bloch states with different symmetries of wave functions exist in the electrodes. Due to the amorphous structure of the barrier, the Bloch states with different symmetries can couple with evanescent states in AlO with a finite tunneling probabilities [42] (see *Figure 1.7*). The Jullieres model assumes that tunneling probabilities are equal for all the Bloch states in the electrodes. This tunneling process can be regarded as an incoherent tunneling.

1.4.3 Coherent magnetic tunneling phenomena

For a long time it was believed that electron tunneling in magnetic tunnel junctions is mainly determined by electron density of states of ferromagnetic electrodes [5, 14]. The realization that the tunneling magnetoresistance depends on the atomic structure of the entire junction, and especially on the ferromagnet/insulator

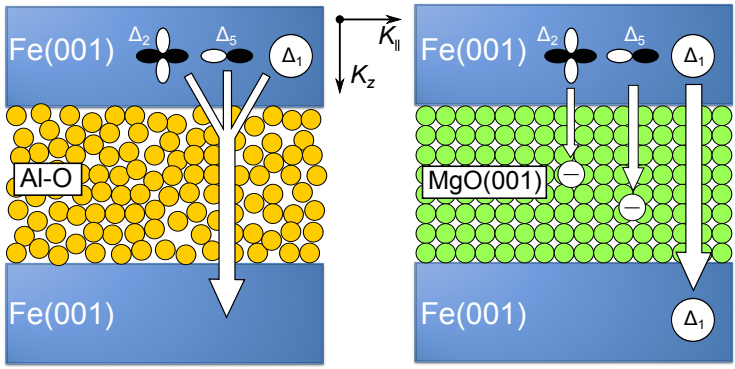

Figure 1.7: Schematic illustrations of electron tunneling through (a) an amorphous AlO barrier and (b) a crystalline MgO(001) barrier. Adapted from [42].

interfaces [43], was followed by the theoretical prediction and experimental discovery of coherent tunneling phenomena in MgO based MTJs. The coherent magnetic tunneling implicates that the wavefunction matching at the interface and, consequently, the symmetry of tunneling electrons plays a fundamental role on transport. This discovery initiated with theoretical calculations by W.H. Butler *et al.* [9] and J. Mathon *et al.* [10] who predicted coherent spin tunneling phenomena in Fe(100) | MgO(100) | Fe(100) magnetic tunnel junctions. The mismatch between Fe-MgO is close to 3%. In the case of ideal coherent tunneling, it is theoretically expected that the tunneling process in the P state is governed by electrons with Δ_1 symmetry through the MgO(001) barrier [9] (see *Figure 1.7* (b)). Then, the coherent tunneling of highly spin-polarized Fe s-like states (Δ_1 bands) are propagating along the direction perpendicular to the plane ($\overrightarrow{k_{\parallel}} = 0$) for thin enough barrier. In this direction, the tunneling probability is the highest, making the main contribution to the large magnetoresistance.

Although, the coherent spin tunneling effect was predicted and observed first in Fe/MgO/Fe, later was found to be even stronger in Co/MgO/Co MTJs [44, 45] and in Half-metallic ferromagnets based on Co Heusler alloys with a chemical composition of Co_2YZ (Y:transition metal, Z:main group element) [46, 47]. This

is due to the the fact that Δ_1 Bloch states are highly spin-polarized and Δ_1 Bloch states are present at low bias at Fermi level.

1.5 Epitaxial Magnetic Tunnel Junctions Fe/ MgO/ Fe(001)

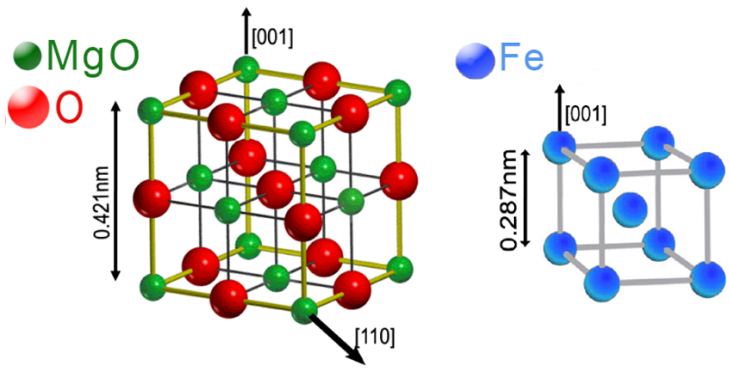

Figure 1.8: Schematic representation of the MgO and Fe crystallized in a cubic structure.

1.5.1 Fe/MgO/Fe(001) Structure

We have previously explained the important advance in the spintronic after to incorporate MgO, due to the high quality of the structure. For this reason in this Thesis, we focus our study in the tunneling transport and low frequency noise in fully epitaxial (single and double) magnetic tunnel junctions based on MgO barrier in (100) direction. Due to the high quality of the barrier and high TMR values, these MTJs are very interesting from a fundamental and applied point of views. One of the main problems, that the scientists were found at first, was the difficulty of grow an ideal interfaces, because the coherent tunneling is very sensitive to the structure of barrier/electrode interfaces. The MgO barrier crystallized in a cubic structure of NaCl type with a lattice parameter $a_{MgO} = 0.421nm$ (*Figure*

1.8). The Fe crystallizes in a cubic centered (bcc) with a lattice parameter $a_{Fe} = 0.287nm$ (*Figure 1.8*). When the epitaxial MTJ structure is growing layer by layer, the Fe atoms is located over the Oxygens atoms and, consequently, the Fe unit cell is rotated by 45° with respect to the MgO unit cell (see *Figure 1.9*). In the [110] direction, the interatomic distance in bulk MgO is $\frac{a_{MgO}}{\sqrt{2}} = 0.298nm$, close to Fe in (100) direction ($a_{Fe} = 0.287nm$).

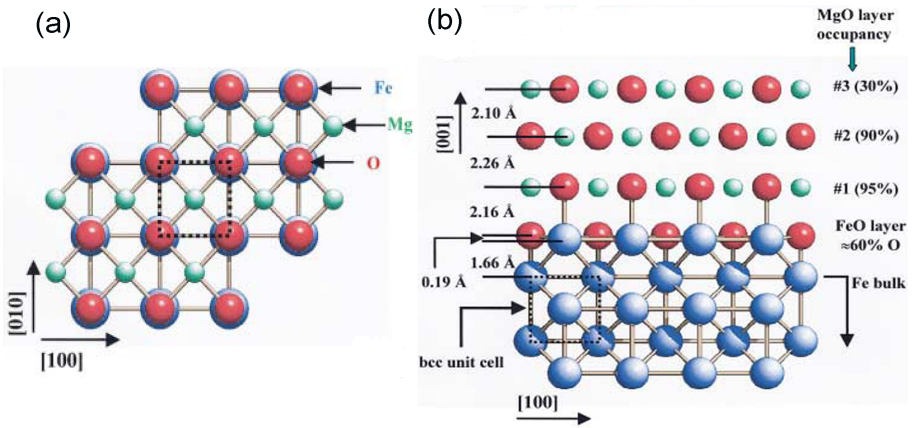

Figure 1.9: Schematic representation of the epitaxial growth of Fe on the MgO, containing the specific epitaxy relations. The Fe lattice is rotated by 45° with respect to the MgO lattice.

The problem is that the lattice mismatch between MgO barrier and Fe(001) is around 3% (see *Figure 1.9*). In fact, the annealing during the MgO growth leads to a reduction of strain interfacial via relaxed the dislocations [7, 48, 49]. But, this mismatch create a stress in the interface between electrode and barrier, which is one of the responsible factors for the TMR reduction respect to the theoretical calculations. Reducing the mismatch between the barrier and the electrode has been widely studied and different electrode compositions were proposed to improve the tunneling transport, mentioned above (FeCo, FeCoB, Heusler alloys, etc). Such studies are known as interface engineering. In this Thesis, we investigate TMR

and noise in MTJs with alternative electrodes (Fe-C, Fe-V), in order to improve the tunneling transport and reduce the low frequency noise.

1.5.2 Theoretical approximation of electron transport in Fe/ MgO/ Fe

The most frequently used model to describe the physics mechanism of tunneling conductance in single-crystal systems was proposed by W.H. Butler *et al.* and Mac Laren *et al.* [9, 50]. When electrons arrive to one of the ferromagnetic electrodes, this act like a filter in terms of the electron symmetry. From equation 1.9, one can see intuitively that the oscillations of the wavefunction parallel to the interface enhance the decay rate perpendicular to the interface ($k_{\parallel} = 0$ enhances κ). The role of the symmetry is to determine the number of nodes of the wavefunction in the plane of the interface. Therefore we can identify different Bloch states, denoted by Δi (propagated along the (100) direction in the crystal), which participate in tunneling transport at Fermi level [48]:

- $\Delta_1(s, p_z, d_{z2})$
- $\Delta_5(p_x, p_y, d_{xz}, d_{yz)}$
- $\Delta_{2\prime}(d_{xy})$
- $\Delta_2(d_{x2-y2})$

Consequently, the attenuation rate of different symmetries will be different as a function of your symmetry respect to $k_{\parallel}$. This simple and intuitive model allows us to roughly understand the contribution of each conductance band in MgO insulator barriers. But really, it were necessary *ab initio* calculations using the LKKR technique to describe the realistic system [9, 50]. In this model, it is possible to obtain the conductance and consequently the TMR through first principles methods. Along the Δ direction, the TMR ratio in single-crystal tunnel

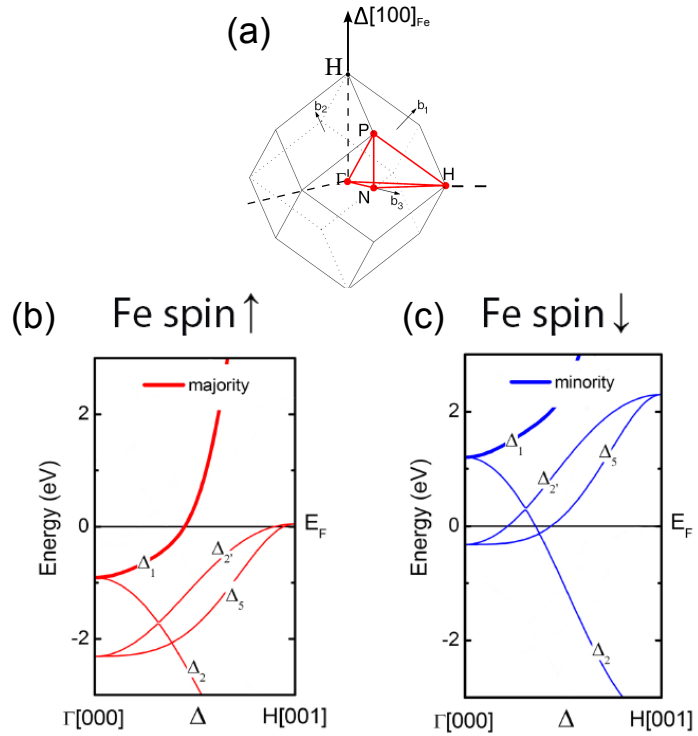

Figure 1.10: (a) Reciprocal space representation of the bcc Fe lattice. Δ direction corresponds to the propagation of electrons perpendicular to the (100) plane in real space. (b) Bulk band structure diagram for the majority spin of bcc Fe. (c) Bulk band structure diagram for the minority spin of bcc Fe.

junctions is determined by the different tunneling mechanisms and symmetry-related decay rates of the Bloch waves functions for the majority and the minority spin channels. For the large thickness of the insulator barrier and based on the bulk band diagram of the Fe, represented in *Figure 1.10*, we can observe that the tunneling in P state is governed for Δ_1 band and in less degree contribution by $\Delta_{5,2'}$ bands. While in the AP state, due to the exchange splitting, at E_F, there is no Δ_1 state for the minority spin *Figure 1.10 (b)*, the conductance is fewer because is dominated by $\Delta_{5,2'}$ bands with large rate of decays. Due to this effect, this model predicts TMR values above 1000% TMR, that have not been achieved

experimentally [16]. This reduction has been attributed to limitations in the grown process, mainly due to the Fe oxidized at the interface. Theoretical calculations reported by Waldron et *al.* [51], with ab initio calculations, shows that the zero bias TMR is reduced from several thousand percent to about 1000% when the Fe/MgO interface is oxidized. The oxidation of even a monolayer at the interface significantly suppresses the TMR effect [52].

Before, we supposed that the dimension crystallographic in the volume is infinite, but in reality the crystal is finite. The situation becomes more complex at low MgO thickness, where the contribution of $k_{\parallel} \neq 0$ electrons is higher. *Ab initio* calculations show that the electronic structure of the surface Fe(001) is weakly affected by the presence of MgO [53]. Consequently, near the interface the bulk band structure is quite different from the surface [9]. Moreover, in the small MgO barrier thickness regime, the tunnel transmission becomes strongly affected by resonant effects at the interfaces [54]. Such interfacial resonant state (IRS) may lead to a resonant tunneling mechanism [54]. These resonant effects locally increase the conductance distribution in particular points in the two-dimensional Brillouin zone. The width of these maximum is determined by the strength of the coupling in the barrier, which decreases exponentially with the barrier thickness.

Therefore, during the study of the tunneling conductance in MTJ based on MgO barrier, following points should be taken into account.

1. The decay rates for each of the Fe(100) Bloch states due to MgO filtering.

2. Interfacial resonant states created between Fe and MgO.

3. The Fe bulk band structure for the majority and minority spin Δ bands.

In order to study how these effects influence the tunneling transport, the dynamic conductance measurements are typically used. Apart from this technique, it seems necessary to use additional tools from which we may obtain extra information, such as noise measurements.

1.6 Noise in magnetic tunnel junctions

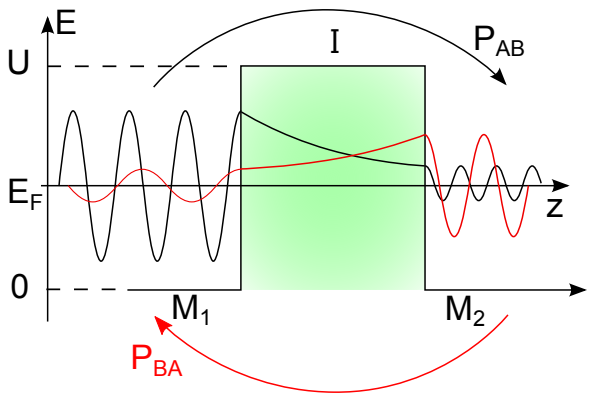

Figure 1.11: Tunneling probability of the incident wave in the barrier.

So far, we have characterized the spintronic devices in terms of tunneling transport, but an additional source from which, we can obtain more information is the power spectral density of voltage (current) fluctuations also called noise. One of the "founding fathers"of mesoscopic physics (Rolf Landauer) said: "The noise is the signal" [55]. Noise is known as spontaneous fluctuations of any parameter. In this Thesis, we will focus on the voltage fluctuations. Not all types of electrical noise are informative. For this reason, we have studied the different contributions as a function of the frequency, applied bias, temperature, magnetic field, etc.

1.6.1 Frequency independent noise

As we have seen above, the tunneling conductance in a tunnel barrier is proportional to the transmission and reflection probabilities. Then, based on the *Figure 1.11*, we define the tunneling transport as a function of voltage as:

1) Without bias ($V = 0V$). When the bias is zero, some spontaneous spikes with e/τ magnitude appear (see *Figure 1.12*). From *Figure 1.11* we can observe

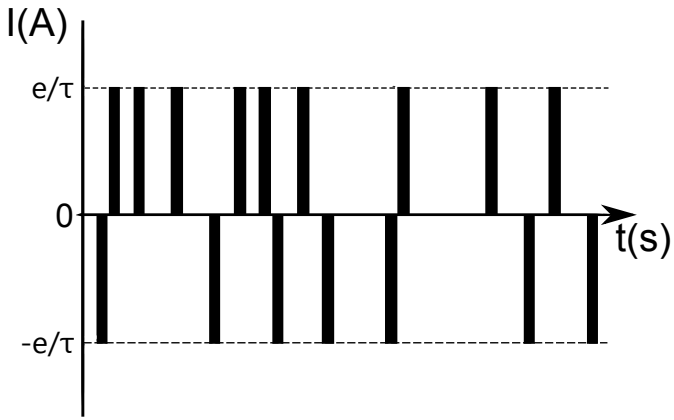

Figure 1.12: Current fluctuation as a function on time at 0 bias.

that the average current and average square current depend on the spontaneous transmission (P_{AB}) and reflection (P_{BA}) probabilities.

$$\left.\begin{array}{r}\langle I\rangle = (\frac{e}{\tau})P_{AB} - (\frac{e}{\tau})P_{BA} \\ \langle I^2\rangle = (\frac{e}{\tau})^2 P_{AB} + (\frac{e}{\tau})^2 P_{BA}\end{array}\right\} \Rightarrow I = \frac{Q}{t} = \frac{e}{\tau} \tag{1.14}$$

As it is expected, the root mean square is proportional to the transmission by reflection ($\mathbf{R} = 1 - \mathbf{T}$) product [56]:

$$\langle \Delta I^2\rangle = \langle I^2\rangle - \langle I\rangle^2 \propto P_{AB}P_{BA} \Rightarrow \langle \Delta I\rangle \propto \mathbf{T}(1-\mathbf{T})$$

2) With bias ($V \neq 0$). The scenario is different, the system energy is shifted because the barrier height change (*Figure 1.13*). Therefore the reflection probabilities will be

$$P_{BA} = P_{AB} e^{-\left(\frac{eV}{k_B T}\right)} \tag{1.15}$$

Where k_B is the Boltzmann constant and T is the temperature. Now, the reflection probability depends on the energy supplied to the system (equation 1.15). From 1.14, we can deduce the average current

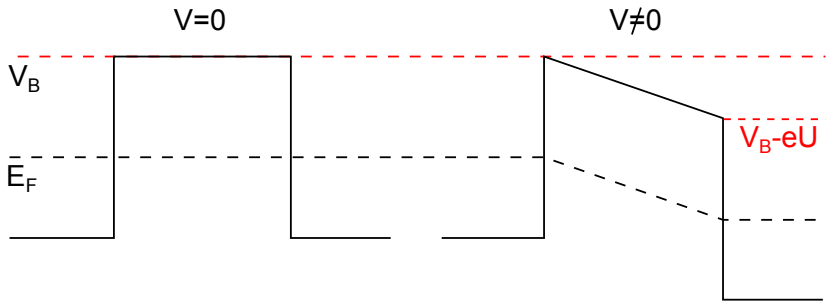

Figure 1.13: (a) Rectangular potential energy by an electron in the barrier without apply bias. (b) Effect of apply bias.

$$\langle \Delta I \rangle = \frac{e}{\tau} P_{AB} \left(1 - e^{-\left(\frac{eV}{k_B T}\right)} \right) \Longrightarrow P_{AB} = \frac{\tau}{e} \langle \Delta I \rangle \left(1 - e^{-\left(\frac{eV}{k_B T}\right)} \right)^{-1} \tag{1.16}$$

Then, the average square current is

$$\langle \Delta I^2 \rangle = (\frac{e}{\tau})^2 P_{AB} \left(1 + e^{-(\frac{eV}{k_B T})} \right) \tag{1.17}$$

Substituting 1.16 in 1.17, we have

$$\langle \Delta I^2 \rangle = \left(\frac{e}{\tau}\right) \langle \Delta I \rangle \left(\frac{1 + e^{-(\frac{eV}{k_B T})}}{1 - e^{-(\frac{eV}{k_B T})}} \right) \Longrightarrow \coth x = \frac{e^{2x} + 1}{e^{2x} - 1} \tag{1.18}$$

The power spectral density is defined as $S_V(f) = \langle \Delta V^2 \rangle / \Delta f$ and using Ohm's law ($\Delta I = \Delta V / R_d$), we obtain the general expression of the noise power (voltage) frequency independent, also known as a white noise, which is a sum of thermal noise and shot noise.

$$S_V = 2eIR_d^2 \coth \left(\frac{eV}{2k_B T} \right) \tag{1.19}$$

More details of the theoretical calculations of white noise can be found in Ref. [56].

1.6.1.1 Thermal Noise

In the equilibrium, we should be able to describe noise within the fluctuation-dissipation theorem (FDT). At certain temperature, thermal excitation causes an electron movement that induce aleatory voltage. The current is defined as a stream of moving charges, then this agitation in turn generates electrical voltage fluctuations known as thermal noise. If we now take the limit $eV \ll 2k_BT$ in equation 1.19), we deduce the general expression of the thermal noise.

$$S_V = 4k_BTR \tag{1.20}$$

As we can see in equation 1.20, the thermal noise is frequency and current independent. Therefore, the thermal noise has not much physical information, but it is a great tool to calibrate the experimental system. Because, once knowing the temperature (or resistance) it easy to know the real resistance (or temperature) that you are measuring.

1.6.1.2 Shot noise

Out of equilibrium, we have another source of noise called shot noise, which are small fluctuations of time-dependent on electric current, due to discrete charge e^-. In two-terminal conductor, if we now take the limit $eV \gg 2k_BT$, to minimize the contribution of other interfering signals [56], we have;

$$S_I = 2e\,\langle I \rangle \tag{1.21}$$

The equation 1.21 is known as a Poisson noise. The shot noise is Poissonian, when the noise does not depend on previous events, i.e., each electron that is transmitted is independent on the previous one. If this does not happen, we can define a new relationship known as the Fano factor, which indicates the variation between the noise and Poisson noise.

$$F = \frac{S}{S_I} = \frac{S}{2e\langle I \rangle} \tag{1.22}$$

The transmission probability in MTJs with MgO barrier is very small ($\mathbf{T}^{\sigma}_{k_{\parallel}} << 1$). This condition is essential for direct tunnel because the product $\mathbf{T} * \mathbf{R} = \mathbf{T} * (1 - \mathbf{T}) \simeq \mathbf{T}$. Taking the limit of high transparency ($\mathbf{T} \sim 1$) the shot noise is suppressed (F < 1) [56]. As for example in a metallic quantum point contact, which is essentially an orifice in a thin insulating layer between two metallic reservoirs, or double magnetic tunnel junctions where appears a sequential tunneling [56].

1.6.2 *1/f* noise

So far, the different types of noise that we have seen were frequency independent, but there is another type of noise source, which has a higher contribution at low frequencies. The 1/f noise (is also called Flicker noise or pink noise) has a dependence inversely proportional to the frequency [57]. Understanding of 1/f noise is one of the great challenges in theory of the fluctuations, in spite of appearing in the resistance of essentially all resistors [58]. For this reason in this Thesis, we want to further study low frequency noise. It is important to remark, that the 1/f noise in electronic systems has the next properties.

- The 1/f noise in the electronic system is a time-invariant. Therefore, we will consider as stationary and ergodic in time.
- The 1/f noise is considered Gaussian, because it is due to several independent fluctuators and thus has a Gaussian distribution [59].
- The presence of noise in the equilibrium. In agreement with the thermodynamics, the fluctuations are related to the dissipations. As we saw previously, the resistance voltage fluctuations in equilibrium are described by the expression 1.20 for each frequency. Then, the contribution of 1/f fluctuations appear in the equilibrium or out of equilibrium due to temperature fluctuations inside the system [60].

1. Introduction

The most extended model that tries to describe the noise in metal films was proposed by Hooge in 1981 [13]. This phenomenological model attribute the 1/f noise to the variation of the density of charge carriers (N_{e^-}), being proportional to Hooge constant (α=10^{-2}), as we can see in equation 1.23. Several years later, it has been discovered that α is not a constant (i.e. depend on the voltage, temperature, etc.). For this reason to compare different samples it is usual to use normalized Hooge parameter.

$$\frac{S_V(f)}{V^2} = \frac{\alpha}{N_{e^-}} \frac{1}{f} \tag{1.23}$$

On the other hand, dependence of the spectral density with temperature led to the suggestion by Dutta et *al.* [60], that the low frequency noise could be due to thermally activated processes. Then, the resistivity in metal films is determined by the density of defects. The movement of the defects is thermally activated and has all the possible activation energies. In thermal equilibrium, the resistivity is determined by the motion of these defects within the sample volume. These models allow us understanding of those factors that affect the 1/f noise. Thus in tunnel junctions, the 1/f noise was attributed to trapping-detrapping processes of electrons in defects. The 1/f noise is affected only by the defects which influence the conductance, so are those located in the barrier or at the interface between electrode and barrier. And now, the 1/f noise will be normalized by the area and not by the volume, because the transport is produced in the area of the junction (A), as we can seen in the next expression.

$$S_V(f) = \frac{\alpha I^2 R^2}{A f^{\beta}} \tag{1.24}$$

Where β is considered between 0.9 and 1.4. Deviations of this values range from the 1/f dependence are usually caused by random telegraph noise (RTN) [60] and could provide Lorentzian contribution, and we will see in more details below.

As we mentioned before, the origin of this model was to understand the sources of 1/f noise in thin metal films. To use this phenomenological model in magnetic

tunnel junctions, which have a strong dependence of conductance with the applied external magnetic field, we must be more careful. The nature of the 1/f noise in these micron-sized MTJs can be categorized by two components: a magnetic field-independent part and a field-dependent part. In the P state, far from the transition, the 1/f noise has a mainly electronic origin (without contribution of magnetic inhomogeneities) and we may consider as valid the previous model. In this magnetic state, we attribute the 1/f noise to the relaxation time of the defects and/or tunneling electrons in or near the barrier. But the scenario is different close to the transition and in the AP sate, which have a strong influence of the magnetic field.

The first 1/f noise studies as a function on magnetic field in magnetic tunnel junctions were carried out on systems with AlO_x barrier [61, 62, 63, 64]. As we have seen before, due to the amorphous structure of the AlO barrier (see *Figure 1.7*), electrons with different symmetries can tunnel from one electrode to the other. Therefore, the role of aluminum oxide on tunneling transport is qualitatively different than with MgO barriers [63]. As expected, the 1/f noise near the transition between P and AP magnetic states must have a very strong magnetic contribution, because the free layer is changing the direction of its magnetization [65]. This influence on the 1/f noise may have a higher contribution than of that in defects in the barrier, as it was reported in previous works [62, 65]. Therefore, we can consider the origin of the fluctuations similar to the ferromagnetic systems and the magnetic fluctuations meets the FDT [66]. The magnetization fluctuations can be consider as [66].

$$S_R(f) = \left(\frac{\partial R}{\partial m}\right)^2 S_m(f) \tag{1.25}$$

Where m is the magnetic moment and R is the resistance. At each field the MTJs may achieve approximate (quasi) thermal equilibrium, due to the large coupling of the resistance to the external magnetic field. For a sample in thermal equilibrium and exhibiting linear response, $S_m(f)$ is given by the FDT relation:

$$S_m(f) = \Omega \frac{2k_B T}{\pi \mu_0 f} \chi_m^{''}(f) \tag{1.26}$$

Where $\chi^{''}$ is the imaginary part of the susceptibility, Ω represent the volume and μ_0 is the vacuum permeability. In the ferromagnetic system the $\chi^{''}$ is a constant. Substituting 1.25 in 1.25, we have

$$S_R(f) = \left(\frac{\partial R}{\partial m}\right)^2 S_m(f) \Rightarrow \left.\frac{\partial R}{\partial H}\right|_{f=0} = \frac{2m\mu_0}{k_B T \Delta R} \int_0^\infty S_R(f) df \tag{1.27}$$

Where 2m is the changes in magnetic moment and ΔR is the resistance under inversion of the magnetization of the fixed layer [65]. The low frequency noise slope is very close to one. Then, the integral of the equation 1.27 is proportional to α.

$$\frac{\partial R}{\partial H} = \frac{2m\mu_0}{k_B T \Delta R} \frac{R^2}{A} ln\left(\frac{f_{max}}{f_{min}}\right) \alpha \tag{1.28}$$

Close to the transition between both magnetic states, the 1/f noise is mainly due to magnetic fluctuations [64, 66]. Then, the 1/f noise scales as dR/dH to the first power.

$$\alpha \propto \frac{dR}{dH} \tag{1.29}$$

Much less clear is the dependence of the low frequency noise deeply in the AP states. For this reason, since 2005 our group has initiated extensive investigation on both tunneling transport and low frequency noise in fully epitaxial MTJ based on MgO barriers [11, 67, 68, 69, 70, 71]. The MgO barriers filtering plays a fundamental role in the tunneling transport [9, 48, 68]. The low frequency noise studies in MTJs with MgO (111) barriers showed strong dependence as a function of the magnetic field, i.e., the magnetic states [11]. Here, we shall discuss noise and transport measurements on MTJs with MgO (100) barriers carried out as a function of the magnetic state and applied biases.

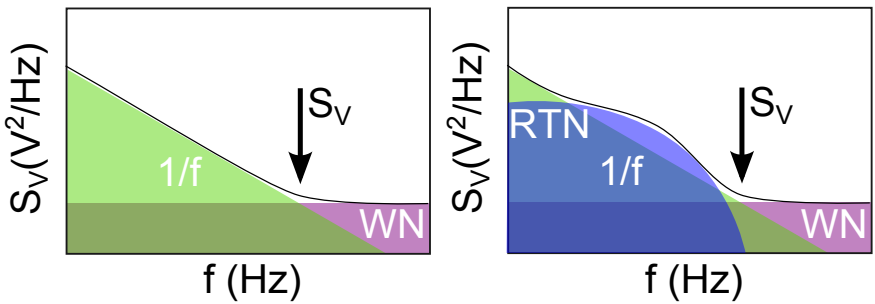

Figure 1.14: MTJ theoretical power spectra with and without RTN, (b) and (a), respectively. S_V stands for the total noise power. Both horizontal (frequency) and vertical (noise power) axis are presented in logarithmic scale. Adapted from [72]

1.6.3 Random telegraph noise

As we have already seen in the previous section, the 1/f noise in magnetic tunnel junctions is affected by defects that influence the tunnel conductance. These defects should be in the barrier and are either ionic reconfigurations that modify the barrier height locally, or defects can be loaded by changing the electric field, thereby altering local conductance. Both processes can be considered thermally activated and each is a two level system. In this case, the fluctuations should appear in the power spectral density as a Lorentzian superimposed on a background 1/f with the next form

$$S_V(f) = \frac{S_0}{1 + (f/f_0)^2} \tag{1.30}$$

In the time domains appears an aleatory noise, knowing by a random telegraph noise. This is because, the device resistance is a lifetime τ_1 in a state of resistance and lifetime τ_2 in another state. These times are determined by the transition probability between two states, so that

$$\frac{\tau_1}{\tau_2} \sim exp(E_i/k_B T) \tag{1.31}$$

And the inverse of the effective time is the sum of the each lifetimes.

$$\frac{1}{\tau} = \frac{1}{\tau_1} + \frac{1}{\tau_2} \tag{1.32}$$

Finally, we note that RTN could be due either of purely "electronic"(defects into the barrier) or "magnetic"(Domain walls) origin.

So, since now we will use to calculate the power spectral density for noise measurements the general expression of equation 1.33, represented in *Figure 1.14*

$$S_V = 2eIR_d^2 \coth\left(\frac{eV}{2k_BT}\right) + \frac{\alpha I^2 R_d^2}{Af^\beta} + \frac{S_0}{1+(f/f_0)^2} \tag{1.33}$$

State of the art on electron transport and low frequency noise in magnetic tunnel junctions explained in the Introduction, allow us to present more clearly the motivation of the present work:

1. Investigate electron transport and noise in fully epitaxial MTJs with MgO (100) barriers.

2. Study the influence of restructuring of Fe/MgO interface and of alloying of Ferromagnetic electrodes on TMR and low frequency noise.

3. Investigate possible Quantum well states in MTJs.

4. Investigate the influence of structural and magnetic inhomogeneities on TMR and specially low frequency noise in submicrom MTJs.

2

Experimental Techniques

2. Experimental Techniques

2.1 Experimental description

As we have seen in the previous Chapter, magnetic tunnel junctions (MTJs) structures, besides intrinsic thermal and shot noise, may also present a voltage variation due to the relative fluctuation of the magnetization angle of the magnetic layers on both sides of the tunnel barrier, fluctuations of domain walls (DWs), as well as RTN and 1/f noise due to defects inside the barrier. Then, it is possible to study the magnetic and electronic noise through changes of the voltage at the junction.

In this Chapter we will present fully automatized experimental technique that we have used for the characterization of the magnetic structure down to 0.3 K. In the Thesis, we have further developed the experimental system for low frequency noise measurement designed previously by our group in 2005 [11, 73]. The improvements will be discussed in detail below and indeed are.

1. Samples protection of the electrostatic discharges and voltage spikes of the circuit due to connecting amplifiers or applying current, putting two potentiometer to the input of the amplifier (one to ground and one on the sample).

2. Experimental system controlled from the PC (practically fully automatized).

3. Development of new cryogenic experimental system capable of measuring simultaneously transport and low frequency noise down to 0.3 K and with the possibility of apply vectorial magnetic field.

So, to make it easier to understand to this Chapter we will organize it follows. The first part of the Chapter is an overview of the experimental setup used for the transport and low frequency noise measurements at room temperature, with principles of operation of each of its elements and our main experimental improvements. The next part is related to the characterization and modeling of the experimental setup and signal channels. We will see how to correct the experimental data and how to take into account the signal propagation through the circuit

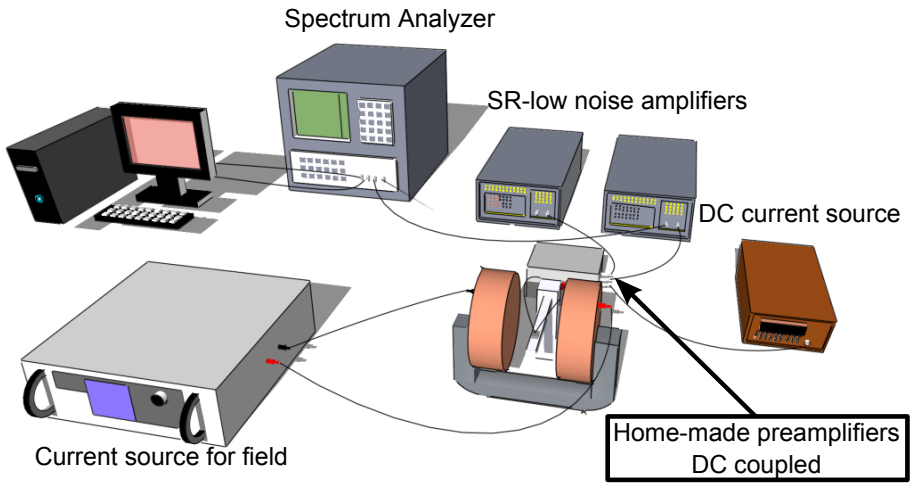

Figure 2.1: Schematic representation of the experimental setup for low frequency noise measurements at room temperature.

with samples. Finally, we will describe a new by developed unique cryogenics system for transport and low frequency noise measurements, with the possibility of apply 3D magnetic fields and temperature range down to 0.3K.

2.1.1 General description

Firstly, we are making a brief description of the experimental system used at room temperature. *Figure 2.1* shows the sketch of the experimental setup. In this configuration, it is possible measure simultaneously tunneling transport and low frequency noise in magnetic tunnel junctions. One of the main difficulties that we have found in our measurements is the large sensitivity of the barrier to possible electrostatic discharges. To solve this problem, we have made significant improvements in the system, greatly improving our chances of success with the measurements, without losing practically any sample by our manipulations (due to such as connecting amplifiers, current, etc.).

The first solution has been to connect the experimental system to ground, in

order to prevent voltage spikes pass through the sample. The second solution was less evident. The most delicate moment in the transport measurements is when the circuit be closed, since any voltage peaks of the devices that may will pass through the sample. This problem was solved by putting a variable resistance of 1 MΩ in series between the sample and the amplifiers. These resistances were varied slowly to zero once the circuit is being closed. With this technique we have achieved decreasing at least in factor 10 the probability to lose sample and even to measuring noise on submicron tunnel junctions.

The sample will be placed in the center of an electromagnet (*Figure 2.1*), powered by KEPCO source current, which creates a magnetic field in the plane parallel to the surface of the sample (typically along the easy axis). The field is uniform as possible across the magnetic tunnel junction. The electromagnet is water cooled and can cover a range of fields from +1.7 to -1.7 kOe. To contact electrically different samples, we have used the four-probe methods to reduce the electric circuit contribution. With this technique, we can apply current in two terminals and measure the differential voltage in the remaining two.

The signal is amplified by two amplifier stages connected in series. The first stage is homemade preamplifiers. At this stage amplifies all response of the sample (both AC and DC signal). In the second stage, we use the commercial amplifiers (SR560) which divide the signal in two parts. The DC signal is measured with a data acquisition card (DAC), and the AC signal is amplified and measured by the spectrum analyzer (SR780) with a bandwidth between DC-102.6 kHz.

The DC current applied on the sample is done either with a Keithley 6221 current source or a battery, depending on whether we want to measure tunneling transport (IVs) or low frequency noise. For the low frequency noise measurement, we have used a battery in series with a variable resistance to apply a constant current, because the noise in the current sources is too high respect to the level of noise that we want measured. In order to change the current, the resistance must be changed manually, because the battery applies a constant voltage. In the sense

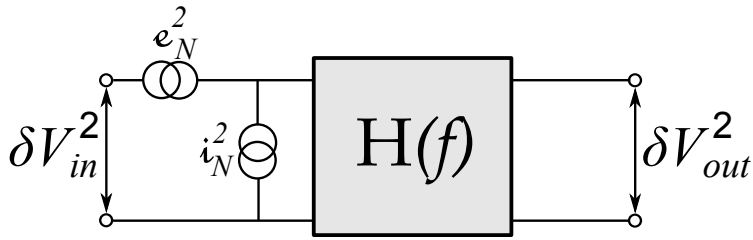

Figure 2.2: Model used to represent a linear system with intrinsic noise. Where e_N^2 and i_N^2 represent the voltage and current noise source, and $H(f)$ is the transfer function.

to automatized the measurements, we have used a AR500KL.25 potentiometer (with a range from 0 to 500 kΩ) controlled by step motor with RS232 protocol from the PC. This implementation has allowed us to carry out the measurement which variable bias 24h/7days. This operation was almost fully-automatized, making it possible to vary the field and the current conditions reducing the time spent on each experiment.

Once we have described our experimental system, we will now analyze in details the different side of the electronic circuit. In order to determine currently the electrical contribution and the resolution of our system.

2.2 Fluctuations in circuits

As first approximation, we can model a circuit as a quadrupole (*Figure 2.2*), which only we are interested to know the input and output of the circuit. Secondly, let us assume ergodicity (invariance of measurements as a function of time) because we are measuring noise in equilibrium. We expect that during reasonable time, at few least minutes, the system to be as stable as possible. Thus, we will have ergodicity in the sample under study, in electronic devices used for their detection, and those used for applying a voltage to the sample. Our goal is to understand how to changes the random signal V(t,s), when it passes through amplifiers and

other linear systems. A linear system is known as one that can be characterized by a transfer function, defined as

$$H(f) = \frac{V_{out}(f)}{V_{in}(f)} \tag{2.1}$$

Applying the Wiener-Kinchin theorem, we will obtain the noise power ($S_V(f)$) taking the Fourier transform of

$$S_{V_{out}}(f) = S_{V_{in}}(f)H(f) * H(f) =\mid H(f) \mid^2 S_{V_{in}}(f) \tag{2.2}$$

This expression for the noise at the output is only valid if the linear system has no intrinsic noise. But this is not generally true. To include the noise introduced by the linear system, we will be modeling two independent sources of fluctuations represented by their respective spectral densities, with units of voltage (e_N^2) and current (i_N^2). In agrement with Norton and Thevenin theorems, the noise sources will be placed as shown in *Figure 2.2*. The current noise is transformer into voltage fluctuations acting on a resistance, so that $\delta V_{i_N}^2 = i_N^2 R^2$. So, an arbitrary resistance will be connected to the system input. Then, the voltage noise generated by our resistance, the voltage noise of our linear system and the fluctuating current are all independent. The resulting spectral density can be calculated by summing of all the spectral densities. This provides the input noise to the system. To calculate the output noise, we just have to be multiplied by the modulus of the function will transfer.

We must keep in mind however that the transfer function of bandwidth will be defined by

$$\Delta f = \int_0^\infty \mid H(f) \mid^2 df \tag{2.3}$$

Which allows us to identify the spectral density in a frequency band sweeping the center frequency. The main problem is that the bandwidth of the filter is inversely proportional to the response time of it, and therefore if we want to

obtain accurately frequency, we will need a very long time. For this reason the frequency sweep experiments are used for high frequency measurements, which is a resolution of the order of kHz. To measure spectra at low frequency is more convenient to use Fourier transform.

The spectral density is the modulus of the Fourier transform ($\mathfrak{F}(t)$), but we need to calculate an infinite time domain and continuous conditions not met in a real experiment. For this reason, we use an approximation of this transform called discrete Fourier transform (DFT), which is to use a total time T and discretize the continuous separate points taking time τ_s. In this way, we obtain a transformed function with a resolution at frequencies of $f_0 = 1/T$, and reaches a maximum frequency $f_{max} = 1/2\tau_s$. The DFT is equal to the continuous, if we select the appropriate frequency domain.

In order to obtain similar values between DFT and continuous function, the transform must meet two conditions:

- The function must not contain frequencies above f_{max}.
- The function must not contain frequencies that are multiples of the resolution.

The way to avoid this effect is limit the range of frequencies that owns the process we want to analyze. To do this, we use filters a very high order, as they typically τ_s is limited by the equipment available. To avoid this spurious effect on the measurements, we have used a spectrum analyzer Stanford Research, model SR780. This equipment is very appropriate, because it has a filter bank which eliminates all frequencies above f_{max}.

Once solved these problems, we have tested that the method is successful and provides a good estimate of the spectrum, although somewhat biased because the variance of the estimator is equal to the magnitude that we are trying to estimate. The solution to this problem is to average, several times, the spectra obtained in this way. This procedure reduces the variance as 1/N, where N is the number of averages.

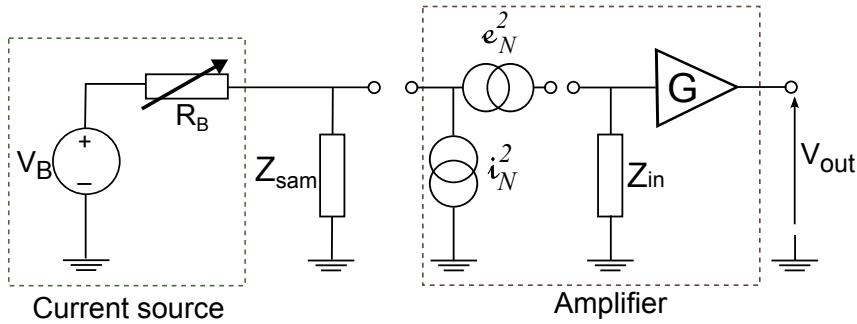

Figure 2.3: Diagram of measuring circuit with noise sources to characterize the noise contributions circuit.

2.3 Modeling of the circuit

In order to characterize the magnetic tunnel junctions, we will use dynamic conductance and low frequency noise measurement as a function of voltage and external magnetic field. As we will discuss in the following Chapters, the voltage fluctuations in these type of samples will be of 1/f contribution, random telegraph noise and white noise component (due to thermal and shot noise excitations). The magnetic tunnel junctions grown for this Thesis exhibit some of the lowest normalized noise levels that have so far been detected [69, 71]. Therefore, we have tried to minimize the external contributions of the circuit as much as possible. For this purpose, we have developed the experimental circuit represented in *Figure 2.3*. We can distinguish two parts of the circuit. The left part is the one that we applied current over the sample and the right one is that we measure the tunneling transport and low frequency noise. Thus, in this section will know the resolution and limitations of our system experimental

2.3.1 Sample excitation with a constant current

To excite the samples at a constant current, we have used a resistance (R_B) and a voltage source (battery), as it is shown in the left part of the circuit of the

Figure 2.3. After testing commercial power sources, rechargeable batteries and batteries, we have found that the batteries are the power sources with the lowest noise. In order to apply a constant current, we have put in series with the battery a variable resistor. For this experiment configuration, the R_B should be much greater than the sample impedance (Z_{sam}) so that the current does not depend on the sample. Because, we have in the input of the amplifiers two resistance in parallel ($R_B \| Z_{sam}$), and under these conditions is approximately equal to Z_{sam}. In the voltage source, the V_B fluctuations appear which we call e_B^2. Then, the new noise source contribution has a form:

$$\delta V_{i_B}^2 = R_{sam}^2 i_B^2 = R_{sam}^2 \frac{e_B^2}{(R_B + R_{sam})^2} \tag{2.4}$$

For this reason, we have used a battery to apply the desired current. The output noise in the battery is really small and need not be taken into account. But, this configuration does not allow us to apply an arbitrary power, as the excitation voltage is fixed, and is difficult to change R_B to any value. To solve this problem, we put in series with the R_B a PC controlled potentiometer with resistance varied by a steps by step motor, which gives us greater precision in the current applied without increasing the noise system.

2.3.2 Detection of voltage fluctuations

To detect the low frequency noise in magnetic tunnel junctions, we have used the INA111 instrumentation amplifier, which has the characteristic values of voltage and current noise, $e_{Ni}^2 = 10nV/\sqrt{Hz}$ and $i_{Ni}^2 = 0.8fA/\sqrt{Hz}$, respectively. As we have discussed in the previous section, each amplifier could be described by the model shown in *Figure 2.2*. In addition, we should take into account the resistance of the wires (R_w) that contributed to the system with thermal noise. Then, the total noise detected by the spectrum analyzer, neglected the noise introduced by the battery, will be:

$$S_V = e_{Ni}^2 + \delta V_{R_{sam}}^2 + i_{Ni}^2 (R_w + R_{sam})^2 \tag{2.5}$$

In order to quantify the level of noise introduced by the amplifier, we define the noise factor ("noise figure") as follows [57].

$$NF(f, R_S) = \frac{S(f)}{\delta V_{R_{sam}}^2(f)} \tag{2.6}$$

In this relation, we can see how the output noise of our amplifier increases respect to the R_{sam} noise. So the perfect amplifier noise measurements will have a noise figure equal to one. Based on the equation 2.5, we want to use amplifiers with lower level of noise current to have lower dependence with the sample resistance. For this reason, we have chosen the INA111 amplifier.

In the setup configuration shows in *Figure 2.3*, we could find two limitations in the resolution of our experimental setup. The first one is easy to see in the equation 2.5, because the minimum noise level that could be detected by our experimental setup will be defined by the voltage and current noise level of the amplifier. This problem is easily solved, since the spectrum analyzer allows us to use cross-correlation technique. This method is capable to discriminate in the noise measured, the sample noise over the circuit noise. To do this, we measured the voltage fluctuations with two identical amplifiers on two different channels and thus obtained two processes S_V^X and S_V^Y. The cross-correlation between these two series are defined as

$$R^{X,Y}(t) = \frac{1}{2T} \int_{-T}^{T} X(\tau) Y(t + \tau) d\tau \tag{2.7}$$

Being zero if both processes are not correlated. It allows us to discriminate the correlated noise between two different processes. Then, applying the Wiener-Kinchin theorem, we can define the cross-correlation power spectrum of the aleatory process and using the Fourier transform of both channels as

$$S_V^{X,Y} = \mathbb{R} \mid \mathfrak{F}[X]^* \mathfrak{F}[Y] \mid \tag{2.8}$$

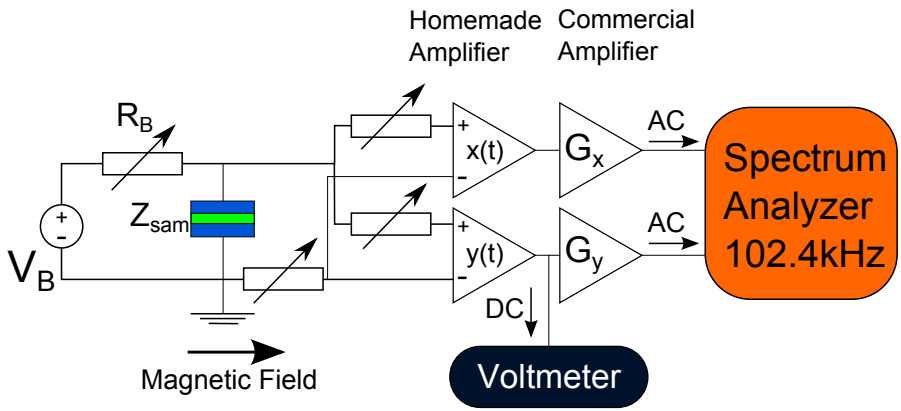

Figure 2.4: Diagram of the experimental system used to detect the power spectral density using cross-correlation method. Not included noise sources.

Where $\mathfrak{F}[X]^*$ is the complex conjugate of the Fourier transform of the channel X. This mathematical method allows us to measure noise signals below the amplifier noise, obtaining in this way a higher resolution.

The second problem is given by the low signal values that we want to detect, of the order of $nV/\sqrt{Hz}$. We solve this problem by putting a second amplification stage in series with the first one (i.e. in cascade), allowing to amplify the signal more than in million times. For the second amplification stage, we have used a SR560 commercial amplifiers. When using two amplifiers in cascade, the "noise figure"of the system will be defined by the equation [57]

$$NF(f, R_S) = NF_1(f, R_S) + \frac{NF_2(f, R_S) - 1}{G_1(f, R_S)} \tag{2.9}$$

This result shows that the noise characteristics of a cascaded system are dominated by the first amplification stage, since the second stage is reduced by the gain of the first stage. For this reason, we have used as first stage the INA111 amplifiers respect to SR560. The schematic representation of the experimental setup

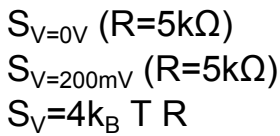

Figure 2.5: Power spectral density measured at room temperature in a resistance of 5 kΩ with and without current applied with battery. The dashed line represents the theoretical thermal noise value expected for this resistance.

is shown in *Figure 2.4*, where it has been incorporated the variable resistance between the samples and amplifiers, to insulate the junction from the voltages peaks of the circuit.

One of the best ways to calibrate the system is to measure the thermal noise in a resistance, since it is a frequency independent and is well known the theoretical value ($S_V = 4k_BTR$). In the *Figure 2.5*, it is shown the power spectral density measured in a resistance of 5 kΩ at room temperature, and it is in good agreement with the theoretical value expected. Moreover, one of the advantages of measuring noise in a resistance is having only thermal noise, therefore, when a current is applied the excess noise is due to the current source. This measurements corroborate that the current source used does not introduce extra noise to our measures.

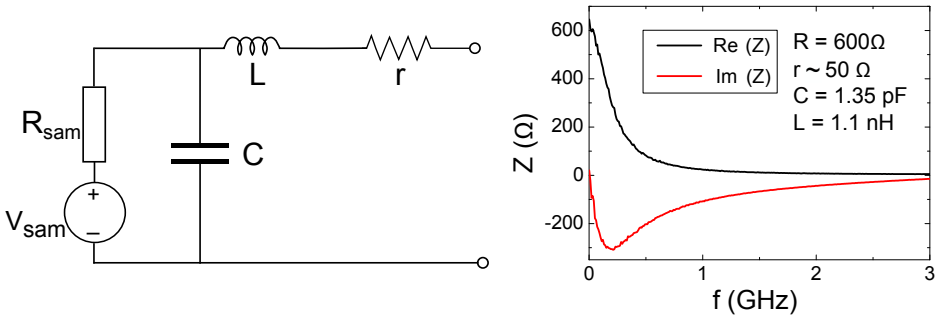

Figure 2.6: (a) Circuit diagram of the sample. C, L, r and R_{sam} represent, respectively, the capacitance between the top and bottom track, the track inductance, resistance and resistance of the junctions. (b) Sample impedance measured of a vector network analyzer (VNA).

2.3.3 Sample characterization

So far, we have described the experimental system that we have used, focusing on the resolution of the employed technique. For this, we have considered the samples as a resistive element, but really it is a impedance. The sample can be modeled electrically as described in *Figure 2.6* (a). From this scheme, we can deduce the complex equivalent impedance of the sample based on the free parameters capacitance (C), inductance (L) and contact resistance (r). These values behaved like a band-pass filter. It is therefore necessary to know these values to see if they affect the range of frequencies measured by the spectrum analyzer. For this reason, we have used a vector network analyzer (VNA) and have measured the impedance of the samples as a function of the frequency. The values of R_{sam}, C and L are intrinsic of the sample and the lithography process [74], while the r is due to the contacts for measuring voltage and is typically a few tens of Ω. In the *Figure 2.6* (b), it is shown the typical impedance of the nanopillar measured in the Chapter 6. The estimation values of capacitance and inductance, allows us to consider that for the frequency range in which we want to measure, we can consider the samples only as

a resistive elements, being able to be neglected the signal filtering in the spectrum.

2.4 Experimental cryogenic system

The system described in the previous section has been used for low frequency noise and electron transport measurements at room temperature. For low temperature measurements, we have introduced the samples in a cryogenic He-3 Janis system with a new design developed during course of this Thesis (see sketch and picture of *Figure 2.7*). Although the low temperature experimental system is more complex, once calibrated, allow us to make accurate measurements, since we can neglected the thermal noise of the wires in the system. Moreover, the cryostat and the preamplifiers box (on top of cryostat) acts as a Faraday cage, reducing even more external noise, increasing the accuracy of the measurement and reducing the effect of the electrostatic charge. So, we have the source current and amplifiers at room temperature (out the cryostat), while the sample is cooled down from room temperature to 0.3 K. The connections between these areas were made using manganin twisted pairs, for both voltage and current excitation. Twisted pairs reduce external couplings that contaminate the signal. The problem is that because the wires are twisted, it increases their capacitance. A wire can be modeled as a resistor in parallel with a capacitor, which acts as a low-pass filtering. In the experimental setup at room temperature, the line is very small and the Cu wires capacitance does not affect us. But now, the length of the wires inside the cryostat is about 1.5 m, and we need to verify the capacitance contribution. The low-pass filter will cut the signal from a certain frequency. At room temperature, the resistance of the wires is $R_w \sim 89\ \Omega$ and the capacitance is close to $C = 320\ pF$. These values give us an upper cutoff frequency of the order of $f_c \sim$ MHz, well above the frequency range in which we have interested.

One of the major advantages of our new cryogenic system is the capability of measuring electron transport and low frequency noise in three different samples

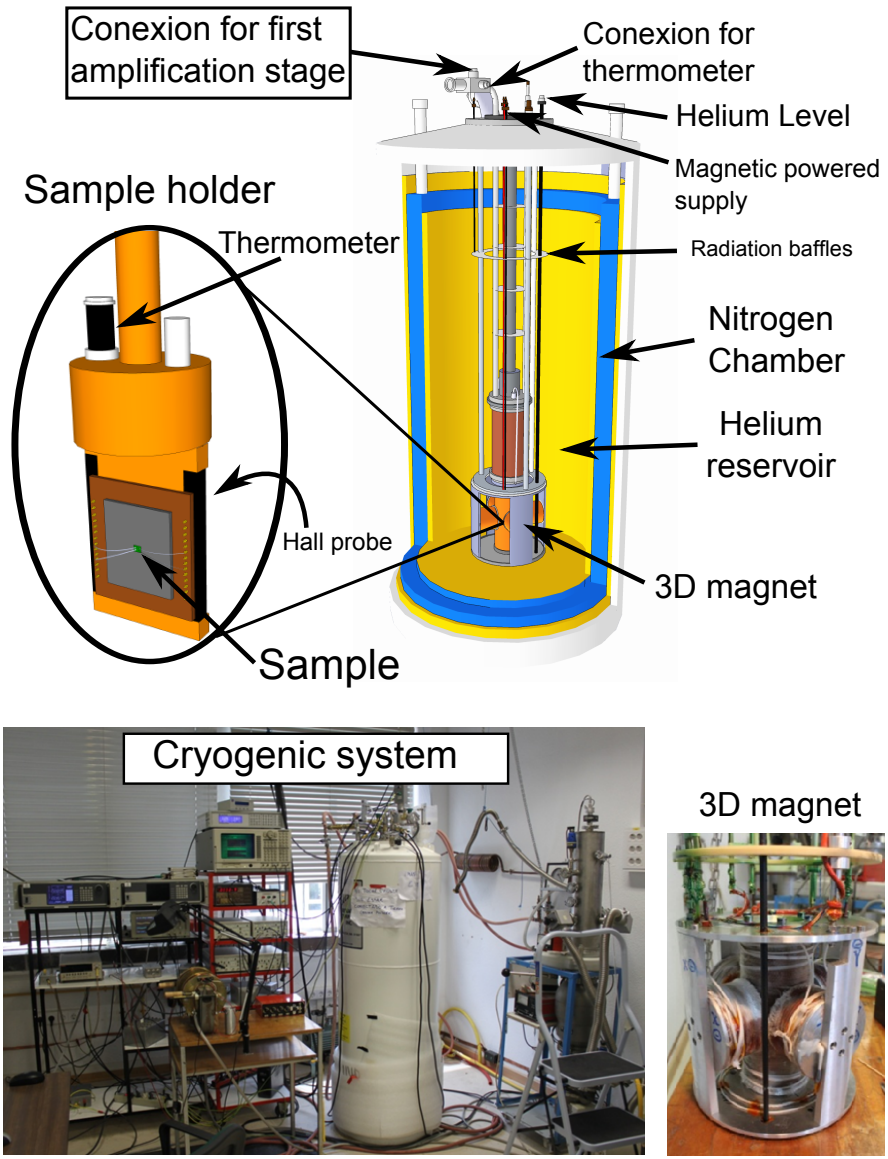

Figure 2.7: (Top) Schematic representation of the cryostat and the sample holder. (Down) Experimental systems and 3D magnet pictures.

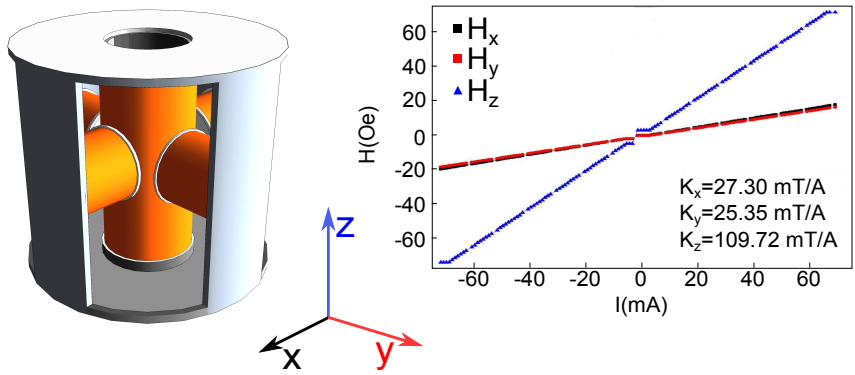

Figure 2.8: Sketch of the 3D magnet and the calibration using hall probe.

every time cool down the temperature, since it has 18 wires. This greatly increases the efficiency of each experiment, because the stress of cooling down the temperature on the barrier might of electronics cause the dielectric breakdown in some of them.

When the sample reaches 2K, we have a need to pump liquid helium inside a boat in thermal contact with the sample, and for 0.3K we have used liquid He-3. The temperature inside the cryostat was measured using a temperature controller Lakeshore 340, which has a temperature control system consisting of a heater of 34Ω and a PID system. Depending on the temperature range, we have used two different thermometers (down to 20 K CERNOX and RuOx between 20 K and 0.3 K) with a standard calibrations.

The cryostat has been designed with the possibility to apply magnetic field in three directions of the space (3D magnets shows in *Figure 2.8*). Such measurements are very interesting to the study of the magnetic anisotropy in magnetic tunnel junctions or magnetic multilayers. Moreover, it is possible to apply magnetic field in the plane and out of the plane of the sample, may allows to study in more detail the spin transfer torque effects in the future. For this purpose, apart from the 18 cables to measure low-frequency lines, the cryostat has also two additional wires

for high frequency (up to 17 GHz). Each electromagnet was made with a 0.5mm diameter of superconducting cable (NbTi), and is powered by a KEPCO current source. The 3D magnet calibration was made using Hall probe and it is shown in *Figure 2.8*.

In this Thesis, all the measurements at low temperature were carried out along the easy axis (z axis in *Figure 2.8*). Actually, the workshop of the University is developing a special source capable of powering the 3D Magnet. In order to obtain good accuracy of the applied magnetic field, a Hall probe is positioned on the back of the sample holder (see sample holder in *Figure 2.7*).

The experimental system is automated using LabView. All the devices were connected to a PC via a GPIB or RS232 protocol controlled by the programming language. Also use a PCI card with 8 differential channels for measuring voltage and 2 digital to analog converter (DAC). The amplification lines not was controlled by the PC. The selection of the amplifier gain in the magnetic state with maximum resistance is necessary, since in this magnetic state is expected to obtain a higher spectral density values on the samples.

2.5 Summary

In summary, we have substantially improved a experimental system for low frequency noise and electron transport measurements. The system is now capable to measuring voltage noise from room temperature to 0.3K. In this system, we have added the possibility to change the way of applying a DC current, so that it contributes the least possible noise measurement. Using a battery minimizing the noise introduced by the current source. We have incorporated in the current source a potentiometer in series with the variable resistance, which has the possibility of have a good control over the applying DC current, without increase the background noise.

We have reduced the probability of dielectric breakdown of the junctions by introducing protection a potentiometer before amplification stage, increasing our

measurement effectivity.

During the development of this Thesis, we have designed an unique cryogenic system, capable of measuring transport and low frequency noise from room temperature to 0.3K, and with the possibility of applying vectorial external magnetic field.

3

Influence of Carbon doping in Fe(100)/MgO/Fe fully epitaxial magnetic tunnel junctions

3. Influence of Carbon doping in Fe(100)/MgO/Fe fully epitaxial magnetic tunnel junctions

3.1 Brief introduction

It was shown in the Introduction of this Thesis, that the first studies of transport and noise in magnetic tunnel junctions (MTJ) were done in MTJs with amorphous Al_2O_3 barrier[61, 62, 63]. In these MTJs, the low frequency noise is either due to magnetic fluctuations or defects in the barrier. In order to obtain devices with higher magnetoresistance (MR) ratios, new barriers with crystalline structure are introduced (such as MgO (001) barrier), which use coherent spin-dependent tunneling in epitaxial MTJ. The Fe(100) | MgO(100) | Fe(100) tunnel junctions, can be grown in a monocrystalline way, due to the low mismatch between the lattice parameter of both materials. Besides, Mathon and Butler et *al.* [9, 10] developed pioneer calculations of conductance, showing that due to the conservation of parallel momentum, it is possible to obtain the conductance and consequently the tunnel magnetoresistance (TMR) through first principles methods. Both models, calculate the probability of transmission and the tunnel density of states associated with the iron electrode yield an effective polarization very close to 100%. Due to the symmetry of the MgO band structure, the iron avancent Bloch states have a different attenuation inside the barrier. Such different attenuation of the wave function reduces the conductance in the antiparallel (AP) state at the Fermi level (E_F) and leads to mentioned above polarization, that results in an increased TMR. Another important result, in these works, is the contribution of the "hot spots"in the reciprocal space. The transmission as a function of the momentum $\overrightarrow{k}$ has a maximum at points with a $\overrightarrow{k_{\shortparallel}} \neq 0$ and the conductance somewhat increases in the AP state leading to a diminished TMR. It should be noted that the contribution of these "hot spots"increases as the disorder at Fe/MgO interface increases. In this Chapter, we will study magnetic tunnel junctions grown with an epitaxial technique. This growing technique creates monocrystalline devices with these smaller spurious effect since the disorder is reduced.

In 2005 our group carried out the first study of transport and noise in fully

epitaxial MTJ based on Fe(110) | MgO(111) | Fe(110) [11]. This work intended to understand the dependence of the TMR for this new crystalline structure. There were two important results reported: firstly, the corroboration of the enhancement of the TMR due to the high polarization in the (110) direction, in agreement with Yuasa's group [75]. Secondly, the observation of the excess of normalized 1/f noise in the AP state. The problem of the (110) direction is related with the number of dislocations at the interface. It is higher for the (110) than for (100) direction and consequently the low frequency noise and TMR are highly affected. For this reason, since 2006 our group moved in the direction to study fully epitaxial MTJs based on MgO barriers grown in the (100) direction.

An increasing of the TMR values, via improvement of the electron transport and a reduction of the low frequency noise in MTJs is needed, because the number of applications of the MTJ is huge (like magnetic memories, ultrasensitive field detectors, wireless communication, etc). The general goal, from the application point of view, is to obtain more sensitive devices (improve the signal to noise ratio) and better robustness (as a function of bias, temperature, etc). The idea of introducing doped electrodes with light elements to improve the tunneling phenomenon is well known. A number of groups have used this method to increase the polarization of the electrodes, reduce the misfit between electrode and barrier, etc. (some examples of different groups are [76, 77, 78, 79]). In this thesis, we doped the MTJs with different elements (Carbon, Nitrogen and Vanadium). In particular, this Chapter presents the case when the bottom electrode is doped with Carbon (C). As we shall see, the Carbon doping has a strong influence on the tunneling transport of the MTJs. The C is diffused from the substrate to the bottom electrode, and the interface presents a new reconstruction c(2×2), that affects the transport in the junctions [48]. The C will play an important role also in noise, probably because it "fills"or relaxes the vacancies and/or substitutes the oxygen in the interface, improving the tunneling transport through the barrier.

3. Influence of Carbon doping in Fe(100)/MgO/Fe fully epitaxial magnetic tunnel junctions

We have measured the dynamical conductance and TMR in Carbon free and Carbon doped samples, in a large bias window, up to 3 V. For C-doped MTJs we observed a strong asymmetry respect to the bias in transport and low frequency noise, probably related to the asymmetry of the structure. Multiple sign inversions of the TMR appear due to interfacial resonance states (IRS). We will compare our experimental results with recent theoretical calculations for C free [9, 10, 80, 81] and for C doped [81, 82] MTJs. In these theoretical calculations, it is assumed that there are no defects in the barrier. However, the real barrier and the interface are not perfect. The fluctuation of these defects should be the responsible of the low frequency noise which has "electronic"character. Also the variation of 1/f noise as a function of bias has not been investigated and has to be understood. The most extended model for MTJs divides the origin of the low frequency noise in two parts. One of them appears at the transition, between the P-AP states. This noise is mainly due to magnetic fluctuations [66]. The other noise contribution is in the saturated state, i.e. far from the P to AP transition, and it is attributed to the relaxation time of the defects and/or tunneling electrons in or near the barrier. Here we will investigate also the low frequency noise in the AP state which could have both "electronic"and magnetic contribution.

So, generally one may expect that the 1/f noise behavior as a function of bias voltage, is different from P state to AP state. The main difference in conductance between both states was briefly explained in the Introduction of this Thesis. The conductance in the P state at E_F is governed by electrons with Δ_1 symmetries bands and in less contribution by $\Delta_{5,2'}$ bands (*Figure 3.1*). In the AP state, at low bias, the conductance is due to electrons with Δ_5 symmetry bands. Therefore, the fluctuation of the defects in the interface of the barrier could have a strong impact on this conductance channel and consequently the noise in the AP state could be enhanced. When we apply large currents, the Fe electrons band structure will be shifted and the electrons with new (Δ_1) symmetry bands will start to contribute

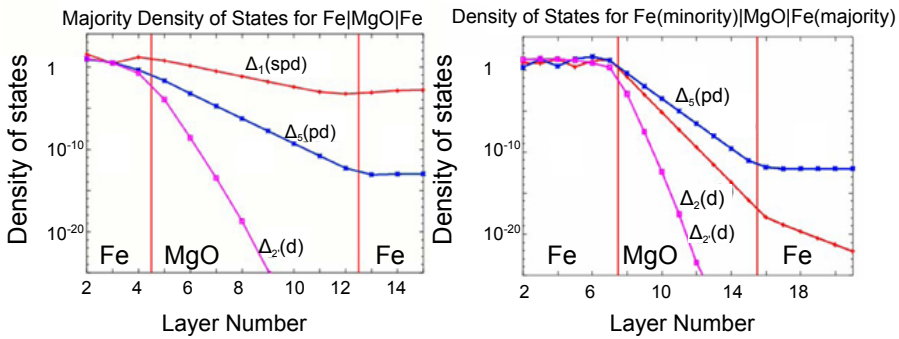

Figure 3.1: Absolute square of the wavefunction for incident electrons of different symmetries as a function of thickness of the barrier. The left figure describe tunneling for parallel alignment of the magnetic moments of the electrodes with $k_{\parallel} = 0$ contributions to $G^{\uparrow\uparrow}$. Similarly, the right describe contributions $G^{\downarrow\uparrow}$. [Adapted from Ref.[9]].

on conductance. The asymmetry as a function of bias, showed for transport, could affect the noise, too. We will also analyze the low frequency noise as a function of magnetic field to verify the possible influence of spin torque (ST) on domain walls (DW) in the AP state. In order to investigate the importance and localization of the defects inside the MgO barrier we shall study the shot noise as well.

3.2 Sample descriptions

3.2.1 Description of the growth process of the samples

The measurements presented in this Chapter were done on magnetic tunnel junctions grown by molecular beam epitaxy (MBE) on MgO (100) substrates, under ultra high vacuum (UHV) conditions, operating with a base pressure of 5×10^{-11} mbar. The samples were grown within a bilateral collaboration project between Magnetrans-UAM group and the Institute Jean Lamour, CNRS-Nancy University (France) with the group of Dr. C. Tiusan (active between 2007 and 2012). The author of this Thesis has made five scientific visits to the CNRS-University of

Nancy within this project to participate in the growth of the MTJ samples under study.

In MBE, the solid source materials are placed in evaporation cells to provide an angular distribution of atoms or molecules in a beam. The substrate is heated to the necessary temperature, about 600°C, and when it is needed, continuously rotated to improve the growth homogeneity. In comparison with the sputtering technique, the most important aspect of the MBE is the slow deposition rate, which allows the films to be grown epitaxially. The epitaxial growth of the samples needs a clean atmosphere to reduce contamination, thus UHV is essential in this technique (close to 10^{-11} mbar).

Here we shall concentrate on two different kinds of junctions. The first type consists of single crystal MgO(100) //MgO (10 nm)/ Fe (45 nm)/ MgO (2.6 nm$\sim$ 10 ML or 3 nm$\sim$ 12 ML)/ Fe (10 nm)/ Co (20 nm)/ Pd (10 nm)/ Au (10 nm). In the second type of junctions the 10nm MgO buffer layer over MgO substrate is absent. The samples were grown on (100) MgO substrates, previously annealed at 600°C during 20 min. Carbon impurities are already present in the MgO substrate before the growth. The initial annealing does not completely remove the carbon impurities from the substrate. Therefore when the Fe layer is directly grown over the MgO substrate, the rest of the Carbon diffuses into the ferromagnetic electrode and MgO barrier. Moreover, the residual C atoms could diffuse and segregate to the Fe top surface. Instead in the second kind of junctions, the bottom electrode surface is preserved. To avoid the diffusion of the carbon, we grow 10 nm of MgO over the substrate, this will serve as an antidiffussion barrier. The reflecting high energy electron diffraction (RHEED) analysis carried out along the [100] direction reflects this situation (see *Figure 3.2*). On the C doped MTJ revealed a c(2×2) reconstruction-related additional pattern that is not present in the carbon free MTJs [83]. As it is suggested below, the carbon plays a fundamental role in the quality of the barrier, because the C probably "fills"or relaxes the vacancies at the

Fe/MgO interface, as well as vacancies inside the MgO barrier. So these two kinds of samples will evidence the role of the C in the transport and noise properties.

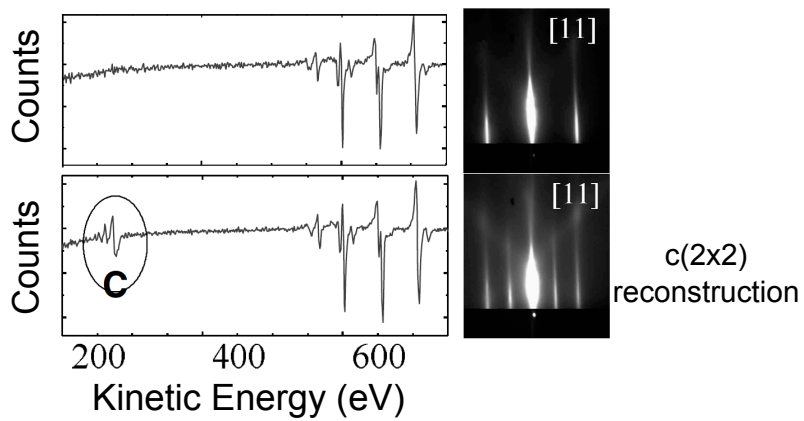

Figure 3.2: RHEED patterns for the bottom Fe(100) surface along the [11] direction corresponding to a clean surface (top) and the c(2×2) reconstructed surface (bottom). The Auger spectra depicted in validate the absence of carbon impurities for clean samples and the presence of carbon for the reconstructed surfaces.

For both types of samples, after preparating the MgO substrate or buffer layer, a 50 nm thickness of Fe is deposited. This will be the soft magnetic layer in the studied MTJs. The iron layer grows pseudomorphically on MgO(100) substrate. To improve the quality of the iron, deposited at room temperature, it is annealed at 725 K for 20 min, in order to obtain an atomically flat surface. In this conditions, the lattice mismatch is around 3.9%, when the Fe unit cell is rotated by 45° with respect to the MgO unit cell, and the surface RMS roughness after annealing, estimated from atomic force microscope images, was about 0.3 nm [84]. After that, a thin MgO insulating layer was subsequently deposited by means of an electron gun at rate of 0.5 nm/min. Insulating barriers with thickness from 10 and 12 ML were grown epitaxially on the Fe layer to obtain a good spin filtering effect [9]. Moreover, these thicknesses are needed to grow a high quality barrier, because after the critical thickness (about 5-6 ML), a plastic relaxation occurs

inducing dislocations within the barrier [48, 85, 86] and two-dimensional layer-by-layer growth was observed by RHEED intensity oscillations, not shown [48]. The second Fe magnetic layer, 10-nm-thick, was epitaxially grown on the top of the insulating MgO barrier at 100 °C. We will refer to it as the hard electrode due to the coupling with the next layers. It was subsequently annealed for flattening at 380 °C for 10 min. A Co layer with thickness of 20 nm was deposited on the top of the hard electrode using an electron gun at 3 nm/min. The RHEED images clearly indicate an epitaxial growth of Co on Fe. To prevent the ex-situ oxidation of the top Co layer and to protect it during the subsequent patterning steps of the lithography, a 10-nm-thick Pd capping layer and 10 nm of Au have been used, like a protective layer. The schematic representation of the samples is shown in *Figure 3.3*.

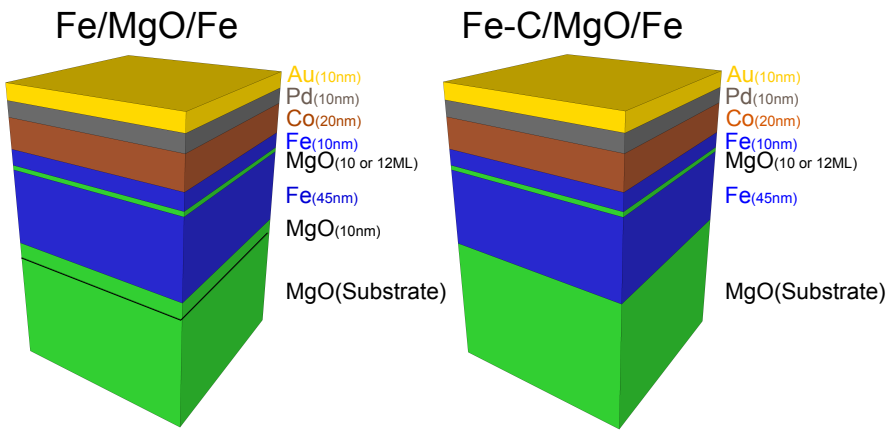

Figure 3.3: Schematic representation of both type of samples (Carbon free and Carbon doped MTJs). Positive current correspond to inject current from the bottom electrode (in our samples the free electrode) to upper electrode.

3.2.2 Photolithography of the magnetic tunnel junctions

By using a standard UV lithography these continuous wafer layers were patterned into micrometric squares, the sizes are down to $10 \times 10\ \mu m^2$ and up to

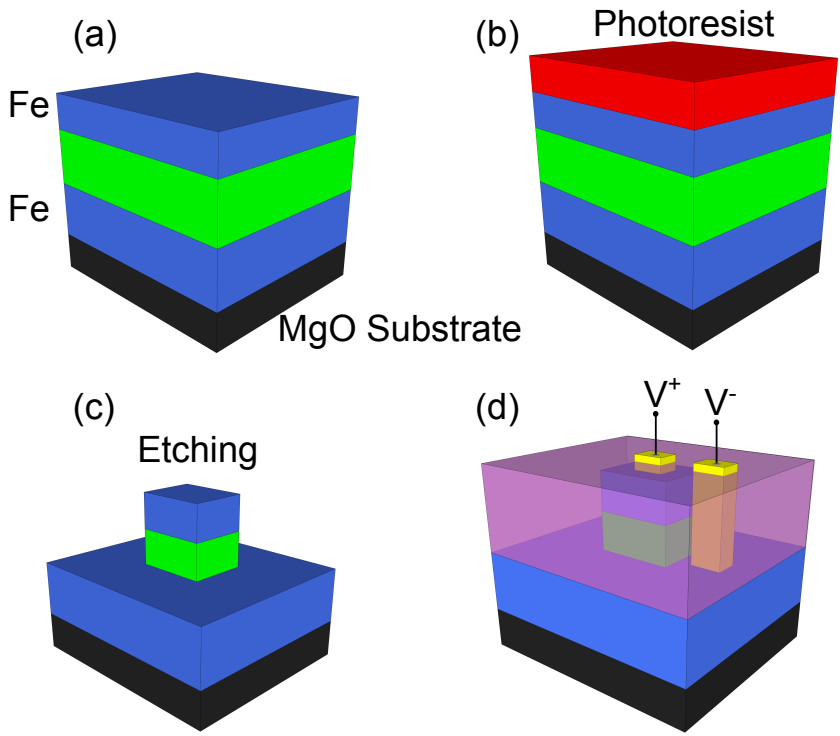

Figure 3.4: Sketch of the photolithography process. (a) sample before the photolithography process. (b) The deposition of the resin. (c) Etching of the top electrode and MgO barrier. (d) MTJ after the photolithography process and deposited the contact pads.

$40 \times 40\ \mu m^2$. The etching of each layer was controlled by *in situ* Auger spectroscopy. This lithography process must fulfill two functions: to make contacts at the top and bottom electrodes and to insulate them. The process for making micrometer MTJs using standard UV lithography is complex and involves several steps, all of them were performed in the microelectronic laboratories of the Faculty of Science Poincare University (Nancy). In a first step, the tunnel junctions were defined by following process: the wafer is cleaned with solvent and dried with nitrogen gas. Then, the surface was coated with a photosensitive resist layer that is distributed as uniformly as possible. All resin of the wafer is put in contact with a

mask (previously designed) and is subjected to UV light, due to the change in the chemical properties of the resin. We can remove the desired part of the resin using a developer solvent. The exposed parts of the samples will be further processed and parts covered with the resin will be kept. In this first step, we etch the exposed part by an argon ion beam down to the MgO barrier electrode. This is achieved by controlling the etching procedure by Auger spectroscopy. This technique provides information on the chemical species on the surface and, therefore, tells us when to stop. The process stops once it reaches the tunnel barrier MgO. After etching, the sample is immersed in a solvent bath to remove the remaining resin and dried with nitrogen.

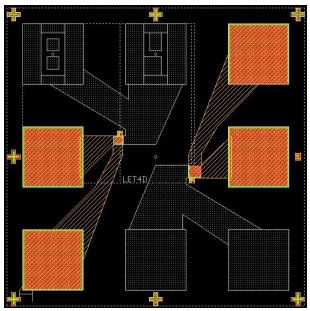

Figure 3.5: Sketch of the contacts pads of the MTJs.

Once we reach the MgO barrier, the second step is the patterning of the bottom electrode, using a different mask and following the same procedure that we use in the first step, ion etching, down to the substrate. The third step consists on the deposition of a 150 nm thick silica layer by sputtering in all the wafer, this isolates the top and bottom electrodes to avoid future short-circuits. In order to open the windows in this insulating layer, a lithography procedure leaves two square of resin aligned with the top and the bottom contact. Then, the resin that we left is lifted off in a bath of acetone and, this opens the windows in the insulating layer, that will be used in the next step.

Finally we designed in another step of lithography and lift off the 150 nm thick of aluminum contacts paths, we proposed the aluminum by sputtering. *Figure 3.4* shows schematically the different lithography steps. The final result is shown in the sketch of *Figure 3.5*. After a final wash and drying, the samples are ready to be measured. More information of the elaboration of the samples and characterization may be found in ref. [48]

3.3 Transport measurements for C free and C doped MTJs

3.3.1 Samples with 10 ML of the barrier thickness

3.3.1.1 Tunnel Magnetoresistance measurements

The typical TMR curves for Fe/MgO/Fe and Fe-C/MgO/Fe MTJs are illustrated in *Figure 3.6*, measured at 0 V DC bias, by using a low amplitude (with excitation below 5 mV) square current wave and at three different temperatures. First, in order to corroborate the quality of the barrier we discuss the TMR at room temperature for both types of samples, which has a value about *160%*. The reduced value of the TMR with respect to theoretical predictions implicates a reduction of the filtering efficiency of the MgO barrier, possibly due to structural imperfections and related to parasitic conductance channels, over the area of tunnel junctions [16, 48]. The defined transition between the P-AP states and the value of the TMR are in agreement with previous works[42], showing the high quality of our MTJs. The TMR value and the temperature dependence with the conductance (see below), clearly evidence the absence of "pinholes" in the barrier [87, 88]. At room temperature, the coercive field for the free electrode (bottom layer) is close to *20 Oe*, whereas the hard electrode is *430 Oe*.

As we have seen in the Introduction, at 0 V bias, in the P state the tunneling process is dominated by electrons coming from Δ_1 symmetry and a minor contri-

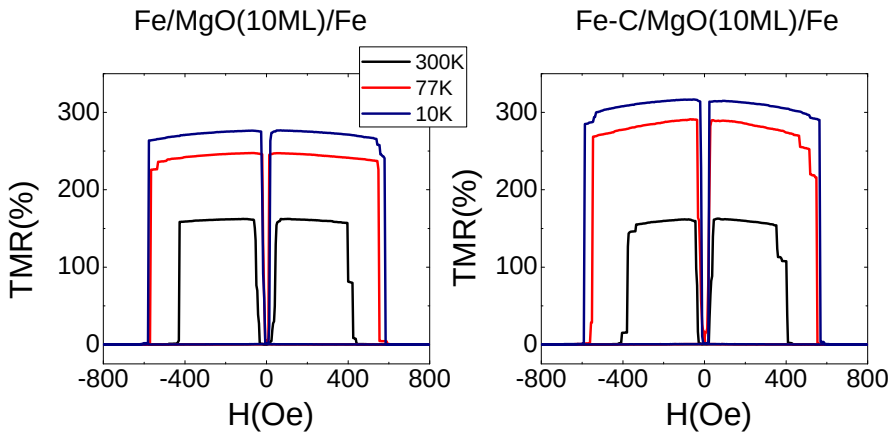

Figure 3.6: TMR at 0 V bias for different temperatures 300 K (black line), 77 K (red) and 10 K (blue) for both types of samples. The TMR and the coercive field increase with decreasing the temperature.

bution by $\Delta_{5,2'}$ bands. Instead, in the antiparallel state (AP) the conductance is dominated by Δ_5 bands, because Δ_1 bands is well above of the E_F (*Figure 3.7*). The other symmetries present at Fermi level are attenuated for this thickness of the barrier (see *Figure 3.1*). As we will show below, the resistance in the P state is seen to be nearly independent of temperature, while in the AP state increases with decreasing temperature [89]. Due to the high influence of the temperature on the AP state conductance, the TMR reaches a value of *300%* at 10 K, in agreement with the results obtained by Matsumoto et *al.* [16]. The first-principles theory does not take into account the dependence of the resistance with temperature [88]. The perturbation in the magnetization alignment of the electrodes due to thermal excitations of spin waves is considered to be the dominant effect on the TMR variation with the temperature, with its influence on R_{AP} being much stronger than R_P. At low temperature the thermal excitations are diminished, thus the magnetic moments are more stable. This is reflected in the higher value of TMR and in the higher coercivities (i.e have a maximum possible of coercive field), and higher fields are needed apply to change the direction of the magnetization of the

hard electrode. As we show in *Figure 3.6*, the coercive field for the hard layer strongly increases with decreasing temperature.

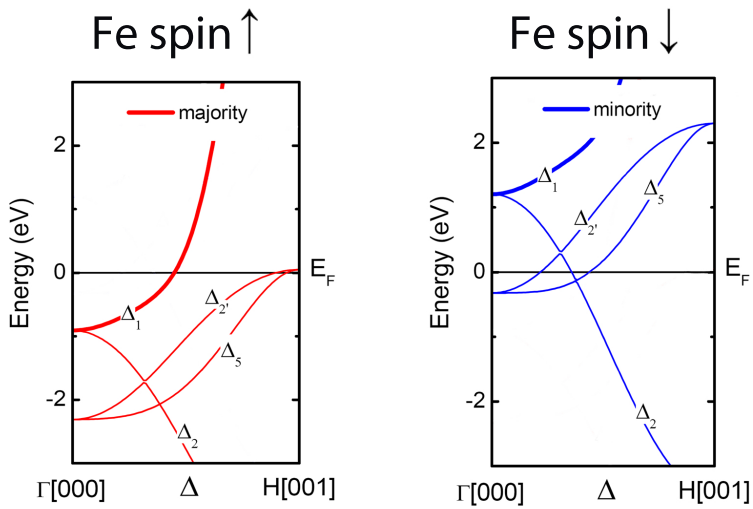

Figure 3.7: Bulk band structure diagram for the majority spin of bcc Fe and for the minority spin of bcc Fe. We highlighted the H direction corresponding to propagating electrons perpendicular to the (100) surface of Fe ($k_{\parallel} = 0$). The states along this direction are labeled by Δ, the different indices corresponding to different symmetries of the wavefunction. [Adapted from Ref.[48]].

3.3.1.2 Dynamic conductance measurements

Let us now turn to analyze the dynamic conductance ($G = dI/dV$) in the two different types of samples as a function of applied bias. *G(V)* for both types of samples is represented in *Figure 3.8(a),(c)*, at 4 K, within a voltage range up to 1.6 V. The influence of Joule heating (estimated to be a few Kelvins at 4 K) on the I-V curves is neglected due to the rather weak low temperature dependence of both G_P and G_{AP} states below 20K [48, 68]. Carbon free and Carbon doped MTJs have a strong dependence with the applied bias voltage and with the polarity. In this subsection we will discuss the causes of that behavior and the role of

the C doping in the dynamic conductance. In an ideal tunnel junction with two identical metallic electrodes, the IV curves should be symmetrical [90]. However, this approximation is not the case in the studied samples, due to the different factors that we attribute to structural differences between both electrodes. Numerous previous studies have tried to understand the structural asymmetry in epitaxial MTJs [48, 77, 91]. They concluded that it is indeed very difficult to make identical upper and lower Fe/MgO interfaces with the same roughness, dislocations, etc. Consequently, the atomic structure could be somewhat different. In a clean MTJ, the bottom interface is nearly perfect, thus there should be a low number of Fe-O hybridizations, because the MgO is grown over the Fe (001) in a two dimensional plane. The top MgO interface, which results from the three dimensional growth of Fe on the MgO barrier, is typically less flat [84]. Such an increased roughness could lead to an enhanced Fe-O hybridization at the upper interface. For this reason, the obtained barriers should exhibit an asymmetric profile, thus the conductance differs when electrons are injected from one side or from the other side of the junction. Nevertheless, this problem is very difficult to solve. In fact, in *Figure 3.8(a)*, we can observe, that for negative bias, when the electrons tunnel into the bottom Fe/MgO electrode, $G_P(V)$ and $G_{AP}(V)$ show an asymmetric local maximum superimposed on a roughly parabolic background. Also, the oxidation in the interface could be responsible for the reduction of the TMR [92].

The presence of Carbon in the interface has a weak influence on the zero bias TMR, but it further increases the asymmetry observed in the clean samples, due to the further enhanced structural difference between both interfaces (Fe-C/ MgO and MgO/ Fe), see *Figure 3.8(b),(d)*. Theoretical calculations have demonstrated that the carbon doping of the bottom Fe-C/ MgO interface leads to a stronger (and more asymmetric) dependence of conductance as a function of bias [82]. Our experimental results corroborate this strong asymmetry. For Fe-C/ MgO (10 ML)/ Fe samples (see *Figure 3.8(c)*) at negative bias, when the electrons tunnel from the

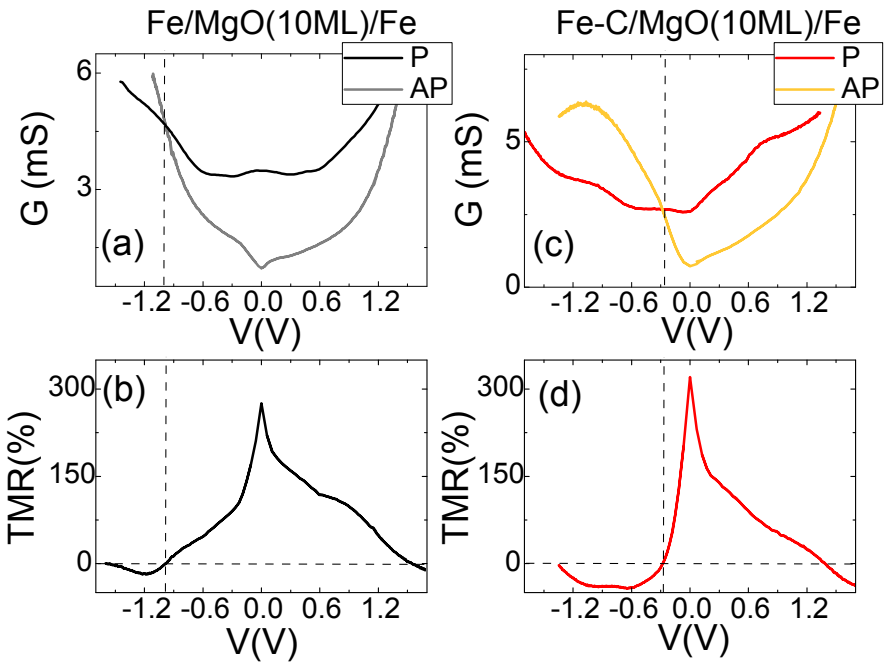

Figure 3.8: (a) Dynamic conductance, at 4 K, for carbon free samples with 10 ML barrier thickness, in P (H = 200 Oe) and AP (H = -100 Oe) states. Dynamic TMR at 4 K, for carbon free (b) and carbon doped (c) samples with 10 ML barrier thickness.

top electrode (C free or reduced C) to the bottom electrode (C doped) and close to -250 mV, a strong interfacial resonant state (IRS) peak appears that enhances the G_{AP} ($G_{AP} > G_P$) in a narrow energy window, associated to the minority Δ_5 surface state (IRS3 in *Figure 3.9*) [81]. This "local"resonant state is better detected in the derivative of the dynamic conductance (see *Figure 3.9*) and leads to the lower voltage for sign reversal of the TMR than observed in the undoped Fe/MgO/Fe MTJs. In Carbon free samples, the behavior of the TMR respect to the polarity is more symmetric than in the samples with Carbon. In these samples, the inversion of the TMR occurs at -1 V, due to the peak of minority Δ_1 surface state (IRS2 in *Figure 3.9*), i.e. at higher voltage than for C doped MTJs, recently observed by Ando and Zermatten et *al.* [80, 93]. Moreover, in the second

derivative of the dynamic conductance of the carbon free MTJs, additional peaks can be detected related to magnon excitation peaks (close to 9mV) and to the minority Δ_5 surface state (IRS1) in *Figure 3.9*, based on Ref.[81].

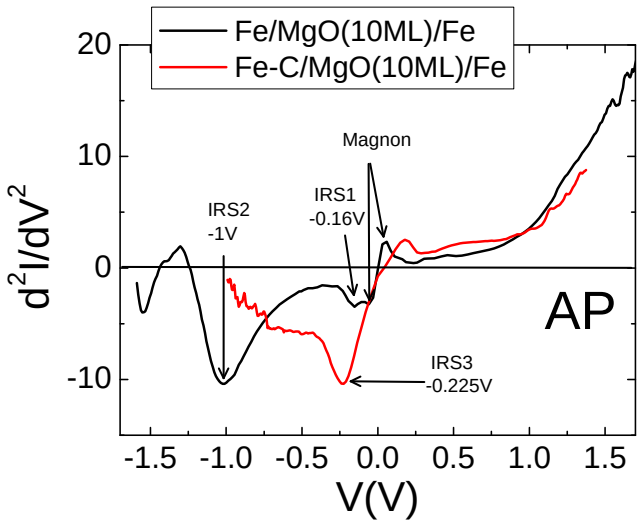

Figure 3.9: d^2I/dV^2 curves measured at 4 K in AP configuration for Fe/MgO(10ML)/Fe without C (black) and with C (red). The peaks marked with IRS correspond to those calculated by Lu *et al.* [81].

For the positive bias, when electrons are injected towards the top electrode (where Carbon is absent for both types of MTJs), the TMR changes the sign above 1.5 V. This is determined by a strong enhancement in the G_{AP}, when electrons with Δ_1 symmetry, in the AP configuration, are injected from the bottom Fe electrode and tunnel to the top electrode, to Δ_5 with an equivalent symmetry in the minority band (see *Figure 3.7*).

Let us focus now on the range of low applied bias voltage. For 10 ML of thickness of MgO barrier, all studied Carbon free MTJs reveal novel properties in the P-state with oscillations in conductance with about four minima at low

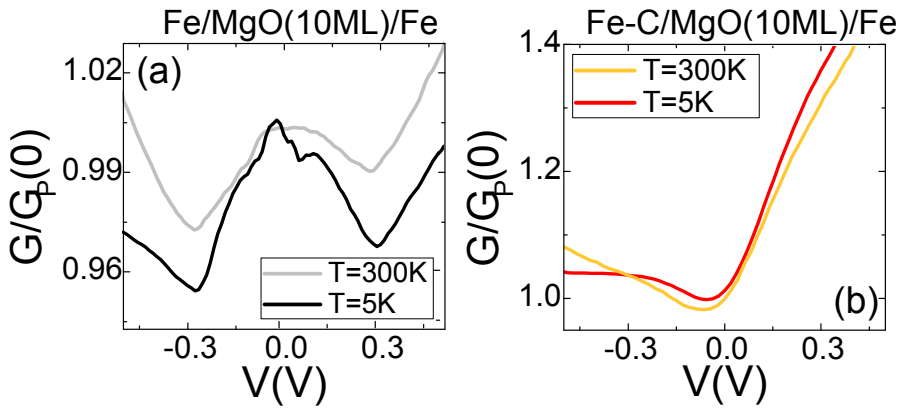

Figure 3.10: Dynamic conductance, at RT and 4 K, for carbon free (a) and Carbon doped (b) samples with 10 ML barrier thickness, in P (H = 200 Oe) and AP (H = -100 Oe) states.

temperature. We note that low-bias conductance minima in the P state have been observed previously at 300 K [48]. However, previously only two local conductance minima were found. These minima were explained by the contribution of electrons with spin majority Δ_5 symmetry in the total conductivity at low bias voltage (see Δ_5 majority band in *Figure 3.7*). An injected electron with Δ_5 symmetry, from the E_F of the right electrode, will find an unoccupied equivalent symmetry in the majority band on the other side. Interestingly, additional local minima appear for positive and negative finite bias voltages, close to 50 mV (*Figure. 3.10*(a)), which could be related to the contribution of the $\Delta_{2'}$ majority band. The origin of low temperature G_P(V) minima observed opens interesting theoretical perspectives. At low applied voltages, Δ_5 and $\Delta_{2'}$ enhance the parabolic conductance mainly associated with the Δ_1. These local minima are not present in the P state in conductance for Carbon doping MTJs, because the addition of the carbon in the bottom layer, seems to modify the surface band structure. It has been recently discovered that in Fe-C/ MgO/ Fe MTJs, the carbon acts as a filter of the electrons with Δ_5 symmetry in the P state [81], as we can corroborate in *Figure 3.10(b)*.

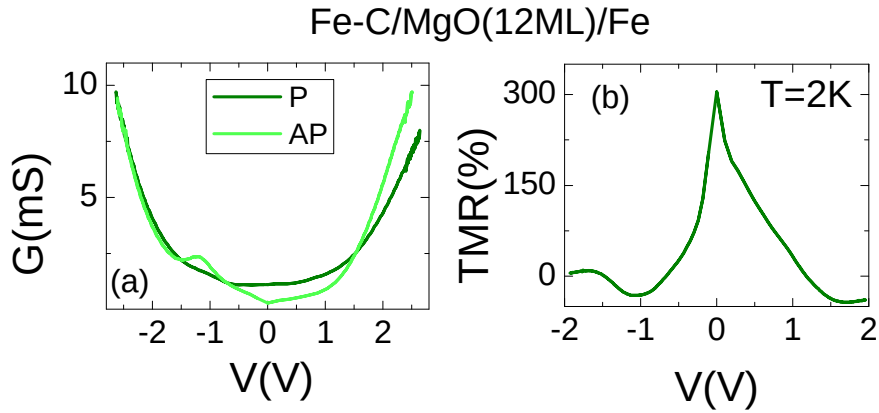

Figure 3.11: Dynamic conductance at 2 K (a) and related TMR(V) (b) for carbon doped MTJs with 12 ML barrier thickness.

3.3.2 Samples with 12 ML of the barrier thickness

Although the MTJs with 10 ML of MgO barrier thickness already have high TMR values (about 160%), one would expect to get still higher TMR values increasing the MgO thickness. In order to corroborate the influence of the C on the transport, thicker MgO barriers, with different R×A (resistance by area) products, have been investigated. For thick MgO barriers, above the plastic relaxation limit, a variation of barrier thickness from 10 to 12 ML has a drastic effect on the density of defects in the barrier, on the roughness of the top MgO interface and on the in-plane structural coherence of the insulator. These effects have drastic consequences on the tunneling and noise. When MgO is grown on Fe (001), after the critical thickness of 5-6 ML, a plastic relaxation occurs inducing dislocations within the barrier [48, 85, 86]. After the relaxation, the number of defects within the barrier and the roughness of the top MgO interfaces increases with the barrier thickness. Phase shift transmission electron microscopy analysis [48] show that dislocations within the MgO barrier have an oblique orientation. This implies that for a specific density of defects, increasing the barrier thickness reduces the defect-free junction

area where coherent tunneling with symmetry filtering occurs. Therefore, the difference in structural quality between a 10 ML and 12 ML MgO barrier becomes significant..

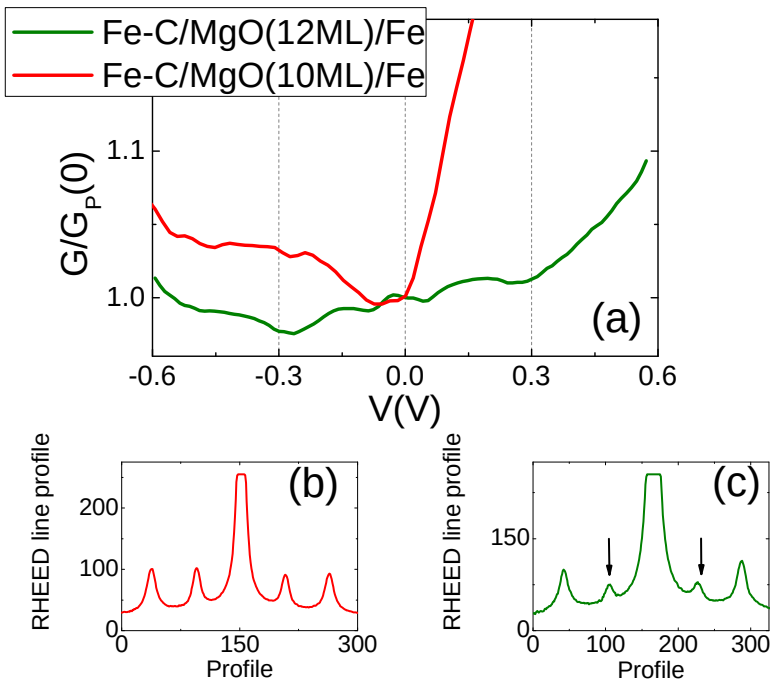

Figure 3.12: (a) Dynamic conductance in the P state at 4.2 K, for samples with carbon in the bottom interface and with two different thickness of the barrier (10 and 12 ML). (b) and (c) represents the RHEED measurement in the bottom electrode showing that the total amount of carbon at the interface is higher in MTJ with 10 ML of MgO.

We have studied the dynamic conductance and TMR for Carbon doped MTJs with 12 ML of MgO barrier (*Figure 3.11*). For this thickness of C doped MTJs, the samples show high stability as a function of bias and temperature. On the contrary, Carbon free junctions with the same barrier thickness, suffer dielectric breakdown of the barrier when the applied bias is higher than about a few hundred

mV. For C doped MTJs, the high quality of the barrier is not only evident from electron transport, but also from low frequency noise (as we will see later in *Figure 3.22*). Surprisingly for Carbon doped MTJs, we could apply voltage up to 3 V, and after the dielectric breakdown and loss of the TMR, some of MTJs recovered the tunnel phenomenon after being kept at 300 K during 2-3 days. In our opinion, a possible scenario is that the carbon atoms occupy the vacancies in the barrier and could "cure" the barrier, thus allowing the recovery of the tunneling phenomenon.

3.3.3 The effect of Carbon at interfaces of Fe/MgO/Fe MTJs

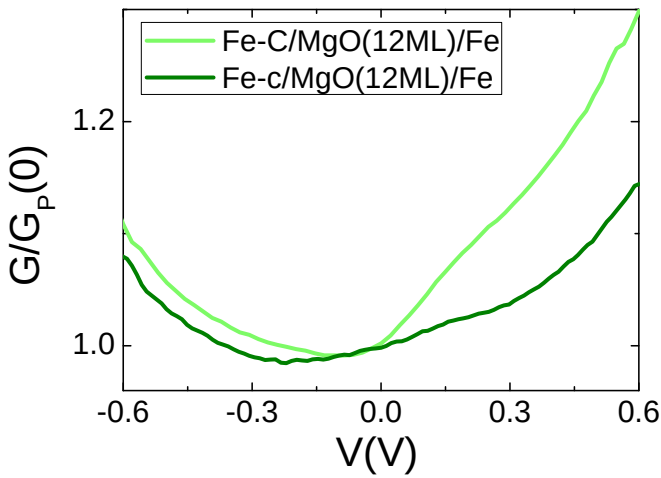

Figure 3.13: Compares the bias dependence of the dynamic conductance, at 300 K, in the P state for two Carbon doped junctions with 12 ML of MgO barriers, marked by dotted and continuous arrows in the *Figure 3.22*.

The dynamic conductance at 4 K for Carbon doped MTJs with 12 ML of thickness of MgO shows an intermediate behavior in respect to the bias dependence observed for the C doped and C free samples with 10 ML of MgO barrier (*Figure 3.11*), with the point of reversal of the TMR sign at about to -650 mV. In principle, the increase of 2 ML in thickness of the MgO barrier should not have a high

influence on the dynamic conductance, except in the zero bias conductance that should be reduced due to the thicker barrier. We think that which is probably should be associated with the amount of Carbon at the interface. Carbon acts as a Δ_5 filters in the P state, so if we look in detail the $G_P(V)$ as a function of bias, we see that it is more similar to the samples with carbon free of 10 ML of MgO barrier (*Figure 3.12* (a)). For low applied voltage and low temperature, the four maxima related to Δ_5 and $\Delta_{2'}$ majority electron bands are present.

In order to understand the different behavior of the $G_P(V)$, for C doped MTJs with different thickness, we analyze the intensity of the RHEED profiles. *Figure 3.12* demonstrates that, in $G_P(V)$, the principal difference between both samples is related to the total amount of carbon at the interface. The samples which show multiple conductance peaks at low voltage have less carbon and therefore its tunneling conductivity contains channels specific to carbon free MTJs (where we observe these features). Even, for Carbon doped samples with 12 ML MgO barrier, the spatial distribution of the Carbon concentration parallel to the interfaces could induce a local variation of the Fe/MgO interface reconstruction between different MTJs from the same substrate, see *Figure 3.13* (experimentally confirmed by in-situ RHEED analysis of the bottom Fe (001) surface). For this reason, new calculations with different concentrations of C to clarify the bulk band structure are probably needed. Recent calculations by T.X. Wang et *al.* [82] have observed that the addition of only one ML of carbon in one of the interfaces has a direct influence on the $k_{\parallel}$ conductance. When one monolayer of C is introduced in the interface between Fe and MgO, the TMR dramatically changes as a function of the bias polarity.

Once analyzed the dynamic conductance for both types of samples, we will conduct the study in low frequency noise to obtain more detailed information of the transport tunneling.

3.4 Noise in epitaxial Magnetic Tunnel Junctions with MgO (100) barrier

3.4.1 Low frequency noise

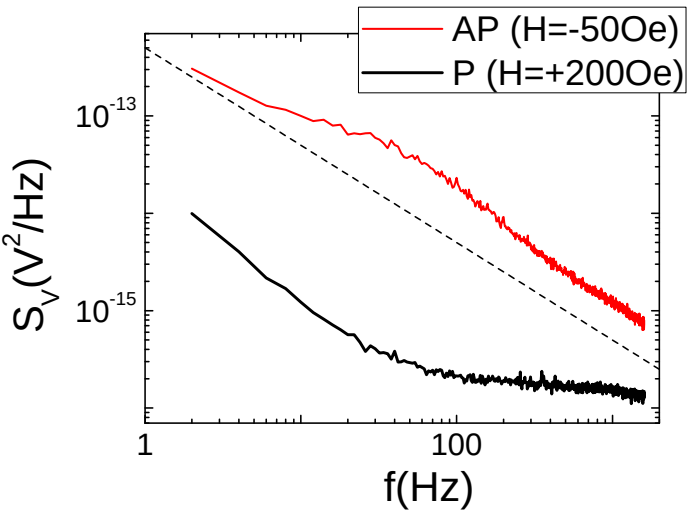

Figure 3.14: Typical noise spectrum measured in carbon doped MTJs in the P and AP states with a positive bias of 200 mV. The dashed line is a guide for the eye for 1/f dependence.

Fluctuations in conductance (or resistance) in the P and AP states may provide additional new information on specifics of electron tunneling and electron correlations which are not available on electron transport measurements. Typical room temperature power spectral density $S_V(f)$, below 1 kHz for P and AP states, are represented in *Figure 3.14*. These spectra have been measured in well defined magnetic states (far from the transition fields, for H = 200 Oe and H = -50 Oe corresponding to the P and AP states, respectively). At high frequency (f > 100 Hz in the shown curves) we observe a frequency independent noise, this is known as white noise (thermal and the shot noise contribution). The low frequency part

of the noise spectrum is clearly dominated by the so-called 1/f noise. In the AP state, in the frequency range studied (depending on the applied bias polarity, see below), the voltage noise may consist of the 1/f noise background superimposed by additional Lorentzian contribution or pure 1/f noise. We shall analyze the 1/f contribution as normalized noise power by means of the widely used phenomenological Hooge parameter (α) defined as $\alpha = fAS_V(f)/V^2$, where A is the junction area, f is the frequency and V is the dc voltage applied to the junction [13].

3.4.1.1 Electronic noise in MTJs

At high magnetic field (far from the transition) and at low bias, the conductance fluctuations are of electronic origin, because the magnetic fluctuations in the electrodes can be neglected. In such conditions, the most commonly accepted phenomenological model of 1/f noise suggested a superposition of multiple relaxation processes in or near the barrier, those process are trapping-detrapping of electrons in defects and the movement of them. Those relaxation times affect the different channels of the conductance, thus provoking the observed resistance noise. As it has been explained in the beginning of the Chapter, the conductance is governed by electrons with Δ_1 (in P state) and $\Delta_{5,2'}$ (in AP state) symmetries at E_F. The conductance in the P state is higher than the AP state, because the propagation of Δ_5 and $\Delta_{2'}$ states are strongly attenuated inside the MgO barrier. As long as to the defects, the excess of the normalized 1/f noise in the AP state may be understand as follows: the flow of electrons with Δ_5 symmetry decreases quickly inside the barrier (see *Figure 3.1*). Therefore, the fluctuation of the defects affecting these channels of conductance will have strong impact on the low frequency noise and consequently the 1/f noise in the AP state is higher than P state, at low bias.

When we apply bias in a well defined P state, the magnetization of both electrodes will be fixed by the external magnetic fields. As a consequence, the magnetic

fluctuations will be very faint. In such conditions, it is expected that the fluctuations in resistance are only of electronic origin and the low frequency noise is very weakly affected by the applied voltage. This can be seen in *Figure 3.15*, where the dependence of normalized low frequency noise for carbon doped and carbon free MTJs is shown (determined for frequency range between 1-50 Hz) as a function of bias, at room temperature. The scenario is completely different in the AP state and when we apply high bias. The low frequency noise is highly affected by magnetic inhomogeneities due to the change of the total magnetization of the one electrode is not uniform and the bulk band structure changes for large biases (previously shown in *Figure 3.7*). Thus the low frequency noise in the AP state could be due to combination of electronic and magnetic noise.

3.4.1.2 Interplay between electronic and magnetic noise

We have found that, at room temperature, the dependence of Hooge factor for carbon doped and carbon free MTJs as a function of bias in the AP state, is qualitatively similar to the TMR vs bias behavior (see *Figure 3.15*). The 1/f noise is weakly bias dependent for the positive bias, where TMR is weakly suppressed by bias. Whereas at negative bias the TMR and 1/f noise decrease in a stronger way. As we explain before, for Fe-C/ MgO(10 ML)/ Fe samples, at negative bias, when the electrons tunnel from the top (C free) electrode to the bottom electrode (C doped), close to 250 mV, a strong IRS peak appears (see *Figure 3.9*). It is reasonable to think that, when the conductance increases in the AP state due to IRS, the 1/f noise and its dispersion decreases, because it is opened a new channel for conductance. Then, this enhancement in conductance will reduce the level of the 1/f noise and it will be the responsible of the TMR inversion. The point of reversal of the TMR coincides with the reduction of noise in the AP state in respect to the 1/f noise in P state. These observations seem to suggest that the Hooge parameter has a strong dependence on the direction of the current (see *Figure 3.15*). In samples free of Carbon, the behavior of the TMR and 1/f noise

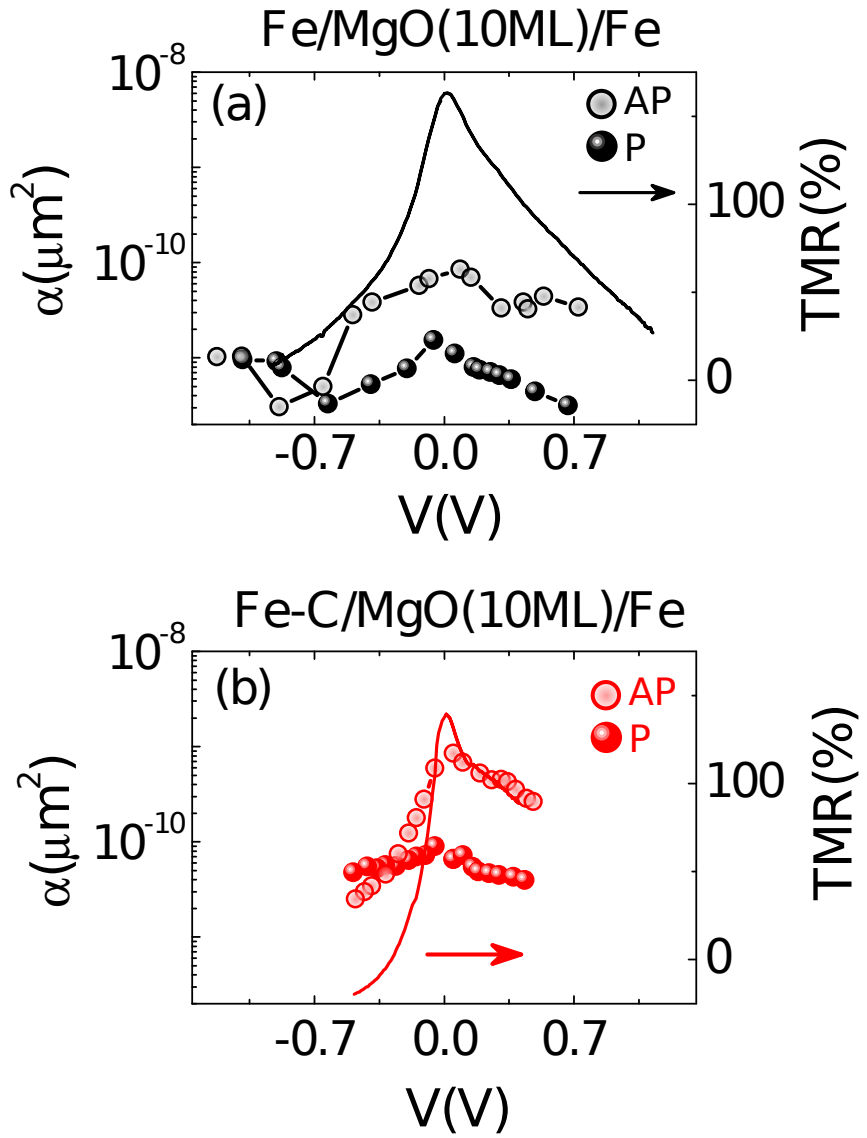

Figure 3.15: Bias dependence of the Hooge parameter (a) for carbon free and (b) for carbon doped MTJs in the P and AP states, evaluated for the frequency range of 2 - 40 Hz (left axis), and TMR vs bias (right axis).

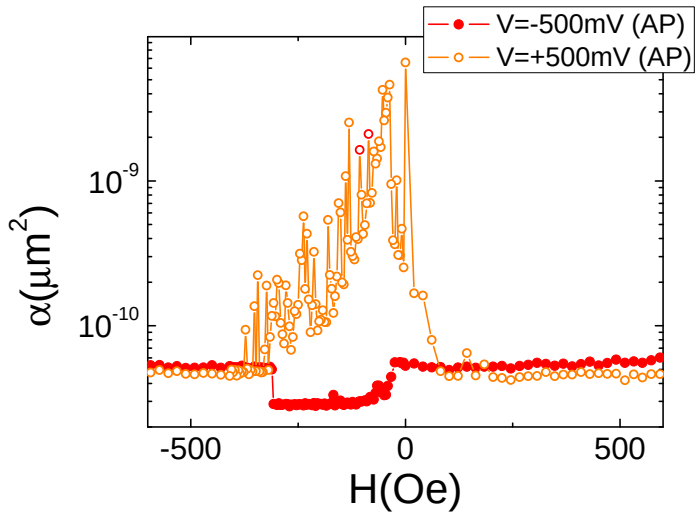

Figure 3.16: Normalized Hooge parameter respect to magnetic field for ±500 mV in AP state (in Carbon doped MTJs).

respect to the bias polarity is more symmetric. For these junctions the peak of IRS in the AP state, occurs at -1V [80] and consequently, the inversion of the TMR and the 1/f noise occurs at higher voltage than for C doped MTJs.

To study in detail the effect of the direction of the current, i.e. IRS, on the 1/f noise, we analyze the normalized Hooge parameter and its relative dispersion for two fixed currents, that correspond to ±500 mV in the AP state. *Figure 3.16* shows the dependence of the Hooge parameter on the magnetic field from +1 kOe to -1 kOe. In the P state, the Hooge parameter is weakly dependent on the external magnetic fields and it is almost constant as a function of voltage. In the AP state, however, it is strongly dependent on the direction of the tunneling current. The dependence of the Hooge parameter respect to magnetic field was studied for AlO_x barriers and it was observed that α is proportional to $\mid dR/dH \mid^2$ [64, 65]. The origin of this low frequency noise is mainly due to magnetic instabilities. In 2005,

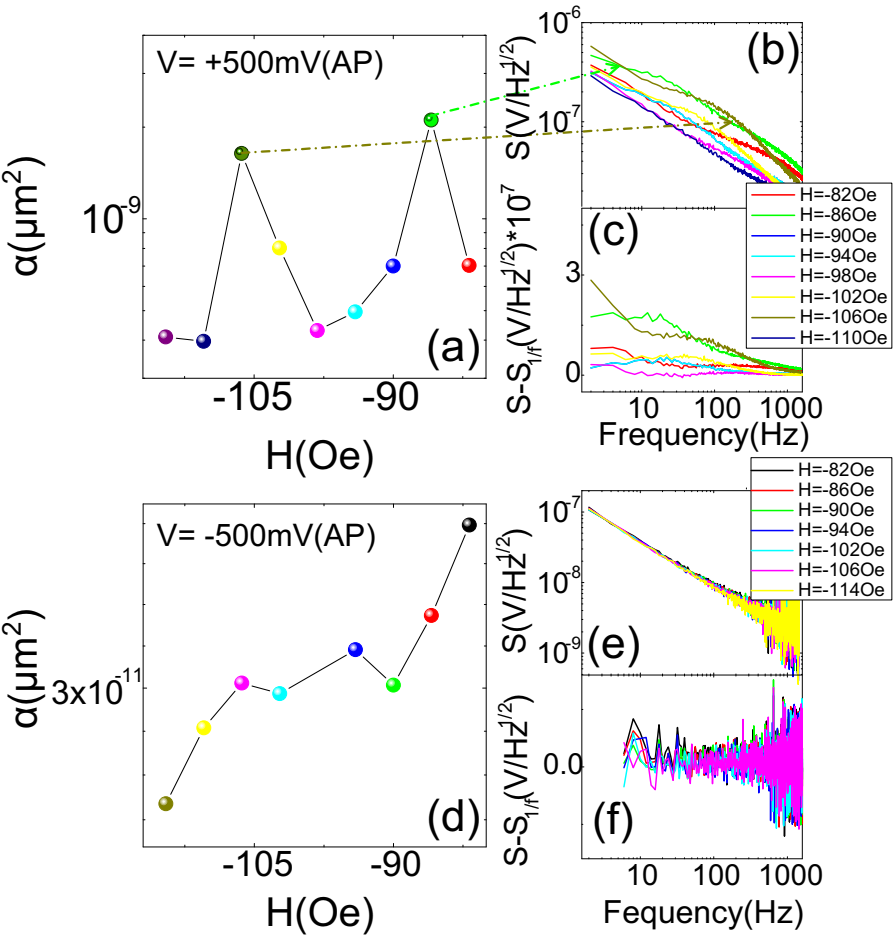

Figure 3.17: (a) The dependence of normalized Hooge parameter with respect to magnetic field for +500 mV in the AP state. (b) Power spectral density in AP state for different fields (between −80 to −115 Oe. (c) Power spectral density after to extract the 1/f background for the same field range of the part (b). (d), (e) and (f) Similar representation to previous figures, but for -500 mV bias voltage in the AP state.

Guerrero et *al.* [11] reported on an enhancement of the level of the normalized 1/f noise in AP state for MTJs with coherent spin tunneling in fully epitaxial magnetic junctions with MgO (111) barriers. For fully epitaxial MTJs, close to the transition between P-AP states, they observed also that the low frequency noise is due to magnetic fluctuations. But far from the transition, where α is not proportional to the $\mid dR/dH \mid^2$, the magnetic state related to electronics fluctuations are the responsible of the low frequency noise. In our case due to the IRS state, the 1/f noise is very sensitive to the applied bias voltage and the direction of the tunneling current (*Figure 3.15*). The influence of the polarity over the dispersion of 1/f noise respect to external magnetic field, in the well defined AP state, seems to indicate that one direction of the current stabilizes and another destabilizes the magnetic fluctuations or inhomogeneities in the magnetic electrodes [69].

Qualitative explanation of the asymmetric behavior of the noise is represented in *Figure 3.17*. The *Figure 3.17* (a),(d) represent the magnified zoom of the Hooge parameter respect to magnetic field in the AP state showed in the *Figure 3.16*. For the positive bias, when the current flows from the bottom to the top electrode, the value of the TMR is 120%. Decreasing the magnetic field high dispersion in the 1/f noise appears. A detailed study of the power spectral density (*Figure 3.17 (b)*) for those fields, apparent shows the presence of the random telegraph noise (RTN) contribution superimposed on 1/f background for +500 mV in the AP state. At the fields when RTN appears, effective α increases. The influence of the RTN may be deduced as an additional Lorenztian type noise on top of the 1/f noise. In order to verify the Lorenztian contribution, *Figure 3.17* (c) shows the spectrum of the different fields after extracting the 1/f noise background. The RTN is probably originated by some two level fluctuator. These magnetic fluctuations could be due to the nonuniform magnetization of the one of the electrodes, for example presence of 360° DWs. These fluctuations are not stable in field (because DW pinned or depinned when varying the magnetic field) and the value of the normalized Hooge

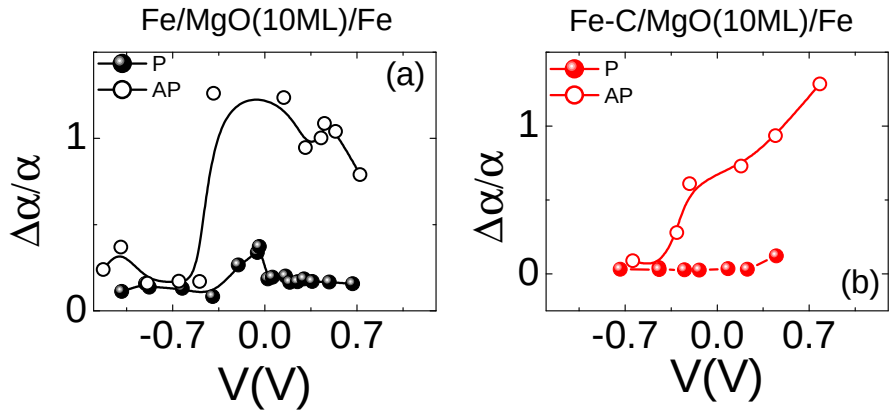

Figure 3.18: Bias dependence of the "noise of the noise"($\Delta\alpha/\alpha$)vs bias in the P and AP states in the both type of samples.

parameter generally decreases as a function of magnetic field with superimposed RTN fluctuations which appears spontaneously.

Contrary, when the current flows in the opposite direction, the conductance in the AP state increases very fast. This effect induces the inversion of the TMR. For example, at -500 mV, where the value of the TMR is about $\sim 20\%$ (*Figure 3.15*), the level of low frequency noise in the AP state decreases respect to the noise in the P state. This reduction of noise not only affects the magnetic state for a fix current, because the Hooge parameter is two orders of magnitude lower respect to the same voltage for opposite direction. Besides that, the main difference between both polarities is that, for negative values of current, the low frequency noise shows 1/f pure dependence, and there are no contributions of RTN (*Figure 3.17* (e),(f)).

So far, we have studied how it is affected the 1/f noise and magnetic stability as a function of magnetic field for a current higher than for the point of reversal of the TMR ($\pm 500\ mV$). Due to the influence of the field on the 1/f noise, it would be interesting to see what is the dependence of the 1/f noise magnetic dispersion as a function of the bias. Based on the idea of book of Kogan [57], where it is

measured the second momentum of the noise measuring power spectral density at different time with the same conditions of the bias and fields. We have considered the possibility of studying the "noise of the noise"as the dispersion value of the 1/f noise for different applied magnetic fields at the same bias, in well defined states (equation 3.1), or in other words, how the low frequency noise is stable when the external magnetic field changes. Thus we define the quantity:

$$\frac{\Delta\alpha}{\alpha} = \sqrt{\frac{\langle(\alpha - \langle\alpha\rangle)^2\rangle}{\langle\alpha\rangle}} \tag{3.1}$$

We had already noted, that the "noise of the noise"in the P state is practically zero. This can be seen in the *Figure 3.18*. Instead in the AP state, similarly to low frequency noise, the "noise of the noise"has a strong dependence on the direction of the current and above of the TMR inversion is almost zero, as we can corroborate in *Figure 3.16*.

In *Figure 3.19*, we show a simple representation of the possible scenario for current induced magnetic instabilities with RTN contribution as a function of the direction of the current in the AP state. The top electrode, in our samples, is the hard electrode due to the coupling with the top Co layer. A disordered alloy is formed in the interface between Fe/Co [44, 84], where a region of magnetic instabilities could be created. Then, due to a structural process at zero bias, in the top electrode will have more magnetic domains than the bottom electrode, which is in contact with the substrate. When a negative current is applied, the electrons flow from the bottom to the top electrode. In the AP state far from the transition, the magnetization of the bottom electrode is well defined, however the magnetization of the top electrode due to the coupling with the top Co layer will have a higher number of magnetic inhomogeneities. On contrary, when the electrons flow from the top to the bottom electrode, the current stabilizes the magnetic inhomogeneities of the top electrode and consequently reduces the level

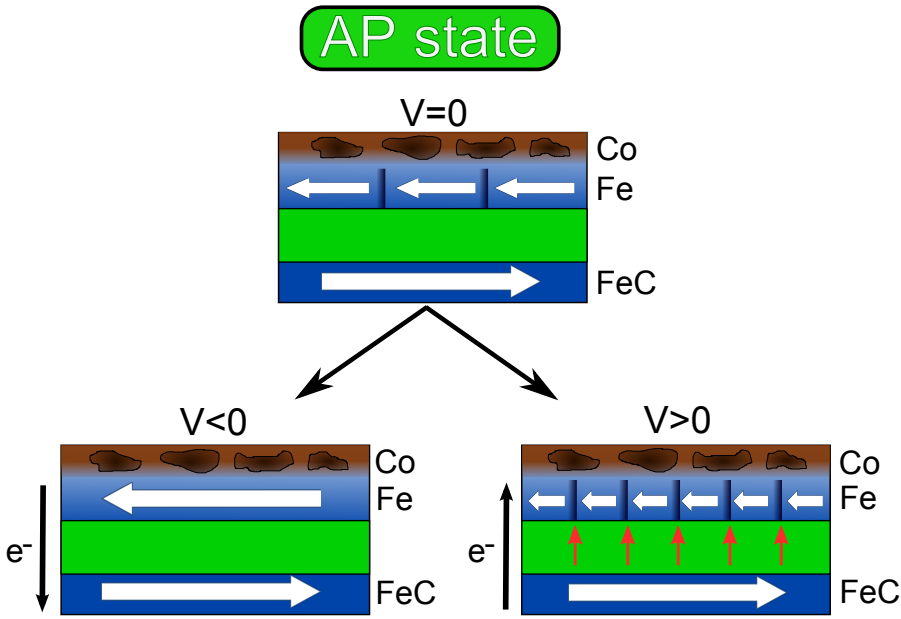

Figure 3.19: Sketch of the possible distribution of the magnetic inhomogeneities (related to examples a 360° DW) in MTJs as a function of the bias polarity.

of 1/f noise related to magnetic instabilities. The idea that current polarity stabilizes and destabilizes the magnetic moments, leads us to think about the possible contribution of spin torque on magnetic domains.

Let us compare in more details the bias dependence of the Hooge factor and TMR. The normalized variation of the noise respect to the noise in the P state at 100 mV, represented in *Figure 3.20*, clearly indicates presence of much stronger asymmetry of the noise vs bias in the Carbon doped MTJ in comparison with undoped MTJs. However, we note that the analysis of the "noise of the noise"is made by normalized corresponding α(V). This important point ensures that asymmetry of the "noise of the noise"is not directly related to TMR. Apart from a practical interest [i.e., could of RTN as a function on the bias direction], this behavior could present a new interesting physics which is Sketched in *Figure 3.19*. Particularly, strong asymmetry of $\frac{\Delta\alpha}{\alpha}$ vs bias could be related to the possible influence of DW

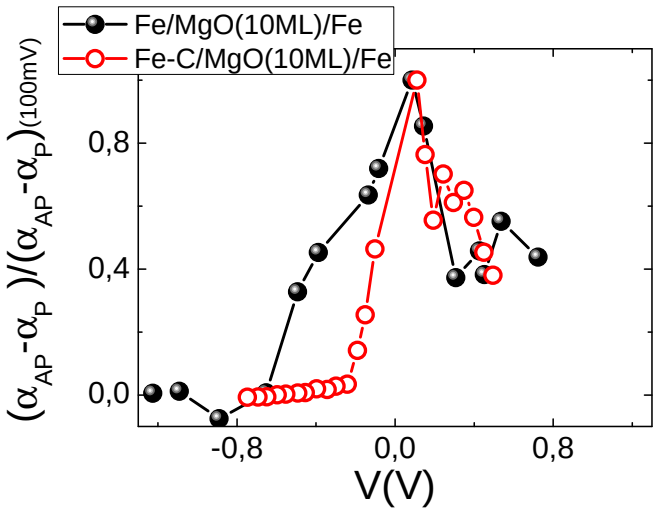

Figure 3.20: Difference between normalized Hooge parameter in the AP state respect to P state. In order to compare different samples, the relation of the noise is normalized by the difference at 100 mV.

which allow local tunneling of current with Δ_1 symmetry in the AP state. Another important aspect is related with the increase/decrease of the stability of DWs and magnetics inhomogeneities vs bias direction. This means that a careful choice of polarity and of the currents value could give us a better relation of the signal/noise. For instance, as it is explained before, we could consider $\pm 500\ mV$, because the TMR is noticeable ($\sim 20\%$), but the low frequency noise is two orders of magnitude smaller, in comparison with the positive bias, and also being reduced even dispersion of the noise (see *Figure 3.15* and *Figure 3.20*)

3.4.2 Comparison between the two barrier thicknesses (10 vs 12 ML MgO)

The influence of carbon on the transport seems evident, as we have seen in the dynamic conductance and 1/f noise measurements. But with noise measurements, we can obtain additional information that could not be seen only with conductance.

3.4 Noise in epitaxial Magnetic Tunnel Junctions with MgO (100) barrier

As we said before, the low frequency noise in the P state (far from the transition) is related to the relaxation time of defects in or near the barrier. Thus we can compare the obtained results with MTJs with 10 and 12 ML of MgO barrier. In this case the number of defects will be enhanced, due to the growth processes. So the 1/f noise seems to be an important tool which will help to further understand the influence of carbon on noise from defects at the interface. Therefore, we compare the noise power spectra in Carbon free and Carbon doped MTJs with 12ML of MgO barrier in the P state (*Figure 3.21*(a)). In the frequency range between 1 and 50 Hz, the power spectral density behaves as $S_V(f) \propto 1/f^{\beta}$ (with $0.5 < \beta < 1.5$) [60], allowing us to describe the noise as 1/f-like. We also note that $\alpha(V)$ correlates with TMR(V) (*Figure 3.15*), indicating that the origin of 1/f noise is due to symmetry dependent tunneling resistance fluctuations. As can be seen in *Figure 3.21*(b), the average low frequency noise power increases approximately as V^2, which indicates dominant 1/f noise. *Figure 3.21* shows a strong suppression of 1/f noise with Carbon doping in MTJs with 12ML of MgO barrier.

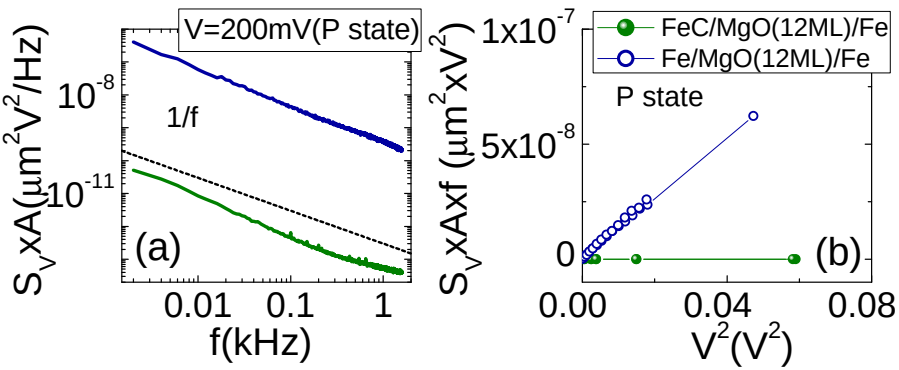

Figure 3.21: (a) Frequency dependence of the typical normalized noise power for Carbon free (dotted) and doped (full lines) MTJs. Black dotted line represents 1/f pure dependence. Part (b) shows proportionality between the noise power and the bias squared for Carbon doped and undoped MTJs.

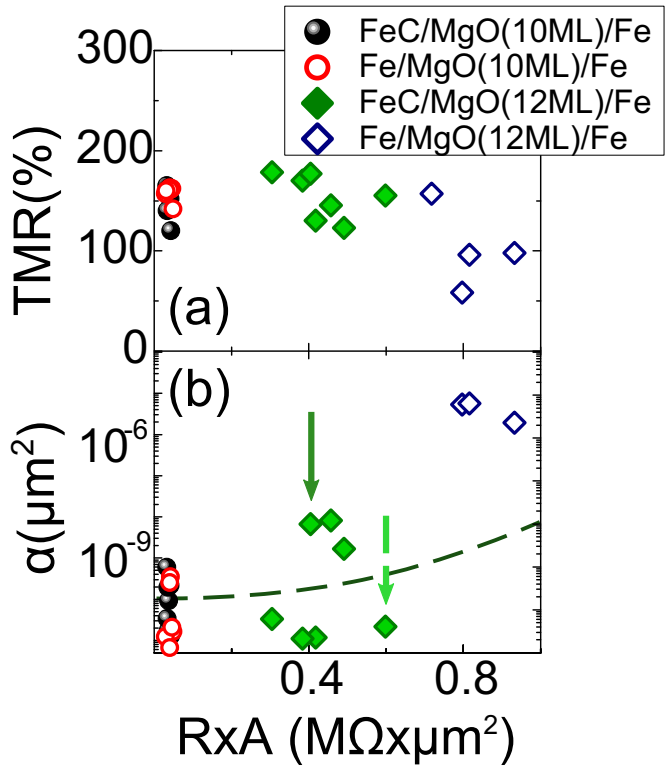

Figure 3.22: TMR (a) and Hooge factor (b) as a function of R×A product for MTJs with 10[69] and 12 ML thick MgO barrier. The dotted line represents the mean empirical value of α reported in Ref.[94]. The green and dark green arrows represent the samples of 3.13 respectively.

According to the results presented the C doping diminishes the noise in the P state in this kind of junctions. The *Figure 3.22* summarize the average value of the TMR and normalized 1/f noise (in the range of frequency between 1-50 Hz) in the P state at +200 mV as a function of R×A product. One clearly observes differences in the influence of Carbon doping for MTJs with 10 ML and 12 ML thick MgO barriers. From the one hand, both MTJs with 10 ML MgO barrier show similar values of low frequency noise and TMR [69], with an average R×A around 30% higher than for carbon free MTJs with 12 ML of MgO. In contrast,

3.4 Noise in epitaxial Magnetic Tunnel Junctions with MgO (100) barrier

Carbon doped samples with 12 ML of MgO show much lower 1/f noise levels than Carbon free junctions. Besides, the R×A for Carbon doped MTJs is about two times smaller than for Carbon free MTJs while the average TMR is somewhat higher for Carbon doped MTJs. It is important to emphasize the effect of carbon on the MTJs with 12 ML of barrier.

If we look in detail the *Figure 3.22*(b), we can see that for 12 ML thick barrier junctions there are two well differentiated groups (representative samples marked with arrows), which as we said in the section that discusses the conductance, have a different concentration of C (see *Figure 3.13*). The samples with lower values of 1/f noise contain higher concentrations of Carbon in the interface. The dotted line represents empirical values of the average α, previously reported for MgO and Al_2O_3 based MTJs [94], clearly indicating that Carbon doping in Fe/ MgO (12 ML)/ Fe MTJs strongly decreases 1/f noise while increasing or maintaining a high TMR level.

A reduced number of defects, even without doping, could implicate a low sensitivity of the low frequency noise in Fe/ MgO (10 ML)/ Fe to Carbon. Then, the dominant tunneling is coherent across the single crystal areas of the MTJ between dislocations, with conservation of $k_{\|}$ and symmetry filtering effects. The situation seems to be very different in Fe/ MgO (12 ML)/ Fe MTJs which show a high level of 1/f noise. For this MgO thickness, interface Carbon doping substantially decreases the 1/f noise.

Electron symmetry changing at the interfaces could probably account for some part of substantial influence of Carbon on 1/f noise for Carbon doped samples. Band structure calculations [81] suggest the change of symmetry of interface resonant states (IRS) from Δ_5 to Δ_1 with Carbon doping. Let us assume that the 1/f noise in the P state is originated from temporal fluctuations of the interface atoms, with uniformly distributed relaxation times, which scatter dominating Δ_1 electrons into the Δ_{5IRS} states or vice versa. Then, for Carbon free MTJ, we could roughly estimate the related normalized fluctuations of conductance as follows:

$$\frac{\langle[\sigma(\Delta_1) - \sigma(\Delta_{5IRS})]^2\rangle}{\langle\sigma^2(\Delta_1)\rangle} \sim 1 \tag{3.2}$$

With $\sigma(\Delta_{5IRS}) << \sigma(\Delta_1)$). At the same time, for the Carbon doped MTJs with IRS dominated by Δ_1 symmetry, fluctuations in the position of interface atoms provide much smaller fluctuations of the conductance:

$$\frac{\langle[\sigma(\Delta_1) - \sigma(\Delta_{1IRS})]^2\rangle}{\langle[\sigma(\Delta_1) + \sigma(\Delta_{1IRS})]^2\rangle} \ll 1 \tag{3.3}$$

In the condition $\sigma(\Delta_{1IRS}) \simeq \sigma(\Delta_1)$).

Other possible explanations is that small concentration of C "fills"all Oxygen vacancies at the interface[82], improving the quality of the barrier, and strongly reducing the low frequency noise. For few junctions, where carbon concentration at interface is not sufficient, probably different reconstruction (c(3×3)) at Fe-C/MgO interface occurs with corresponding partial reduction of the 1/f noise.

3.4.3 Shot noise

As we discussed in the Introduction, shot noise measurement present important (complementary to conductivity) tool to determine presence of correlation in tunneling process. In particular, for single barrier, tunneling measurements of shot noise provide tool to discriminate between direct and sequential tunneling in MTJs [12]. We remind that for uniform distribution of defects, sequential tunneling is predicted [56] and observed [12] to reduce the Fano factor to 2/3. This situation could be different in MgO based MTJs without defects where is expected direct tunneling.

Figure 3.23 represents typical shot noise measurements, from the Gaussian distribution frequency independently of $S_V(f)$, carried out at T=5 K, for both kinds of MTJs samples (free and Carbon doped). The solid line shows the "theoretical" expectation for the shot noise, for electron tunneling having Poissonian character: $S_V = 2e\langle I\rangle/G^2$, with G as the dynamic conductance measured in *Figure 3.8*.

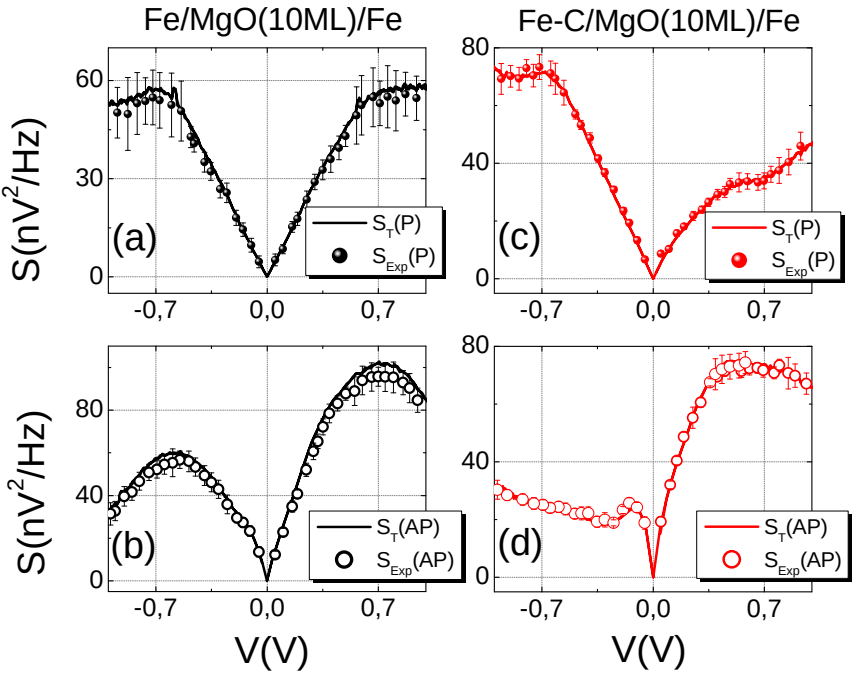

Figure 3.23: Shot noise measurements in P and AP states measured at 4 K in bias. The lines (Black line is for C free and red line is for C doped) correspond to theoretical value of the Poissonian transport and points correspond to experimental results.

The points represent the mean value of the power spectral density in the range where it is independent of the frequency. Error bars show the dispersion of the shot noise (white spectrum) obtained as half of within the Gaussian distribution. The experimental data reveals Poissonian shot noise, i.e. Fano Factor equal to one, which clearly indicates the absence of electron correlations and/or sequential tunneling phenomena[68]. This is valid for P and AP states, confirming that spin dependent conductances is due to a direct tunnel between electron bands, as it is expected for coherent tunneling [56]. Previous experimental results, which investigate MTJs with Al_2O_3 barriers by Jiang et *al.* [65] and, very recently, by Sekiguchi et *al.* for CoFeB/MgO(1.5 nm)/CoFeB [95] have observed direct tunneling. Our

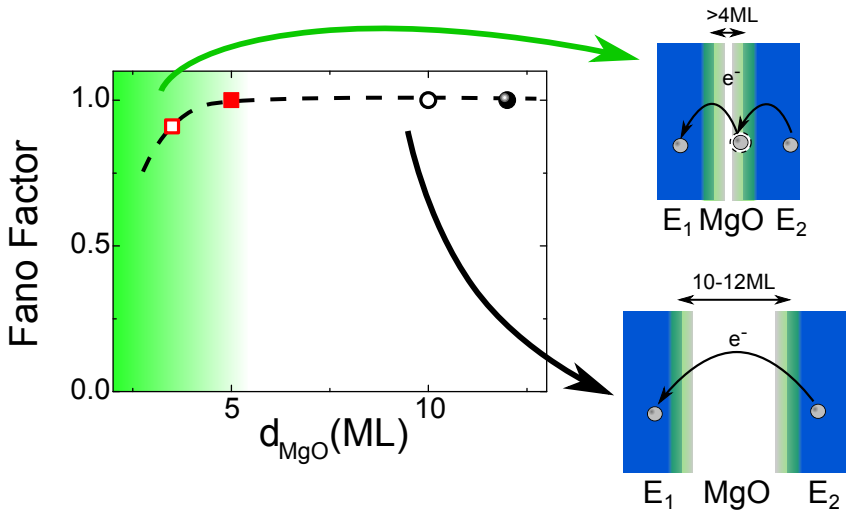

Figure 3.24: Sketch of the contribution in tunneling transport of the defects in MTJs as a function of the Thickness of the MgO barrier. Summarizes the Fano factor measurement obtained in this Chapter and in previous works [68, 95, 96]. Our experimental results are represented with circle and the experimental results of other groups are represented by squares.

results are on $F \simeq 1$, very important result, because they are a direct probe that the contribution of the defects in the barrier on the sequential tunneling process on transport can be neglected.

Recently, sub-Poissonian shot noise has been observed in MTJs with ultra-thin MgO barriers[96]. Previous work on shot noise in MTJs with Al_2O_3 barrier, by Guerrero et *al.* [12], also measured a reduction of the Fano Factor depending on the situation of the defects in the barrier. We believe that suppress of F<1 observed in single barriers MTJs could be attributed the anomalous reduction of small barrier thickness ($d_{MgO} = 1.05nm$). It is very complex to grow a perfect thin barrier, without defects and dislocations, and the contribution of the defects in the barrier has a strong impact on the sequential tunneling process. A possible scenario of this situation is shown in the sketch of the *Figure 3.24*, where for MTJs with barrier thickness well above the plastic relaxation (>5 ML) the Fano Factor

is close to 1. On the contrary, when barrier is below <5 ML, the density of defects is high, inside the barrier, and the sequential tunneling process appears to become important. Further experimental work is needed to investigate the shot noise in magnetic tunnel junctions with better control over the intermediate states, for example by growing double barrier MTJs.

3.5 Conclusions

As it is expected for a single MTJ, the tunneling transport is direct in both states for both types of samples. The diffusion of the Carbon from the substrate to the bottom electrode does not affect the tunneling phenomenon. With these results, we can deduce that the main contribution of the C is in the interface between electrode and barrier.

It is important to remark that the phenomenological model of 1/f noise is not fully understood. In the P state, the low frequency noise is related to the relaxation time of the defects and is almost constant as a function of bias and magnetic field. In the AP state, we can observe a strong correlation between dynamic conductance and low frequency noise as a function of bias. For negative current, when the electrons flow from the top to the bottom electrode, the TMR and 1/f noise decreases due to peak in the interfacial resonant state which is the responsible of the increasing the dynamic conductance in the AP state. Interestingly, from a critical current, the low frequency noise has a pure 1/f dependence. Also it is reduced the "noise of the noise". Whereas for positive bias, the low frequency noise increases by two levels system fluctuator. The contribution of the RTN increases the level of 1/f noise. It seems that the direction of the current has a strong influence on the stability of the magnetic inhomogeneities in the interface between electrode and barrier. This idea leads us to think in the spin torque effect. Probably we are detected the influence of the spin torque over domain walls, due to magnetic inhomogeneities. These results show a high potential for integration of the fully epitaxial MTJs into spintronic devices. In order to corroborate this

results it is needed measure small samples, where it is possible to apply higher current density. For this reason, in the Chapter 6 it is shown the experimental results in elliptic MTJs with an area between 0.0245 and 0.117 μm^2.

The sensitivity of the devices comes from the relationship between the signal and noise. For 12ML of the MgO barrier, well above the plastic relaxation, the C has a drastic effect on the density of defects in the barrier. Therefore, the low frequency noise in the P state (related to the defects) and in the AP state (for larger current) have a strong reduction. The fully epitaxial magnetic tunnel junctions are difficult to make at high scale. For the industry is better to use alternative technics, like sputtering, with higher low frequency noise values. But, due to the low frequency noise observed, this devices are very interesting ultrasensitive field detectors. For example in medicine, where it is needed to detect fields down to pT/Hz, the high quality of these junctions open news perspective.

We would like to note that recently it has been achieved similar values on low frequency noise in MTJs grown with electron-beam evaporated MgO barriers [97]. But, in our opinion the fully epitaxial magnetic tunnel junctions measured in this Chapter have better implementation than the samples growth with this technic, due to strong enhancement that occurs on Hooge parameter in the AP state (more than one order of magnitude higher than our results). In addition, contrary to our results (see *Figure 3.15*), the Hooge parameter in the AP state at ±500 mV is still one order of magnitude higher than P state.

4

Strongly suppressed 1/f noise in epitaxial Fe-V/MgO/Fe magnetic tunnel junctions

4. Strongly suppressed 1/f noise in epitaxial Fe-V/MgO/Fe magnetic tunnel junctions

4.1 Brief introduction

As we have seen in the previous Chapter, the fully epitaxial magnetic tunnel junctions (MTJ) based on (100) MgO barriers are very interesting systems for investigation both from the fundamental and applied points of view. The seminal MTJs with composition Fe(100) | MgO | Fe were the first to reveal high TMR at room temperature, due to the high spin polarization of electrons at Fermi level (E_F) with Δ symmetry in Fe bands and the filtering capability of the MgO barrier. Theoretical calculations have predicted large tunnel magnetoresistance (TMR) values, approximately 1000% [9, 10], but these were not achieved experimentally at room temperature due to structural limitations ($\sim$ 200%) [7, 8, 48, 68, 98, 99]. This reduction of the TMR is due to several reasons and the understanding of the origin of these limitations is a fundamental issue to accurately control the spin polarized tunneling. One of the possible reasons have been explained in the previous Chapter. The oxidation that occurs at the Fe/MgO interface during the growth process of the MTJs [51, 92] leads to a reduction of the TMR values. Another important limitation is some (small) structural lattice mismatch between the MgO barrier and the Fe layer. In the Fe (100)/ MgO/ Fe junctions, the Fe lattice is rotated by 45° with respect to the MgO [48]. With a bcc crystalline structure, the lattice parameter of the MgO is $a_{MgO} = 0.421\ nm$. Consequently, in the [110] direction, the interatomic distance in bulk MgO is $\frac{a_{MgO}}{\sqrt{2}} = 0.298\ nm$, close to Fe in the (100) direction ($a_{Fe} = 0.287\ nm$). The problem is that the lattice mismatch between both elements is around to 3.9%, which induces a stress within the MgO barrier. The strain is partially relaxed during the MgO growth via interfacial dislocations [7, 48, 49]. These may be partially responsible of the reduced TMR below 1000% and should also determine substantially the defect related 1/f noise [11, 69]. Then, in order to search alternative electrodes, that meet which may yield large TMR values, it is critical to choose a ferromagnetic electrode which satisfies several characteristics.

- A bcc structure for electrode is necessary to maintain the sensitivity of the tunneling to states with Δ symmetry to magnetic states (P vs AP) [9].
- The lattice parameter of the electrode should be close to that of MgO.
- The spin polarization of the ferromagnetic material has to be large, in particular, the spin polarization of tunneling Δ electrons.

To improve the TMR values of MTJs, other alternative to Fe electrodes, which have a high spin polarization of the Δ bands at the E_F, as for example FeCo[100] and bcc Co[44] have been introduced. The advantage of using Co, in contrast to Fe, is that (at small biases) only electrons with Δ_1 symmetry contribute to the transport at E_F for the majority-spin band, because the E_F level is well above of $\Delta_{5,2'}$ bands. Consequently, in the antiparallel (AP) state, it is expected that all the states are reflected at $\overrightarrow{k_{\parallel}} = 0$. Based on this hypothesis, Yuasa et *al.* in several works [44, 45], grew two types of different samples Co (100)/ MgO/ Fe and Co (100)/ MgO/ Co MTJs, reaching values of TMR at room temperature (RT) of 270% and 410%, respectively. But, one of the problems is similar the one encountered in Fe electrodes, namely that the lattice parameter of the Co is even lower than that of the Fe ($a_{Co} = 0.251\ nm$).

More recently, half-metallic ferromagnets have been used as an electrode in the MTJs. These Half-metallic ferromagnets are based on Co Heusler alloys with a chemical composition of Co_2YZ (Y:transition metal, Z:main group element). Values of the TMR reaching up to 400% at room temperature have been achieved [47, 101, 102]. The advantage of these electrodes is that they have a band gap at the E_F level for one spin direction and exhibit 100% spin polarization at E_F. These junctions use electrodes with large values of effective spin polarization, in order to obtain high values of TMR, in agreement with the model of Julliere [14] (i.e. no spin filtering by insulating barrier is needed). For this reason, these MTJs are very interesting for future studies and potential applications.

4. Strongly suppressed 1/f noise in epitaxial Fe-V/MgO/Fe magnetic tunnel junctions

With the aim of looking for ferromagnetic materials with similar lattice parameter as that of MgO and reducing the stress of the barrier new material combinations have been probed. For example, amorphous CoFeB crystallize in a bcc structure in the (001) direction and depending on the temperature of the annealing one can obtain similar lattice parameter to these of the MgO barrier[15, 100, 103]. The CoFeB (001)/ MgO/ CoFeB MTJs has reached TMR ratios about 600% at RT due to the highly oriented crystalline structure [15].

Other strategies have been used recently by Bonell et *al.* [17] trying to improve the tunneling transport with the control of the order/disorder at the interface electrode/insulating interface using Fe electrode with oxidized surfaces. But at the end, the obtained experimental results show lower TMR values than those expected for control MTJs.

In this Chapter, we study MTJs with a new ferromagnetic electrode formed by a Fe alloy with different concentrations of vanadium, which provides the reduced mismatch at the electrode/barrier interface. It was known that substitution of Fe with vanadium decreases the magnetic damping [104] and increases the lattice parameter of the electrode and therefore reduces the misfit [77] with the MgO barrier. This type of interface engineering may be expected to enhance the low frequency electronic stability of MTJs via suppressed noise related to defects. Indeed, the quality of the metal-insulator interface in MTJs determines the 1/f noise, mainly through defect induced charge trapping /de-trapping processes [60, 62, 105].

We have carried out a study of a total of 89 MTJ samples at room temperature, 61 of which had a MgO thickness of 9.5 ± 0.5 ML and 28 had a 13 ML MgO thickness. The electron transport and low frequency noise were measured in fully epitaxial $Fe_{(1-x)}V_x$/ MgO/ Fe and Fe/ MgO/ $Fe_{(1-x)}V_x$ MTJs. We have observed an increase of TMR of about 10% for the thinner barrier and of 35% for the thicker barrier, with a relatively small vanadium doping of the bottom electrode (x about 0.1), and a remarkable reduction, in nearly two orders of magnitude, of

the normalized 1/f noise (Hooge factor) in the nonmagnetic (parallel) state. An even stronger noise reduction was observed in the magnetic (antiparallel) state in the conditions of a substantially enhanced TMR. For the control Fe/MgO/Fe MTJs, small differences in TMR and 1/f noise values in comparison with the MTJs discussed in the previous Chapter are present due to their growth in different molecular beam epitaxy (MBE). All the samples discussed in this Chapter were grown in the same MBE at the Faculty of Science of the Poincare University (Nancy), including the reference MTJs.

The dynamic conductance and low frequency noise have been studied using a four-probe method. The voltage noise power was studied in the frequency range f = 2 to 1600 Hz using a cross correlation technique. More details on the experimental setup may be found in the Experimental methods Chapter.

4.2 Samples descriptions

4.2.1 Elaboration of the samples

The samples that have been studied in this Chapter were grown by the group of Prof. Stephane Andrieu within bilateral collaboration between UAM and the Institute Jean Lamour, CNRS-Nancy University. The single-crystal multilayers on MgO(001) were deposited by molecular beam epitaxy (MBE) typically with base pressure of 8×10^{-9} Pa. As it was explained in the previous Chapter, before the stacking deposition, the substrates were outgassed at 875 K of about 10nm of MgO layer was grown at 725 K, in order to prevent the diffusion of residual carbon through the bottom electrode and its segregation at the interface with MgO[106]. The bottom electrode was grown using Fe-V alloys with different concentration of vanadium, obtained by Fe and vanadium co-evaporation. The Fe was evaporated in a Knudsen cell and it is heated to 1523 K. On the other hand, the vanadium was evaporated by the heat of electron beam evaporation at different rates depending on the concentration needed. Evaporation rates are calibrated by quartz

4. Strongly suppressed 1/f noise in epitaxial Fe-V/MgO/Fe magnetic tunnel junctions

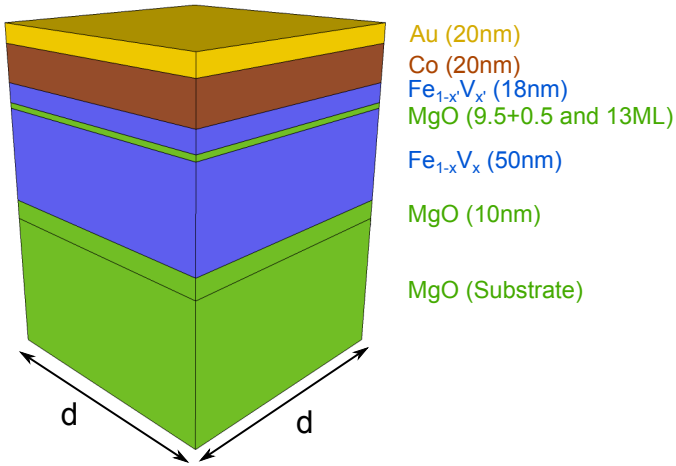

Figure 4.1: Sketch of the composition of the samples. MgO// MgO(7.5 nm) / $Fe_{1-x}V_x$ /MgO 9.5 ± 0.5 and 13 ML/ $Fe_{1-x'}V_{x'}$ / Co(20 nm) /Au(20 nm).

microbalance. The vanadium concentration was checked after growth by X-ray photoelectron spectroscopy (XPS). In order to improve the quality of the films reducing the roughness of the surface, the structure is annealed 20 min. at 825 K. In our samples, the bottom electrode is the magnetically soft electrode. On top of the bottom $Fe_{(1-x)}V_x$ electrode, a MgO barrier between of 9 and 10 ML was deposited for the thinner barriers and 13 ML for thicker barrier. The barrier thickness was controlled by reflection high energy electron diffraction (RHEED) intensity oscillations. A 18 nm thick top $Fe_{(1-x')}V_{x'}$ electrode was deposited on top of the MgO barrier and annealed 10 min at 475 K. The top Fe-V alloy electrode is the magnetically hard electrode due to the coupling with the above situated 20 nm thick Co. Finally, to protect the samples from the oxidation a 20 nm Au film was grown on top. The full stack of the samples measured in this Chapter is MgO//Fe-V (50 nm)/ MgO (9.5 ± 0.5 and 13 ML)/ Fe(18 nm)/ Co(20 nm)/ Au(20 nm) and Fe(50 nm) /MgO(9.5 ± 0.5 and 13 ML) /Fe-V(18 nm)/ Co(20 nm)/ Au(20 nm) (see a Sketch of the sample in *Figure 4.1*). The MTJs were patterned

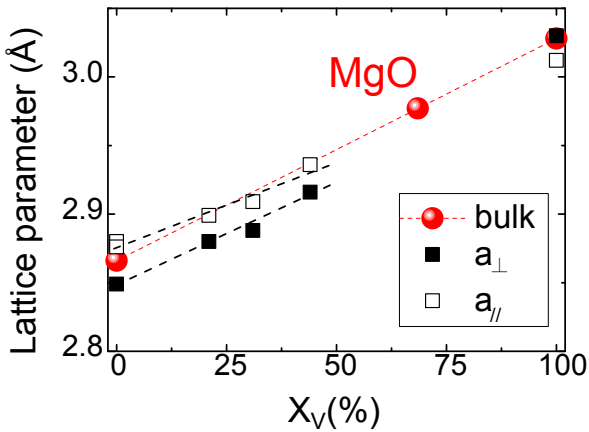

Figure 4.2: In-plane (empty squares) and out-of-plane (full squares) lattice parameters of 50-nm-thick Fe-V films grown on MgO (001), measured by XRD. Circles are the lattice parameters of bulk Fe and vanadium and the one of MgO divided by $\sqrt{2}$. [Adapted from Ref.[77]].

by UV photolithography (described in the previous Chapter) and Ar etching in squares, with lateral dimension ranged from 10 to 50 μm. Additional preparation details can be found in Refs. [77, 107].

4.2.2 Characterization of the Fe-V alloy electrode

In the introduction of this Chapter, we have discussed that in order to obtain large TMR values, the electrodes should satisfied three main conditions. The first condition is satisfied because the Fe-V alloy has a bcc crystal structure in the (100) direction [108]. Next below, we shall discuss if the two following conditions are satisfied for Fe-V alloys, varying the concentration of vanadium.

4.2.2.1 Lattice parameter of the Fe-V alloys

In order to verify the second condition, we need to know how the lattice parameter of the Fe-V alloys varies with respect to the concentration of vanadium. It is well know that the lattice parameter of vanadium is $a_V = 0.303\ nm$ and variation of the

concentration of vanadium in the Fe-V alloy electrode will change the interatomic distance [109]. Therefore, we want to know what is the optimal concentration of vanadium so that the matching between electrode and barrier is the best. In order to measure the interatomic distance in Fe-V alloys, X-ray diffraction (XRD) in the so called $\theta - 2\theta$ configuration has been used in Ref. [77]. The advantage of using a diffractometer is that it allows to measure the lattice parameters in all directions of the space, so that it is possible to measure the parameters of the cells in parallel direction ($a_{\shortparallel}$) and perpendicular ($a_{\perp}$) to the surface (see *Figure 4.2*). The X-ray diffraction technique is particularly common and follows the same principles as the diffraction of electrons. In particular, with wavelength of the radiation of about 0.1nm, the technique reveals the atomic-scale spatial periodicity. The main difference with electron diffraction is the large penetration depth of X-rays (in the micrometer range), which provides access to average information in the volume of the layer studied. The [110] interatomic distance of bulk MgO $\frac{a_{MgO}}{\sqrt{2}} = 0.298$ nm lies between those of Fe and vanadium, and the misfit between the MgO and Fe-V layers varies with vanadium concentration. Consequently, as we can see in the *Figure 4.2*, the lattice parameter (a_x) of 50nm thick $Fe_{(1-x)}V_x$ films varies almost linearly with the concentration of vanadium (x) between the parameters of Fe ($a_{Fe} = 0.287\ nm$), when $x = 0$ and vanadium ($a_V = 0.303\ nm$), when $x = 1$ [77]. With a concentration of vanadium in the electrode close to 70%, the lattice parameter of the Fe-V electrode is practically the same as the MgO. Consequently, the matching between electrode and barrier is then almost perfect.

It is well known that during a layer by layer growth process, the growing film is pseudomorphic to the substrate, up to a critical thickness h_c at which plastic relaxation occurs and dislocations nucleate [48, 85, 86]. The lower is the misfit, the higher is the critical thickness, and the lower the dislocations density after the plastic relaxation. This means that the dislocations density in the MgO barrier is reduced with increasing vanadium content. Above h_c, the lattice parameter of the

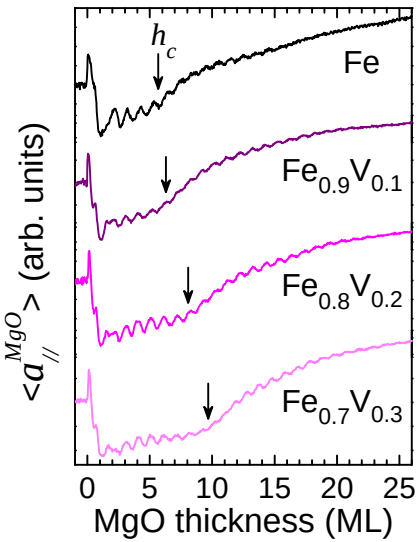

Figure 4.3: Variation in the average surface in-plane lattice parameter of MgO measured by RHEED during the growth on several FeV (001) surfaces.

film increases with h and tends to reach the bulk value. Therefore, a good way to determine h_c is to measure the average lattice parameter during the growth, which is possible by using electron diffraction. The average surface in-plane lattice parameter of MgO has been measured by RHEED during the growth on several Fe-V alloys. For this purpose, the distance between (220) and ($\overline{2}\,\overline{2}\,0$) diffraction rods, which is inversely proportional to the average surface parameter was monitored. As shown in *Figure 4.3*, a sudden increase of the average in-plane distance is observed in all cases. This behavior corresponds to the appearance of the dislocations in the MgO film that changes the average lattice spacing [77]. The corresponding critical thickness h_c is about 5 ML on Fe and substantially increases with x up to 10 ML with 30% of vanadium. Even though dislocations will be still present in our 9.5 ML thick MgO barriers for $x < 0.3$, their density is reduced. Considering the pessimistic case of a fully relaxed film, the average distance L between two dislocations in the MgO [100] or [010] in-plane directions would be $L(x) = \frac{a_{MgO}}{2f(x)}$

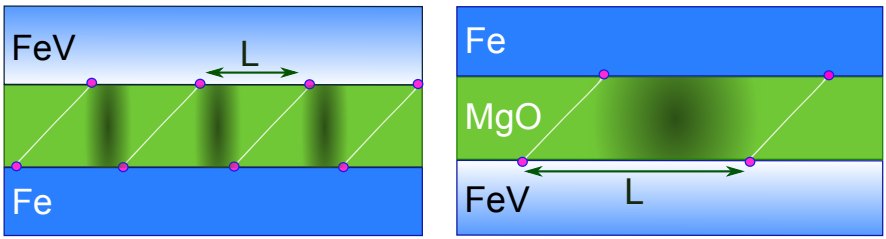

Figure 4.4: Schematic representation of the coherent tunneling for two different samples using Fe-V alloys in the top and bottom electrode. The shadow area is the defect-free junction area.

where the misfit $f(x) = \frac{a_{MgO}}{a(x)\sqrt{2}} - 1$. The dependence of L with x is likely to be stronger in our thin films stacking due to a partial relaxation.

Note that the thinner a stressed film is the lower required energy for nucleating a dislocation. Therefore, dislocations are easier to nucleate in a growing MgO film than in a completed one. The density of dislocations is thus mainly determined by the mismatch with the supporting (bottom) layer and to a lower extent by the top one. As a consequence, for a MTJ with two different electrodes, the density of dislocations depends on the stacking sequence. It is lower in an $Fe_{(1-x)}V_x$/ MgO/ Fe MTJ than in an Fe/ MgO/ $Fe_{(1-x)}V_x$ one. The dislocations within the MgO barrier have an oblique orientation [48]. Then, for Fe-V alloy in the bottom electrode the defect-free junction area for coherent tunneling is larger than in other type of sample. The scenario of this situation is shown in *Figure 4.4*, where the shadow area shows the region where tunneling is possible through the barrier in the area without dislocations.

High resolution transmission electron microscopy (HRTEM) images confirm the decrease of density of dislocations between Fe-V/ MgO and MgO/ Fe interfaces and the increase of the critical thickness for plastic relaxation [77, 110]. *Figure 4.5* (a), shows HRTEM image for samples with 20% of the concentration of vanadium in the bottom electrode. The high quality of the structure due to a continuous MgO

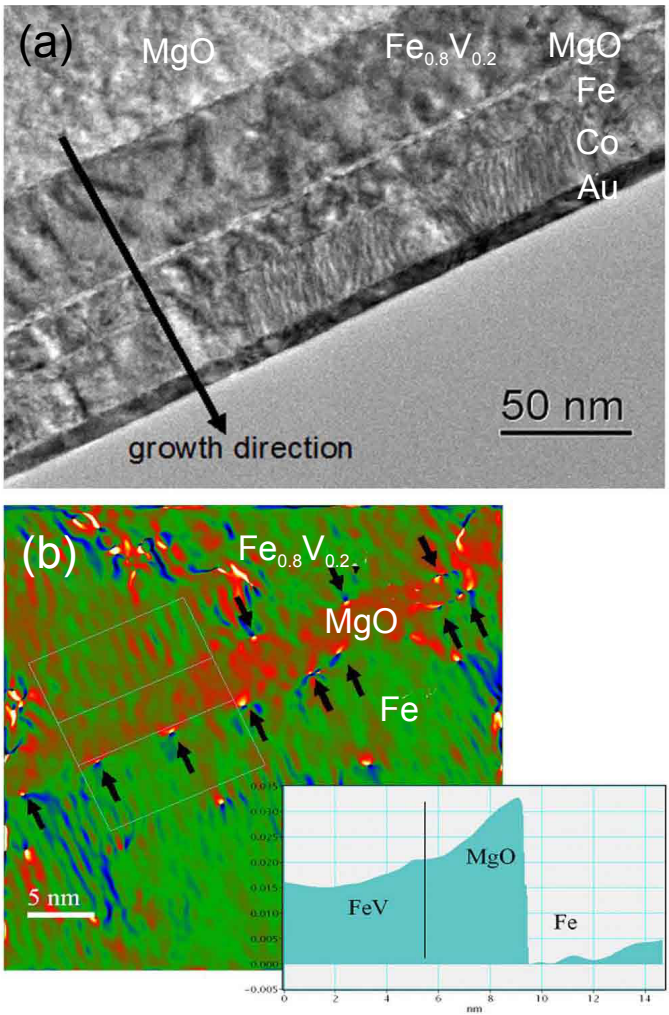

Figure 4.5: (a) Local phase images of the MTJs $Fe_{0.8}V_{0.2}$/ MgO/ Fe. (b) Map of strain in atomic planes normal to the interface [(200) MgO and (110) Fe-V]. The graph shows a profile of strain across the barrier, integrated in the zone delimited by the white borders. Values are given in %, taking the Fe (110) layer as reference. [Adapted from Ref.[77]].

barrier of the sample is evident. As a consequence of the change in the lattice parameter of the Fe-V alloy electrode, the number of dislocations is reduced in comparison with the electrode which has only Fe. In the map of strain around the barrier (*Figure 4.5* (b)), we can see the dislocations at the interface marked with arrows. The strain is localized in the vicinity of the dislocations and the density of dislocation in the Fe-V/ MgO interface is lower than in the MgO/ Fe interface. Therefore, it is not necessary to have a very high concentration of vanadium in the electrode to reduce the number of dislocations at the interface. Because as seen in *Figure 4.5* (b), with only 20% of vanadium in the electrode the dislocation density is reduced to nearly one half. This confirms that the misfit with MgO is reduced and the crystalline quality of the barrier and the interfaces is improved.

4.2.3 Polarization of the electrodes as a function of vanadium concentration

The MTJs doped with vanadium in the bottom electrode satisfy the two first conditions for large values of TMR, but we need to check whether vanadium meets the last condition (i.e large values of spin polarization). Once we know that the crystallinity of the barrier is improved at low vanadium concentrations in the bottom electrode, the spin polarization studies should probe magnetism of these alloys. The spin polarization of the tunneling current and its dependence on the magnetic state determine the amplitude of the TMR. In MTJs with a thick enough MgO barrier (001), the polarization allows us to consider the tunneling current as a mixture between the polarization of the electrons with different Δ bands symmetry at the E_F and the efficiency of the filter symmetry of the barrier, due to the attenuation of the states with $\overrightarrow{k_{\parallel}} \neq 0$. Using Fe-V alloys as ferromagnetic electrodes, we aim to improve or at least not degradate the efficiency of filtering symmetry. It is necessary to know the polarization of the bands in the Fe-V alloys regardless the tunnel process, in order to know what is the dependence of the spin polarization of Δ bands as a function of the concentration of vanadium. Based on

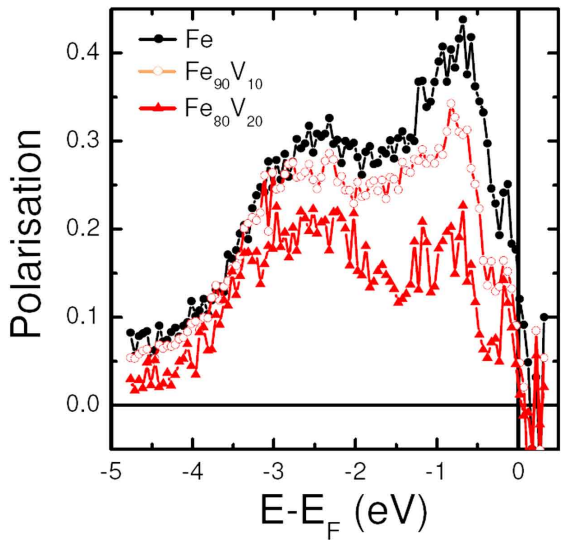

Figure 4.6: Spin polarization of Fe-V alloys covered with MgO (2 ML) measured by SR-XPS ($h\nu$ = 60 eV, Sherman function S = 0.12). [Adapted from Ref.[77]].

the model of Julliere [14], we consider that the effective polarization ($\mathcal{P}$), for this thickness of the MgO barrier, can be defined by the expression (More details of this expression are described in the Introduction of the Thesis):

$$\mathcal{P} = \frac{n_\uparrow - n_\downarrow}{n_\uparrow + n_\downarrow} \Longrightarrow TMR = \frac{2\mathcal{P}_1\mathcal{P}_2}{1 - \mathcal{P}_1\mathcal{P}_2} \tag{4.1}$$

Here $n_\uparrow$ and $n_\downarrow$ are related to the spin majority and minority bands, respectively. In *Figure 4.6*, it is possible to see the total spin polarization obtained for $Fe_{(1-x)}V_x$ (50 nm)/ MgO(2 ML) for different vanadium concentration. As can be easily seen in this *Figure*, when we increase the vanadium concentration of the electrode, the total spin polarization of Δ bands decreases [112]. Despite that the best mismatch between (Fe-V/ MgO) layers is with a vanadium concentration of 70%, the polarization decreases rapidly when it exceeds 20%. Consequently, the Fe-V alloys with low concentration of vanadium (less than 20%) seem the best candidates to be used as electrodes in MTJs.

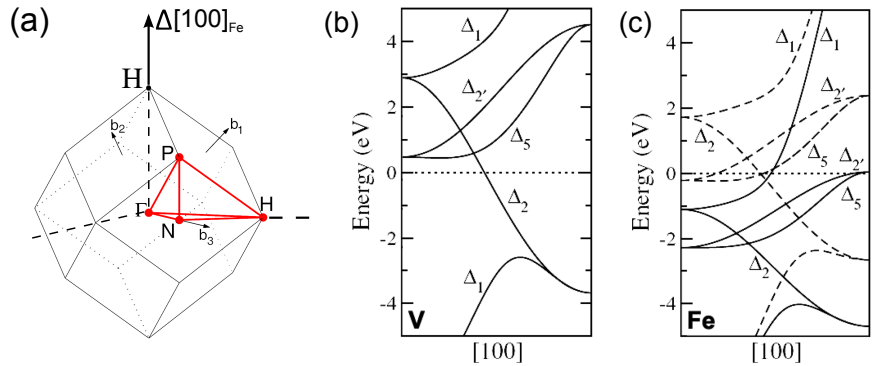

Figure 4.7: (a) Reciprocal space representation of the bcc Fe lattice. Δ direction corresponds to the propagation of electrons perpendicular to the (100) plane in real space. (b),(c) show the bulk band structure diagram for V and Fe in bcc structure in the Δ direction, respectively. [Adapted from Ref.[48, 111]]. In part (c), full and dotted lines represents the majority and minority spin bands, respectively.

4.2.4 Bulk band structure calculations

Before analyzing the dynamic conductance vs bias, it would be important to discuss the electronic structure of Fe-V alloys with bcc structure, particularly the densities of states (DOS) for majority and minority spin electrons with Δ symmetry. For pure Fe or vanadium electrodes, the bulk band structures in the Δ direction for each of the elements are the one shown in *Figure 4.7*. In the majority Δ bands of the Fe at E_F, the tunneling process is dominated by the propagation of electrons with Δ_1 symmetry and with lower degree of contribution from $\Delta_{5,2'}$ bands. But for pure vanadium, these bands ($\Delta_{5,2'}$) are well above the E_F [9, 50, 111].

In our case, we have Fe-V alloys as electrodes. The bulk band structure of the Fe will be modified when vanadium is introduced and when the alloy is disordered. Therefore, we need to study what happens at the majority and minority density of states as a function of vanadium concentrations. The vanadium has 23 electrons and the electronic configuration is $1s^2 2s^2 2p^6 3s^2 3p^6 4s^2 3d^3$. According to Hunds

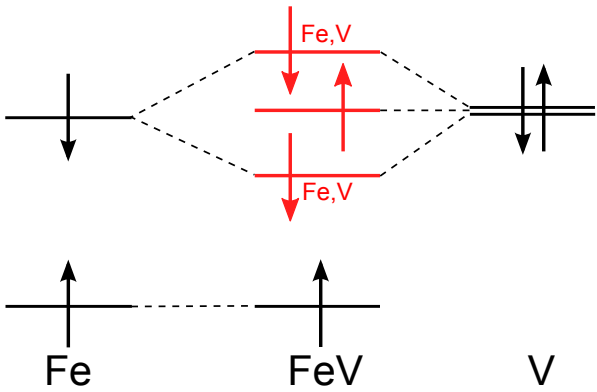

Figure 4.8: Schematic energy diagram of Fe-V alloy. [Adapted from Ref.[108]].

rule, it is energetically favorable for the majority spin d states to be fully occupied. The electrons with $d_{Fe\downarrow}$ take advantage of this situation leading to hybridization of the Fe and vanadium band (schematic diagram of energies in *Figure 4.8*) [110]. On the contrary, in the bands $d_{Fe\uparrow}$ and $d_{V\uparrow}$ there is no hybridization, because their bands are relatively large to hybridize. It should be also remembered, that the majority density of states of the vanadium is very unpopulated [113]. This scenario is possible to check analyzing the electronic structure of Fe-V alloys. In the *Figure 4.9*, adapted from the paper recently publish by Belhadji *et al.* [114], we can observe that the minority spin electrons with Δ_1 and Δ_5 symmetries, are practically unaffected when the concentration of vanadium increasing few %, indicating the hybridization of the Fe bands $d_{\downarrow}$. At the same time the DOS peaks, close to E_F, of the majority spin electrons related to these bands are highly attenuated.

It is important to remind, that the conductance in the P states comes from the electrons with Δ_1 symmetry. On the other hand, the Δ_1 band is forbidden in the AP state. The electrons with Δ_5 symmetry in the majority spin band practically disappear when the concentration of vanadium is increased in the electrode, and then the conductance in the AP increases with respect to a pure Fe electrode. We

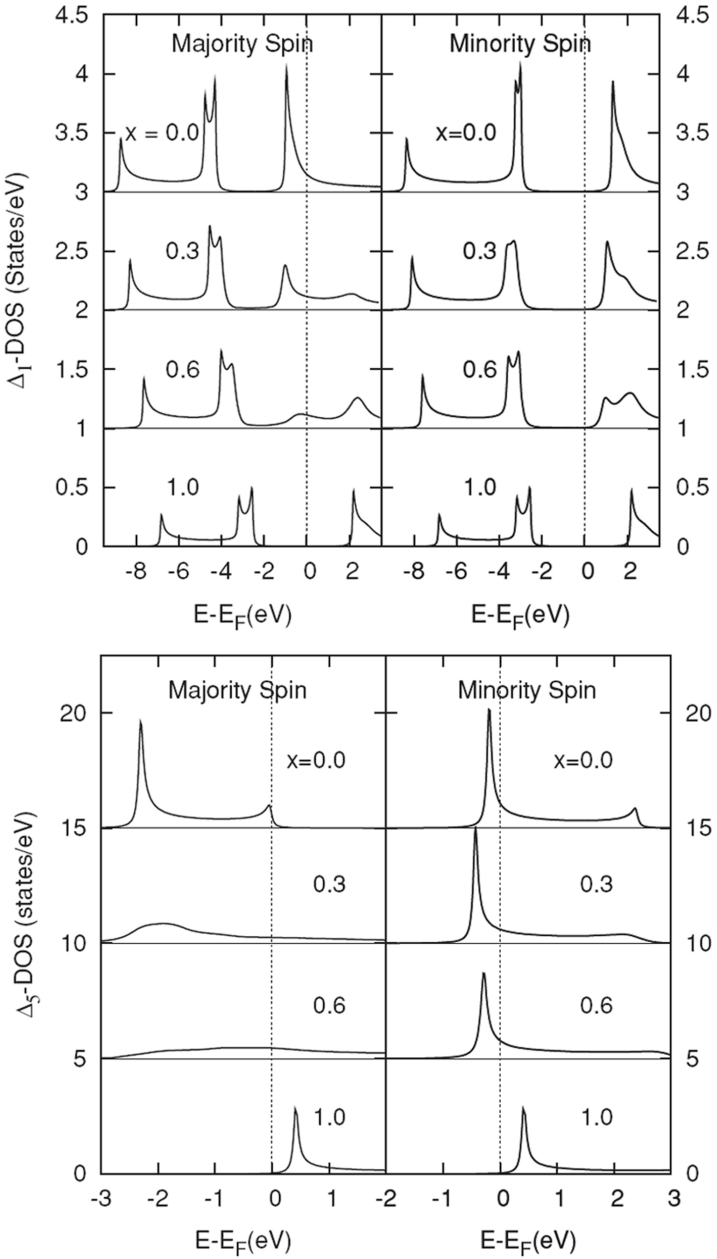

Figure 4.9: Density of states with Δ_1 and Δ_5 (upper and lower figure, respectively) symmetry for $Fe_{(1-x)}V_x$ alloys with x = 0.0, 0.3, 0.6, and 1.0. Results for majority and minority spin electrons are, respectively, shown on the left- and right-hand sides. [Adapted from Ref.[114]].

shall use these theoretical calculations to discuss the experimental measurements of tunneling conductance and TMR in the next section.

4.3 TMR and Dynamic conductance

4.3.1 TMR at zero bias

So far, we have seen that low concentration of vanadium improves the misfit at the Fe-V/ MgO interface and that due to structural processes of the growth, the density of dislocations is lower when the Fe electrode containing vanadium in the bottom electrode. The problem remains with the fact that the high concentrations of vanadium decreases the total spin polarization and affects the Δ_1 and Δ_5 majority bands. In order to verify these effects, we have measured the tunneling transport and low frequency noise in two types of MTJs (using Fe-V alloy in the bottom or top electrode) and with different thickness of the MgO barrier (9.5±0.5 and 13 ML). We have compared these results with the reference samples (Fe/MgO/Fe).

Figure 4.10 shows the typical TMR measured at 0 V bias, by using a low amplitude (with excitation below 10 mV) square current wave. Part (a) shows the TMR of the MTJs with the thinner (9.5±0.5 ML) barrier. For these MTJs, the reference sample has a value of TMR close to 185% at room temperature. When we use $Fe_{90}V_{10}$ alloys in the top electrode, the TMR decreases to about 130%. This is because the density of dislocations at the Fe/ MgO interface is large (respect to Fe-V/ MgO) when the MgO barrier is grown on the Fe electrode. Besides, the top electrode is formed by a Fe-V alloy, where the total spin polarization is lower than the bottom electrode and, consequently, the TMR decreases respect to the TMR value of the reference samples. In contrast, for the samples with $Fe_{92}V_{08}$ in the bottom electrode, the density of dislocations at the interface should significantly decrease, which will improve the tunneling conductance and the TMR values will increase up to 210%. For this concentration of vanadium the total spin polarization

4. Strongly suppressed 1/f noise in epitaxial Fe-V/MgO/Fe magnetic tunnel junctions

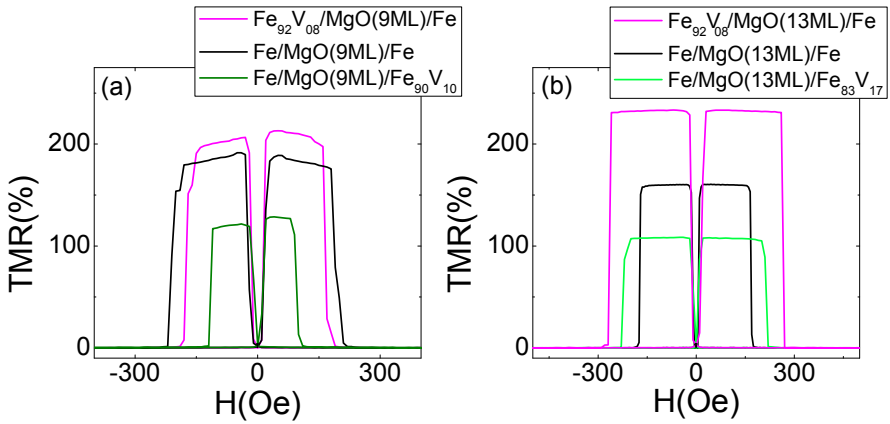

Figure 4.10: (a),(b) TMR of various $Fe_{1-x}V_x$/ MgO (9.5±0.5 and 13 ML)/ $Fe_{1-x'}V_{x'}$ MTJs versus applied magnetic field at RT and 0 applied bias, respectively.

of the bottom electrode is lower than the top Fe electrode but not yet significantly decreased. Due to the competition between the mismatch and spin polarization, for small concentrations of vanadium, the first term is more relevant and the TMR increases.

Similar effects were observed in tunneling transport when the thickness of the barrier is higher (confirmed by preliminary report [112]). When we use the $Fe_{92}V_{08}$ alloy in the bottom electrode the value of the TMR increases in a 60% in comparison with the reference sample *Figures 4.10* (b)). Based on the reasoning explained in the previous Chapter, the difference in the TMR for the thicker barrier may be due a plastic relaxation that occurs after to growth 5-6 ML of MgO barrier. In this thickness range an increase of the thickness of the barrier increases the density of defects. Therefore, when we use pure Fe as the bottom electrode the density of defects is higher and propagates through all the structure. As a consequence the effective tunneling conductance will be reduced and the value of TMR, too (compare *Figures 4.10*(a)-(b)). On the contrary, if the bottom electrode is a Fe-V

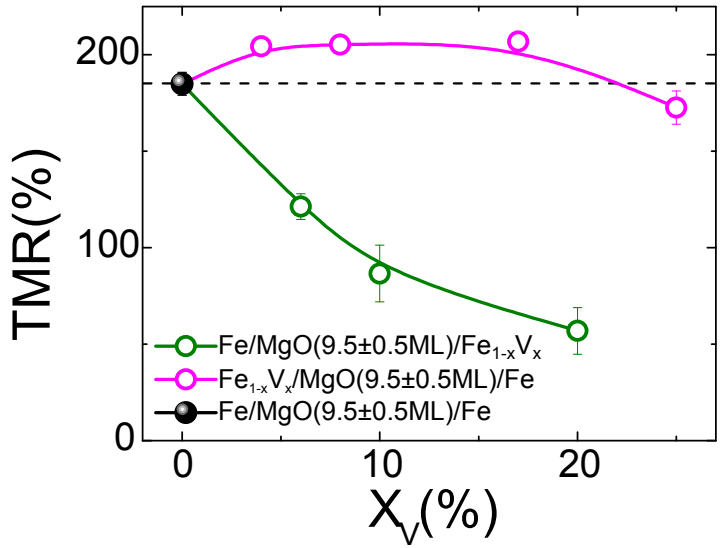

Figure 4.11: TMR variation at RT versus vanadium concentration x for the different series of MTJs with thickness of the MgO 9.5±0.5 ML.

alloy, it will have reduced the mismatch improving the effective tunneling transport through the barrier and increasing the TMR with respect to thinner barrier due to Δ_5 filtering of the MgO barrier.

Further below we discuss in more details the TMR in MTJs with different concentrations of vanadium. As we can see in *Figure 4.11*, for MTJs with 9.5±0.5 ML thickness of the MgO barrier with Fe-V alloys as the top electrode, the TMR values are monotonically decreasing as a function of vanadium concentration. On the other hand, for Fe-V alloys as the bottom electrode (for $x < 20\%$) the TMR is higher than the reference sample (via a decrease of the number of the dislocations) and for the $x > 20\%$ TMR values decrease with respect to control samples (due to the decrease of the total spin polarization of the bottom electrode). A similar behavior has been observed for thicker barrier [112]. Given that the density of defects is related to the low frequency noise, we shall go into more detail in the noise section of this Chapter related to noise studies.

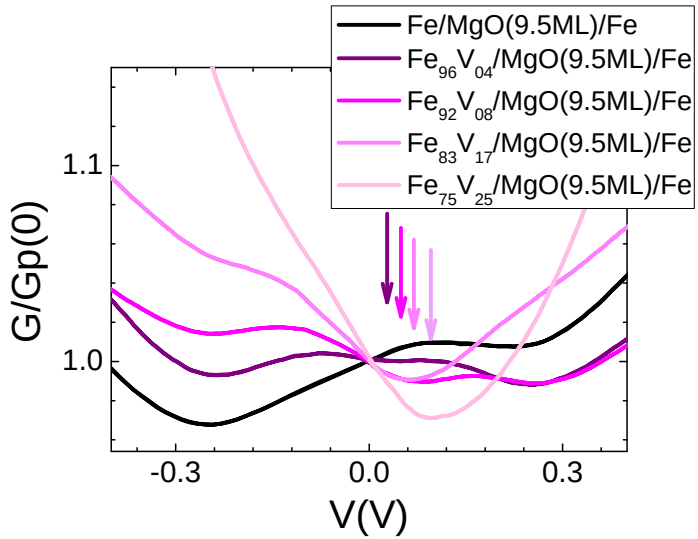

Figure 4.12: Dynamic conductance of the $Fe_{1-x}V_x$/ MgO (9 ML)/Fe normalized by $G_P(0)$ in the P state at RT. The position of the minima in conductance respect to bias are marked with arrows.

4.3.2 Dynamic conductance in Fe-V/MgO/Fe MTJs

So far, we have discussed spin tunneling transport at zero bias for different concentration of vanadium. It is needed, however, to understand the tunneling transport at applied bias in comparison with band structure calculations. For this reason, we have measured the dynamic conductance ($G = dI/dV$) as a function of bias at room temperature. Firstly, we focus on $Fe_{1-x}V_x$/ MgO (9.5 ± 0.5 ML)/ Fe samples, where the concentration of vanadium has a strong influence on the growth process and, consequently, in the conductance. To facilitate the understanding of the dynamic conductance measurements as a function of bias, we followed the same criteria of the direction of current as the one in the previous Chapter. Namely, the negative bias corresponds to the electrons tunneling from the top electrode

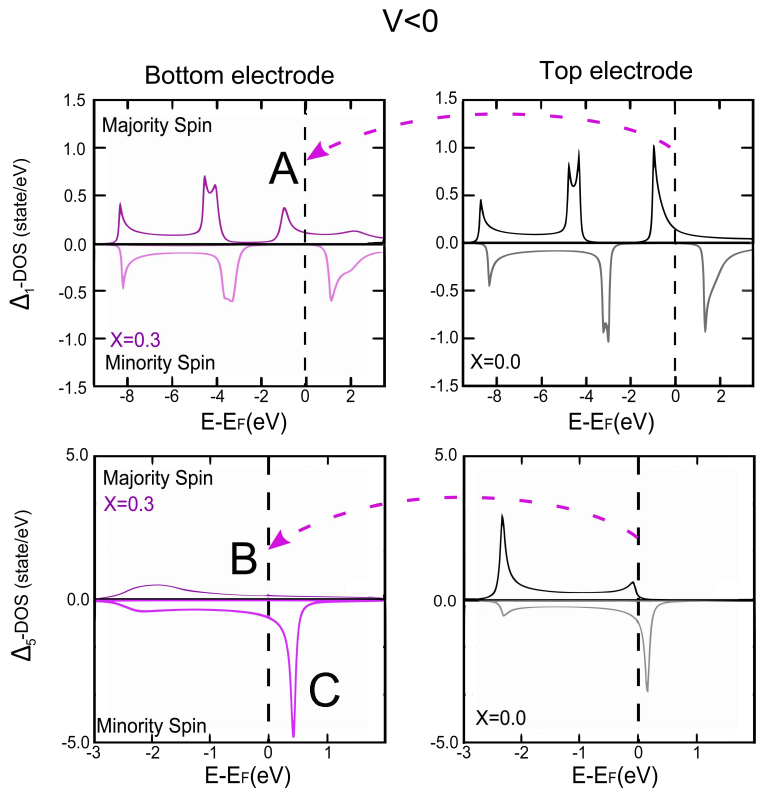

Figure 4.13: Density of states with Δ_1 and Δ_5 symmetry for $Fe_{(0.7)}V_{0.3}$ (bottom electrode, left part) and pure Fe (top electrode, right part), showing the specific channels of conductance in the P and AP states.

(vanadium free) to the bottom electrode (Fe-V alloy). *Figure 4.12* shows the normalized dynamic conductance in the P state as a function of bias. For the P state, the electrons of the spin majority/minority bands from one of the electrodes tunneling from the majority/minority bands of the other electrode, respectively. In the dynamic conductance, we can see a parabolic behavior respect to bias, due to the electrons with Δ_1 symmetry (marked with A in *Figure 4.13*). For low bias in the reference samples, the parabolic background conductance increases due to the contribution of Δ_5 bands [48]. As we increase the concentration of vanadium, we could see how changes the G_P, because changes the bulk band structure of the Fe-

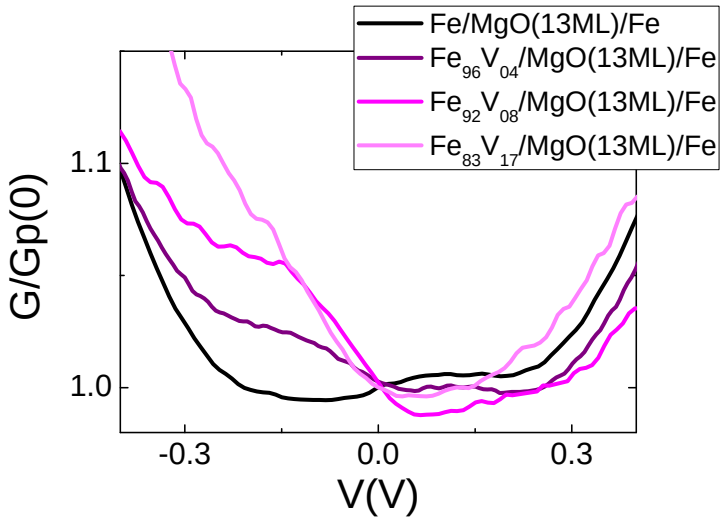

Figure 4.14: Dynamic conductance, at RT, for different concentration of vanadium in the bottom electrode for 13 ML of MgO barrier.

V alloy. The majority spin electrons with Δ_5 symmetry of the top Fe electrode are trying to tunnel to equivalent symmetry states in the bottom Fe-V alloy electrode. But now, Δ_5 band is displaced to higher energies (shown with region B in *Figure 4.13*). As a consequence, the G_P increases very fast for negative bias. In the reverse case, when electrons are injected from the bottom electrode, an additional minimum appears at lower energies (see arrows in *Figure 4.12* (a)). The energy of this new contribution depend linearly on the concentration of vanadium. In the reference samples, at low temperatures, we have seen in the previous Chapter that a minimum appears at 50 mV [68] in the P state, due to the contribution of electrons with $\Delta_{2'}$ symmetry. This additional minimum could be associated with this band of conductance and new calculations are needed to corroborate this hypothesis.

We have seen a similar effect on the dynamic conductance for thicker MgO barriers (13 ML) using vanadium alloys. But now, the filtering of the electrons with Δ_5 symmetry is higher, due to the width of the barrier [9]. Therefore, the

vanadium makes that the maximum of the density of states of Δ_5 bands moves to lower energies and the filtering of the MgO barrier makes that the electrons with Δ_5 symmetry is stronger. For this reason, we observe that the normalized dynamic conductance in the P state of the samples with 17% of vanadium in the bottom electrode for thicker barrier has a similar behavior respect to bias than 25% of vanadium with 9 ML of thickness of the barrier (compare *Figure 4.14* and *Figure 4.12*).

Let us now analyze the dynamic conductance for both states in the large bias windows (up to 1 V). For the positive bias, an additional maximum appears in the P state (marked with arrows in *Figure 4.15*) at +0.5 V with increasing vanadium concentration. This maximum could be associated with the peak of the spin minority Δ_5 bands in the DOS (marked with C in the *Figure 4.13*). On the other hand, in the AP state, the electrons of the majority/minority spin bands from one electrode tunnel to the minority/majority spin bands of the other electrode, respectively. In the previous Chapter, for negative bias in the AP state of the reference samples, the conductance was found to be increasing due to interfacial resonant states (IRS) at -1 V [81]. As we increase the concentration of vanadium, it seems that the point of the inversion of the TMR for negative bias, expected for -1 V, shifts to higher biases. In principle we can consider two possible situations. The first is that this shift could be due to the fact that in the AP state, the majority spin electrons with Δ_5 symmetry of the pure Fe electrode tunnel to the spin minority bands of the Fe-V alloy (marked with B in the *Figure 4.13*). When we increase the concentration of vanadium in the bottom electrode the maximum in DOS of the minority spin electrons with Δ_5 symmetry is shifted to lower energies, reflecting as an enhancement in tunnel conductance in the AP state to higher negative biases. Another possible situation is that the conductance in the P state is enhanced due to the influence of the minority Δ bands. As we have seen in section 3.2.4 of this Chapter, due to the hybridization of Fe bands, we can see how appears, for the highest concentrations of vanadium, the conductance peak

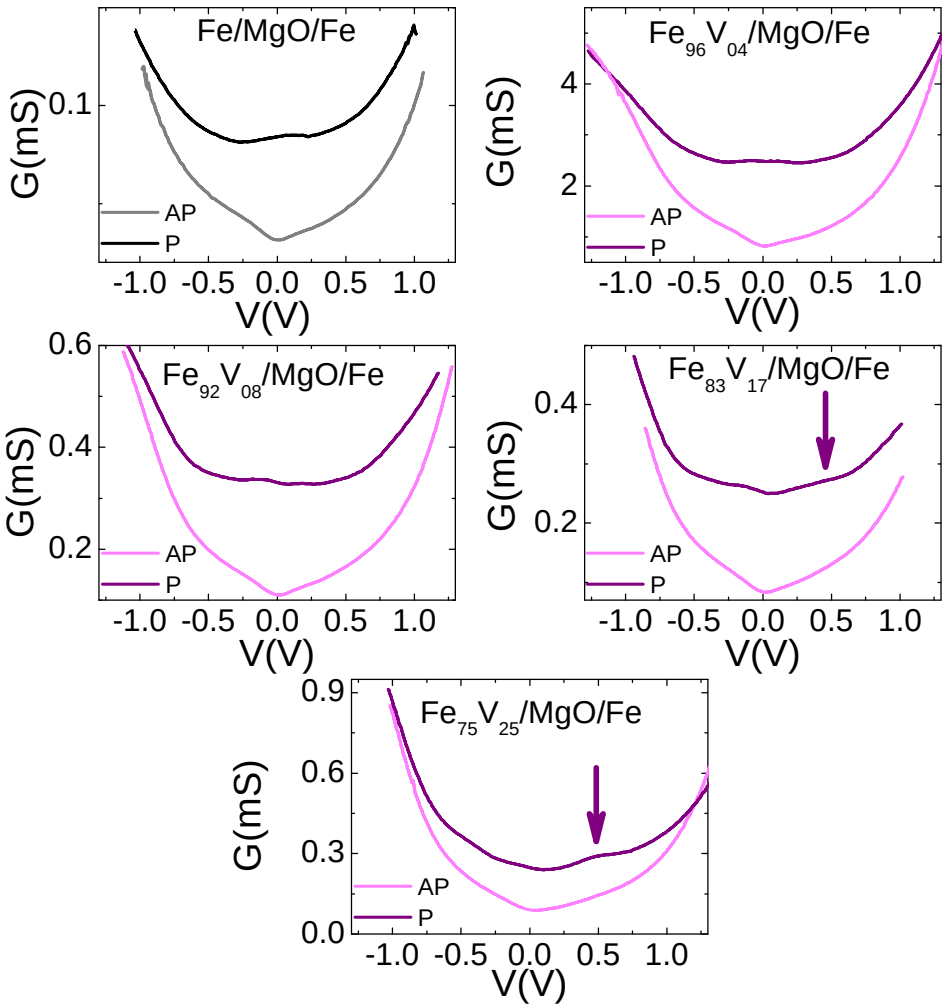

Figure 4.15: Dynamic conductance at room temperature for different concentration of vanadium in the bottom electrode (from 25% vanadium concentration to control sample, without vanadium), in the P state (H = 200 Oe) and AP state (H = -100 Oe). The arrows show the increase in dynamic conductance in the parallel state for positive bias.

associated to hybridization of the minority bands for electrons with Δ_5 symmetry (marked with C in *Figure 4.13*).

In order to corroborate the previous supposition, we decreased the temperature to T = 4 K. We have measured the $G = dI/dV$ up to 3 V and also analyze the derivative of the dynamic conductance d^2I/dV^2. The measurements of the second derivative of the conductance respect to bias are well known in inelastic electron tunneling spectroscopy (IETS). This method detects several different excitations in tunnel junction interfaces. We have studied as a reference, a MTJ with 17% of vanadium concentration in the bottom electrode. Because, as we have seen in *Figure 4.11*, the influence of the vanadium improves the quality of the interface between electrode and barrier, and the polarization is still high. *Figure 4.16* (a) shows the corresponding dynamic conductance. The G_{AP} has a similar behavior respect to bias as expected for reference MTJ samples (explained in the previous Chapter), but the main difference is in the G_P. While for positive bias, we do not observe any appreciable change in the dynamic conductance, a strong increasing of the G_P appears for negative bias (which electrons flow from Fe electrode to the Fe-V alloy electrode) in a energy window between -0.8 and -1.4 V. This effect is the responsible of the shift of the reversal point of the TMR to -1.7 V. The relation of the TMR vs bias, represented in *Figure 4.16 (b)*, shows more clear the rising of the G_P and TMR inversion.

The IETS measurement (*Figure 4.16 (c)*) corroborates similar behavior to the one expected for reference MTJs in the AP state [81]. This is because electrons of the majority spin bands from the pure Fe electrode tunnel to the minority spin bands of the Fe-V alloy electrode. As the minority spin bands do not change a lot (*Figure 4.13*), the d^2I/dV^2 curve shows the interfacial resonant state expected for Fe/MgO/Fe MTJs. We can identify the peaks of IRS1 and IRS2 from Ref. [81] (represented in our *Figure* as P5 and P6, respectively). We will not go into details of the d^2I/dV^2 in the AP state, as we did that already in the previous Chapter. We focus here in the P state where the scenario seems to be completely different.

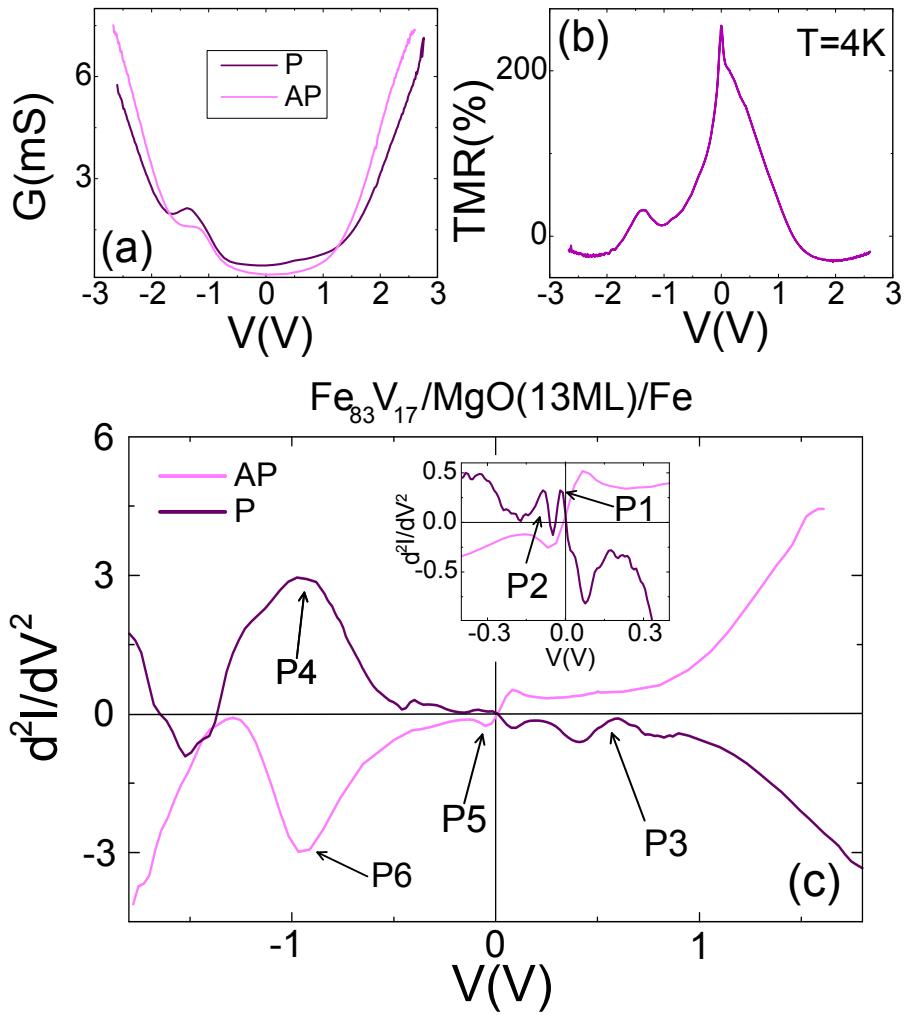

Figure 4.16: (a) Dynamic conductance, at 4 K, for 17% concentration of vanadium in the bottom electrode, in P (H = 200 Oe) and AP (H = -100 Oe) states. (b) Corresponding TMR (V) obtained from part (a). (c) d^2I/dV^2 curves measured at 4 K in P (purple) and AP (pink) configurations. The insets show the magnified zoom of the low bias region.

In the inset of *Figure 4.16 (c)*, the magnified zoom of the low bias region is shown. In this voltage region, the P1 and P2 peaks appear to correspond to well known energies. The first peak (P1) is at 9 mV and is associated to magnon excitations. The second peak (P2) close to 80 mV matches with the phonon frequency energy of the Mg-O [115, 116]. An additional peak (P3) appears at +0.5 V, that could be associated to the minority spin Δ_5 band and could be responsible for the increasing of the G_P at the same voltage (marked with arrows in *Figure 4.15*). Finally, the d^2I/dV^2 measurements confirm the shifted in energy of the point of reversal of the TMR. Strong enhancement in the d^2I/dV^2 at -1 V (peak P4) is due to the increase in energy of the density of states associated to majority spin Δ_1 bands (*Figure 4.13*). To obtain more detailed information of the tunneling process in this kind of samples, more theoretical calculations are needed to support these hypothesis.

4.3.3 Dynamic conductance in Fe/ MgO/ Fe-V MTJs

When the top electrode is doped with vanadium, the scenario becomes essentially different. We discussed above that the order of the layers in the growth process is an important factor. For Fe/ MgO/ Fe-V MTJs, the vanadium does not reduce the number of dislocations. Besides increasing the vanadium concentration in the top electrode reduces its total spin polarization. All these effects are reflected in the TMR values and the dynamic conductance. *Figure 4.17* shows the dynamic conductance of the Fe/ MgO (9.5±0.5 ML)/ $Fe_{1-x}V_x$ MTJs. It is easy to see that the G_V curves are much more noisy than the previous one (for Fe-V/MgO/Fe MTJs), which is probably because the quality of the barrier in Fe/MgO/Fe-V is worse than in samples with bottom electrode doped by vanadium. The vanadium makes that the tunnel conductance has a more parabolic behavior. It seems as if now, in the P state, the filtering of the conduction band of Δ_5 had a greater dependence on the vanadium. The *Figure 4.18 (a)* analysis this effect in more details, showing the normalized G_P vs bias. Negative bias

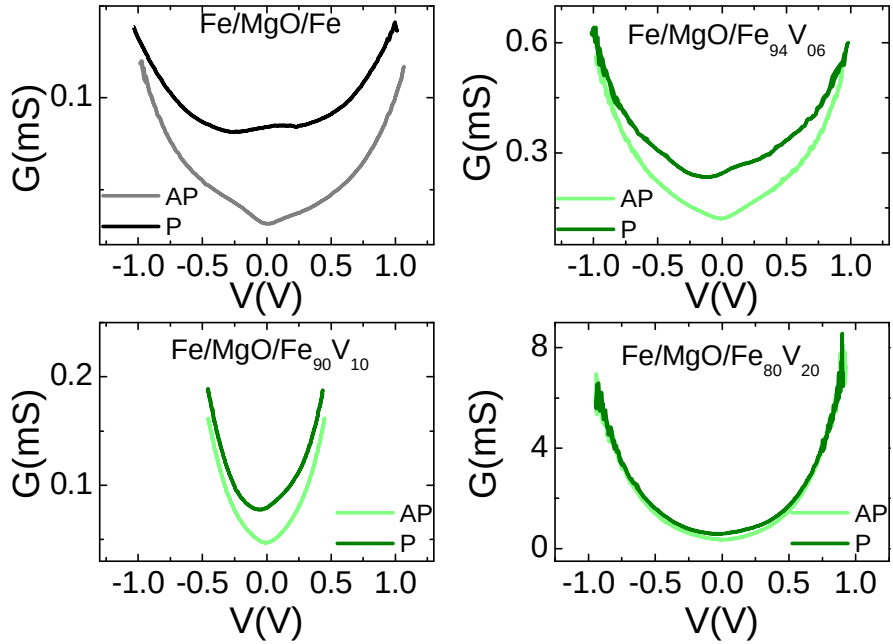

Figure 4.17: Dynamic conductance, at RT, for different concentration of vanadium in the top electrode, in P (H = 200 Oe) and AP (H = -100 Oe) states.

corresponds to the electrons tunneling from the top (Fe-V alloy) electrode to the bottom (vanadium free) electrode. For low vanadium concentration, the majority spin electrons with Δ_5 symmetry (*Figure 4.9*) are rapidly attenuated for the negative bias. As a consequence, the minimum in G_P (see arrows in *Figure 4.18 (a)*) trends to zero as a function of vanadium concentration.

Using the dynamic conductance and TMR measurements as a function of applied voltage, for both magnetic states, we have been able to corroborate the results previously obtained on the structural quality of the barrier. Still, the effects of vanadium do not seem extremely relevant in transport, since the increase in TMR is only about 20% for the thinner barrier and 60% for the thicker one. Instead, it seems that it could be crucial in the noise characteristics at low frequencies. It is well known that in the P state, the low frequency noise is due to the relaxation

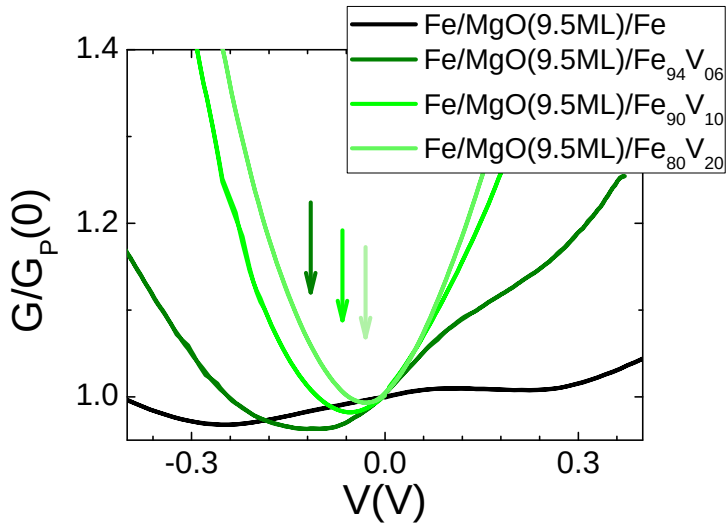

Figure 4.18: Dynamic conductance of the Fe/ MgO (9 ML)/ $Fe_{1-x}V_x$ normalized by $G_P(0)$ in the P state at RT. The Position of the minimum in conductance respect to bias are marked with arrows.

time of the defects in or near the barrier. Therefore, the barrier related to 1/f noise could give us a more clear idea of how the vanadium concentration affects the interface misfit.

4.4 Low frequency noise

It has been described several times during this Thesis the phenomenological Hooge model of the low frequency noise, which present the power spectral density (see formula in the Introduction). In *Figure 4.19 (a)* comparative typical noise power spectra times area ($\alpha \times$A, for which Hooge factor is being analyzed) are represented in the P state for the junctions with undoped, bottom or top Fe-V electrodes. Clearly, vanadium doping of the bottom Fe electrode trends to reduce the low frequency contribution to the noise, while vanadium doping of the upper electrode trends to enhance the normalized 1/f noise. *Figure 4.19 (b)* is an expansion of

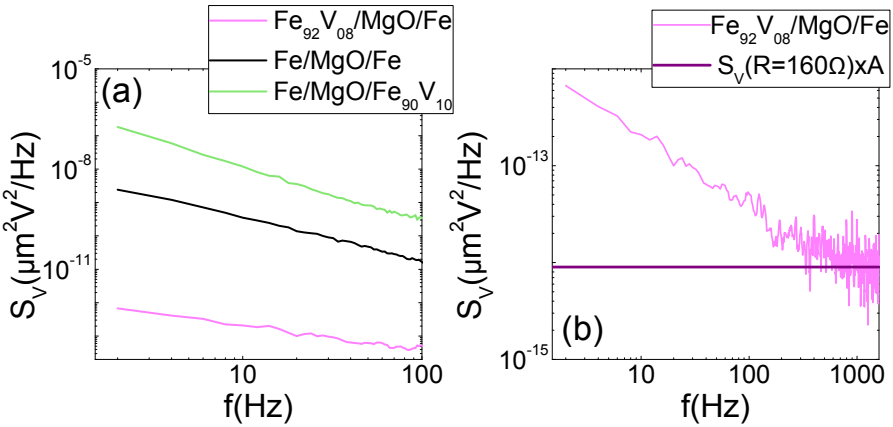

Figure 4.19: (a) Voltage noise power spectral density times area measured on the junctions with undoped, bottom doped or top doped electrodes with bias of 200 mV in the P state at RT. (b) Power spectral density (up to 2000 Hz) for the junction with bottom doped electrode. The purple horizontal line marks the noise power times area expected level of $Fe_{92}V_{08}$/ MgO(9.5±0.5 ML) /Fe with resistance of 160 Ω and direct electron tunneling processes (Shot noise + thermal noise).

the spectra up to 2000 Hz. It is shown that noise for MTJ with bottom doped electrode ($Fe_{92}V_8$/ MgO (9 ML)/ Fe) may be accounted by the junction resistance in the conditions of direct electron tunneling (i.e Poissonian shot noise + thermal noise).

4.4.1 Influence of vanadium concentration on 1/f noise

For low concentrations of vanadium, as we noted in the figure above, the power spectral noise at low frequencies decreases when using Fe-V alloy as the bottom electrode due to the smaller number of dislocations in the interface between electrode and barrier. We now extend this study to all concentrations of vanadium for which we measured the dynamic conductance vs bias. *Figure 4.20* shows the variations of the zero bias TMR and normalized low frequency noise (Hooge parameter analyzed between 1-50 Hz)), averaged for each set of samples of ($Fe_{(1-x)}V_x$ / MgO(9.5 ± 0.5 and 13 ML) / $Fe_{(1-x')}V_{x'}$), as a function of vanadium content

(x). The error bars represent the dispersion of the corresponding values measured within each junction sets. In our convention, negative x values correspond to a bottom $Fe_{(1-x)}V_x$ electrode, whereas positive x values correspond to a top $Fe_{(1-x)}V_x$ electrode. First, we study the influence of vanadium for thinner (9.5±0.5 ML) barrier (*Figure 4.20* (a)). In the latter case (top $Fe_{(1-x)}V_x$ electrode), the TMR systematically decreases with x being lower than for control (standard) Fe/MgO/Fe MTJs (185% at room temperature). As was shown before, the TMR decreases due to the reduced total spin polarization of Δ states in Fe-V alloys [77]. In the presence of a bottom Fe-V electrode and for $x < 0.17$, we observe an increase of TMR from 185% to 207%, whereas the TMR again decreases for larger vanadium contents. Similar trends are observed with a thicker MgO barrier (13ML) as shown in *Figure 4.20* (b), the TMR reaching up to 240% at RT in the latter case [77], due to a better spin filtering when increasing the MgO barrier [117]. It was shown that the optimum TMR results from the competition between the reduction of the electrodes polarization (detrimental to the TMR) and the structural improvement of the barrier (beneficial to the TMR) [77]. Indeed, when used as the supporting bottom electrode, Fe-V alloys reduce the dislocations density and therefore the strain of the barrier and its roughness.

Our main experimental finding is the observation of a strong (nearly two orders of magnitude) decrease of the Hooge factor measured in the P state (i.e. defect related noise) with vanadium doping of the bottom Fe electrode for the thinner (9.5±0.5 ML) barrier (*Figure 4.20* (a)). We note also that the minimum of the normalized nonmagnetic noise (α_P) roughly coincides with the maximum TMR of about 207%. This corresponds to an enhancement of the signal to nonmagnetic noise ratio by more than 2 orders of magnitude in $Fe_{(1-x)}V_x$/ MgO/ Fe ($0.08 \leq x \leq 0.17$) MTJs, in comparison with the reference Fe/MgO/Fe one. Although additional vanadium doping further decreases the lattice mismatch at the Fe-V/MgO interface, contrary to expectations, the normalized noise values start to increase when x exceeds 17%. One possible reason could be the increased chemical

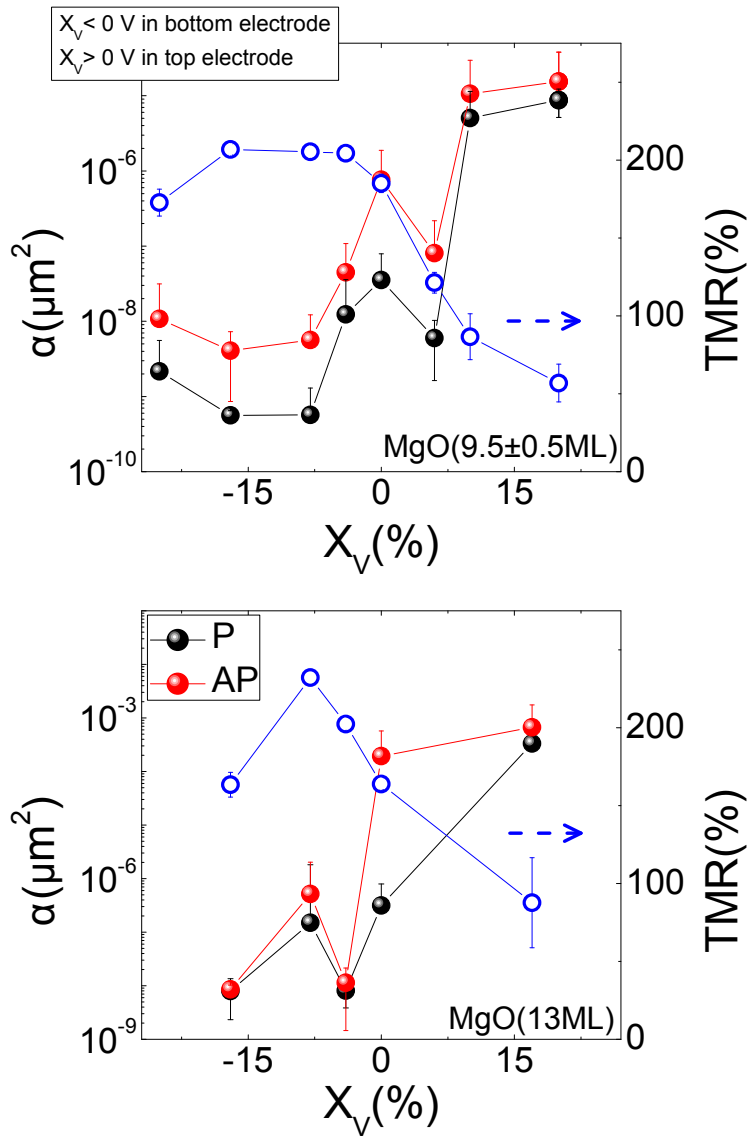

Figure 4.20: Dependence of zero bias TMR and normalized noise (Hooge factor), averaged over each set, as a function of vanadium content in the bottom (x<0) and upper (x>0) electrodes.

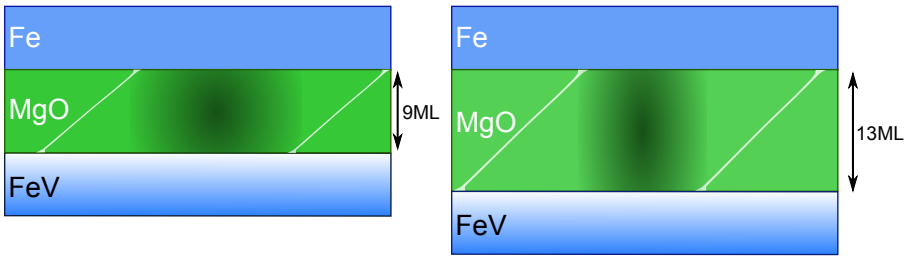

Figure 4.21: Schematic representation of the coherent tunneling for samples using Fe-V alloys in the bottom electrode with different thickness of the barrier. The shadow area represent the defect-free junction area.

disorder at the Fe-V/MgO interface, and the related spatial fluctuations of the potential. In contrast, vanadium doping of the upper electrode in Fe/MgO/Fe-V MTJs results in an increase of the nonmagnetic noise. Contrary to the case of a bottom Fe-V electrode, a top Fe-V one acts much less on the strain of the barrier because dislocations mainly nucleate during the growth of MgO. Here, the noise variations could reflect the increasing of chemical disorder.

Qualitatively, similar behavior of 1/f noise and TMR as a function of vanadium content is observed for thicker MgO barrier (13 ML). But now, contrary to observed in tunneling transport, the reduction of the normalized low frequency noise as a function of concentration of vanadium is lower than for thinner barrier. One of the possible scenarios is shown in *Figure 4.21*. The tunneling transport is affected by the mismatch and the filtering of the MgO barrier. For thicker barrier the filtering of the Δ_5 is higher and consequently also the TMR [9, 42]. On the other hand, the low frequency noise measurements are more sensitive to the tunneling process than the dynamic conductance. As we increase the number of layers of the MgO barrier, due to the oblique orientation of the dislocation the effective tunnel area is reduced (see sketch of *Figure 4.21*) and the low frequency noise will be affected.

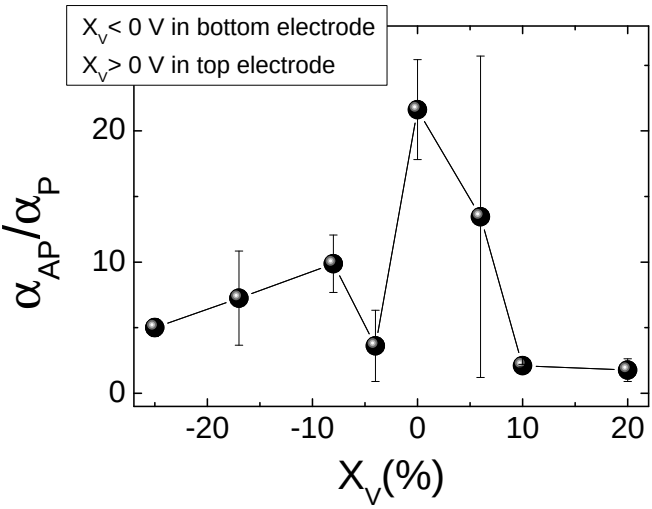

Figure 4.22: Normalized relative variation in the noise between AP and P alignments, as determined from *Figure 4.20* as a function of vanadium content.

The normalized difference of the 1/f noise between AP and P states defined as $(\alpha_{AP} - \alpha_P)/\alpha_P$ (see *Figure 4.22*) shows an interesting trend as a function of vanadium alloying, which may be important for applications of these MTJs. One observes that an enhanced TMR with vanadium alloying is accompanied by a reduced relative noise in the AP state. We tentatively attribute this unexpected behavior to the minority Fe-V band hybridization [109]. As long as the minority Δ bands control the conductance in the AP state [9, 10], the Fe-V minority band hybridization could reduce the corresponding 1/f noise level produced by the defects through enhanced charge screening.

4.5 Conclusions

In this Chapter, we have studied the influence of vanadium substitution on electron transport and low frequency noise in $Fe_{(1-x)}V_x$/ MgO(9.5 ± 0.5 and 13 ML)/ $Fe_{(1-x')}V_{x'}$ MTJs. We show that alloying the Fe electrode changes electronics

characteristics of fully epitaxial magnetic tunnel junctions at small vanadium concentrations of the bottom electrode, satisfying three fundamental conditions for large TMR values. From both fundamental and applied points of view, it would be interesting to investigate these alloys of vanadium in the bottom electrode for concentrations below 20%.

Improving the interface by reducing the dislocations, increases the area of the barrier which is free of dislocations, and therefore improves the coherent tunneling. We observed this via TMR measurements at zero bias and dynamic conductance. However, the influence of vanadium in the Fe electrode on the tunneling transport is not extremely large, providing TMR increase of only 20% for the thinner barrier ($9.5 \pm 0.5\ ML$). The influence of vanadium alloying is much more relevant for the low frequency noise, where the noise in the P state (non magnetic noise) is reduced by more than two orders of magnitude with a low concentration of vanadium ($8\% \leq x \leq 16\%$). From an applied point of view, such type of junctions are very interesting, since very small concentrations of vanadium enormously improve the signal/noise relation. It is also important to note, that both the non magnetic noise (P state) and the magnetic noise (AP state) decrease with vanadium alloying.

As we already said before, it would be important to verify the implementation of a similar strategy in MTJs with thinner barriers and smaller resistance times area (R×A) products, which are more relevant for applications. Such new growth strategies could have great value for the industry. For example recent work [105] shows strong relation between the presence of interface traps (which appear due to lattice mismatch) and the robustness of magnetic tunnel junctions. Beside for technology, it is very important to have more sensitive field sensing devices. We found that as we increase concentration of vanadium in the bottom electrode the low frequency noise in both states (P and AP) and their relation are reduced (*Figure 4.22*).

4. Strongly suppressed 1/f noise in epitaxial Fe-V/MgO/Fe magnetic tunnel junctions

5

Electron transport in double magnetic tunnel junctions with dielectric breakdown

5. Electron transport in double magnetic tunnel junctions with dielectric breakdown

5.1 Brief introduction

Until now, we have studied fully epitaxial magnetic tunnel junctions with a single barrier (SMTJ), which are very important devices in the field of spintronics. Recent theoretical predictions [9, 10] followed by experimental observations of coherent tunneling in SMTJs with MgO barriers [7, 8, 83, 98, 99] have boosted research of $F_1/I/F_2$ MTJs [5, 6, 14] (here F_1 and F_2 are ferromagnetic layers and I is a thin insulating barrier). The schematic SMTJ representation is shown in *Figure 5.1* (a). Here the z axis is perpendicular to the junction and the interface between the bottom electrode (F_1) and the barrier (I) is located at z = 0. For thin enough electrodes, electron tunneling in devices with few interfaces may reveal resonant features due to quantum well states (QWS) leading to oscillations in conductance and TMR [118]. Spin-polarized resonant tunneling allows to develop functional spin-electronic devices based on coherent transport. One principal application is for example as a resonant-tunneling diode (diode with a resonant-tunneling structure in which electrons can tunnel through some resonant states at certain energy levels). Early studies explored the simplest way to produce resonant tunneling by growing a thin nonmagnetic layer (NM) between a ferromagnetic electrode and the barrier in standard SMTJ structures $F_1/I/NM/F_2$ (see *Figure 5.1* (b)) [119, 120, 121]. Different nonmagnetic elements like Cu and Cr were used. The current/voltage characteristic often exhibits negative differential resistance regions. Resonant tunneling in double MTJs (DMTJs) $F_1/I/F_2/I/F_3$ (represented in *Figure 5.1* (c)) may have advantages in comparison with the standard MTJs, mainly due to their enhanced tunneling magnetoresistance (TMR) [21, 22, 23, 24, 25] and resonant spin-torque effects [26, 27, 28]. Apart from this, TMR in DMTJs varies only weakly at low bias voltages[122], which is crucial for applications. Last but not least, the current driven magnetization reversal occurs at extremely low current densities in DMTJs [28].

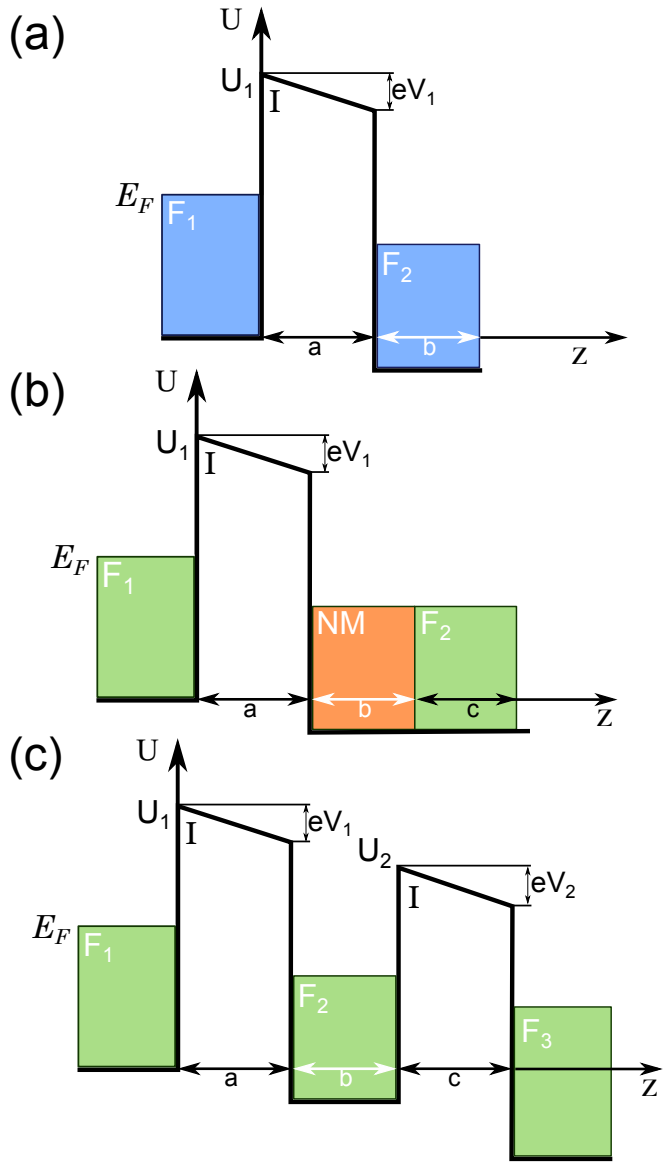

Figure 5.1: Schematic potential energy diagram for (a) single magnetic tunnel junction, (b) single magnetic tunnel junction with a thin nonmagnetic layer between insulator and electrode and (c) double magnetic tunnel junction with ferromagnetic configuration. The z axis is perpendicular to the junction and U is the barrier height.

5. Electron transport in double magnetic tunnel junctions with dielectric breakdown

Basically a DMTJ is different from a SMTJ in that there is a ferromagnetic electrode within the barrier. This electrode (F_2 in *Figure 5.1* (c)) could be a continuous or a discontinuous ferromagnetic layer. Recently, Nozaki et *al.* [123] have reported on resonant tunneling effects in DMTJs with Fe nanoislands incorporated into the thick MgO barrier. This results have been interpreted as due to the combined influence of QWS and Coulomb blockade (CB) effects [124]. In DMTJs the QWS can strongly influence electron transport only if the central F_2 layer has submonolayer roughness and its thickness exceeds 1nm minimizing CB effects [125, 126]. According to the quantum model, there is a nonvanishing (larger than zero) probability for an electron on one side of the barrier to reach the other side. Thus in quantum mechanics, the tunnel junctions are considered to be resistive materials, where the conductance has an exponential dependence on the barrier thickness. But from a purely classical electrodynamics model, one electron may not cross a tunneling barrier. Then, two conductors separated by an insulating barrier is both a resistive and a capacitive device. Due to the discreteness of electrical charge, the current through the tunnel junction is a series of events in which exactly one electron tunnels through the barrier. Where the capacitance of the tunnel junction is small, the CB contribution to the transport becomes stronger (U = e/C). From the other side, the F_2 layer should also be thin enough so that the energy separation of QWS substantially exceeds the thermal energy. These conditions are hardly fulfilled in the macroscopic DMTJs [48, 126], where resonant tunneling through QWSs was not observed mainly due to the absence of atomically flat surfaces over the entire junction lateral dimensions.

Previously, oscillations in resistance as a function of bias in the AP state (where magnetization of the middle electrode is antiparallel to the magnetization of the outer electrodes) have been studied in DMTJs with continuous middle electrode by Zeng et *al.* [127]. The DMTJs with Al-O barrier of amorphous structure and without pinhole formation show anomalous oscillations respect to bias, in principle, more complex than simple elastic resonant tunneling. Probably, the contribution

by magnons or spin waves due to the spin accumulation in the middle layer could affects the tunneling conductance in the AP state.

One of the advantage of the devices based on DMTJs, not yet mentioned, could be the possible low frequency noise reduction respect to SMTJs. Basically, in the first approximation, for large spin flip scattering we could consider a DMTJ as two SMTJ connected in series. For arrays of SMTJs connected in series it is expected an improvement of the detectivity (D) of the sensors [128], which is defined by $D = \frac{S_V}{\Delta V/\Delta H}$ (S_V is the power spectral density and $\Delta V/\Delta H$ is the sensor sensitivity). But in fact, the tunneling transport in DMTJs is more complex than only assuming two junctions connected in series, for example, due to the contribution of the resonant tunneling effect [129], etc. Although this Chapter focuses only on tunneling transport as a function of bias, to study in detail low frequency noise in DMTJs is needed to clarify these supposition.

The main motivation of this Chapter is the study of resonant tunneling due to the middle free layer in DMTJs. We will investigate the electronic transport in epitaxial macroscopic Fe (100)/ MgO/ Fe/ MgO/ Fe double magnetic tunnel junctions with "soft"dielectric breakdown ("hot spot"), due to reduction of the effective height of the barrier. The specificity of these junctions is nitrogen doping of the MgO barrier, which provides a "soft"dielectric breakdown at biases about 0.5 V. In the junction with "hot spot", the tunneling current is concentrated where the effective barrier is reduced, reaching high current densities in these regions. We observe quasi-periodic changes in the resistance and in the TMR as a function of bias voltage which point out the formation of quantum well states in the middle Fe continuous free layer. A simple model of tunneling through formation of single or multiple "hot spot"in the DMTJ has been proposed by Dugaev and Barnas [70] to explain qualitatively this effect. The middle electrode is thick enough (5 nm) to neglect the CB contribution in comparison with the resonant QWS effect.

Based on the previous reported calculations by Vedyayev et *al.* [26], the spin-transfer torque (STT) is affected by resonant tunneling due to the middle free

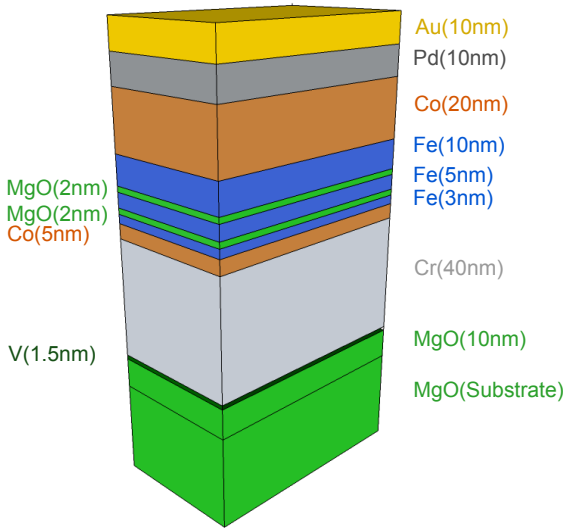

Figure 5.2: Schematic representation of the stack of the DMTJs.

layer in DMTJs. The STT is the transfer of angular momentum from spin current to each electrode. In order to destabilize the magnetic moment of the free electrode and enhance the STT effect it is very common to apply in plane external magnetic field few degrees of the easy (100) axis (**EA**) or hard (110) axis (**HA**) (see Ref. [130]). For this reason, we have measured the tunneling transport for three different in plane orientations (**EA**, **HA** and in intermediate axis (**IA**)) to verify possible presence of local STT effects near of "hot spot"and compare these results with theoretical predictions [26].

5.2 Samples description

5.2.1 Description of the growth process of the samples

Similar by the previous Chapters, the magnetic tunnel junctions under study were grown in Institute Jean Lamour, CNRS-Nancy University, within a bilateral collaboration project between Spain-France. The full stack of the measured

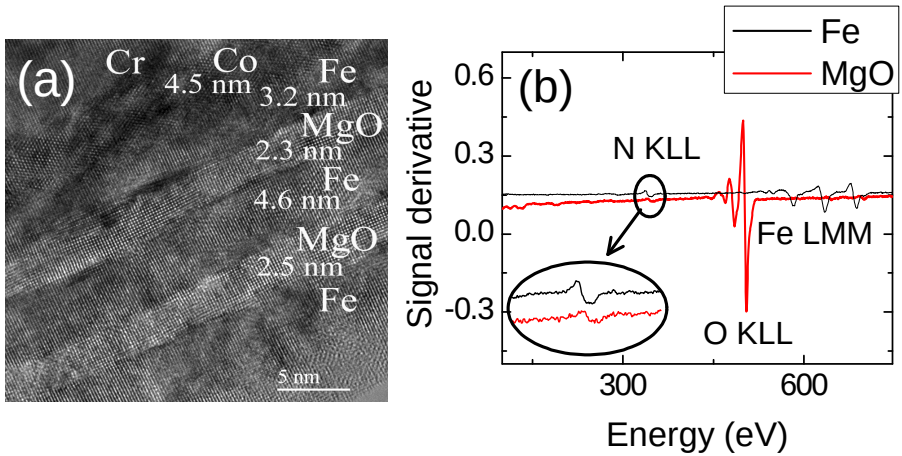

Figure 5.3: (a) Cross-sectional TEM image of the DMTJ. (b) Auger experiment which shows presence of nitrogen doping in the Fe and MgO layers of our DMTJs.

epitaxial samples is the following: MgO(100)// MgO (10 nm)/V (1.5 nm)/ Cr (40 nm)/ Co (5 nm)/ Fe (3 nm)/ MgO (8 ML)/ Fe (5 nm)/ MgO (8 ML)/ Fe (10 nm)/Co (20 nm)/ Pd (10 nm)/ Au (10 nm) (see sketch in *Figure 5.2*). The DMTJ stacks were grown by molecular-beam epitaxy with the base pressure of 5×10^{-10} Torr in the presence of atomic nitrogen. The samples have been grown on (100) MgO substrates, previously annealed at 600°C for 20 min. To prevent the diffusion of the carbon impurities from the substrate, a 10-nm-thick MgO underlayer was grown at 450°C. The 3-nm-thick Fe bottom electrode was grown at room temperature and annealed to 450°C for 20 min in order to obtain an atomically flat surface. The thickness of the bottom Fe electrode is well above from the critical thickness of the plastic relaxation. The MgO barrier and the Fe layers were grown at room temperature. The Fe was annealed to 450°C for 20 min in order to improve its surface quality. On top of the bottom electrode, 8 ML of MgO barrier were deposited at room temperature. The second ferromagnetic electrode, that correspond to the middle layer, was epitaxially grown over the MgO in the same conditions of the bottom electrode. And the steps described above to achieve

the next barrier with a corresponding electrode on top were repeated again. As we have mentioned in previous Chapters, the dislocations propagate through the MTJ stack. We would like to remark that the annealing process is crucial in this kind of samples, because if you do not have good quality in the interface, it is very probable that pinholes form in the barrier. The high resolution cross-sectional TEM images (*Figure 5.3* (a)) generally corroborate the good structural quality and homogeneity of our DMTJs. More details of standard double barrier samples growth may be found in Refs. [48, 131]. The specificity of the samples studied here is a nitrogen doping of all the layers achieved during the growth process, with a nitrogen concentration roughly estimated to be less than 2%. Although further studies are needed to determine the concentration of nitrogen inside the MgO barrier, it has been recently reported by Parkin et *al.* [132], that MgO barrier in MTJs may be doped up to 2.5% of nitrogen without changes in the crystalline structures. In our samples, the structural analysis by RHEED, Auger spectroscopy and magnetometry demonstrate that, despite the nitrogen doping (as evidenced from Auger, see *Figure 5.3* (b)), the structural and magnetic properties are not essentially affected. The RHEED patterns of Fe and MgO (not presented here) are identical to those of nitrogen-free samples seen in Ref. [131]. What is important for the studies presented in this Chapter is that, from electrical transport point of view, the barrier doping by nitrogen is responsible for local "soft"dielectric breakdown [133], with reduced breakdown voltage. This breakdown may be expected to keep the barrier and central Fe electrode compositions nearly unchanged. After the MBE growth of the multilayer stack, the MTJ structures were patterned to $10\times10\ \mu m^2$ by UV lithography and Ar-ion etching, step-by-step controlled in situ by Auger spectroscopy.

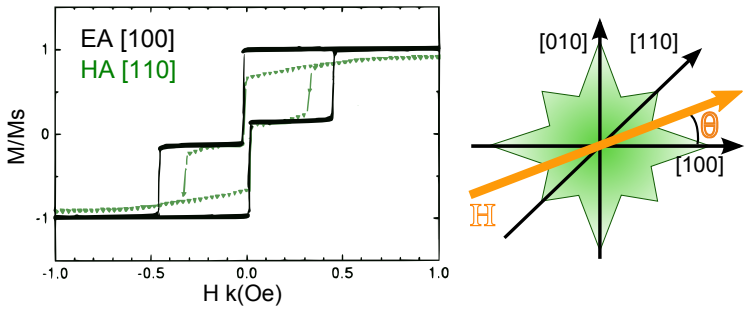

Figure 5.4: Normalized magnetization for MgO(100)/Fe along the EA [100] and HA [110] (Adapted from Ref.[84]), with the corresponding sketch of the fourfold anisotropy.

5.3 Magnetic Characterization

Once we have described the structural composition of the samples that we have measured in this Chapter, it is important to characterize MTJs from a magnetic point of view. As we have mentioned in the Introduction, it is more interesting to investigate electron transport in these samples with a magnetic field within few degrees deviated from the magnetic axis (**IA** orientation). Therefore, firstly, in order to know the coercive fields of the three ferromagnetic electrodes we have studied the magnetization as a function of the field to the extreme axes (**EA** and **HA**). The magnetic anisotropy of epitaxial SMTJs with a bcc structure is determined by the crystallographic structure, as is shown in *Figure 5.4*, previously reported by Popova et *al.* [84]. The **EA** has a better defined transition and higher value than in the **HA**, because in this direction the magnetic disorder is lower. The domains tend to align along the **EA** and the rotation of the magnetization is a consequence of the nucleation and propagation of domains wall. Then, when the magnetic field is applied along the **HA** orientation, the rotation of the magnetization is a continuous fluctuation between **EA** and **HA**, that reduce the effective magnetization [134]. Consequently, due to the crystalline anisotropy in the magnetic layers, it

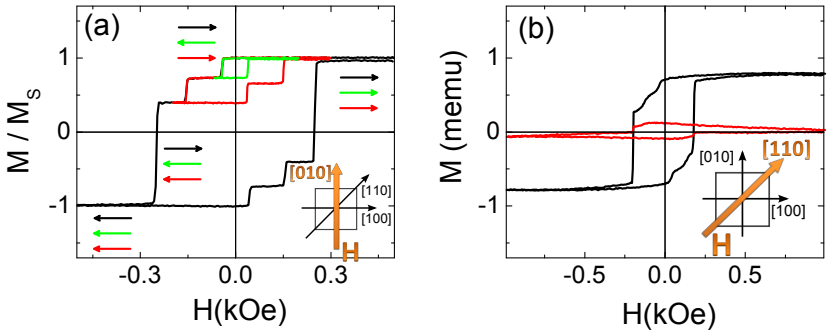

Figure 5.5: Magnetization curve for unpatterned DMTJ in EA and HA, respectively. Arrows indicate magnetization configurations of top (black), middle (green) and bottom (red) layers.

is possible to reduce the creation of magnetic inhomogeneities in the electrodes, which have a strong influence on the tunneling transport properties of the MTJ devices [84, 135]. Schematic representation of the four-fold magnetization as a function of the magnetic field along different in plane orientations is represented in *Figure 5.4* [134].

The magnetic properties of the our samples are shown in *Figure 5.5* (a),(b) at room temperature with magnetic field along the **EA** and **HA**, respectively. In the **EA**, one observes well defined transitions of the three distinct Fe layers. This is an indirect indication of epitaxy and conservation of magnetic properties (fourfold anisotropy) for nitrogen doped DMTJs. Firstly, let us focus on the magnetization behavior along the **EA**. From a magnetic point of view, the Co is harder than Fe and is used to increase the coercivity of the ferromagnetic electrode. Then, the bottom electrode (marked with a red arrow in *Figure 5.5(a)*) is softer than the top electrode (marked with a black arrow in *Figure 5.5(a)*), because, the next cobalt layer is thinner. So as the middle ferromagnetic electrode (marked with a green arrow in *Figure 5.5(a)*) is magnetically free. For a large magnetic field, the magnetization of the three electrodes are aligned in the same direction and

this state is defined as a parallel state (P). Changing the sign of the field, the first electrode which changes its magnetization direction is the middle electrode following the field direction. In this range of fields, we have an antiparallel state (AP) which provides the highest resistance at zero bias, in which the magnetization of the outer electrodes is opposite to the central one. If we continue increasing the magnetic field, the magnetization of the bottom electrode reverses and now, the bottom electrode and the middle electrode are parallel, but antiparallel with respect to the top electrode (AP2 state).

The magnetization curve in the **HA** shows a different dependence with the magnetic field (*Figure 5.5(b)*). As we have mentioned, the magnetization in the **HA** the transition between different states is less abrupt and higher fields are needed to saturate the different electrodes. Similar result have been previously reported by Nozaki et *al.*[23] in DMTJs.

5.4 Tunneling Transport measurements

5.4.1 Dielectric breakdown of the DMTJs

Now, we will study in detail the tunneling transport in DMTJs doped with nitrogen. Along the **EA**, the tunnel magnetoresistance has been measured at room temperature and the typical value before the dielectric breakdown is close to 30% at zero DC bias (see *Figure 5.6(a)*). As we have seen both in TEM images and magnetization measurements, the DMTJs seem to have a good structural quality, but the low value of the TMR gives us an indication that the tunneling conductance is not as good as expected. Possibly, the nitrogen weakens the barrier even before reaching their dielectric breakdown. After application of the bias exceeding roughly 500 mV, the TMR values are reduced abruptly down to about 4% (compare *Figures 5.6(a) and (b)*). The TMR reduction through the dielectric breakdown of the barrier can be due to several factors. One of them could be the

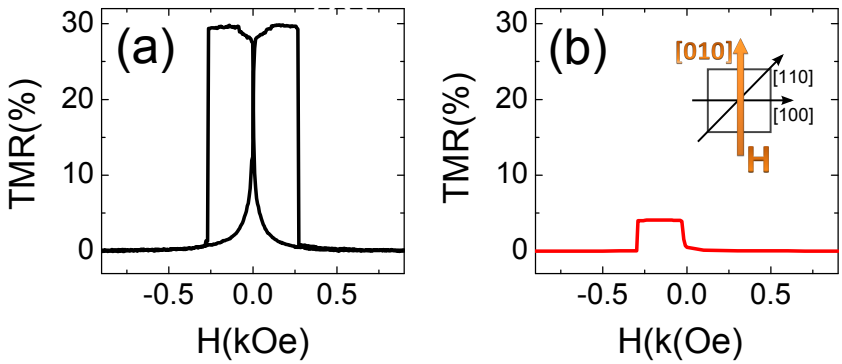

Figure 5.6: (a), (b) Typical zero bias TMR of the DMTJ without and with dielectric breakdown, respectively, measured along the **EA**.

poor growth of the barrier, and it would not even be necessary to apply voltages to break the barrier[136]. This is not our case (see *Figure 5.3* (a))). Another important factor which influences the dielectric breakdown is due to stress bias voltages, that can be achieved either by applying a high voltage or by applying a voltage for a long time [105, 137, 138, 139]. After applying a large enough voltage, the dielectric breakdown occurs in the barrier and is very likely to arise multiple pinholes, through which the current concentrates thus reducing the tunneling effect [139]. Upon breaking the barrier at room temperature, the atoms of the barrier suffer a thermal activation that make them move. Furthermore, if we add to this that we are applying current, under these conditions it is easy to assume that the pinhole will be moving and could also change its size. Therefore, when the pinholes become large enough, we will have a very large current density at these points, because there will be locally two metals in contact, and the tunnel effect will be lost [138].

However, we believe that this scenario is not taking place. It is evident that after bias exceeds about 500mV, the reduction of the effective barrier occurs (see *Figure 5.6*). We believe that in the "hot spot"formation the nitrogen has a cru-

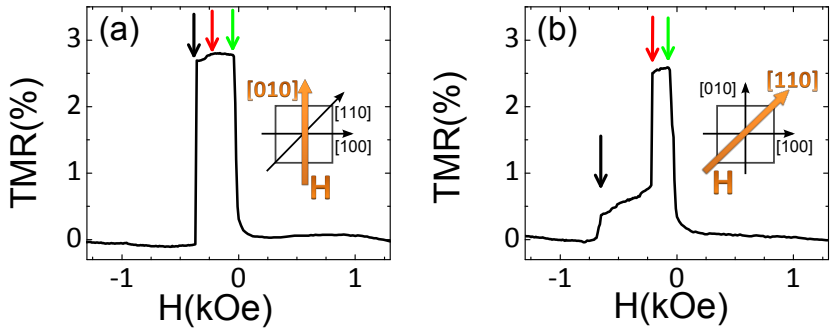

Figure 5.7: The figures show the TMR measured with a magnetic field applied along the (a) **EA** and the (b) **HA** directions. The vertical arrows remark the coercive fields of the different layers with the same colors criteria as in *Figure 5.5*.

cial role in the reorganization of the atoms of the barrier. Apart from the TMR reduction, two other observations indicate indirectly that this breakdown only decreases the effective MgO barrier height most probably by transforming locally nearly crystalline MgO regions near a "hot spot"into amorphous ones due to the influence of nitrogen [132]. Firstly, we can observe in the *Figure 5.7* that the coercive field of the central free Fe layer remains unchanged after breakdown ($H_c = 45$ Oe), while coercive fields of the upper and bottom electrodes increase substantially about 50%. These changes are most probably due to hardening of the Fe/Co interfaces by high current density close to the "hot spot". The second indication for the possible amorphization of the MgO barrier during the breakdown with intact middle electrode is our experimental observation of the signature of QWS in the electron transport in some of the broken DMTJs which we will discuss in the next Section.

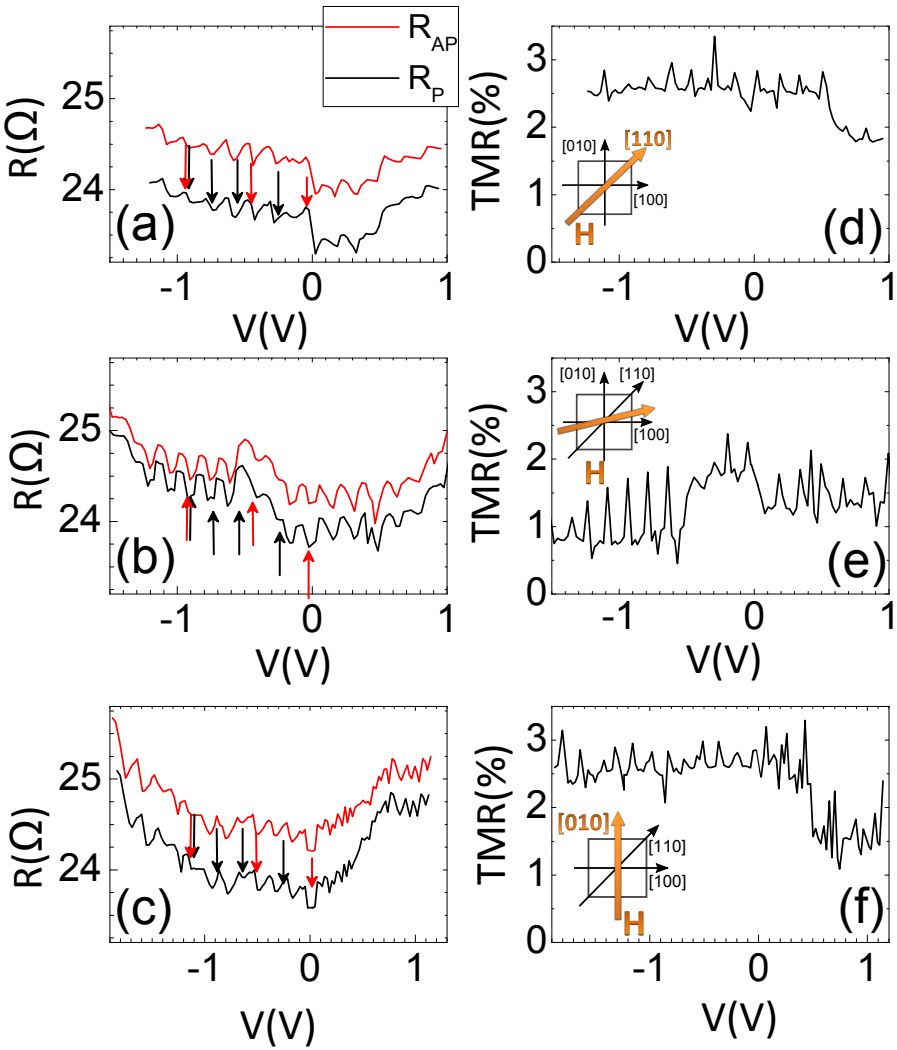

Figure 5.8: Resistance vs. bias measured for P (black line) and AP (red line) states with magnetic field applied along the **HA** (part a), **IA** (part b) and **EA** (part c) directions. Here we assign as antiparallel state the one just after the inversion of the central Fe free layer, marked by a green arrow in *Figure 5.5*. The red and black arrows indicate the theoretical predictions by Wang *et al.* [124] for the resonant tunneling in the parallel state with QWS above (red arrows) and below (black arrows) the Fermi level. Parts (c,e,f) show TMR vs. bias for magnetic field applied along the **HA**, **IA** and **EA** directions, respectively.

5.4.2 Tunneling transport in "soft"dielectric breakdown in DMTJs

We have carried out a detailed study of the room temperature resistance as a function of magnetic field with three different field orientations: **EA**, **HA** and in intermediate axis (**IA**) situated approximately at 10 degrees from the **EA**. Here, we present typical results obtained at bias voltages up to 1.5V and with steps of 25mV for those broken DMTJs which showed reproducible signatures of the changes in the resistance with bias (*Figure 5.8*). In the first approximation, if we do not take into account the oscillations in resistance, we could see in *Figure 5.8* that the resistance has a nearly linear dependence on voltage. Previously in the unbroken MTJs, a parabolic behavior was observed as discussed in previous Chapters, due to the Δ bands. Almost ohmic behavior is an indirect proof that the effective height of the barrier is reduced. When the "hot spot"are sufficiently large or numerous, we will have a purely resistive material, because we will have in contact three ferromagnetic electrodes and, consequently, the TMR will be lost. However, in this range of voltages, we do not reach the above discussed situation, since as is shown in the *Figure 5.8*, we have different resistance values in both states (P and AP).

Figure 5.8 shows the typical bias dependence of the resistance (R) for P and AP states with a magnetic field along the three different orientations. One observes an oscillatory behavior of R and TMR with a period close to 150 mV in both P and AP states. It is important to remark that these oscillations, more clearly resolved for negative bias when the current flows from the top to the bottom electrodes (*Figure 5.8* (a),(b) and (c)), have a period that is in reasonable agreement with the predictions reported by Wang et *al.* [124]. In *Figure 5.8* (a),(b) and (c) the majority spin QWS energies calculated within about 1V above (in red) and below (in black) the Fermi energy[124] are marked with arrows. This theoretical work [124] tries to understand and support the experimental results reported by Nozaki

et *al.* [123] obtained for DMTJs with a discontinuous middle ferromagnetic electrode. They have only investigated oscillations in the P state due to majority-spin Δ bands influenced by Coulomb blockade. Our scenario, although similar because the tunnel conductance has preferred areas for tunneling, has some slight differences since the middle electrode is continuous. Firstly, the effect of CB is neglected due to the the middle electrode thickness (5 nm). And secondly, because there are oscillations in both states (P and AP). As we have a "soft"dielectric breakdown, the tunneling conductance is affected by the hot spots (due to reduction of the effective height of the barrier) and, consequently, the MgO filtering of the Δ majority and minority spin bands will be different than reported by Ref. [9] for 8 ML of MgO thickness.

The zero bias TMR varies substantially along the three mentioned directions. Though the absolute values of TMR measured with the field along the **IA** are reduced in comparison with those for the fields along the **EA** and **HA**, the relative changes of the TMR with bias are substantially enhanced (see *Figure 5.8* (d),(e) and (f)). In order to understand this effect we remind that the measurements of tunnel resistance with the field along the **IA** are usually observed [140] to be most sensitive to small variations in the angle between magnetizations of the fixed and free layers in comparison with the **EA** and **HA** configurations [6]. We suggest here that the strongest relative changes in TMR(V) for the **IA** configuration could be a consequence of local spin-torque effects affected by resonant tunneling due to the middle free layer, which are predicted to be enhanced with intermediate alignment of the ferromagnetic layers [27]. *Figure 5.9* (a),(b) and (c) represent 3D plots of TMR vs magnetic field and bias with magnetic fields applied along the **HA**, **IA** and **EA**, respectively. The dependence of TMR on bias is observed to be more asymmetric with the field along the **IA** (*Figure 5.9* (a),(b)), which is in agrement with the possible influence of local spin torque effects in the breakdown regions.

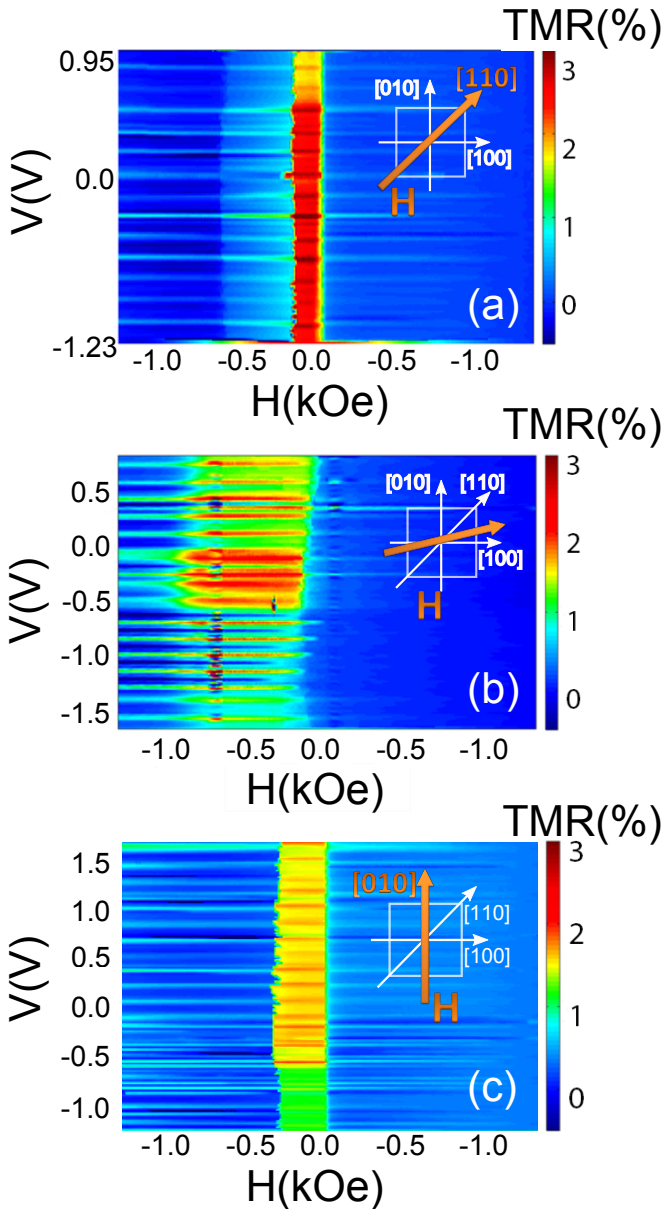

Figure 5.9: 3-D-plot with magnetic field along x, bias voltage along y and TMR along z directions. Part (a) corresponds to magnetic field along the **HA**, part (b) along **IA** and part (c) in **EA** orientation.

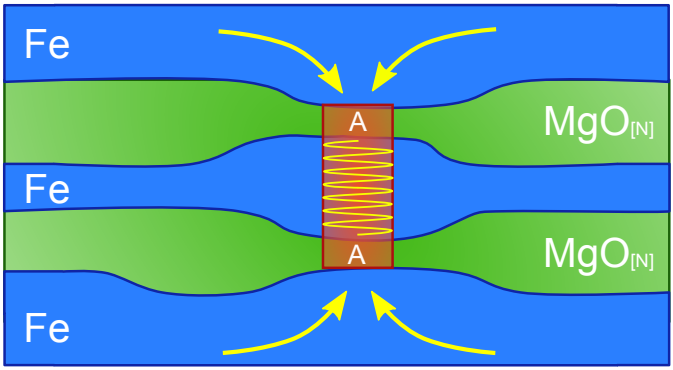

Figure 5.10: Model of local amorphization of the DMTJs. The red area shows the region where the current is concentrated due to the reduction of the effective height of the barrier.

Let us now discuss physical mechanisms which could be behind the main experimental findings. Before the dielectric breakdown occurs, the current is roughly uniform across the junction area and weak interface disorder might introduce decoherence, suppressing the effects due to QWS. The "soft" dielectric breakdown of the nitrogen doped MgO barrier may create defects and local amorphization which locally reduce the MgO barriers leading to creation of "hot spot" which connect the macroscopic Fe and Fe/Co leads with the central Fe layer (see *Figure 5.10*). With "hot spot" of sufficiently small lateral dimensions, electrons tunneling to the central layer can sample well defined structure of QWS due to lack of decoherence. The remaining part of the macroscopic DMTJ provides then some averaged featureless background signal. The feasibility of the above scenario is qualitatively supported by the good correspondence of the observed periodic variations in R vs. bias and the theory taking into account QWS formed within 4.6 nm thick central Fe electrode [124] (see *Figure 5.8*). The differences with the above theory, such as variation of the resistance both in parallel and antiparallel states, could be due to deviation from MgO crystallinity, i.e. the local amorphization of the MgO barrier.

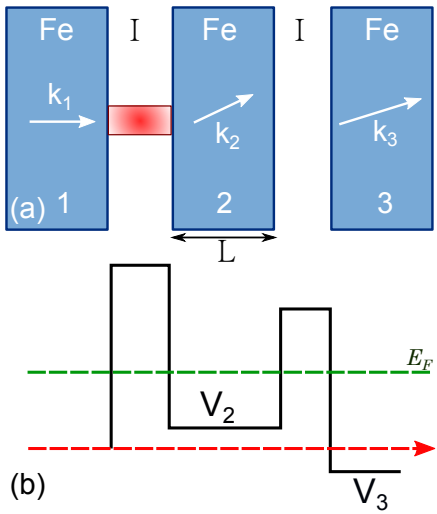

Figure 5.11: (a) Schematic presentation of the model with a single spot and (b) the corresponding energy profile.

5.5 Model of the DMTJ with "hot spot"

This paragraph discusses a model of electron tunneling in double magnetic tunnel junctions with "hot spot" which was developed by Dugaev and Barnas [70]. In order to describe the observed features, we consider a DMTJ (*Figure 5.11*) with barriers including a number of "hot spot". The average conductance of the structure is [141]

$$\sigma \simeq \sum_i \int p_i(\Gamma_i)\, \sigma_i(\Gamma_i)\, d\Gamma_i, \tag{5.1}$$

where $\sigma_i(\Gamma_i)$ is the conductance due to a single i-th spot, $p_i(\Gamma_i)$ is the probability of realization of a certain configuration of the i-th spot, and Γ_i is a set of parameters characterizing this configuration.

Let us assume that a particular "hot spot" is characterized by its lateral dimension a. The current through the spot can be then calculated as

5. Electron transport in double magnetic tunnel junctions with dielectric breakdown

$$I = \frac{e\hbar}{m}\int_{\varepsilon_F - eV}^{\varepsilon_F} d\varepsilon \int \frac{d^3\mathbf{k}_1}{(2\pi)^3}\,\delta\left(\frac{\hbar^2(k_1^2 + k_{1l}^2)}{2m} - \varepsilon\right) \times \sum_{k_2 < k_{2m}} w_{\mathbf{k_1 k_2}}(a)\, T_{k_1 k_2} T_{k_2 k_3} k_3 \tag{5.2}$$

where k_1, k_{1l} are the normal and lateral wavevector components of the incoming wave (layer 1), k_2 and k_3 are the normal components of the wavevector in layers 2 and 3, respectively. Here we assumed that the in-plane component of k is conserved for tunneling from layer 2 to 3, whereas for tunneling through the spot there is no conservation of the in-plane component, and the scattering can be described by an angle distribution function $w_{\mathbf{k_1 k_2}}(a)$. In our calculations we use the approximation $w_{\mathbf{k_1 k_2}}(a) \simeq a^2 e^{-ak_{2l}}$, which means that scattering to the state with a large in-plane component k_{2l} is effectively suppressed. Equation 5.2 includes transmission probabilities $T_{k_1 k_2}$ and $T_{k_2 k_3}$ for tunneling from the layer 1 to 2 and from 2 to 3, respectively. The sum over k_2 runs over discrete values satisfying the quantization condition $k_2 L = n\pi$. It should be emphasized that this condition is related only to the thickness L of the layer 2 and is the same for any other "hot spot".

Calculating the integral over k_{1l} we find

$$I = \frac{ea^2}{\hbar}\int_{\varepsilon_F - eV}^{\varepsilon_F} d\varepsilon \int_0^{k_{1m}} dk_1 \sum_{k_2 < k_{2m}} e^{-ak_{2l}} T_{k_1 k_2} T_{k_2 k_3} k_3. \tag{5.3}$$

The conductance I/V as a function of bias V for a single spot is presented in *Figure 5.12(a)* for different values of a. We assume that $L = 4.6$ nm, the barrier width is $L_B = 2.4$ nm, $\varepsilon_F = 0.9$ eV, and the barrier height is $U_B = \varepsilon_F + 3.8$ eV. As we see, the oscillation peaks related to the level quantization in the layer 2 are more pronounced for wide spots, and they are effectively damped for small a. This is because the small spot enables tunneling with nonconserved in-plane component of the wave vector, which weakens the quantization selection of transmitted electrons.

Taking into account tunneling from many different spots, we obtain qualitatively the same picture corresponding to a mean value of a, and proportional to

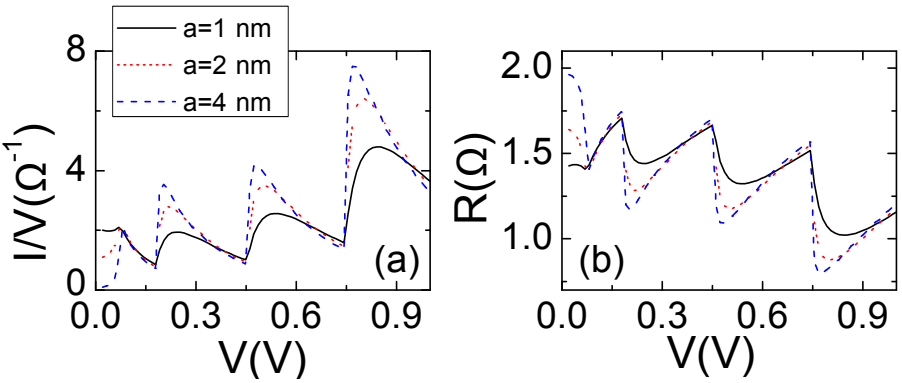

Figure 5.12: (a) Calculated conductance (I/V) for a DMTJ with a single spot in P state for different spot dimensions. (b) Resistance vs. bias for a DMTJ with multiple spots in the P state for different average spot dimensions.

the number of spots. The total conductance of the structure includes a constant non-oscillating part, σ_0, related to the tunneling without spots. In *Figure 5.12(b)* we present the resistance calculated as $R = (\sigma_0 + N_i\sigma_i(\overline{a}))^{-1}$, where N_i is the number of spots and $\overline{a}$ is the mean value of a. We note that the variation of barrier heights at the spot does not affect the position of the peaks and does not change the shape of the peaks, changing only the amplitude. Thus, averaging over randomly distributed a and barrier heights U_B gives a similar picture as for a single spot with some mean values of a and U_B.

The applicability of the above model requires a number of conditions. Although the location of the oscillation peaks does not depend on the spot dimension (a), the "hot spot" dimension should not exceed the average dimensions over which the central electrode is atomically flat. Also, as we see from *Figure 5.12(a),(b)*, decreasing the parameter a makes the oscillations less visible (damped). Therefore we expect the "hot spot" to be roughly of nm lateral size. Secondly, the positions of band edges is important for the location of the peaks. If within this model one reverses the magnetic moments in one or two layers (AP alignment), the resistance becomes very large because the minority Δ_1 band will be displaced well

above the Fermi energy. However realistically speaking the "hot spot"region of the MgO barrier may be not fully epitaxial either due to structural defects and/or nitrogen doping. This can strongly reduce the spin filtering of the Δ_1 band in the AP alignment, substantially suppressing the TMR in real DMTJs with "hot spot".

5.6 Conclusions

In summary, we have presented evidence for local resonant tunneling through the quantum well states in the middle continuous free layer of double magnetic tunnel junctions doped with nitrogen. The oscillations have been observed at room temperature in both magnetic configurations (P and AP state) and for both bias polarizations. Owing to specific features of the breakdown junctions, we were able to observe QWS in continuous magnetic layers. To observe similar effects in the nitrogen-free DMTJ, the junction area should be smaller than the size of terraces of the Fe central layer.

Although we can not have control over where there is a weakening of the barrier, or how many "hot spot"can be formed, we would like to remark that according to the proposed theoretical model, the resonant period is not essentially dependent on these factors. These factors only affect the amplitude of the resonant quantum well states.

The nitrogen play an important role to provide the "soft"dielectric breakdown of the MgO barrier at low biases of about 400 mV. At a "hot spot", the current density is strongly enhanced and could locally induce the spin transfer torque [142]. The understanding of electron transport in magnetic tunnel junctions with defects and hot spots is of great importance from both fundamental and applied points of view. Indeed, recent reports link spin-torque oscillations with record low bandwidth to the presence of defects and hot spots inside the MgO barrier of MTJs [37, 143].

6

Low frequency noise in submicron sputtered FeCoB/MgO/FeCoB magnetic tunnel junctions

6. Low frequency noise in submicron sputtered FeCoB/MgO/FeCoB magnetic tunnel junctions

6.1 Brief introduction

Until now, we have investigated the tunneling phenomenon in fully epitaxial magnetic tunnel junctions based on the bcc Fe (001)/ MgO/ Fe structure. But as we have mentioned before, these epitaxial spintronic devices are difficult to implement in the industry, due to the high cost and longer time required for manufacturing respect to sputtered MTJs. From a fundamental point of view, however the epitaxial MTJs have been very useful to understand better the physical mechanisms responsible for the tunneling and noise processes. In the last Chapter of the Thesis, we would like to pay special attention to one of the most important magnetic tunneling structures currently used in Hard Disk Drive (HDD) read heads and magnetic random access memories (MRAM), which are based on CoFeB/MgO/CoFeB MTJs [144].

In the previous Chapters, we have seen that the Fe/ MgO/ Fe MTJs were characterized by 4-fold in plane magnetic anisotropy [84]. One of the ferromagnetic (FM) electrodes is soft (the top electrode in our samples) and its magnetization is aligned along the field direction. For the other electrode it is necessary to apply higher fields to rotate its magnetization due to the coupling with the adjacent layer (for example Co). But to use MTJs in the industry, we need to have the magnetization of one of the electrodes to be well fixed and the other one to be free, but able to change its direction in relatively small fields [19]. This type of pinned layer structure is obtained using the exchange bias phenomenon. This MTJ scheme is indispensable for the device applications, because of its robust exchange-bias and small stray magnetic field acting on the top free layer [144, 145]. The total composition of the hard electrode will consist of a synthetic ferrimagnetic (SyF) structure (antiferromagnetically coupling between FM/ NM/ FM trilayer) which is exchange-biased by the antiferromagnetic (AF) next layer, as we can see in *Figure 6.1*. The exchange-biased phenomenon owes its name to the fact that the hard magnetization behavior of an AF thin film causes a shift in the soft

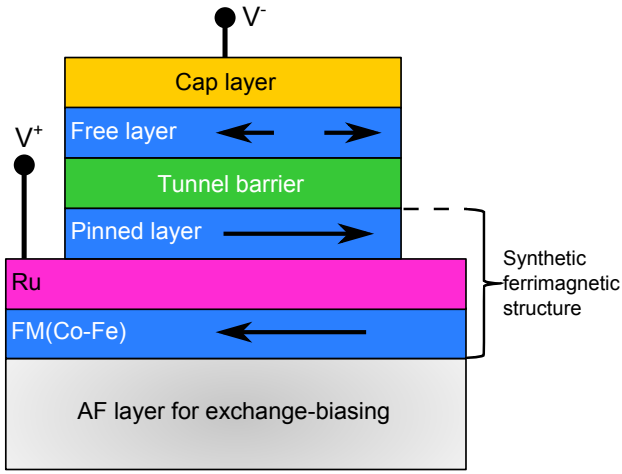

Figure 6.1: Schematic representation of the MTJ for applications. Pinned layer should be same with as Ru layer. Adapted from [144]

.

magnetization curve of a FM film [146], as is shown in *Figure 6.2*. Then, the hard electrode is well pinned due to the strong coupling with the adjacent layers.

Also, it is crucial for applications to have low R×A products (resistance by area), in order to obtain a good impedance matching in an electronic circuit for a high-speed operation of an electronic device, being possible to make spintronic devices with higher recording densities [145]. Then, while MTJs with sizes of tens of microns are optimal for magnetic field detectors [20], junctions below 250 nm are used for read heads applications [144, 145].

Apart from the low impedance due to lateral size and barrier thickness, one of the advantage of the low dimensional MTJs with similar geometry to the one represented in *Figure 6.1* is the transfer of angular momentum from spin current to each electrode. This phenomenon is known as spin-transfer torque (STT)[30, 37, 143, 147, 148, 149, 150]. The STT induced ferromagnetic resonance (FMR) is detected electrically by magnetoresistance [151]. For STT effect, we need one of

6. Low frequency noise in submicron sputtered FeCoB/MgO/FeCoB magnetic tunnel junctions

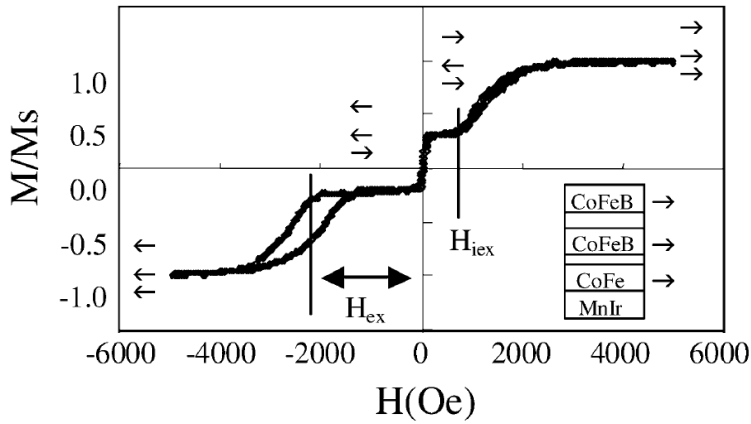

Figure 6.2: Hysteresis loops of a MTJ with a hard layer coupled using a exchange-biased phenomenon. The arrows indicate the direction of the magnetization of the ferromagnetic layers. Adapted from [152].

the magnetic layer to act as a spin-polarizer of current. In our configuration, it will be the bottom electrode because it is well pinned by the exchange-bias. The spin-polarized current crosses the barrier and transfers angular momentum to the free magnetic top layer. For nanopillars, critical current densities for this magnetic dynamic excitations are close to 10^7 A/cm^2. For this reason, in order to reach these current densities it is important to reduce the area of the MTJs (typically below <250 nm of the lateral dimensions). Moreover, reducing the barrier dimensions will decrease the contribution of the Oersted field produced by the flowing current.

This types of junctions are very interesting for microwave applications, too. As we have mentioned above, the STT has a strong influence on the free layer. According to the Landau-Lifshitz-Gilbert -Slonczewski equation, we could induce a steady precession in this electrode at FMR frequency. This situation occurs when the damping term cancels out the STT term. Now, the steady precession of the free electrode creates an ac current at microwave frequency [37, 143] detected by other sensors.

Previous studies of low frequency noise (magnetic, nonmagnetic and electronic) and random telegraph noise (RTN) focus on MTJs above micron size with Al_2O_3 [63, 65, 153] and MgO [11, 20, 69, 97, 154, 155, 156] barriers. Electron transport and low frequency magnetic noise remains poorly understood in submicron MTJs of some hundreds of nanometers, where single magnetic inhomogeneities (MI) [157] and domain walls (DW) play an important role in magnetization reversal.

In this Chapter, we present a detailed study at room temperature of tunneling magnetoresistance and low frequency noise in elliptic submicron CoFeB/ MgO/ CoFeB MTJs, with 1.1 nm thick MgO barriers and areas from 0.117 μm^2 to 0.0245μm^2. The low frequency noise is strongly affected by magnetic inhomogeneities (MIs) and domain walls (DWs), showing as a function of the area two qualitatively different, robust and reproducible behaviors. In the smaller area junctions we found an unexpected random telegraph noise (RTN1), deeply in the parallel state (P), possibly due to stray field induced MI/DWs in the hard layer. The second noise source (RTN2) is observed in the antiparallel state (AP) for the largest junctions. The strong asymmetry of RTN2 related to resistance steps with current, indicate the possible influence of the spin torque, acting on the MI/DWs in the soft layer at very low current densities below 5×10^5 A/cm^2.

6.2 Samples descriptions

Magnetic tunnel junction nanopillars studied in this Chapter were grown by the group of Prof. G. Reiss of the Department of Physics in Bielefeld University, Germany. The layer stack was deposited by magnetron sputtering in a Timaris PVD cluster tool from Singulus Technologies. Its MTJs structure is Ta (5)/ CuN (90)/ Ta (5)/ PtMn (20)/ $Co_{70}Fe_{30}$ (2.2)/ Ru (0.8)/ $Co_{60}Fe_{20}B_{20}$ (2)/ Mg (0.8) +1200s oxidation+Mg (0.3)/ $Co_{60}Fe_{20}B_{20}$ (2)/ Ta(10)/ CuN(30)/ Ru(7) (thicknesses in nm). A schematic representation of the sample stack is shown in *Figure 6.3*. The base pressure before deposition was under 7×10^{-9} Torr. The stack was

6. Low frequency noise in submicron sputtered FeCoB/MgO/FeCoB magnetic tunnel junctions

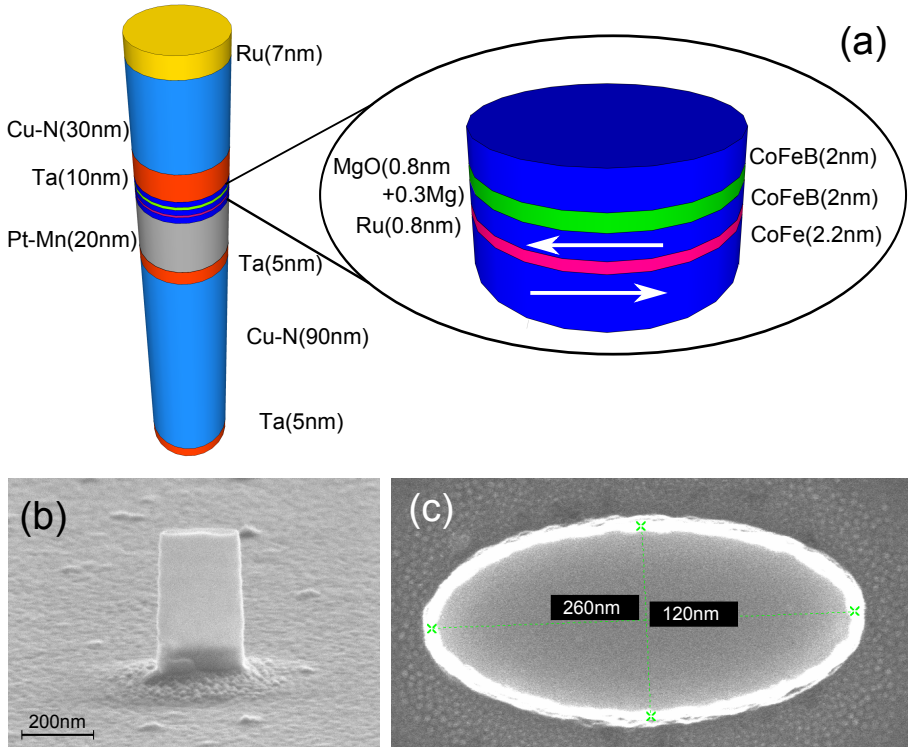

Figure 6.3: (a) Schematic representation of the stack of the elliptic MTJ. (b) Side view of a pillar after etching. The resist mask is still on top of the pillar. The layer stack is the dark area on the bottom of the pillar. (c) Top view of pillar after etching with resist mask still on top. We usually measure the size using this view.

annealed for 90 min. at 360°C [158] and cooled in a field of 1 Tesla to establish the exchange bias. In these type of samples, it is well known that to obtain large TMR values, the annealing temperature of the electrodes is between 350-500°C [158, 159, 160, 161]. Also, we have deposited on top of the upper electrode Ta as a capping layer, which has a strong influence on the TMR. This is probably because the cap layer can influence the crystallization of the upper CoFeB electrode [162, 163].

Using electron beam lithography and ion beam milling, the stack was patterned into elliptic nanopillars tunnel junctions with different sizes from 600 nm×

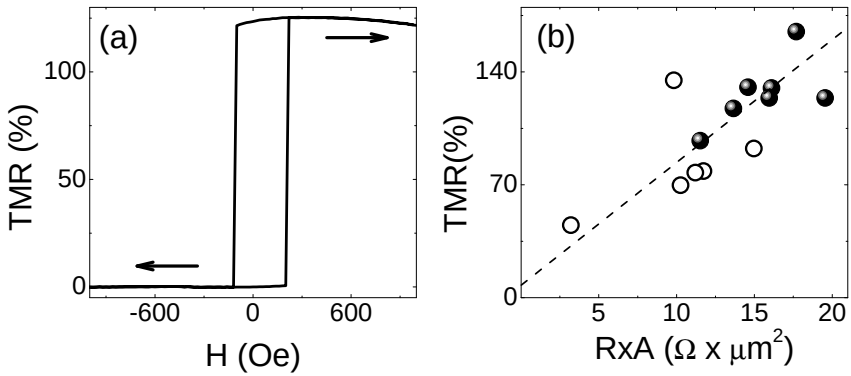

Figure 6.4: (a) Typical hysteretic TMR at room temperature and 0 V bias. (b) Normalized TMR vs. R×A. Dashed line is a guide for the eyes. Closed dots indicate MTJs for which noise measurements have been done.

250 nm to 260 nm× 120 nm. More details of the growth process can be found in Ref. [164]. The zero bias TMR was between 45% and 160% and R×A products between $3\Omega \times \mu m^2$ and $19\Omega \times \mu m^2$. The typical TMR curve at room temperature is illustrated in *Figure 6.4* (a), measured at 0 V DC bias, by using a low amplitude square current wave (with excitation below 5 mV). Out of 13 MTJs with TMR at room temperature exceeding 45% (*Figure 6.4* (b)), we present low frequency (1 Hz-10 kHz) noise measurements for 7 MTJs which reversibly stood biases between 100 mV and 400 mV. We measured the power spectral density $S_V(f)$ [11] and TMR along the easy (elliptic) axis. To compare the low frequency noise level in different MTJs, we have used the Hooge factor (α) from the low frequency noise phenomenological equation described several times in this thesis [13]. Strong deviations from the 1/f dependence are usually caused by RTN [60] and could provide a Lorentzian contribution on top of the 1/f noise background. The following arguments rule out an explanation of the RTN in terms of pinholes or "hot spot"in the samples measured in this Chapter:(i) large TMR values, (ii) robustness of the MTJs to bias and multiple field scans and (iii) low values of the Hooge factor in

the saturated P state ($\alpha = 3.1\times10^{-11}\ \mu m^2$), close to the one expected from the empirical summary [94].

Once we have measured the tunneling transport and rejected the MTJs with low TMR values in all the samples grown, we turn to details of the study of the low frequency noise.

6.3 "Field training" effect

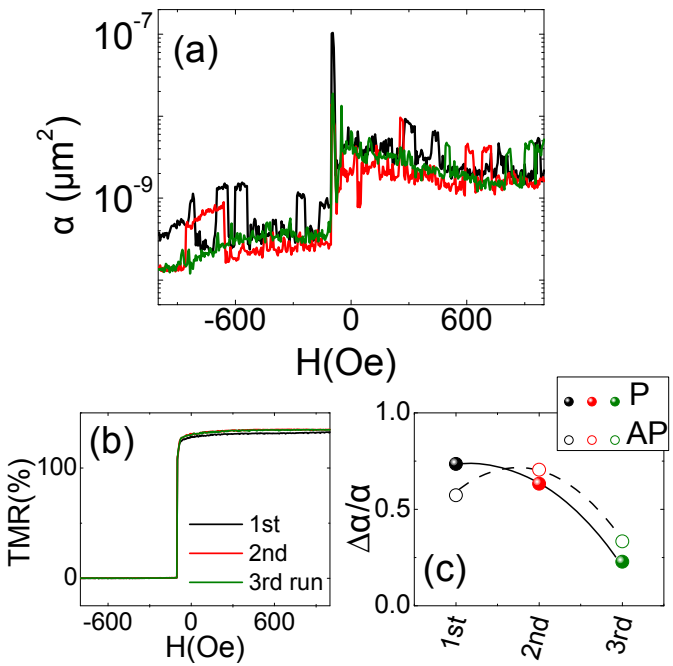

Figure 6.5: Variation of (a) normalized low frequency noise (Hooge factor) during the "field training" (rate of 1 Oe /min) applied to a MTJ with an area of 0.0245 μm^2 and (b) tunneling magnetoresistance. Part (c) plots the change of dispersion of the Hooge factor with training evaluated for the AP state for the field interval between 700 and 300 Oe.

Until now, the training effects have been studied mainly in exchange bias systems or other systems which involve formation of DWs. The magnetization of

this systems is strongly affected by the magnetic cycles [146]. We have observed that, typically, after three slow field sweeps between AP and P states (with rates of about 1 Oe/min) most of the samples showed a noticeable decrease of the dispersion of noise (*Figure 6.5*) both for parallel and antiparallel states. The *Figure 6.5* (a) shows the normalized 1/f noise (Hooge factor) determined for a bias of 200 mV in the AP state (J = 6.8×10^5 A/cm^2) and a frequency range between 200 and 1000 Hz for MTJs with small dimensions (A=0.0245 μm^2). The noise reduction is accompanied by a small TMR increase of about 1-2% (*Figure 6.5* (b)). These multiple slow field sweeps minimize fluctuations from metastable magnetic states and lead to two qualitatively distinct but remarkably reproducible (within each junction) types of the noise behavior depending on the junction area.

6.4 Influence of RTN type I on magnetic inhomogeneities in the smallest junctions

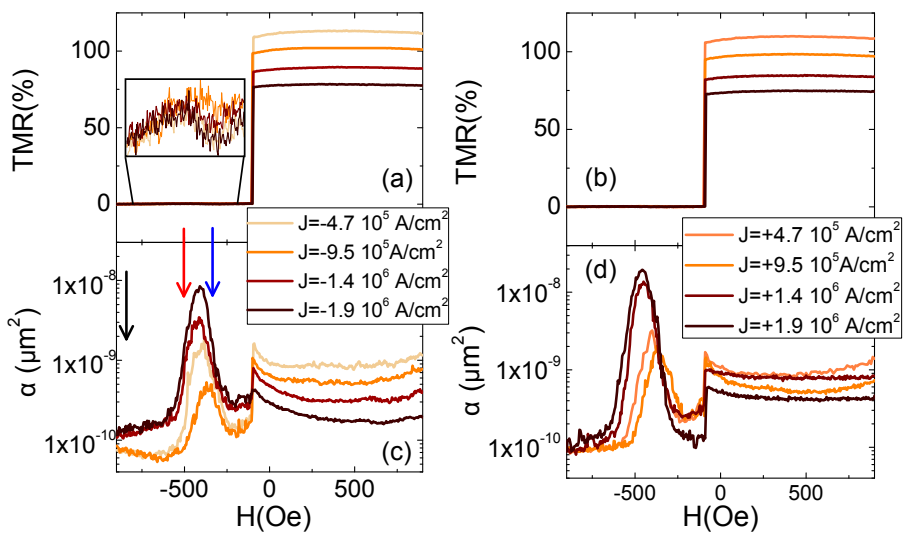

Figure 6.6: (a) and (b) TMR in MTJ of 0.0245 μ m^2 for negative and positive current, respectively. (c) and (d) Hooge factor for the same current densities of part (a) and (b), respectively.

6. Low frequency noise in submicron sputtered FeCoB/MgO/FeCoB magnetic tunnel junctions

After multiple slow field sweeps, most of the smallest junctions (0.0245 μm^2-0.0503 μm^2) reveal enhancement of the noise deeply in the P state for positive (the electrons are injected from the hard to the free electrode) and negative bias, as we can see in *Figure 6.6*. As it is expected, the TMR decreases with increasing current up to 400 mV [158], but if we look the details of the noise power as a function of the magnetic field for a fixed current, it appears that a strong increase of the low frequency noise in the P state (*Figure 6.6*), has a RTN origin (further RTN1), and is accompanied by a change in the resistance of less than 0.2%. Our estimations show that changes of RTN1 with bias polarity (*Figure 6.6*) could be partially due to the influence of the self-field. For positive bias the enhancement of the low frequency noise occurs at higher fields, probably because the magnetic moments are MIs better pinned.

To study in more detail the dependence of the low frequency noise as a function of magnetic field, we have measured temporal traces of resistance in these fields. *Figure 6.7* (a) shows two typical time series with the corresponding histograms of RTN1 for magnetic fields above and below the maximum of noise in P state (marked with arrows in *Figure 6.6* (c)). We can fit both histogram distributions of these two levels systems to two Lorentzian curves and use the area under these curves to account for the relative population of these levels. As long as the RTN is caused by magnetic fluctuations, the lifetimes ratio of these states could give us a rough estimation of the magnetic moment of the effective two level system. The Lorentzian contribution over the 1/f noise background due to RTN1 is also detected in the power spectral density (see *Figure 6.7* (b)). Then, to estimate the effective fluctuating magnetic moment (Δm) of the two level systems, we have measured the field and bias dependence of the ratio between inverse attempt transition rates [63, 65]:

$$\frac{\tau_1}{\tau_2} \sim exp(-2\Delta mH/k_BT) \tag{6.1}$$

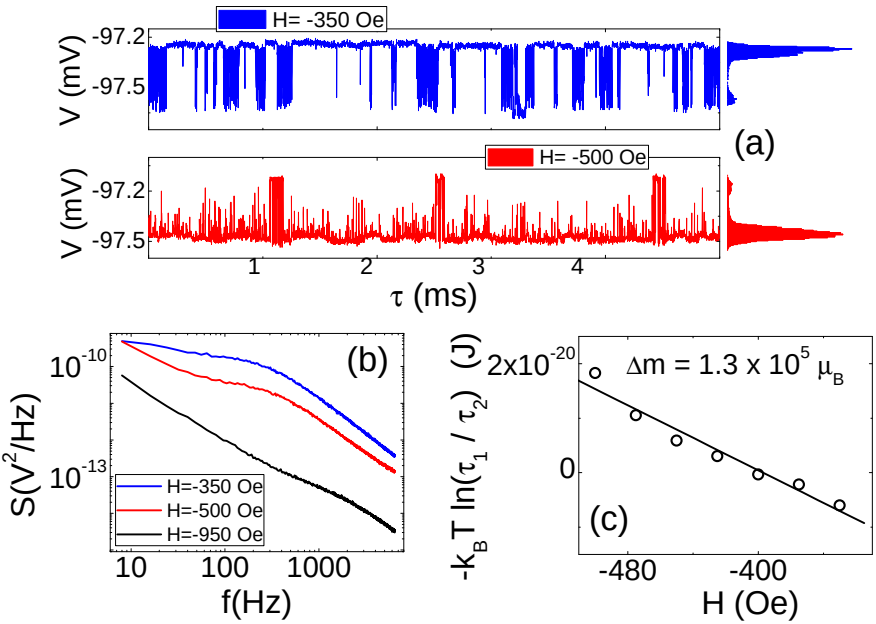

Figure 6.7: (a) Time series and corresponding histograms measured in two fields above and below the maximum in low frequency noise, marked with arrows in *Figure 6.6* (c) for J=-1.9×10^6 A/cm^2. (b) Power spectral densities of the corresponding time series. (c) Logarithm of the relation between inverse attempt transition rates as a function of magnetic field. The solid line is a mean square fit.

Here τ_1 and τ_2 are the average time spent in each of the two activated states. This relation considers the magnetization directions of fluctuating states being P-AP to the external field. A linear fit of $\ln(\tau_1/\tau_2)$ vs. H (*Figure 6.7* (c)) provides an estimation of the fluctuating moment of 1.5×10^5 μ_B and within 10% being independent of the bias polarity up to 400 mV. With these results, we estimate that DW/MI occupy about 10% of the soft electrode area (with CoFeB moment per atom of $1\mu_B$ [165]). To account for the maximum 0.2% variation of the resistance in the P state near RTN1, we suppose that the related DW/MI should be located in the hard layer outside the MTJ stack.

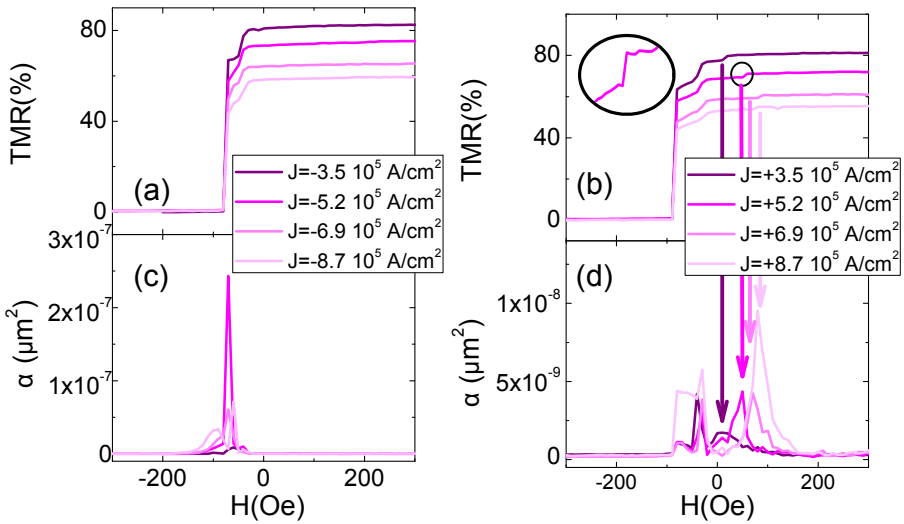

Figure 6.8: (a) and (b) shows the TMR for different current densities in elliptical nanopillars of A=0.0675 μm^2 for negative and positive current, respectively. (c) and (d) Hooge factor for the same current densities of part (a) and (b), respectively.

6.5 Influence of RTN type II on magnetic inhomogeneities in larger junctions

On the contrary, the largest submicron MTJs (A=0.0565 μm^2- 0.0675 μm^2) do not show noise anomalies in the P state, but reveal (*Figure 6.8*) a strong noise enhancement for positive bias, corresponding to the injection of electrons from the hard to the soft electrode, in the AP state above the AP-P transition, also originated from RTN (further RTN2). *Figure 6.8* shows the dependence of the TMR and Hooge parameter as a function of the external magnetic field. As it is expected, close to the transition between AP-P state, low frequency noise maxima appears related to magnetic fluctuations, which are proportional to $(dR/dH)^2$ [65]. Apart from this maximum, at positive bias at least 100 Oe above the AP-P transition strong enhancement in the Hooge parameter is observed. Now, (contrary to what was seen for RTN1) the enhancement in the low frequency noise is accompanied

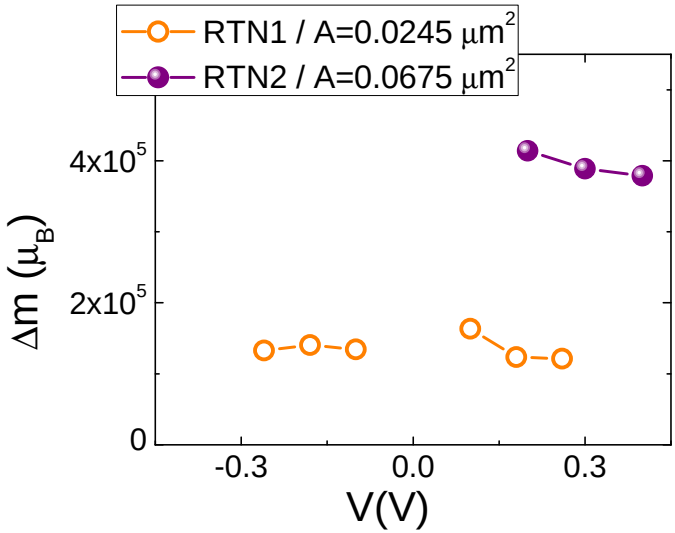

Figure 6.9: Comparative bias dependencies of estimated fluctuating moments obtained from RTN1 and RTN2.

by clear resistance steps (see *Figure 6.8* (b)). For this reason we think that the MI/DWs, which originate the RTN2, are probably located in the free electrode. Indeed, its estimated fluctuating area is about 7%, in rough agreement with 2% reduction of TMR in the AP state (*Figure 6.8*).

The absence of RTN2 for negative biases and the dependence on the position of the maximum respect to the magnetic field as a function of the current density indicates the possible influence of spin torque on DW/MI. If the positive bias favors the P alignment, it will destabilize the AP alignment, while the negative bias direction would favor an AP alignment of both electrodes and suppress RTN2. Combination of 1/f and RTN noises in the AP state most probably originated by STT has been reported also by Han et *al.* in submicron MTJs [166]. However we can not be able to get a clear relationship between the magnetic inhomogeneities localization with the size of the junctions, because we do not know the total stack of the samples measured in this work. Unlike RTN1, fluctuations similar to RTN2

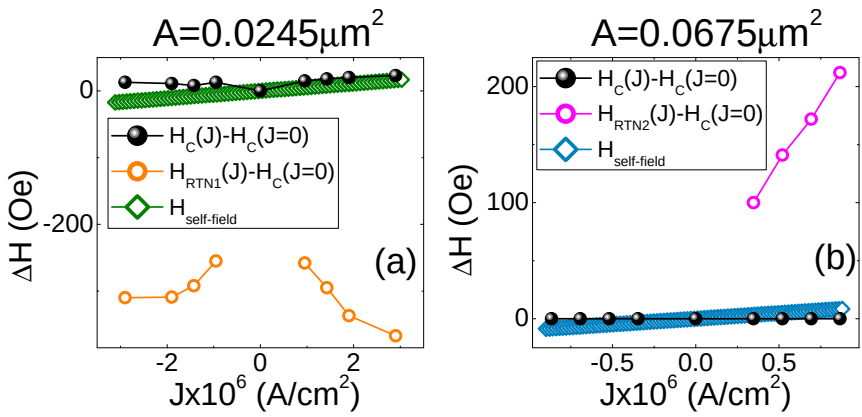

Figure 6.10: (a) Estimated maximum self-field ($H_{self-field}$) in comparison with the dependence of the coercive field (H_C) of the soft layer, and characteristic field (H_{RTN1}) where resistance steps and RTN1 in the AP state are observed (referenced to H_C at zero bias) as a function of the applied current density. (b) Similar calculations for samples with RTN2 contribution.

also were seen in GMR nanopillars [167, 168, 169], but at current densities above 10^7 A/cm^2

Based on equation 6.1, the investigation of the RTN2 time series as a function of magnetic field provides fluctuating moment of 4×10^5 μ_B. The *Figure 6.9* compares the typical magnetic fluctuating moment as a function of bias for samples with area 0.0245 and 0.0675 μm^2.

6.6 Influence of the external magnetic field

As we have mentioned above, the self-fields could, in principle, influence the DWs/MI by shifting the maximum in low frequency noise respect to magnetic field. To estimate the self-fields ($H_{self-field}$), we assume circular nanopillars with uniform current density J. The surface integral of the J crossing surface σ equals the line integral of the self-field $H_{self-field}$ along the σ contour, $\partial\sigma$:

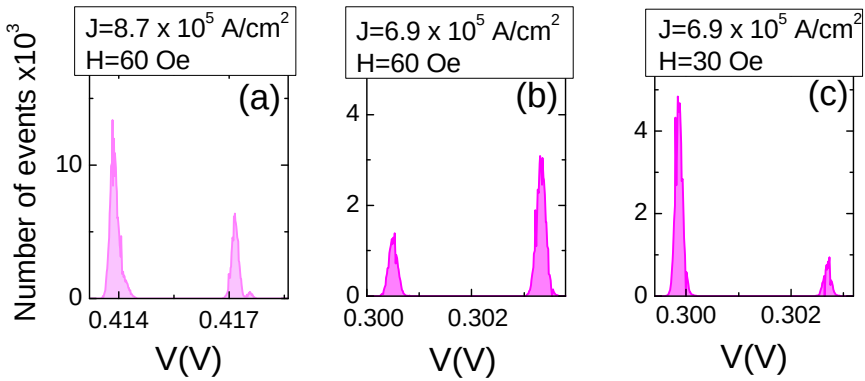

Figure 6.11: (a) to (c) show that the variation of RTN2 due to the change in bias current (with an estimated change in self-field below 2 Oe) is roughly compensated by an external magnetic field of 30 Oe.

$$\oint_{\partial\sigma} \vec{H}\,\vec{dl} = \int\int_{\sigma} \vec{J}\,d\vec{S} \tag{6.2}$$

For a circular path $\partial\sigma$ of radius r this provides that

$$H_{self-field} = \mid \vec{J} \mid \times r/2 \tag{6.3}$$

In this approximation, the $H_{self-field}$ would be of about few hundred Oe for GMR nanopillars [168]. Our estimations show that changes of RTN1 with applied bias polarity (*Figure 6.10* (a)) could indeed be partially attributed to the self-field created by the tunneling current, which may reach values of about 20 Oe, in the pessimistic case. To verify similar scenario for RTN2, *Figure 6.10* (b) compares the estimated $H_{self-field}$ with the dependence of the soft layer coercive field (Hc) and the fields where resistance steps and RTN2 in the AP states are observed (H_{RTN2}) (both referenced to H_C at zero bias) as a function of J. This analysis rules out any significant influence of the self-field on RTN2. We further checked the effects of self-fields on the RTN2 kinetics by attempting to compensate them

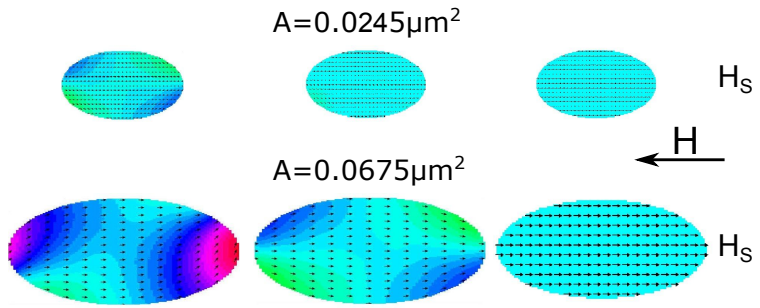

Figure 6.12: The simulation with OOMMF (Ref. [170]) of the small (0.0245 μm^2 top) and largest (0.0675 μm^2 bottom) soft electrodes corresponding to a 7% reduction of the magnetization in the larger dot due to the appearance of DW/MI2. The parameters used are a saturation magnetization of 1150×10^3 A/m, an exchange stiffness of 2×10^{-11} J/m, and a magnetization damping of 0.01. Qualitatively similar results were obtained in the presence of an uniaxial anisotropy K_u=1990 J/m [171]

with changes in magnetic field. *Figure 6.11* show that to compensate the changes related to current with the estimated variation of self-field below 2Oe one should vary the external field by about 30 Oe. This indicates that the effects of self-fields are not sufficient to explain the asymmetry in the RTN2 kinetics.

6.7 Model and Simulations

In order to understand our results, we propose a simple scenario that qualitatively explains the possible origin of both RTN1 and RTN2. While the soft electrodes in the smallest MTJs remain in a single domain state, close to the magnetization inversion the largest electrodes show for the same fields (independently of anisotropy [171] as confirmed by simulations) DW/MI formation with a 7% reduction of the magnetization of the soft layer (*Figure 6.12*), which could provide RTN2. After reaching the saturation field of the soft electrode, we decrease the magnetic field to the value corresponding to 7% reduction of magnetization in the larger dot. When these magnetic field conditions has been applied to a smaller electrode, we can

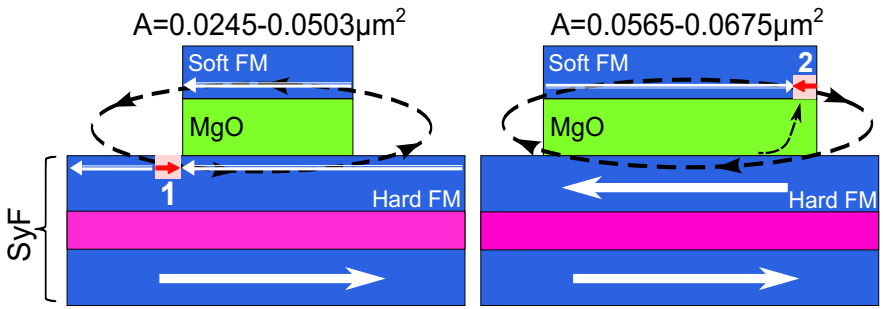

Figure 6.13: Sketch of MTJs. DW/MIs inside hard and soft electrodes indicated as (1) and (2), respectively. Dotted lines inside MgO indicate spin current with Δ_1 symmetry into DW/MI2 in the AP state. The dashed line sketches the stray field.

see in *Figure 6.12*, that the relative change in the magnetization is much lower. Therefore, this change in the magnetization of the larger electrode due to MI could be the responsible for the steps in TMR observed in *Figure 6.8* (b). Similar steps asymmetric on the bias direction R(H) were recently observed in MTJs with special design shape to control DWs [172]. The half-ring shape permit to have a good control of the localization of the DW.

Formation of the small (10^5 μ_B) DW/MI2 in the AP state could affect the current distribution (which is mainly due to electrons with Δ_5 symmetry for the ideal AP alignment [9, 10]) creating "pseudo-hot spots"for electrons with Δ_1 symmetry (*Figure 6.13*). This spin current excess, along the large perpendicular STT [173], could explain the influence of spin current on RTN2 already at current densities, below 10^6 A/cm^2, which are at least a factor of 10 smaller than for GMR nanopillars [167, 168, 169]. On the contrary, the RTN1 is most probably due to DW/MI1 located in the SyF biased layer outside and close to the edge of the MTJ pillar (*Figure 6.13*). The origin of the DW/MI1 could be due to 360° DWs [174] pinned by the stray field of the soft layer (*Figure 6.13*). Edge-domains in submicron elliptical nanopillars could probably affect switching probably as was recently observed by Seki et *al.* [175].

Figure 6.14 summarizes the characteristic magnetic fields where the reproducible maxima of RTN(1,2) were observed. The absence of RTN1 in the largest MTJs with reduced influence of the edge stray field (*Figure 6.14*) contradicts the explanation on RTN1 being due to defects in the MgO influenced by magnetostriction.

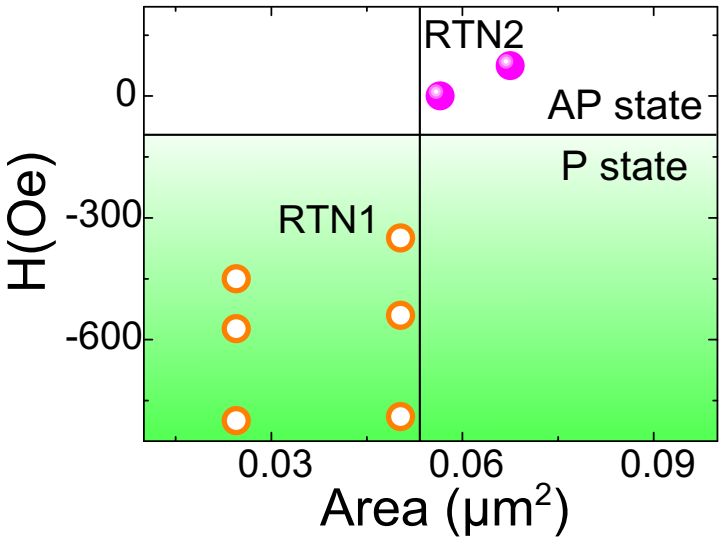

Figure 6.14: Characteristic magnetic fields of RTN1 and RTN2 as a function of area.

6.8 Discussion of spin torque effects on DWs in FM wires, AF multilayers and MTJs

The study of domain wall motion and spin transfer torque is one of the hot topics within the development of novel types of magnetic devices based on information storage for MRAMs. There are few lines of research which use the magnetic domains in different systems:

6.8 Discussion of spin torque effects on DWs in FM wires, AF multilayers and MTJs

- Ferromagnetic wires: The racetrack memory (RM) consist of silicon or permalloy nanowires, in which the magnetic domains are used to store information in columns of magnetic material arranged perpendicularly to the surface [176]. The advantage of the RM for the industry is that it is relatively simple and potentially cheaper to fabricate. The RM uses a spin-coherent electric current to move the magnetic domains. The DWs are shifted along the racetrack by nanosecond current pulses using the phenomenon of spin-momentum transfer. The problem of these devices is that to move the DWs it is necessary to apply current densities exceeding 10^8 A/cm^2, which heats the devices very close to the Curie temperature [177].

- Antiferromagnetic multilayers: Spin torque on antiferromagnetic system has been suggested as an alternative way to solve the problem of high critical currents [178]. Experimentally, such possibility was investigated in our group recently, using DWs in $[Fe/Cr]_{10}$ synthetic antiferromagnetic (SAF) systems [39]. A detailed study of DW magnetoresistance and low frequency noise in AF coupled Fe/Cr magnetic multilayers (MML) revealed an unexpected dependence of DW induced low frequency noise on the current density [39]. We have attributed this observation to current-induced magnetization dynamics that occurs at a critical current density that is smaller than the typical current densities observed in ferromagnetic materials, typically above 10^7 A/cm^2. *Figure 6.15* (a) shows the low-temperature in-plane magnetoresistance in a sample with composition $[Fe\ (2.4\ nm)/\ Cr\ (1.3\ nm)]_{10}$. The normalized magnetoresistance, measured at a temperature of 77 K in this type of MML, for the low magnetic field regions where DWs are nucleated at $H = H_n$ and annihilated at $H = H_a$.

  When the current density exceeds $2\times10^5\ A/cm^2$ at T = 77K, the excess noise observed for low magnetic fields, where DWs are created and propagated, is suppressed in the field interval for stronger DW pinning. The excess noise

6. Low frequency noise in submicron sputtered FeCoB/MgO/FeCoB magnetic tunnel junctions

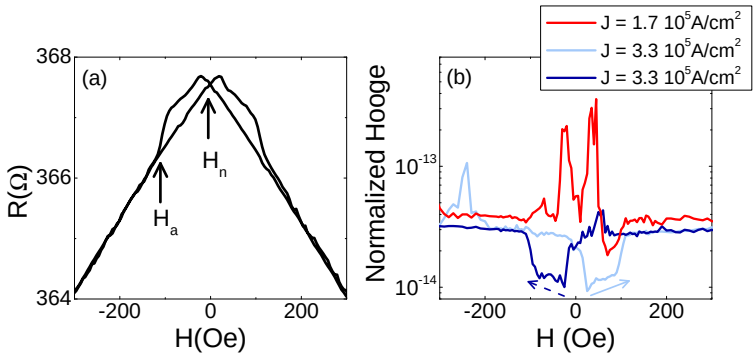

Figure 6.15: (a) Low-field magnetoresistance measured at T = 77 K with very small current density and with the current parallel to the external magnetic field. (b) Hooge factor plotted on a logarithmic scale vs magnetic field for [Fe (2.4 nm)/ Cr (1.3 nm)]$_{10}$ at 77 K with two different applied current densities. The normalized noise vs field measurements are done with a current density of $J = 3.3 \times 10^5$ A/cm^2 and the results are shown both for increasing and decreasing magnetic field. The experiments have been carried out with the dc current parallel to the external magnetic field and to the magnetic easy (001) axis.

and the deviation from the 1/f-like frequency dependence is attributed to non-equilibrium noise present at low fields to a RTN-type contribution to the noise at low biases. Despite this deviation, our work uses the Hooge factor as a simplified parameter for the analysis of the normalized noise. The clear suppression of the excess low frequency noise (Hooge factor) related to DW appears for sufficiently high current densities (*Figure 6.15* (b)). The possible scenario of the substantial suppression of magnetic noise in the vicinity of the depinning field with high current densities $J_c > 2 \times 10^5$ A/cm^2 is may be the reduction in the local magnetic disorder induced by large DW movement. In other words, it is proposed that the downward and upward variations in the magnetic noise at low fields appear due to the competition between local magnetic disorder (which provides the background magnetic noise) and its reduction by the moving domain walls due to larger currents.

- Magnetic tunnel junctions: A novel mechanism for DW motion under effect

of current is proposed in this Chapter. This mechanism is related with DW motion under perpendicular tunneling current and with very low current densities. Similar effects have been reported recently from TMR measurements by Chanthbouala et. *al.* [172]. In this paper a half-ring shape of the MTJ was designed in order to detect the DW motion by vertical current injection. The displacement of DW at low current densities by the tunneling current could be used to create new kind of MRAM using lower current densities.

6.9 Conclusions

In this Chapter, we have observed in elliptical submicron MTJs with dimensions close to the transition to the single domain regime, the presence of single magnetic inhomogeneities in the soft and hard layers at room temperature detected by tunneling transport, low frequency noise and corroborated by random telegraph noise measurements. The magnetic inhomogeneities show a strong correlation with the area of the junctions and we have been able to distinguish two well defined regions.

For smaller elliptical nanopillars (0.0245 μm^2-0.0503 μm^2) an anomalous enhancement of the low frequency noise deeply in the P state ($\sim$ 300Oe above the transition) appears for both bias polarities. This enhancement in low frequency noise is due to two-level magnetic fluctuations (RTN1). Since the change in resistance is less than 0.2%, we believe that RTN1 are caused by magnetic inhomogeneities outside, but close to the edge of the MTJ hard electrode. The changes in RTN1 with applied bias polarity could be roughly due to self-fields created by the tunneling current.

On the contrary, for the larger elliptical nanopillars (A=0.0565 μm^2, 0.0675 μm^2), the random telegraph noise fluctuations (RTN2) and the related resistance steps (of about 2%) in the AP state due to MI/DWs are asymmetrically influenced by the current. We suggest that this effect is mainly due to spin torque on DWs/MI driven by the perpendicular tunneling current.

6. Low frequency noise in submicron sputtered FeCoB/MgO/FeCoB magnetic tunnel junctions

7

Summary

I would like to conclude this thesis emphasizing the most relevant experimental results:

We have designed a cryogenic system capable of measuring electron transport and low frequency noise from room temperature down to 0.25 K, with the possibility of applying a vectorial external magnetic field. We have improved the experimental setup, reducing the probability of dielectric breakdown due to electrostatic discharge.

In order to improve the tunneling transport in epitaxial magnetic tunnel junctions by reducing the number of defects in the interface, we have investigated junctions doped with different elements using various strategies. We have doped the ferromagnetic electrodes with carbon, which seemingly replaces oxygen atoms and fills vacancies at the interface. On the other side, doping with vanadium the ferromagnetic electrode pretends to improve the misfit between the electrode and barrier by changing the lattice parameter of the electrode. And finally, doping with nitrogen was used to achieve a reduction of the effective barrier in order to create a soft local breakdown of the MgO barrier .

7. Summary

We have found that using different concentrations of carbon and vanadium for different barrier thicknesses the tunneling transport is improved through the reduction of low frequency noise. The sensitivity of the devices comes from the relationship between signal and noise. For example, for 12 ML MgO barrier in Fe/MgO/Fe, the MTJs are well above the plastic relaxation and the introduction of carbon or vanadium in an electrode has a drastic effect on the density of defects in the interface. Therefore, the low frequency noise in the P state (related to the relaxation time of the defects) is strongly reduced. In addition, these elements play a fundamental role in the tunneling transport as a function of the direction of current. For carbon doped MTJs, we have found that for negative currents (the electrons tunnel from the top electrode to the bottom electrode) the inversion of the tunnel magnetoresistance is accompanied by a strong reduction of the 1/f noise in the AP state, due to interfacial resonant states. In this bias window, the magnetic domains are found to be more stable, allowing us to have a less noisy signal as a function of current and a more stable response as a function of external magnetic field. We attribute these effects to the possible influence of local spin torque on domain walls. Thus the low frequency noise is related to the dynamic conductance, and is influenced by the spin filtering of the MgO barrier and by the bulk band structure of the Fe. We have also confirmed through shot noise measurements that the tunneling phenomenon in magnetic tunnel junctions with a single barrier is direct.

Room temperature resistance oscillations have been observed in both the parallel and antiparallel magnetic configurations and for both bias polarizations. These anomalies were attributed to resonant tunneling through local quantum well states in the middle continuous free layer of double magnetic tunnel junctions doped with nitrogen. Nitrogen plays an important role to achieve the "soft" dielectric breakdown of the MgO barrier at low biases.

These days, magnetoelectronic devices for applications are fabricated with less area to achieve higher recording density. We have studied conductance and low frequency noise in submicron sized down to A = 0.0245 μm^2, exchange-biased MTJs with FeCoB electrodes. We have observed that the TMR and low frequency noise in submicron MTJs are strongly affected by the magnetic inhomogeneities/ domain walls (MI/ DWs) depending on the area of the sample. In the smallest junctions, we have found an unexpected random telegraph noise, deeply in the parallel state, accompanied by an extremely small change in resistance. This noise is weakly influenced by the external bias and is probably due to stray field induced MI/DWs in the hard layer. The second noise source is observed in the antiparallel state for larger junctions, above A = 0.0565 μm^2. The strong asymmetry of second type of random telegraph noise, the related resistance drop with current as well as the insignificance of the self-field indicate spin torque acting on the MI/DWs in the soft layer at current densities below 5×10^5 A/cm^2.

Conclusiones generales

Me gustaría finalizar esta Tesis destacando los resultados más relevantes que hemos obtenido:

En el desarrollo de esta Tesis se ha diseñado un nuevo sistema criogénico, capaz de medir transporte túnel y ruido de baja frecuencia desde temperatura ambiente hasta 0.25 K. Se ha incorporado además, la posibilidad de aplicar campo magnético vectorial mediante tres bobinas superconductoras. También se ha mejorado el sistema experimental inicial, reduciendo significativamente el número de muestras que sufren ruptura dieléctrica por descargas electrostáticas, lo que ha mejorado la eficacia de las medidas.

Entender y mejorar el transporte en uniones túnel magnéticas plenamente epitaxiales, reduciendo el número de defectos en la intercara es necesario. Para ello hemos investigado uniones túnel dopadas con diferentes elementos, usando estrategias alternativas que mejoran el transporte. En primer lugar, hemos dopado con carbono el electrodo inferior, el cual probablemente se coloca reemplazando átomos de oxígeno o en las vacantes de la intercara Fe/MgO. En segundo lugar, hemos dopado tanto el electrodo inferior como el superior con diferentes concentraciones de vanadio, para mejorar el solape entre el electrodo y la barrera, dado que podemos modificar el parámetro de red de dicho electrodo. Por último, hemos dopado toda la estructura con nitrógeno, el cual reduce la altura efectiva de la barrera creando una ruptura dieléctrica débil.

Usando diferentes concentraciones de carbono y vanadio para diferentes espesores de barrera, se ha observado una mejora sustancial del transporte debido a una reducción del ruido de baja frecuencia. La sensitividad de los dispositivos magnéticos viene definida por su relación señal/ruido. El ruido 1/f en el estado paralelo, lejos de la transición, está relacionado con el tiempo de relajación de los defectos en o cerca de la barrera. Por ejemplo, para una unión túnel magnética con 12 ML de espesor de barrera MgO, el carbono y el vanadio tienen un efecto

drástico sobre la densidad de los defectos en la intercara, como podemos observar en las medidas de ruido de baja frecuencia. Aún más, estos dos elementos, juegan un papel fundamental en el transporte en función de la dirección de la corriente. Para las uniones túnel dopadas con carbono, se ha visto que cuando los electrones se inyectan desde el electrodo superior al inferior, se produce una inversión en el signo de la magnetorresistencia túnel, acompañada de una disminución del ruido 1/f, debido a estados resonantes interfaciales. En esta ventana de voltaje, hemos podido comprobar mediante las medidas de ruido de ruido que los dominios magnéticos estan más anclados, lo que nos permite tener medidas menos ruidosas en función de la corriente y más estables en función del campo magnético externo. Nosotros atribuimos este efecto a posibles influencias sobre los dominios magnéticos debido a la transferencia de espín. Además, hemos confirmado que en este tipo de uniones túnel magnéticas con barrera única el túnel es directo.

Por otro lado, se ha visto túnel resonante, debido a estados cuánticos bien definidos en el electrodo intermedio de una unión túnel magnética con doble barrera, dopada con nitrógeno, mediante oscilaciones en resistencia, para ambos estados y ambas polaridades. El nitrógeno juega un papel fundamental en la estructura, provocando una ruptura dieléctrica suave de la barrera a bajas excitaciones.

Actualmente se fabrican dispositivos magnetoeléctricos cada vez con menor área, para poder alcanzar mayores densidades de grabación en las memorias magnéticas. Por ello, hemos estudiado la conductancia y el ruido de baja frecuencia, en uniones túnel magnéticas de área sub-micrométrica, por encima de 0.0245 μm^2. Se ha observado que en este tipo de uniones, la magnetoresistencia túnel y el ruido de baja frecuencia, está fuertemente afectado por las inhomogeneidades magnéticas y paredes de dominio, dependiendo del área del electrodo libre del dispositivo. En las uniones túnel con menor área, aparece un inesperado ruido telegráfico aleatorio en el estado paralelo, lejos de la transición, acompañado por un suave cambio en resistencia. Este ruido está débilmente influenciado por el voltaje aplicado, y muy probablemente se deba a las inhomogeneidades magnéticas que aparecen en

el electrodo magnéticamente duro, creadas por el campo magnético inducido por la corriente aplicada. La segunda fuente de ruido, se observa en el estado antiparalelo, para uniones con áreas superiores a 0.0565 μm^2. La fuerte asimetría de este ruido telegráfico con la polaridad y los saltos en resistencia, nos hacen pensar en la posible influencia de la transferencia del momento de espín, actuando sobre las inhomogeneidades magnéticas en la capa magnéticamente blanda.

References

[1] N. M. Baibich, J. M. Broto, A. Fert, F. Nguyen Van Dau, F. Petroff, P. Eitenne, G. Creuzet, A. Friederich, and J. Chazelas, "Giant Magnetoresistance of (001)Fe/(001) Cr Magnetic Superlattices," *Phys. Rev. Lett*, vol. 6, p. 2472, 1988. vi, 2, 9

[2] G. Binasch, P. Grünberg, F. Saurenbach, and W. Zinn, "Enhanced magnetoresistance in layered magnetic structures with antiferromagnetic interlayer exchange," *Phys. Rev. B*, vol. 39, p. 4828, 1989. vi, 2, 9

[3] S. S. P. Parkin and B. W. Wessels, "Giant magnetoresistance in magnetic nanostructures," *Annual Review of Materials Science*, vol. 25, pp. 357–388, 1995. vii, 4

[4] Y. Lu, R. A. Altman, A. Marley, S. A. Rishton, P. L. Trouilloud, G. Xiao, W. J. Gallagher, and S. S. P. Parkin, "Shape-anisotropy-controlled magnetoresistive response in magnetic tunnel junctions," *Appl. Phys. Lett.*, vol. 70, no. 19, pp. 2610–2612, 1997. vii, 2

[5] J. Moodera, L. R. Kinder, T. M. Wong, and R. Meservey, "Large Magnetoresistance at RT in Ferromagnetic Thin Film Tunnel Junctions," *Phys. Rev. Lett*, vol. 74, p. 3273, 1995. vii, 2, 16, 128

[6] T. Miyazaki and N. Tezuka, "Giant magnetic tunneling effect in Fe/Al_2O_3/Fe junction," *J. Magn. Magn. Mater.*, vol. 139, pp. 94–97, 1995. vii, 2, 128, 142

[7] S. Yuasa, T. Nagahama, A. Fukushima, Y. Suzuki, and K. Ando, "Giant room-temperature magnetoresistance in single-crystal Fe/MgO/Fe magnetic tunnel junctions.," *Nat. Mater.*, vol. 3, pp. 868–71, Dec. 2004. vii, 3, 19, 92, 128

[8] S. Parkin, C. Kaiser, A. Panchula, P. M. Rice, B. Hughes, M. Samant, and Y. S-H, "Giant tunnelling magnetoresistance at room temperature with MgO (100) tunnel barriers," *Nat.Mater*, vol. 3, p. 862, 2004. vii, 3, 92, 128

[9] W. Butler, X.-G. Zhang, T. Schulthess, and J. MacLaren, "Spin-dependent tunneling conductance of Fe—MgO—Fe sandwiches," *Phys. Rev. B*, vol. 63, pp. 1–12, Jan. 2001. vii, 3, 17, 20, 22, 30, 52, 54, 55, 57, 92, 93, 104, 112, 123, 124, 128, 142, 165

[10] J. Mathon and A. Umerski, "Theory of tunneling magnetoresistance of an epitaxial Fe/MgO/Fe(001) junction," *Phys. Rev. B*, vol. 63, p. 220403R, 2001. vii, 3, 17, 52, 54, 92, 124, 128, 165

[11] R. Guerrero, F. G. Aliev, R. Villar, J. Hauch, M. Fraune, G. Güntherodt, K. Rott, H. Brückl, and G. Reiss, "Low-frequency noise and tunneling magnetoresistance in Fe(110)/MgO(111)/Fe(110) epitaxial magnetic tunnel junctions," *Appl. Phys. Lett.*, vol. 87, no. 4, p. 042501, 2005. ix, 30, 34, 53, 78, 92, 153, 155

[12] R. Guerrero, F. Aliev, Y. Tserkovnyak, T. Santos, and J. Moodera, "Shot Noise in Magnetic Tunnel Junctions: Evidence for Sequential Tunneling," *Phys. Rev. Lett.*, vol. 97, pp. 1–4, Dec. 2006. x, 86, 88

[13] F. N. Hooge, T. G. M. Kleinpenning, and L. K. J. Vandamme, "Experimental studies on l/f noise," *Rep. Prog. Phys*, vol. 44, no. December 1980, 1981. x, 28, 73, 155

[14] Jullière, "Tunneling between ferromagnetic films," *Phys.Lett.*, vol. 54A, pp. 225–226, 1975. 2, 15, 16, 93, 103, 128

[15] S. Ikeda, J. Hayakawa, Y. Ashizawa, Y. M. Lee, K. Miura, H. Hasegawa, M. Tsunoda, F. Matsukura, and H. Ohno, "Tunnel magnetoresistance of 604 at 300K by suppression of Ta diffusion in CoFeB/MgO/CoFeB pseudo-spin-valves annealed at high temperature," *Appl. Phys. Lett.*, vol. 93, no. 8, p. 082508, 2008. 3, 94

[16] R. Matsumoto, A. Fukushima, T. Nagahama, Y. Suzuki, K. Ando, and S. Yuasa, "Oscillation of giant tunneling magnetoresistance with respect to tunneling barrier thickness in fully epitaxial Fe/MgO/Fe magnetic tunnel junctions," *Appl. Phys. Lett.*, vol. 90, no. 25, p. 252506, 2007. 3, 22, 61, 62

[17] F. Bonell, S. Andrieu, A. M. Bataille, C. Tiusan, and G. Lengaigne, "Consequences of interfacial Fe-O bonding and disorder in epitaxial Fe/MgO/Fe(001) magnetic tunnel junctions," *Phys. Rev. B*, vol. 79, p. 224405, Jun 2009. 3, 94

[18] C. Chappert, A. Fert, and F. N. Van Dau, "The emergence of spin electronics in data storage," *Nat. Mater.*, vol. 6, pp. 1476–1122, nov. 2007. 3, 4

[19] S. Parkin, X. Jiang, C. Kaiser, A. Panchula, K. Roche, and M. Samant, "Magnetically engineered spintronic sensors and memory," *Proceedings of the IEEE*, vol. 91, pp. 661 – 680, may 2003. 3, 4, 150

[20] R. C. Chaves, P. P. Freitas, B. Ocker, and W. Maass, "Low frequency picotesla field detection using hybrid MgO based tunnel sensors," *Appl. Phys. Lett.*, vol. 91, no. 10, p. 102504, 2007. 3, 151, 153

[21] J. Barnaś and A. Fert, "Magnetoresistance Oscillations due to Charging Effects in Double Ferromagnetic Tunnel Junctions," *Phys. Rev. Lett.*, vol. 80, pp. 1058–1061, Feb 1998. 4, 128

[22] A. G. Petukhov, A. N. Chantis, and D. O. Demchenko, "Resonant Enhancement of Tunneling Magnetoresistance in Double-Barrier Magnetic Heterostructures," *Phys. Rev. Lett.*, vol. 89, p. 107205, Aug 2002. 4, 128

[23] T. Nozaki, A. Hirohata, N. Tezuka, S. Sugimoto, and K. Inomata, "Bias voltage effect on tunnel magnetoresistance in fully epitaxial MgO double-barrier magnetic tunnel junctions," *Appl. Phys. Lett.*, vol. 86, no. 8, p. 082501, 2005. 4, 128, 137

[24] A. Kalitsov, A. Coho, N. Kioussis, A. Vedyayev, M. Chshiev, and A. Granovsky, "Impurity-Induced Tuning of Quantum-Well States in Spin-Dependent Resonant Tunneling," *Phys. Rev. Lett.*, vol. 93, p. 046603, Jul 2004. 4, 128

[25] L. Jiang, H. Naganuma, M. Oogane, and Y. Ando, "Large Tunnel Magnetoresistance of 1056% at Room Temperature in MgO Based Double Barrier Magnetic Tunnel Junction," *Appl. Phys. Express*, vol. 2, no. 8, p. 083002, 2009. 4, 128

[26] A. Vedyayev, N. Ryzhanova, B. Dieny, and N. Strelkov, "Resonant spin-torque in double barrier magnetic tunnel junctions," *Phys. Lett. A*, vol. 355, no. 3, pp. 243 – 246, 2006. 4, 128, 131, 132

[27] I. Theodonis, A. Kalitsov, and N. Kioussis, "Enhancing spin-transfer torque through the proximity of quantum well states," *Phys. Rev. B*, vol. 76, p. 224406, Dec 2007. 4, 128, 142

[28] M. Watanabe, J. Okabayashi, H. Toyao, T. Yamaguchi, and J. Yoshino, "Current-driven magnetization reversal at extremely low threshold cur-

rent density in (Ga,Mn)As-based double-barrier magnetic tunnel junctions," *Appl. Phys. Lett.*, vol. 92, no. 8, p. 082506, 2008. 4, 128

[29] J. M. Almeida and P. P. Freitas, "Field detection in MgO magnetic tunnel junctions with superparamagnetic free layer and magnetic flux concentrators," *J. Appl. Phys.*, vol. 105, no. 7, p. 07E722, 2009. 4, 5

[30] S. Petit, C. Baraduc, C. Thirion, U. Ebels, Y. Liu, M. Li, P. Wang, and B. Dieny, "Spin-Torque Influence on the High-Frequency Magnetization Fluctuations in Magnetic Tunnel Junctions," *Phys. Rev. Lett.*, vol. 98, p. 077203, Feb 2007. 4, 151

[31] N. Locatelli, V. V. Naletov, J. Grollier, G. de Loubens, V. Cros, C. Deranlot, C. Ulysse, G. Faini, O. Klein, and A. Fert, "Dynamics of two coupled vortices in a spin valve nanopillar excited by spin transfer torque," *Appl. Phys. Lett.*, vol. 98, no. 6, p. 062501, 2011. 4, 6

[32] P. P. Freitas, R. Ferreira, S. Cardoso, and F. Cardoso, "Magnetoresistive sensors," *J. Phys.: Condens. Matter*, vol. 19, p. 165221, Apr. 2007. 5, 6

[33] S. Ikeda, J. Hayakawa, Y. M. Lee, T. Tanikawa, F. Matsukura, and H. Ohno, "Tunnel magnetoresistance in MgO-barrier magnetic tunnel junctions with bcc-CoFe(B) and fcc-CoFe free layers," *J. Appl. Phys.*, vol. 99, no. 8, p. 08A907, 2006. 5

[34] S. Ikeda, J. Hayakawa, Y. M. Lee, F. Matsukura, Y. Ohno, T. Hanyu, and H. Ohno, "Magnetic Tunnel Junctions for Spintronic Memories and Beyond," *Electron Devices, IEEE Transactions on*, vol. 54, pp. 991 –1002, may 2007. 5

[35] J. Slonczewski, "Current-driven excitation of magnetic multilayers," *J. Magn. Magn. Mater.*, vol. 159, pp. L1–L7, June 1996. 6

[36] L. Berger, "Multilayers as spin-wave emitting diodes," *J. Appl. Phys*, vol. 81, p. 4880, 1997. 6

[37] D. Houssameddine, S. H. Florez, J. A. Katine, J. Michel, U. Ebels, D. Mauri, O. Ozatay, B. Delaet, B. Viala, L. Folks, B. D. Terris, and M. Cyrille, "Spin transfer induced coherent microwave emission with large power from nanoscale MgO tunnel junctions," *Appl. Phys. Lett.*, vol. 93, no. 2, p. 022505, 2008. 6, 148, 151, 152

[38] W. Thomson, "On the electrodynamic qualities of metals: effects of magnetization on the electric conductivity of nickel and iron," *Proc. Roy. Soc. London*, vol. 8, pp. 546–550, 1857. 8

[39] D. Herranz, R. Guerrero, R. Villar, F. G. Aliev, A. C. Swaving, R. A. Duine, C. van Haesendonck, and I. Vavra, "Anomalous low-frequency noise in synthetic antiferromagnets: Possible evidence of current-induced domain-wall motion," *Phys. Rev. B*, vol. 79, p. 134423, Apr 2009. 9, 167

[40] A. Cebollada, J. L. Martnez, J. M. Gallego, J. J. de Miguel, R. Miranda, S. Ferrer, F. Batallán, G. Fillion, and J. P. Rebouillat, "Antiferromagnetic ordering in co-cu single-crystal superlattices," *Phys. Rev. B*, vol. 39, pp. 9726–9729, May 1989. 9

[41] B. Dieny, V. S. Speriosu, S. S. P. Parkin, B. A. Gurney, D. R. Wilhoit, and D. Mauri, "Giant magnetoresistive in soft ferromagnetic multilayers," *Phys. Rev. B*, vol. 43, pp. 1297–1300, Jan 1991. 10

[42] S. Yuasa and D. D. Djayaprawira, "Giant tunnel magnetoresistance in magnetic tunnel junctions with a crystalline MgO(001) barrier," *J. Phys. D: Appl. Phys.*, vol. 40, pp. R337–R354, Nov. 2007. 16, 17, 61, 123

[43] J. De Teresa, A. Barthelemy, A. Fert, J. Contour, F. Montaigne, and P. Seneor, "Role of metal-oxide interface in determining the spin polarization of

magnetic tunnel junctions," *Science*, vol. 286, pp. 507–509, OCT 15 1999. 17

[44] S. Yuasa, T. Katayama, T. Nagahama, A. Fukushima, H. Kubota, Y. Suzuki, and K. Ando, "Giant tunneling magnetoresistance in fully epitaxial body-centered-cubic Co/MgO/Fe magnetic tunnel junctions," *Appl. Phys. Lett.*, vol. 87, no. 22, p. 222508, 2005. 17, 80, 93

[45] S. Yuasa, A. Fukushima, H. Kubota, Y. Suzuki, and K. Ando, "Giant tunneling magnetoresistance up to 410% at room temperature in fully epitaxial Co/MgO/Co magnetic tunnel junctions with bcc Co(001) electrodes," *Appl. Phys. Lett.*, vol. 89, no. 4, p. 042505, 2006. 17, 93

[46] Y. Miura, H. Uchida, Y. Oba, K. Nagao, and M. Shirai, "Coherent tunnelling conductance in magnetic tunnel junctions of half-metallic full Heusler alloys with MgO barriers," *J. Phys.: Cond. Matt.*, vol. 19, no. 36, p. 365228, 2007. 17

[47] S. Tsunegi, Y. Sakuraba, M. Oogane, K. Takanashi, and Y. Ando, "Large tunnel magnetoresistance in magnetic tunnel junctions using a Co_2MnSi Heusler alloy electrode and a MgO barrier," *Appl. Phys. Lett.*, vol. 93, no. 11, p. 112506, 2008. 17, 93

[48] C. Tiusan, F. Greullet, M. Hehn, F. Montaigne, S. Andrieu, and A. Schuhl, "Spin tunnelling phenomena in single-crystal magnetic tunnel junction systems," *J. Phys.: Condens. Matter*, vol. 19, p. 165201, Apr. 2007. 19, 20, 30, 53, 58, 61, 63, 64, 67, 68, 92, 98, 100, 104, 111, 130, 134

[49] J. L. Vassent, M. Dynna, A. Marty, B. Gilles, and G. Patrat, "A study of growth and the relaxation of elastic strain in MgO on Fe(001)," *J. Appl. Phys.*, vol. 80, no. 10, pp. 5727–5735, 1996. 19, 92

[50] J. MacLaren, X.-G. Zhang, W. Butler, and X. Wang, "Layer KKR approach to Bloch-wave transmission and reflection: Application to spin-dependent tunneling," *Phys. Rev. B*, vol. 59, pp. 5470–5478, Feb. 1999. 20, 104

[51] D. Waldron, V. Timoshevskii, Y. Hu, K. Xia, and H. Guo, "First Principles Modeling of Tunnel Magnetoresistance of Fe/MgO/Fe Trilayers," *Phys. Rev. Lett.*, vol. 97, p. 226802, Nov 2006. 22, 92

[52] X.-G. Zhang, W. Butler, and A. Bandyopadhyay, "Effects of the iron-oxide layer in Fe-FeO-MgO-Fe tunneling junctions," *Phys. Rev. B*, vol. 68, pp. 6–9, Sept. 2003. 22

[53] J. A. Stroscio, D. T. Pierce, A. Davies, R. J. Celotta, and M. Weinert, "Tunneling spectroscopy of bcc (001) surface states," *Phys. Rev. Lett.*, vol. 75, pp. 2960–2963, Oct 1995. 22

[54] O. Wunnicke, N. Papanikolaou, R. Zeller, P. H. Dederichs, V. Drchal, and J. Kudrnovský, "Effects of resonant interface states on tunneling magnetoresistance," *Phys. Rev. B*, vol. 65, p. 064425, Jan 2002. 22

[55] C. Beenakker and C. Schönenberger, "Quantum shot noise," *Physics Today*, vol. 56, no. 5, pp. 37–42, 2003. 23

[56] Y. M. Blanter and M. Büttiker, "SHOT NOISE IN MESOSCOPIC CONDUCTORS," *Phys. Repor.*, vol. 336, 2000. 24, 25, 26, 27, 86, 87

[57] S. Kogan, *Electronic noise and fluctuations in solids.* Cambridge University press, 1996. 27, 42, 43, 79

[58] M. B. Weissman, "1/f noise and other slow, nonexponential kinetics in condensed matter," *Rev. Mod. Phys.*, vol. 60, pp. 537–571, Apr 1988. 27

[59] M. de Diego, A. Gonzalez, and G. Piñero, *Introduccion a las señales aleatorias.* Universidad Politcnica de Valencia, Valencia, 1999. 27

[60] P. Dutta and P. M. Horn, "Low-frequency fluctuations in solids: 1/f noise," *Rev. Mod. Phys.*, vol. 53, pp. 497–516, Jul 1981. 27, 28, 83, 94, 155

[61] E. R. Nowak, R. Merithev, M. B. Weissman, I. Bloom, and S. S. P. Parkin, "Noise properties of ferromagnetic tunnel junctions," *J. Appl. Phys.*, vol. 84, no. 11, p. 6195, 1998. 29, 52

[62] E. R. Nowak, M. B. Weissman, and S. S. P. Parkin, "Electrical noise in hysteretic ferromagnet/insulator/ferromagnet tunnel junctions," *Appl. Phys. Lett.*, vol. 74, no. 4, p. 600, 1999. 29, 52, 94

[63] S. Ingvarsson, G. Xiao, R. Wanner, P. Truoilloud, Y. Lu, W. J. Gallagher, A. Marley, K. Roche, and S. S. Parkin, "Electronic noise in magnetic tunnel junctions," *J. Appl. Phys.*, vol. 85, p. 5270, Apr. 1999. 29, 52, 153, 158

[64] S. Ingvarsson, G. Xiao, S. S. Parkin, W. J. Gallagher, G. Grinstein, and R. H. Koch, "Low-frequency magnetic noise in micron-scale magnetic tunnel junctions.," *Phys. Rev. Lett.*, vol. 85, pp. 3289–92, Oct. 2000. 29, 30, 76

[65] L. Jiang, E. Nowak, P. Scott, J. Johnson, J. Slaughter, J. Sun, and R. Dave, "Low-frequency magnetic and resistance noise in magnetic tunnel junctions," *Phys. Rev. B*, vol. 69, pp. 1–9, Feb. 2004. 29, 30, 76, 87, 153, 158, 160

[66] H. T. Hardner, M. B. Weissman, M. B. Salamon, and S. S. P. Parkin, "Fluctuation-dissipation relation for giant magnetoresistive 1/f noise," *Phys. Rev. B*, vol. 48, pp. 16156–16159, Dec 1993. 29, 30, 54

[67] R. Guerrero, F. Aliev, R. Villar, J. Hauch, M. Fraune, G. Guntherodt, K. Rott, H. Bruckl, and G. Reiss, "Low-frequency noise and inelastic tunneling spectroscopy in Fe(110)/MgO(111)/Fe(110) epitaxial magnetic tunnel junctions," *J. Magn. Magn. Mater.*, vol. 300, pp. 132–135, May 2006. 30

[68] R. Guerrero, D. Herranz, F. G. Aliev, F. Greullet, C. Tiusan, M. Hehn, and F. Montaigne, "High bias voltage effect on spin-dependent conductivity

and shot noise in carbon-doped Fe(001)/MgO(001)/Fe(001) magnetic tunnel junctions," *Appl. Phys. Lett.*, vol. 91, no. 13, p. 132504, 2007. 30, 63, 87, 88, 92, 112

[69] F. G. Aliev, R. Guerrero, D. Herranz, R. Villar, F. Greullet, C. Tiusan, and M. Hehn, "Very low 1/f noise at room temperature in fully epitaxial Fe/MgO/Fe magnetic tunnel junctions," *Appl. Phys. Lett.*, vol. 91, no. 23, p. 232504, 2007. 30, 40, 78, 84, 92, 153

[70] D. Herranz, F. G. Aliev, C. Tiusan, M. Hehn, V. K. Dugaev, and J. Barnaś, "Tunneling in Double Barrier Junctions with "Hot Spots"," *Phys. Rev. Lett.*, vol. 105, p. 047207, Jul 2010. 30, 131, 145

[71] D. Herranz, F. Bonell, A. Gomez-Ibarlucea, S. Andrieu, F. Montaigne, R. Villar, C. Tiusan, and F. G. Aliev, "Strongly suppressed 1/f noise and enhanced magnetoresistance in epitaxial Fe-V/MgO/Fe magnetic tunnel junctions," *Appl. Phys. Lett.*, vol. 96, no. 20, p. 202501, 2010. 30, 40

[72] J. M. Almeida, P. Wisniowski, and P. P. Freitas, "Low-Frequency Noise in MgO Magnetic Tunnel Junctions: Hooge's Parameter Dependence on Bias Voltage," *IEEE Trans. Magn,*, vol. 44, pp. 2569–2572, Nov. 2008. 31

[73] R. Guerrero, *Conductancia y Ruido en Uniones Tnel Magnticas.* Thesis of Universidad Autnoma de Madrid, Spain, 2007. 34

[74] D. Pozar, *Microwave Engineering.* volume Third Edition. John Wiley and Sons, Inc: Cambridge University press, 2005. 45

[75] S. Yuasa, T. Sato, E. Tamura, Y. Suzuki, H. Yamamori, K. Ando, and T. Katayama, "Magnetic tunnel junctions with single-crystal electrodes: A crystal anisotropy of tunnel magneto-resistance," *EPL (Europhysics Letters)*, vol. 52, no. 3, p. 344, 2000. 53

[76] J. Z. Sun, D. W. Abraham, K. Roche, and S. S. P. Parkin, "Temperature and bias dependence of magnetoresistance in doped manganite thin film trilayer junctions," *Appl. Phys. Lett.*, vol. 73, no. 7, pp. 1008–1010, 1998. 53

[77] F. Bonell, S. Andrieu, F. Bertran, P. Lefevre, A. T. Ibrahimi, E. Snoeck, C. Tiusan, and F. Montaigne, "MgO-Based Epitaxial Magnetic Tunnel Junctions Using Fe-V Electrodes," *IEEE Trans, Magn.*, vol. 45, pp. 3467–3471, Oct. 2009. 53, 64, 94, 97, 98, 99, 100, 101, 103, 121

[78] J. C. Read, J. J. Cha, J. William F. Egelhoff, H. W. Tseng, P. Y. Huang, Y. Li, D. A. Muller, and R. A. Buhrman, "High magnetoresistance tunnel junctions with Mg-B-O barriers and Ni-Fe-B free electrodes," *Appl. Phys. Lett.*, vol. 94, no. 11, p. 112504, 2009. 53

[79] H. Kurt, K. Oguz, T. Niizeki, and J. M. D. Coey, "Giant tunneling magnetoresistance with electron beam evaporated MgO barrier and CoFeB electrodes," *J. Appl. Phys.*, vol. 107, no. 8, p. 083920, 2010. 53

[80] P.-J. Zermatten, G. Gaudin, G. Maris, M. Miron, a. Schuhl, C. Tiusan, F. Greullet, and M. Hehn, "Experimental evidence of interface resonance states in single-crystal magnetic tunnel junctions," *Phys. Rev. B*, vol. 78, pp. 1–4, July 2008. 54, 65, 76

[81] Y. Lu, H. Yang, C. Tiusan, M. Hehn, M. Chshiev, C. Bellouard, G. Kierren, B. Lengaige, A. Duluard, D. Lacour, and F. Montaigne, "Symmetry Dependent Scattering by Minority Interface Resonance States in Single-crystal Magnetic Tunnel Junctions," *ARXIV*, vol. arXiv:1106.1861, June 2011. 54, 65, 66, 67, 85, 113, 115

[82] T. X. Wang, Y. Li, K. J. Lee, J. U. Cho, D. K. Kim, S. J. Noh, and Y. K. Kim, "Influence of interface state in Fe/MgO/Fe magnetic tunnel junction system: C modified interfaces-a first principle study," *J. Appl. Phys.*, vol. 109, no. 8, p. 083714, 2011. 54, 64, 71, 86

[83] C. Tiusan, M. Sicot, M. Hehn, C. Belouard, S. Andrieu, F. Montaigne, and A. Schuhl, "Fe/MgO interface engineering for high-output-voltage device applications," *Appl. Phys. Lett.*, vol. 88, no. 6, p. 062512, 2006. 56, 128

[84] E. Popova, J. Faure-Vincent, C. Tiusan, C. Bellouard, H. Fischer, M. Hehn, F. Montaigne, M. Alnot, S. Andrieu, a. Schuhl, E. Snoeck, and V. da Costa, "Epitaxial MgO layer for low-resistance and coupling-free magnetic tunnel junctions," *Appl. Phys. Lett.*, vol. 81, no. 6, p. 1035, 2002. 57, 64, 80, 135, 136, 150

[85] J. L. Vassent, M. Dynna, A. Marty, B. Gilles, and G. Patrat, "A study of growth and the relaxation of elastic strain in MgO on Fe(001)," *J. Appl. Phys.*, vol. 80, no. 10, pp. 5727–5735, 1996. 58, 68, 98

[86] M. Klaua, D. Ullmann, J. Barthel, W. Wulfhekel, J. Kirschner, R. Urban, T. L. Monchesky, A. Enders, J. F. Cochran, and B. Heinrich, "Growth, structure, electronic, and magnetic properties of MgO/Fe(001) bilayers and Fe/MgO/Fe(001) trilayers," *Phys. Rev. B*, vol. 64, p. 134411, Sep 2001. 58, 68, 98

[87] J. Ventura, J. M. Teixeira, J. P. Araujo, J. B. Sousa, P. Wisniowski, and P. P. Freitas, "Pinholes and temperature-dependent transport properties of MgO magnetic tunnel junctions," *Phys. Rev. B*, vol. 78, p. 024403, Jul 2008. 61

[88] S. Wang, R. Ward, G. Du, X. Han, C. Wang, and A. Kohn, "Temperature dependence of giant tunnel magnetoresistance in epitaxial Fe/MgO/Fe magnetic tunnel junctions," *Phys. Rev. B*, vol. 78, pp. 2–5, Nov. 2008. 61, 62

[89] Q. L. Ma, S. G. Wang, J. Zhang, Y. Wang, R. C. C. Ward, C. Wang, A. Kohn, X.-G. Zhang, and X. F. Han, "Temperature dependence of resistance in

epitaxial Fe/MgO/Fe magnetic tunnel junctions," *Appl. Phys. Lett.*, vol. 95, no. 5, p. 052506, 2009. 62

[90] W. Brinkman, R. Dynes, and J. Rowell, "Tunneling Conductance of Asymmetrical Barriers," *J. Appl. Phys.*, vol. 41, p. 1915, 1970. 64

[91] C. Wang, A. Kohn, S. Wang, L. Chang, S.-Y. Choi, A. Kirkland, A. Petford-Long, and R. Ward, "Structural characterization of interfaces in epitaxial Fe/MgO/Fe magnetic tunnel junctions by transmission electron microscopy," *Phys. Rev. B*, vol. 82, pp. 1–9, July 2010. 64

[92] J. P. Velev, K. D. Belashchenko, S. S. Jaswal, and E. Y. Tsymbal, "Effect of oxygen vacancies on spin-dependent tunneling in Fe/MgO/Fe magnetic tunnel junctions," *App. Phys. Lett.*, vol. 90, no. 7, p. 072502, 2007. 64, 92

[93] Y. Ando, T. Miyakoshi, M. Oogane, T. Miyazaki, H. Kubota, K. Ando, and S. Yuasa, "Spin-dependent tunneling spectroscopy in single-crystal Fe/MgO/Fe tunnel junctions," *Appl. Phys. Lett.*, vol. 87, no. 14, p. 142502, 2005. 65

[94] A. Gokce, E. R. Nowak, S. H. Yang, and S. S. P. Parkin, "1/f noise in magnetic tunnel junctions with MgO tunnel barriers," *J. Appl. Phys.*, vol. 99, no. 8, p. 08A906, 2006. 84, 85, 156

[95] K. Sekiguchi, T. Arakawa, Y. Yamauchi, K. Chida, M. Yamada, H. Takahashi, D. Chiba, K. Kobayashi, and T. Ono, "Observation of full shot noise in CoFeB/MgO/CoFeB-based magnetic tunneling junctions," *Appl. Phys. Lett.*, vol. 96, no. 25, p. 252504, 2010. 87, 88

[96] T. Arakawa, K. Sekiguchi, S. Nakamura, K. Chida, Y. Nishihara, D. Chiba, K. Kobayashi, A. Fukushima, S. Yuasa, and T. Ono, "Sub-Poissonian shot noise in CoFeB/MgO/CoFeB-based magnetic tunneling junctions," *Appl. Phys. Lett.*, vol. 98, no. 20, p. 202103, 2011. 88

[97] Z. Diao, J. F. Feng, H. Kurt, G. Feng, and J. M. D. Coey, "Reduced low frequency noise in electron beam evaporated MgO magnetic tunnel junctions," *Appl. Phys. Lett.*, vol. 96, no. 20, p. 202506, 2010. 90, 153

[98] M. Bowen, V. Cros, F. Petroff, A. Fert, C. M. Boubeta, J. L. Costa-Krämer, J. V. Anguita, A. Cebollada, F. Briones, J. M. de Teresa, L. Morellón, M. R. Ibarra, F. Güell, F. Peiró, and A. Cornet, "Large magnetoresistance in Fe/MgO/FeCo(001) epitaxial tunnel junctions on GaAs(001)," *App. Phys. Lett.*, vol. 79, no. 11, pp. 1655–1657, 2001. 92, 128

[99] J. Faure-Vincent, C. Tiusan, E. Jouguelet, F. Canet, M. Sajieddine, C. Bellouard, E. Popova, M. Hehn, F. Montaigne, and A. Schuhl, "High tunnel magnetoresistance in epitaxial Fe/MgO/Fe tunnel junctions," *App. Phys. Lett.*, vol. 82, no. 25, pp. 4507–4509, 2003. 92, 128

[100] S. Yuasa, Y. Suzuki, T. Katayama, and K. Ando, "Characterization of growth and crystallization processes in CoFeB/MgO/CoFeB magnetic tunnel junction structure by reflective high-energy electron diffraction," *Appl.Phys. Lett.*, vol. 87, no. 24, p. 242503, 2005. 93, 94

[101] W. Wang, H. Sukegawa, R. Shan, S. Mitani, and K. Inomata, "Giant tunneling magnetoresistance up to 330% at room temperature in sputter deposited Co_2FeAl/MgO/CoFe magnetic tunnel junctions," *Appl. Phys. Lett.*, vol. 95, no. 18, p. 182502, 2009. 93

[102] N. Tezuka, N. Ikeda, F. Mitsuhashi, and S. Sugimoto, "Improved tunnel magnetoresistance of magnetic tunnel junctions with Heusler $Co_2FeAl_{0.5}Si_{0.5}$ electrodes fabricated by molecular beam epitaxy," *Appl. Phys. Lett.*, vol. 94, no. 16, p. 162504, 2009. 93

[103] W. G. Wang, C. Ni, A. Rumaiz, Y. Wang, X. Fan, T. Moriyama, R. Cao, Q. Y. Wen, H. W. Zhang, and J. Q. Xiao, "Real-time evolution of tunneling

magnetoresistance during annealing in CoFeB/MgO/CoFeB magnetic tunnel junctions," *Appl. Phys. Lett.*, vol. 92, no. 15, p. 152501, 2008. 94

[104] C. Scheck, L. Cheng, I. Barsukov, Z. Frait, and W. E. Bailey, "Low Relaxation Rate in Epitaxial Vanadium-Doped Ultrathin Iron Films," *Phys. Rev. Lett.*, vol. 98, p. 117601, Mar 2007. 94

[105] S. Amara-Dababi, R. C. Sousa, M. Chshiev, H. Béa, J. Alvarez-Hérault, L. Lombard, I. L. Prejbeanu, K. Mackay, and B. Dieny, "Charge trapping-detrapping mechanism of barrier breakdown in MgO magnetic tunnel junctions," *Appl. Phys. Lett.*, vol. 99, no. 8, p. 083501, 2011. 94, 125, 138

[106] M. Sicot, S. Andrieu, C. Tiusan, F. Montaigne, and F. Bertran, "On the quality of molecular-beam epitaxy grown Fe/MgO and Co/MgO(001) interfaces," *J. Appl. Phys.*, vol. 99, no. 8, p. 08D301, 2006. 95

[107] F. Bonell, A. M. Bataille, S. Andrieu, C. Tiusan, B. Kierren, G. Lengaigne, and D. Lacour, "Influence of interfacial oxygen on single-crystal magnetic tunnel," *Eur. Phys. J. Appl. Phys*, vol. 361, pp. 357–361, 2008. 97

[108] J. B. Staunton, S. S. A. Razee, M. F. Ling, D. D. Johnson, and F. J. Pinski, "Magnetic alloys, their electronic structure and micromagnetic and microstructural models," *J. Phy. D: Appl. Phys.*, vol. 31, no. 19, p. 2355, 1998. 97, 105

[109] D. D. Johnson, F. J. Pinski, and J. B. Staunton, "The Slater-Pauling curve: First principles calculations of the moments of $Fe_{1-c}Ni_c$ and V_cFe_{1-c}," *J. Appl. Phys.*, vol. 61, no. 8, pp. 3715–3717, 1987. 98, 124

[110] F. Bonell, *Analyse du transport dans les jonctions tunnel magntiques pitaxies barrire de MgO(001) par manipulation des interfaces, de la barrire et des lectrodes.* Thesis of luniversit Henri Poincar, Nancy, 2009. 100, 105

[111] B. Peric, T. Valla, M. Milun, and P. Pervan, "On the electronic structure of vanadium: the angular resolved photoelectron spectroscopy of V(100) surface," *Pergamon*, vol. 46, no. 8-10, p. 1181 to 1183, 1995. 104

[112] F. Bonell, S. Andrieu, C. Tiusan, F. Montaigne, E. Snoeck, B. Belhadji, L. Calmels, F. Bertran, P. Le Fèvre, and a. Taleb-Ibrahimi, "Influence of misfit dislocations on the magnetoresistance of MgO-based epitaxial magnetic tunnel junctions," *Phys. Rev. B*, vol. 82, pp. 1–4, Sept. 2010. 103, 108, 109

[113] B. Drittler, N. Stefanou, S. Blügel, R. Zeller, and P. H. Dederichs, "Electronic structure and magnetic properties of dilute Fe alloys with transition-metal impurities," *Phys. Rev. B*, vol. 40, pp. 8203–8212, Oct 1989. 105

[114] B. Belhadji and L. Calmels, "Bulk electron states with Δ symmetry in disordered Fe-based alloys for magnetic tunnel junctions," *Phys. Rev. B*, vol. 83, p. 092401, Mar 2011. 105, 106

[115] G.-X. Miao, K. B. Chetry, A. Gupta, W. H. Butler, K. Tsunekawa, D. Djayaprawira, and G. Xiao, "Inelastic tunneling spectroscopy of magnetic tunnel junctions based on CoFeB/MgO/CoFeB with Mg insertion layer," *Appl. Phys. Lett.*, vol. 99, no. 8, p. 08T305, 2006. 117

[116] K. Tamanoi, M. Sato, M. Oogane, Y. Ando, T. Tanaka, Y. Uehara, and T. Uzumaki, "Electrical conductance properties for magnetic tunnel junctions with MgO barriers," *J. Magn. Magn. Mater.*, vol. 320, no. 22, pp. 2959 – 2962, 2008. ¡ce:title¿Eighth Perpendicular Magnetic Recording Conference¡/ce:title¿. 117

[117] R. Matsumoto, A. Fukushima, K. Yakushiji, S. Yakata, T. Nagahama, H. Kubota, T. Katayama, Y. Suzuki, K. Ando, S. Yuasa, B. Georges,

V. Cros, J. Grollier, and A. Fert, "Spin-torque-induced switching and precession in fully epitaxial Fe/MgO/Fe magnetic tunnel junctions," *Phys. Rev. B*, vol. 80, p. 174405, Nov 2009. 121

[118] T. Nagahama, S. Yuasa, Y. Suzuki, and E. Tamura, "Quantum-well effect in magnetic tunnel junctions with ultrathin single-crystal Fe(100) electrodes," *Appl. Phys. Lett.*, vol. 79, no. 26, pp. 4381–4383, 2001. 128

[119] P. LeClair, H. J. M. Swagten, J. T. Kohlhepp, R. J. M. van de Veerdonk, and W. J. M. de Jonge, "Apparent Spin Polarization Decay in Cu-Dusted $Co/Al_2O_3/Co$ Tunnel Junctions," *Phys. Rev. Lett.*, vol. 84, pp. 2933–2936, Mar 2000. 128

[120] S. Yuasa, T. Nagahama, and Y. Suzuki, "Spin-Polarized Resonant Tunneling in Magnetic Tunnel Junctions," *Science*, vol. 297, no. 5579, pp. 234–237, 2002. 128

[121] F. Greullet, C. Tiusan, F. Montaigne, M. Hehn, D. Halley, O. Bengone, M. Bowen, and W. Weber, "Evidence of a Symmetry-Dependent Metallic Barrier in Fully Epitaxial MgO Based Magnetic Tunnel Junctions," *Phys. Rev. Lett.*, vol. 99, pp. 5–8, Nov. 2007. 128

[122] J. Peralta-Ramos, A. M. Llois, I. Rungger, and S. Sanvito, "I-V curves of Fe/MgO (001) single- and double-barrier tunnel junctions," *Phys. Rev. B*, vol. 78, p. 024430, Jul 2008. 128

[123] T. Nozaki, N. Tezuka, and K. Inomata, "Quantum Oscillation of the Tunneling Conductance in Fully Epitaxial Double Barrier Magnetic Tunnel Junctions," *Phys. Rev. Lett.*, vol. 96, p. 027208, Jan 2006. 130, 142

[124] Y. Wang, Z.-Y. Lu, X.-G. Zhang, and X. F. Han, "First-Principles Theory of Quantum Well Resonance in Double Barrier Magnetic Tunnel Junctions," *Phys. Rev. Lett.*, vol. 97, p. 087210, Aug 2006. 130, 140, 141, 144

[125] K. Majumdar and S. Hershfield, "Magnetoresistance of the double-tunnel-junction Coulomb blockade with magnetic metals," *Phys. Rev. B*, vol. 57, pp. 11521–11526, May 1998. 130

[126] G. Feng, S. van Dijken, and J. M. D. Coey, "MgO-based double barrier magnetic tunnel junctions with thin free layers," *J. Appl. Phys.*, vol. 105, no. 7, p. 07C926, 2009. 130

[127] Z.-M. Zeng, X.-F. Han, W.-S. Zhan, Y. Wang, Z. Zhang, and S. Zhang, "Oscillatory tunnel magnetoresistance in double barrier magnetic tunnel junctions," *Phys. Rev. B*, vol. 72, p. 054419, Aug 2005. 130

[128] R. Guerrero, M. Pannetier-Lecoeur, C. Fermon, S. Cardoso, R. Ferreira, and P. P. Freitas, "Low frequency noise in arrays of magnetic tunnel junctions connected in series and parallel," *J. Appl. Phys.*, vol. 105, no. 11, p. 113922, 2009. 131

[129] A. N. Useinov, J. Kosel, N. K. Useinov, and L. R. Tagirov, "Resonant tunnel magnetoresistance in double-barrier planar magnetic tunnel junctions," *Phys. Rev. B*, vol. 84, p. 085424, Aug 2011. 131

[130] M. H. Jung, S. Park, C.-Y. You, and S. Yuasa, "Bias dependences of in-plane and out-of-plane spin-transfer torques in symmetric MgO-based magnetic tunnel junctions," *Phys. Rev. B*, vol. 81, p. 134419, Apr 2010. 132

[131] C. Tiusan, F. Greullet, M. Sicot, M. Hehn, C. Bellouard, F. Montaigne, S. Andrieu, and A. Schuhl, "Engineering of spin filtering in double epitaxial tunnel junctions," *Appl. Phys. Lett.*, vol. 99, no. 8, p. 08A903, 2006. 134

[132] C. Yang, M. Samant, and S. Parkin *APS2009 March Meeting*, vol. 59, no. 1, 2009. 134, 139

[133] D. V. Dimitrov, Z. Gao, X. Wang, W. Jung, X. Lou, and O. G. Heinonen, "Dielectric breakdown of MgO magnetic tunnel junctions," *Appl. Phys. Lett.*, vol. 94, no. 12, p. 123110, 2009. 134

[134] J. Costa-Krämer, J. Menéndez, A. Cebollada, F. Briones, D. Garcia, and A. Hernando, "Magnetization reversal asymmetry in Fe/MgO(001) thin films," *J. Magn. Magn. Mater.*, vol. 210, no. 1-3, pp. 341 – 348, 2000. 135, 136

[135] C. Martínez Boubeta, J. L. Costa-Krämer, and A. Cebollada, "Epitaxy, magnetic and tunnel properties of transition metal/MgO(001) heterostructures," *J. Phys.: Condens. Matter*, vol. 15, no. 25, p. R1123, 2003. 136

[136] H. Xi, S. Franzen, J. I. Guzman, and S. Mao, "Degradation of magnetic tunneling junctions caused by pinhole formation and growth," *J. Magn. Magn. Mater.*, vol. 319, pp. 60 – 63, 2007. 138

[137] V. Da Costa, C. Tiusan, T. Dimopoulos, and K. Ounadjela, "Tunneling Phenomena as a Probe to Investigate Atomic Scale Fluctuations in Metal/Oxide/Metal Magnetic Tunnel Junctions," *Phys. Rev. Lett.*, vol. 85, pp. 876–879, Jul 2000. 138

[138] K.-S. Kim, B. K. Cho, T. W. Kim, and W. J. Park, "Junction area dependence of breakdown characteristics in magnetic tunnel junctions," *Appl. Phys. Lett.*, vol. 93, no. 10, pp. 8364–8366, 2003. 138

[139] A. Thomas, V. Drewello, M. Schäfers, A. Weddemann, G. Reiss, G. Eilers, M. Münzenberg, K. Thiel, and M. Seibt, "Direct imaging of the structural change generated by dielectric breakdown in MgO based magnetic tunnel junctions," *Appl. Phys. Lett.*, vol. 93, no. 15, p. 152508, 2008. 138

[140] X. Liu, C. Ren, and G. Xiao, "Magnetic tunnel junction field sensors with hard-axis bias field," *Phys. Rev. Lett.*, vol. 92, no. 8, pp. 4722–4725, 2002. 142

[141] I. Lifshitz and V. Y. Kirpichenkov, "On tunnel transparency of disordered systems," *Sov. Phys. JETP*, vol. 50, p. 499, 1979. 145

[142] J.-G. Zhu, "Pinholes and spin transfer effect in magnetic tunnel junction heads," *J. Appl. Phys.*, vol. 97, no. 10, p. 10N703, 2005. 148

[143] D. Houssameddine, U. Ebels, B. Dieny, K. Garello, J.-P. Michel, B. Delaet, B. Viala, M.-C. Cyrille, J. A. Katine, and D. Mauri, "Temporal Coherence of MgO Based Magnetic Tunnel Junction Spin Torque Oscillators," *J. Appl. Phys.*, vol. 102, p. 257202, Jun 2009. 148, 151, 152

[144] Y. Nagamine, H. Maehara, K. Tsunekawa, D. D. Djayaprawira, N. Watanabe, S. Yuasa, and K. Ando, "Ultralow resistance-area product of 0.4 $\Omega(\mu$ m$)^2$ and high magnetoresistance above 50% in CoFeB/MgO/CoFeB magnetic tunnel junctions," *Appl. Phys. Lett.*, vol. 89, no. 16, p. 162507, 2006. 150, 151

[145] K. Tsunekawa, D. D. Djayaprawira, M. Nagai, H. Maehara, S. Yamagata, N. Watanabe, S. Yuasa, Y. Suzuki, and K. Ando, "Giant tunneling magnetoresistance effect in low-resistance CoFeB/MgO(001)/CoFeB magnetic tunnel junctions for read-head applications," *Appl. Phys. Lett.*, vol. 87, no. 7, p. 072503, 2005. 150, 151

[146] S. Brems, K. Temst, and C. Van Haesendonck, "Origin of the training effect and asymmetry of the magnetization in polycrystalline exchange bias systems," *Phys. Rev. Lett.*, vol. 99, p. 067201, Aug 2007. 151, 157

[147] S. Petit, N. de Mestier, C. Baraduc, C. Thirion, Y. Liu, M. Li, P. Wang, and B. Dieny, "Influence of spin-transfer torque on thermally activated ferromagnetic resonance excitations in magnetic tunnel junctions," *Phys. Rev. B*, vol. 78, p. 184420, Nov 2008. 151

[148] T. Wada, T. Yamane, T. Seki, T. Nozaki, Y. Suzuki, H. Kubota, A. Fukushima, S. Yuasa, H. Maehara, Y. Nagamine, K. Tsunekawa, D. D.

Djayaprawira, and N. Watanabe, "Spin-transfer-torque-induced rf oscillations in CoFeB/MgO/CoFeB magnetic tunnel junctions under a perpendicular magnetic field," *Phys. Rev. B*, vol. 81, p. 104410, Mar 2010. 151

[149] Z. M. Zeng, P. K. Amiri, G. Rowlands, H. Zhao, I. N. Krivorotov, J.-P. Wang, J. A. Katine, J. Langer, K. Galatsis, K. L. Wang, and H. W. Jiang, "Effect of resistance-area product on spin-transfer switching in MgO-based magnetic tunnel junction memory cells," *Appl. Phys. Lett.*, vol. 98, no. 7, p. 072512, 2011. 151

[150] R. Matsumoto, A. Chanthbouala, J. Grollier, V. Cros, A. Fert, K. Nishimura, Y. Nagamine, H. Maehara, K. Tsunekawa, A. Fukushima, and S. Yuasa, "Spin-Torque Diode Measurements of MgO-Based Magnetic Tunnel Junctions with Asymmetric Electrodes," *Appl. Phys. Express*, vol. 4, p. 063001, June 2011. 151

[151] A. Tulapurkar, Y. Suzuki, A. Fukushima, H. Kubota, H. Maehara, K. Tsunekawa, D. Djayaprawira, H. Watanabe, and S. Yuasa, "Spin-torque diode effect in magnetic tunnel junctions," *Nature*, vol. 3, pp. 339–342, Nov. 2005. 151

[152] K. Komagaki, K. Yamada, K. Noma, H. Kanai, K. Kobayashi, Y. Uehara, M. Tsunoda, and M. Takahashi, "Large Exchange Bias and High Blocking Temperature of MgO-Barrier-MTJs With $L1_2$-Ordered Mn3Ir," *Magnetics, IEEE Transactions on*, vol. 43, pp. 3535 –3537, aug. 2007. 152

[153] A. Ozbay, A. Gokce, T. Flanagan, R. A. Stearrett, E. R. Nowak, and C. Nordman, "Low frequency magnetoresistive noise in spin-valve structures," *Appl. Phys. Lett.*, vol. 94, no. 20, p. 202506, 2009. 153

[154] J. Scola, H. Polovy, C. Fermon, M. Pannetier-Lecœur, G. Feng, K. Fahy, and J. M. D. Coey, "Noise in MgO barrier magnetic tunnel junctions with

CoFeB electrodes: Influence of annealing temperature," *Appl. Phys. Lett.*, vol. 90, no. 25, p. 252501, 2007. 153

[155] R. Stearrett, W. G. Wang, L. R. Shah, A. Gokce, J. Q. Xiao, and E. R. Nowak, "Evolution of barrier-resistance noise in CoFeB/MgO/CoFeB tunnel junctions during annealing," *J. Appl. Phys.*, vol. 107, no. 6, p. 064502, 2010. 153

[156] D. Mazumdar, X. Liu, B. D. Schrag, M. Carter, W. Shen, and G. Xiao, "Low frequency noise in highly sensitive magnetic tunnel junctions with (001) MgO tunnel barrier," *Appl. Phys. Lett.*, vol. 91, no. 3, p. 033507, 2007. 153

[157] C. Tiusan, T. Dimopoulos, K. Ounadjela, M. Hehn, H. A. M. van den Berg, V. da Costa, and Y. Henry, "Correlation between micromagnetism and tunnel magnetoresistance in magnetic tunnel junctions using artificial ferrimagnets," *Phys. Rev. B*, vol. 61, pp. 580–593, Jan 2000. 153

[158] A. Reinartz, J. Schmalhorst, and G. Reiss, "Influence of annealing temperature and thickness of a CoFeB middle layer on the tunnel magnetoresistance of MgO based double barrier magnetic tunnel junctions," *J. Appl. Phys.*, vol. 105, no. 1, p. 014510, 2009. 154, 158

[159] D. D. Djayaprawira, K. Tsunekawa, M. Nagai, H. Maehara, S. Yamagata, N. Watanabe, S. Yuasa, Y. Suzuki, and K. Ando, "230% room-temperature magnetoresistance in CoFeB/MgO/CoFeB magnetic tunnel junctions," *App. Phys. Lett.*, vol. 86, no. 9, p. 092502, 2005. 154

[160] J. Hayakawa, S. Ikeda, F. Matsukura, H. Takahashi, and H. Ohno, "Dependence of Giant Tunnel Magnetoresistance of Sputtered CoFeB/MgO/CoFeB Magnetic Tunnel Junctions on MgO Barrier Thickness and Annealing Temperature," *Jpn. J. Appl. Phys.*, vol. 44, no. 19, pp. L587–L589, 2005. 154

[161] W. G. Wang, C. Ni, A. Rumaiz, Y. Wang, X. Fan, T. Moriyama, R. Cao, Q. Y. Wen, H. W. Zhang, and J. Q. Xiao, "Real-time evolution of tunneling magnetoresistance during annealing in CoFeB/MgO/CoFeB magnetic tunnel junctions," *Appl. Phys. Lett.*, vol. 92, no. 15, p. 152501, 2008. 154

[162] K. Tsumekawa, D. Djayaprawira, M. Nagai, H. Maehara, S. Yamagata, and N. Watanabe, "Effect of capping layer material on tunnel magnetoresistance in CoFeB-MgO-CoFeB magnetic tunnel junctions," in *Magnetics Conference, 2005. INTERMAG Asia 2005. Digests of the IEEE International*, pp. 1983 – 1984, april 2005. 154

[163] P. W. T. Pong and W. F. Egelhoff, "Enhancement of tunneling magnetoresistance by optimization of capping layer thicknesses in CoFeB/MgO/CoFeB magnetic tunnel junctions," *J. Appl. Phys.*, vol. 105, no. 7, p. 07C915, 2009. 154

[164] W. Skowroński, T. Stobiecki, J. Wrona, K. Rott, A. Thomas, G. Reiss, and S. van Dijken, "Interlayer exchange coupling and current induced magnetization switching in magnetic tunnel junctions with MgO wedge barrier," *J. Appl. Phys.*, vol. 107, no. 9, p. 093917, 2010. 155

[165] J. Bednarik, J. Kova, V. Kaveansky, and P. Kollar *J. Electr. Eng.*, vol. 53, p. 170, 2002. 159

[166] G. C. Han, B. Y. Zong, P. Luo, and C. C. Wang, "Magnetic field dependence of low frequency noise in tunnel magnetoresistance heads," *J. Appl. Phys.*, vol. 107, no. 9, p. 09C706, 2010. 161

[167] S. Urazhdin, N. O. Birge, W. P. Pratt, and J. Bass, "Current-Driven Magnetic Excitations in Permalloy-Based Multilayer Nanopillars," *Phys. Rev. Lett.*, vol. 91, p. 146803, Oct 2003. 162, 165

[168] M. Covington, M. AlHajDarwish, Y. Ding, N. J. Gokemeijer, and M. A. Seigler, "Current-induced magnetization dynamics in current perpendicular to the plane spin valves," *Phys. Rev. B*, vol. 69, p. 184406, May 2004. 162, 163, 165

[169] J. Cucchiara, Y. Henry, D. Ravelosona, D. Lacour, E. E. Fullerton, J. A. Katine, and S. Mangin, "Telegraph noise due to domain wall motion driven by spin current in perpendicular magnetized nanopillars," *Appl. Phys. Lett.*, vol. 94, no. 10, p. 102503, 2009. 162, 165

[170] M. J. Donahue and D. G. Porter, "(Object Oriented Micro Magnetic Framework) Users Guide, Version 1.0, Interagency Report NISTIR 6376, National Institute of Standards and Technology, Gaithersburg, MD," *OOMMF*, Sept.1999. 164

[171] D. Kirk, A. Kohn, K. B. Borisenko, C. Lang, J. Schmalhorst, G. Reiss, and D. J. H. Cockayne, "Structural study of amorphous CoFeB thin films exhibiting in-plane uniaxial magnetic anisotropy," *Phys. Rev. B*, vol. 79, p. 014203, Jan 2009. 164

[172] A. Chanthbouala, R. Matsumoto, J. Grollier, V. Cros, A. Anane, A. Fert, A. V. Khvalkovskiy, K. A. Zvezdin, K. Nishimura, Y. Nagamine, H. Maehara, K. Tsunekawa, A. Fukushima, and S. Yuasa, "Vertical-current-induced domain-wall motion in MgO-based magnetic tunnel junctions with low current densities," *Nat. Phys.*, vol. 7, no. 8, pp. 626–630, 2011. 165, 169

[173] J. C. Sankey, Y.-T. Cui, J. Z. Sun, J. C. Slonczewski, R. A. Buhrman, and D. C. Ralph, "Measurement of the spin-transfer-torque vector in magnetic tunnel junctions," *Nature Phy.*, no. 4, pp. 67–71, 2008. 165

[174] M. D. Mascaro, C. Nam, and C. A. Ross, "Interactions between 180 and 360 domain walls in magnetic multilayer stripes," *Appl. Phys. Lett.*, vol. 96, no. 16, p. 162501, 2010. 165

[175] T. Seki, A. Fukushima, H. Kubota, K. Yakushiji, S. Yuasa, and K. Ando, "Switching-probability distribution of spin-torque switching in MgO-based magnetic tunnel junctions," *Appl. Phys. Lett.*, vol. 99, no. 11, p. 112504, 2011. 165

[176] S. S. P. Parkin, M. Hayashi, and L. Thomas, "Magnetic Domain-Wall Racetrack Memory," *Science*, vol. 320, no. 5873, pp. 190–194, 2008. 167

[177] A. Yamaguchi, S. Nasu, H. Tanigawa, T. Ono, K. Miyake, K. Mibu, and T. Shinjo, "Effect of joule heating in current-driven domain wall motion," *Appl. Phys. Lett.*, vol. 86, no. 1, p. 012511, 2005. 167

[178] A. S. Nuñez, R. Duine, P. Haney, and A. MacDonald, "Theory of spin torques and giant magnetoresistance in antiferromagnetic metals," *Phys. Rev. B*, vol. 73, p. 214426, 2006. 167